University of California

Los Angeles

Observations of

Crab Nebula and Pulsar with VERITAS

A dissertation submitted in partial satisfaction

of the requirements for the degree

Doctor of Philosophy in Physics

by

Özlem Çelik

2008

The dissertation of Özlem Çelik is approved.

Katsushi Arisaka

Ferdinand Coroniti

Kevin McKeegan

René Ong, Committee Chair

University of California, Los Angeles

2008

To my parents ...

for their endless love and support at all times.

Table of Contents

List of Figures

List of Tables

Acknowledgments

I would first like to thank my adviser, Rene Ong, for all his support, encouragement, and patience, and his confidence in me throughout my graduate years. In fact, it was a seminar he gave during my first year of graduate school that sparked my interest in the astroparticle physics field, and which eventually led to my decision to work in this field for my PhD research. Throughout that research, he provided endless amounts of help, feedback and direction. He showed me the big picture when I was mired in the details, and he allowed me to work at my own pace. During the frantic thesis writing time, he spent a great deal of time reading my thesis -and reading it again- and, he offered untold numbers of constructive comments and criticism, and he even corrected my English.

I would also like to thank to Vladimir Vassiliev for all of his time and the explanations he gave on various subjects, all of which helped me gain a deeper understanding of the detector hardware, analysis methods, and of astrophysics in general. Likewise, I want to thank Simon Swordy for providing me a work space during my years in Chicago and advising me on various research issues as well as on possible career paths and for writing me those valuable reference letters, of course. I cannot adequately thank Trevor Weekes for his supervision on my work while I was in Tucson, for the discussions I had with him about the optical pulsar data, and for making time available to write all of those reference letters for me.

I would like very much to thank to the VERITAS group at UCLA: Steve, Ken, Matthew, Amanda, Tim, and our STACEE friend, Alex, all of whom worked with me on this project. Thanks for all of the discussions and exchanges of ideas during the group meetings. I learned a lot from all of you... Special thanks also go to Steve, Matthew, Ken, and Mary, who read my thesis and corrected my English.

I cannot thank enough especially to Steve, who read more than half of my thesis and gave copious amounts of valuable feedback to improve it.

Many thanks to all my fellow astronomy department graduate students for sharing this graduate school experience with me. Thanks for all of the funny emails you sent to the grads' mail list, which made my day most of the time with the laughter they inspired... And, of course, thanks to the fairies for the mobile and the hat!

Additional thanks go to my friends Mary, Judy, and Tatiana. Thank you for your valuable friendship, for meeting with me for lunches, dinners, movies, and for all the fun we had together. You were like my family in the States, and your special friendship and support was crucial fuel for me to get through all the graduate years.

Of course, I cannot forget my roommates, Gülden, Sinem, and Melis. I started this journey with Gulden and Sinem, and ended with Melis. Thank you all for sharing this home with me, for putting up with all my physical explanations for everything in daily life, (Gülden: it was the Sun not the Moon :)), and Melis, thanks for all the conversations "in odd hours". Finally, special thanks to Mustafa for enduring all the mess at home and my constant change of plans during the thesis writing period, and for going over my thesis.

And finally, I am grateful to my parents, for their endless love, support and trust in me at all times. Without them, I would not be the person I am. And my dear brothers, Orhan and Mustafa: you were always there for me.

Vita

October 29, 1976	Born in Bursa, Turkey
1993-1998	Boğaziçi (Bosphorus) University, Istanbul, Turkiye
1998	B.S. Physics, Boğaziçi (Bosphorus) University, Istanbul, Turkiye
1998-2000	Teaching Assistant, Boğaziçi (Bosphorus) University, Istanbul, Turkiye
2000-2001	M.S. Physics, University of California, Los Angeles
2000-2008	University of California, Los Angeles
2001-2002	Teaching Assistant, Department of Physics and Astronomy, UCLA.
2002–2008	Research Assistant, Department of Physics and Astronomy, UCLA.
2008	Ph.D. Physics, University of California, Los Angeles

Publications and Presentations

Ozlem Celik for the VERITAS Coll., "Observations of Crab Nebula and Pulsar". Poster presented at the AAS/High Energy Astrophysics Division Meeting, 10, #12.09, Los Angeles(April, 2008).

Ozlem Celik et al., "Observations of the Crab Nebula and Pulsar with VERITAS". In Proceedings of the 30th ICRC, Merida, Mexico. arXiv:0709.3868. (September, 2007)

Ozlem Celik for the VERITAS Coll., "Observations of the Crab Nebula and Pulsar with VERITAS". Paper presented at the 30th ICRC, Merida, Mexico (July, 2007).

Ozlem Celik for the VERITAS Coll., "Status and Performance of VERITAS". Talk presented at the APS April Meeting, Jacksonville (April, 2007).

Abstract of the Dissertation

Observations of Crab Nebula and Pulsar with VERITAS

by

Özlem Çelik

Doctor of Philosophy in Physics

University of California, Los Angeles, 2008

Professor René Ong, Chair

The Crab Nebula, the standard candle in very-high-energy (VHE) astronomy, is one of the most studied sources in all of astronomy. It is scientifically important to measure the energy spectrum of the Crab Nebula close to the inverse Compton peak or above 10 TeV where a deviation from the power law, seen at energies between 300 GeV and ∼5 TeV, may occur. Additionally, it is important to search for pulsed emission from the Crab Pulsar at energies beyond 10 GeV which is the upper limit of the EGRET detection of pulsed emission. Since current models predict a cut-off in the pulsed emission between 10 and 100 GeV, measurements at energies close to this range may help to discriminate between them. With these motivations, the Crab has been observed during the 2-, 3-, and 4-telescope phases of the commissioning of the Very Energetic Radiation Imaging Telescope Array System (VERITAS). The energy spectrum of the Crab Nebula between 350 GeV and 6 TeV is constructed from these data sets. A simple power law, $\frac{\mathrm{dN}}{\mathrm{dE}} = (3.19 \pm 0.07_{\mathrm{stat}} \pm 0.70_{\mathrm{sys}}) \times 10^{-7} \, (\frac{\mathrm{E}}{1\mathrm{TeV}})^{(2.40 \pm 0.03_{stat} \pm 0.17_{sys})} \, \mathrm{TeV}^{-1}\mathrm{m}^{-2}\mathrm{s}^{-1}$, is

found to give the best fit to the data obtained with the full 4-telescope array of VERITAS. Furthermore, a periodic modulation is searched for in the gamma-ray emission above 100 GeV at the Crab Pulsar period of 33 ms. The Crab data set from the 2006-2008 VERITAS observations did not show any significant pulsed excess, so an upper limit on the pulsed emission from the Crab Pulsar is obtained. This upper limit constrains the cutoff energy of the spectrum to be less than 50 GeV, assuming that the differential energy spectrum of the pulsed emission has an exponential cutoff.

CHAPTER 1

Gamma-Ray Astronomy

1.1 Introduction

The core of the research described in this thesis is the study of very-high-energy gamma-ray emission from the Crab Nebula and the search for pulsed emission in the same energy regime from the Crab Pulsar using data recorded by the Very Energetic Radiation Imaging Telescope Array System (VERITAS). VERITAS is a ground-based observatory comprised of an array of four Cherenkov telescopes, designed to detect gamma rays above $\sim$100 GeV. It uses the imaging atmospheric Cherenkov technique to detect gamma rays by imaging the Cherenkov light of the extensive air shower generated when a gamma ray enters the Earth's atmosphere.

Gamma-ray astronomy is experiencing a very exciting and fruitful period. Viewing the Universe in gamma rays, which is one of the last remaining unexplored windows in the electromagnetic spectrum, reveals to us a very dynamic and violent face of our Universe, which enhances our understanding of numerous astronomical objects and some of the highest energy phenomena. Similar to all new areas of science, it also generates myriad new questions of its own and exposes more mysteries about nature. Pulsars are one of these mysteries. Indeed, we still do not know how and where they accelerate particles in their environment to lead to their high-energy emission. Currently, there are a few popular models that attempt to explain the high-energy pulsed emission from pulsars, and these

can be tested by the detection and study of their highest energy emission and by determining its cut-off energy. To date, the highest energy pulsed emission from pulsars was detected by the EGRET experiment around 10 GeV with no significant evidence of a cut-off. This provided the impetus for this research to search for the pulsed emission and its cut-off in the higher energy band in which VERITAS is sensitive.

The Crab Nebula is a pulsar wind nebula system, and it is considered as the standard candle of gamma-ray astronomy due to its strong and steady emission. With the Crab Pulsar at its center, it provides a good opportunity to both study its steady emission and calibrate the newly commissioned VERITAS instrument, while simultaneously searching for pulsed emission. Study of the steady emission from the Crab Nebula has its own scientific merits as well: the power-law nature of its energy spectrum is well established between $\sim$300 GeV and $\sim$10 TeV; however, a test of the reported deviations from this simple power-law near the inverse-Compton peak of the spectrum around 100 GeV is important. With this intention, the energy spectrum of the steady emission from the Crab Nebula is measured as a part of the research reported in this thesis.

In the following sections gamma-ray astronomy is introduced and the major gamma-ray detectors operated to date are summarized. A brief discussion of main astrophysical sources of gamma rays is also presented in this chapter. At the end of this chapter, a guide to the thesis is given.

1.2 Gamma Rays

Gamma rays represent light in the highest energy range in the electromagnetic spectrum (Figure 1.1). They possess energies from $\sim$1 MeV to 10^{20} eV. Light in

this energy range has wavelengths shorter than 10^{-12} m and frequencies above $\sim 10^{21}$ Hz. A gamma ray has an energy of more than 6 to 20 orders of magnitude greater than the energy of a visible light photon.

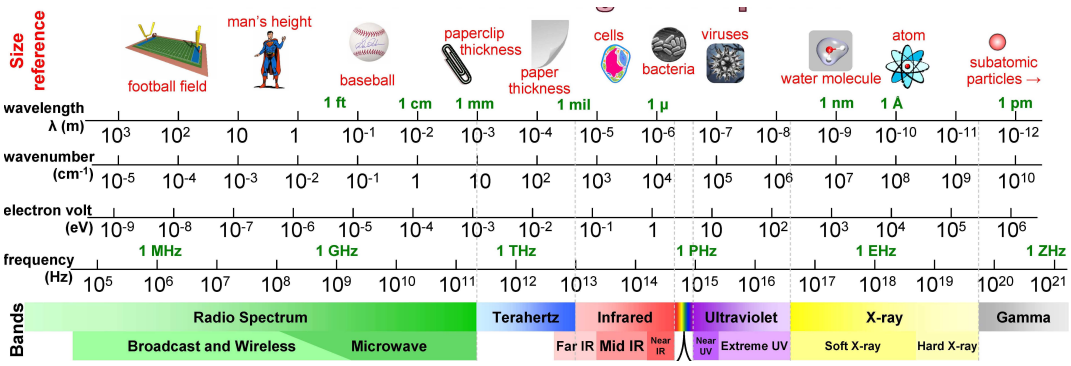

Figure 1.1: The various wavelength, frequency and energy bands of the electromagnetic spectrum are shown.

Since the span of the energy range of gamma rays is almost as many decades as the rest of the electromagnetic spectrum, dividing the gamma-ray energy range into smaller bands is quite useful in order to be more specific. This division is historically made such that the gamma-ray energy band between 30 MeV and 10 GeV is defined as high-energy (HE) [17], between 10 GeV and 100 TeV as very-high-energy (VHE), between 100 TeV to 100 PeV as ultra-high-energy (UHE), and between 100 PeV and 100 EeV as extremely-high-energy (EHE) [19]. In time, as the gamma-ray astronomy field advanced, this division was changed slightly so that the VHE band is now accepted to begin around 100 GeV [20], at the approximate energy that divides the separate accessible energy regions of space- and ground-based detectors.

Although both gamma rays and visible light represent the same type of electromagnetic radiation and differ only in energy, the processes producing them are significantly different. While lower energy photons are typically produced by

thermal mechanisms, only non-thermal processes have sufficient energy budgets to create gamma rays. In the universe, gamma rays are produced by hadronic or leptonic particle interactions in regions of extreme gravitational or magnetic fields and by the charged particles accelerated to nearly the speed of light at sites where fast-moving flows of energetic particles are produced. In these natural laboratories where extreme physical conditions are at work, gamma rays are the best probe to study the universe at the highest energies.

1.3 Motivations for Gamma-Ray Astronomy

Aside from gamma rays, another important example of non-thermal particles are cosmic rays. Cosmic rays were discovered almost a century ago by Victor Hess [21], but they are still mysterious in many ways. Their spectrum spans roughly fourteen decades of energy from 10^6 eV to 10^{20} eV, with no indication of thermal characteristics. Their spectrum is almost a featureless power law throughout this range, except at three points where the slope changes slightly. It was reported recently that the flux of cosmic rays begins to show a strong suppression above 4×10^{19} eV [22], as expected from the Greisen-Zatsepin-Kuzmin (GZK) cutoff due to the interactions between cosmic rays and the photons of the microwave background radiation. A power-law spectrum extending to such high energies is evidence for the non-thermal nature of production of cosmic rays at powerful astrophysical accelerators.

Unfortunately, due to their charge, cosmic rays below 10^{17} eV are significantly deflected by galactic magnetic fields, losing all information about their initial direction. Thus, it is impossible to trace most of them back to their origins for astrophysical identification and to study their sources. On the other hand, the hadronic or electromagnetic processes that produce cosmic rays can also produce

gamma rays as secondary particles. Since uncharged gamma rays are not affected by magnetic fields, they can be traced back to their origin to obtain information about the sources capable of the production or acceleration of particles to these extreme energies. Detecting gamma rays to learn about the origin of cosmic rays was first suggested in 1958 [23], and it was the primary motivation for gamma-ray astronomy.

In time, with the discovery of many new sources of different types, gamma-ray astronomy has become a field of its own, independent of cosmic-ray research, and with its own questions and goals. Gamma rays represent one of the last unexplored windows of electromagnetic spectrum in the universe. As with every new energy window, it reveals a new view of the universe. This gamma-ray universe is a violent one in which there are powerful sources capable of emitting photons of extreme energy. It is a universe where a single explosion releases more energy than the amount released by our Sun in a billion years and where black holes accelerate particles to the speed of light in the jets formed from the accretion of matter. Consequently, the primary motivation for gamma-ray astronomy is to understand as much as possible about these highest energy astrophysical accelerators, to study these sources in which conventional physics operates under extreme conditions, and to possibly encounter new phenomena for which new physics laws are required.

Driven by these motivations, gamma-ray astronomy has rapidly flourished after the first detection of astrophysical gamma rays in the late 1960s by satellite missions in space and after the development of indirect detection methods which made gamma-ray observations by ground-based observatories possible.

1.4 Gamma-Ray Detectors

The Earth's atmosphere absorbs gamma rays preventing them reaching the ground, which is fortunate because such energetic radiation is harmful to life. Thus, detecting gamma rays directly is only possible with high-altitude balloons or satellites in space. There is also the possibility for the use of indirect detection methods to detect them from the ground. Another problem with directly detecting high-energy gamma rays is that they pass through any lens or mirror leaving no chance of focusing them with a telescope. Thus, compared to other branches of astronomy gamma ray detectors must use different techniques more suitable to handling high-energy particles.

1.4.1 Space-Based Detectors

Gamma-ray photons are detected by space-based detectors through the pair-production process (see Section 3.2). The resulting electron-positron pair can be easily and unambiguously identified as two tracks originating from the same point in the tracking system of a space-based detector and they represent a signature of the initial gamma ray. The tracks of the resulting pair are used to reconstruct the arrival direction of the initial gamma ray. Examples of tracking detectors are the use of several layers of silicon strip detectors as in the case of Large Area Telescope (LAT) in the Fermi Gamma-ray Space Telescope (FGST) [24] or the spark chambers as used in the EGRET experiment [25] discussed below. The energy of the initial gamma ray can be found by another central component of a space-based detector, the calorimeter, which absorbs the electromagnetic particles to record their total energy. This recorded energy is used to reconstruct the energy of the incident gamma-ray. One major obstacle of a space-based detector is dealing with the enormous background flux of charged cosmic-ray

particles which leave similar signatures as gamma rays. Space detectors use an anti-coincidence shield surrounding the main detector to detect and reject charged cosmic-ray particles. Thus, a signal of similar signature in the tracking detector is not identified as a gamma ray if the anti-coincidence shield detects the passage of a charged particle. The three main components of a space-based detector can be seen in Figure 1.2, for in the case of the LAT detector on FGST, which is the current operating space-based gamma-ray detector.

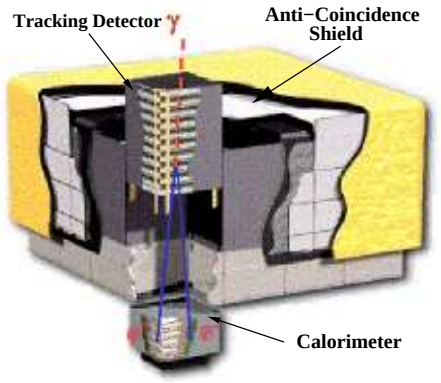

Figure 1.2: Three main components of a space-based detector are labeled on the model of the LAT detector [26] for FGST: The anti-coincidence shield, the tracking detector and the calorimeter. How these components are used to detect a gamma ray is explained in the text.

Space-based detectors unfortunately have relatively small collection areas because of the technical difficulty in launching a large detector. Due to the decrease in gamma-ray flux with increasing energy, these detectors have limited access to gamma rays with energies higher than around 100 GeV. Fortunately, at around the same energy of 100 GeV, gamma rays can be detected indirectly on Earth with ground-based detection techniques.

The first significant detection of astrophysical gamma rays was made by large

balloon-borne detectors in the late 1960s and early 1970s; they discovered gamma-ray emission in the HE band from the Crab Pulsar [27, 28, 29]. They were ultimately limited by their inability to distinguish the HE gamma rays from the extensive background of cosmic rays. Due to this difficulty, the only significant detection was the Crab Pulsar, thanks to its timing properties which helped to extract the gamma-ray signal from random background.

The first successful gamma-ray space telescopes were the SAS-II (Small Astronomy Satellite-II), launched in 1972, and the COS-B (COsmic ray Satellite-B), launched in 1975. They demonstrated the possibility of detecting high-energy gamma rays from space. Their results include the discovery of a number of point sources of gamma rays and the detection of the diffuse gamma-ray glow of our galactic plane. Out of four sources discovered by SAS-II, the Crab and Vela pulsars, Cygnus X-3 and $\gamma 195 + 5$, the first three were identified based on their timing properties, and the last source remained unidentified due to the instrument's large angular resolution of $\sim 2^{\circ}$. The data from the first three years of observations with COS-B experiment led discovery of 25 sources, with only the Crab, Vela, 3C273 and the ρ-Ophiuchi cloud complex identified. The energy range of the SAS-II was 35 MeV - 1 GeV, while the energy range for COS-B was 150 MeV - 5 GeV. More details can be found in [30] and [31].

The Compton Gamma Ray Observatory (CGRO) was launched in 1991 and it remained in orbit until 2000 (Figure 1.4). This observatory was one of NASA's "Great Observatories" and it revolutionized gamma-ray astronomy. It carried four scientific instruments, BATSE [32], OSSE [33], COMPTEL [34] and EGRET [25, 35] which were designed to simultaneously cover the gamma-ray energy range from 15 keV to 30 GeV. EGRET, which was the highest energy instrument on CGRO, sensitive in the energy range of 20 MeV to $\sim$30 GeV, made the most

impact to high energy gamma-ray astronomy. Before its launch only one extragalactic high energy gamma-ray source was known, a quasar 3C273. After the first four years of operation, EGRET extended the high energy gamma-ray source catalog to more than 250 sources above 100 MeV, as listed in the "Third EGRET catalog" [35] (Figure 1.3). The highlights of its results were about 90 extragalactic sources, mostly of the blazar type, six pulsars with emission extending above $\sim$5 GeV and 170 unidentified sources not clearly associated with any known astrophysical object. It also detected gamma rays from the Magellanic Clouds and from solar flares, and it made a detailed map of the diffuse emission along the galactic plane (Figure 1.3).

AGILE, Astro-rivelatore Gamma a Immagini LEggero (Light Imaging Detector for Gamma-ray Astronomy), is a currently operating space-based telescope launched in April 2007. Its main goal is to make simultaneous hard X-ray and gamma-ray observations of sources. It is a typical pair conversion space-telescope sensitive to radiation in the range of $10-40$ keV and 20 MeV-50 GeV. It is carrying three instruments on board, the GRID (Gamma-ray Imaging Detector) sensitive in the energy range of $\sim$30 MeV to $\sim$50 GeV, MC (Mini-Calorimeter) sensitive in the $0.3-300$ MeV range, and Super-AGILE which makes hard X-ray observations. AGILE is designed to be a bridge between the EGRET and FGST detectors. AGILE, though smaller than EGRET, has a comparable on-axis sensitivity, a wider field of view (1/4 of the sky), better angular resolution (5-20 arcmins), and smaller dead-time ($<$ 1 msec). It is ideal for detecting active galactic nuclei flaring activity, gamma-ray bursts, pulsars, transient sources and solar flares. More detailed information can be found in [37].

Fermi Gamma-ray Space Telescope (FGST, formerly known as GLAST) [24] is a next generation space telescope launched in June 2008. It uses the same

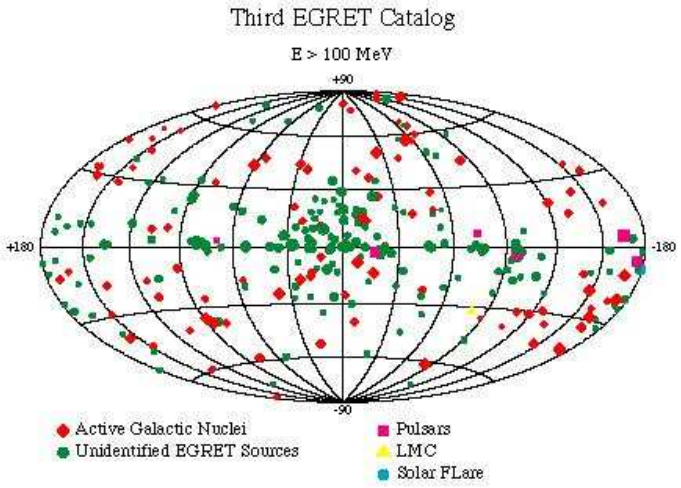

(a)

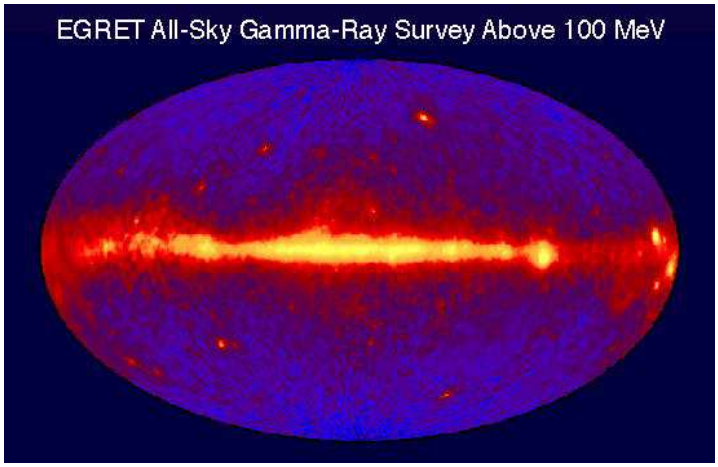

(b)

Figure 1.3: The results of the EGRET experiment (see text). (a) The point sources in the third EGRET source catalog are shown in galactic coordinates [35]. Different types of sources are shown with different symbols, as given in the figure legend. (b) The all-sky gamma-ray emission map by EGRET $> 100\,\mathrm{MeV}$ is shown [36]. Bright point sources, galactic diffuse emission (along the center of the image), and a fainter extragalactic emission (blue areas) can be seen.

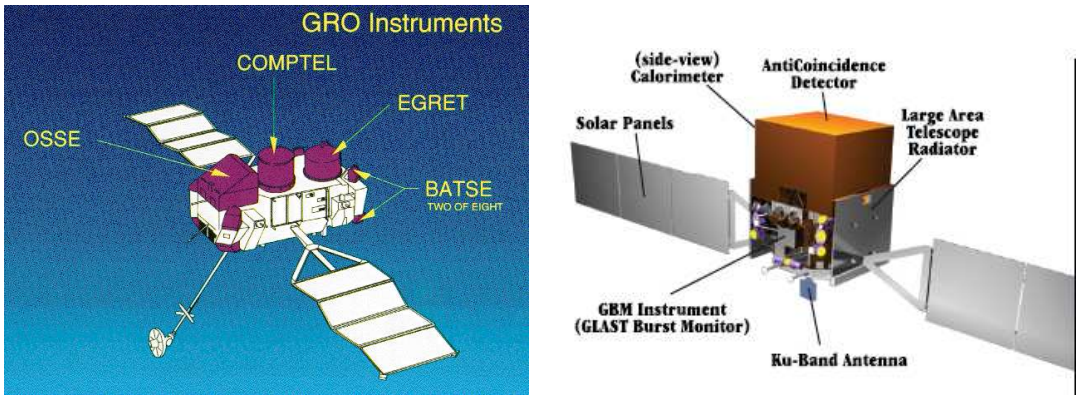

(a) (b)

Figure 1.4: (a) The CGRO is shown with its four instruments labeled ([38]). (b) The FGST observatory is shown with its instruments labeled. The telescopes are described in the text.

technique as EGRET and other space based telescopes to detect gamma rays from space, and it is sensitive in the energy range from 20 MeV to more than 300 GeV with a complementary coverage between 10 keV to 25 MeV for gamma ray bursts (GRBs). It carries two scientific instruments on board (Figure 1.4). The Large Area Telescope (LAT) is the main instrument with a large collection area (∼8 times of EGRET), having access to wider energy range. The LAT has twice of the field of view of EGRET with > 2.5 sr. It has a point source sensitivity > 10 times better than EGRET above 100 MeV for a 1-year survey. The angular resolution of the instrument is also improved to have a positional location accuracy of 30 arc seconds to 5 arc minutes and it will have a point source sensitivity of $1.6 \times 10^{-9}\,\mathrm{cm}^{-2}\mathrm{s}^{-1}$ for a two year operation. The GLAST Burst Monitor (GBM) instrument has a complementary coverage of 10 keV to 25 GeV and its main goal is to detect and produce alerts for GRBs in the field of view. The GBM is projected to detect ∼200 GRBs per year.

The key objectives of the FGST mission are to understand the mechanisms for particle acceleration in Active Galactic Nuclei (AGNs), pulsars and supernova remnants (SNRs), to study AGNs and super-massive black holes to understand the process of jet formation, to resolve the diffuse gamma-ray emission into point sources, to find out the types of the EGRET unidentified sources, to determine the high energy behavior of GRBs and other transient sources, and to search for dark matter and relics from the early universe. FGST will be the first space-based telescope whose energy range will overlap with the ground-based observatories. It thus will be able to fully explore this important window of the electromagnetic spectrum.

1.4.2 Ground-based Detectors

At VHE energies, gamma-ray observations are possible from the ground. The first suggestion of the possibility of observing gamma rays using ground-based detectors arose around the same time as the first suggestion of observing gamma rays to determine the origin of cosmic rays [23, 39]. The approach to observing gamma rays from the ground exploits the fact that VHE gamma rays interact in the atmosphere, thus giving rise to extensive air showers, the particles of which in turn generate Cherenkov light that can be detected on the ground.

Throughout the 1960's and 70's, a number of detectors were built which operated based on this approach with no statistically significant or reproducible detection of a gamma-ray source. The main problem of those experiments was their failure to extract a gamma-ray signal from the overwhelming background of cosmic rays. Success finally came with the development of the imaging technique, which relies on distinguishing between the cosmic rays and gamma rays based on the image of the shower recorded by an array of photomultiplier tubes. This

technique is known as the imaging atmospheric Cherenkov technique (IACT) and it was initially suggested by Weekes and Turver [40] and used by the Whipple Observatory.

The first successful detection of a gamma-ray source from the ground was the detection of the Crab Nebula by the Whipple collaboration [41]. Following this discovery, several other ground-based observatories commenced operation in the 1990's using this technique. These include HEGRA, the Telescope Array, the Durham Mark 6, CAT, TACTIC, the Crimean Observatory and SHALON. Among these, the Whipple and HEGRA experiments made the most notable contributions to the field; thus, they will be discussed later in this section. Currently, the next generation of ground-based telescopes are in operation: CANGAROO-III, MAGIC(-II), HESS and VERITAS. All of these are arrays of large aperture ($> 10\,\mathrm{m}$) telescopes that explore stereoscopic imaging techniques following the example of HEGRA. A brief description of those observatories appears below.

Whipple 10m Observatory

The Whipple observatory [42] is located in southern Arizona, United States at an altitude of 2300 m. It was built in 1968 and is still in operation. It employs a Davies-Cotton design reflector of aperture 10 m with a total mirror area of $75\,\mathrm{m}^2$. Whipple was the first telescope to use an imaging camera. This led, in turn, to the first significant detection of a VHE gamma-ray source. Its camera contained 37 pixels upon initial operation, and it was subsequently upgraded to 91, 109, 151, 331, 490 and 379 pixels. Whipple has a field of view (FOV) of 3.5°, and an energy threshold of 250 GeV.

The important detections by the Whipple Observatory include the Crab Nebula [41], the blazars Markarian 421 [43], Markarian 501 [44], 1ES 2344+514 [45], and H1426+428 [46], and the Galactic Center [47].

HEGRA

The HEGRA (High Energy Gamma-Ray Astronomy) [48] observatory was an array of five small Cherenkov telescopes located in La Palma, Spain, at an altitude of 2200 m. It was the first observatory to use the stereoscopic imaging technique in ground-based gamma-ray astronomy and it operated from 1997 to 2002. Each telescope had a reflector of 3.4 m diameter with a mirror area of 8.5 m^2. The cameras had 271 pixels covering a FOV of 4.6°. The energy threshold of the system was ∼500 GeV.

Important detections by the HEGRA observatory included the supernova remnant Cassiopeia A [49], an unidentified source TeV J2032 + 4130 [50] and the radio galaxy M87 [51].

CANGAROO-III

The CANGAROO-III (collaboration of Australia and Nippon for Gamma-Ray Observatory in the Outback) observatory [52] is an array of four telescopes located in Woomera, Australia, at an altitude of 160 m. It is operating in pseudo-stereo mode, combining events from different telescopes using their time stamps. The telescopes are arranged in a diamond shape with a distance of 100 m between adjacent telescopes. Each telescope has a reflector of 10 m aperture, with a total mirror area of 57 m^2. Each camera contains 256 pixels covering a FOV of 3°. The CANGAROO-III observatory has an energy threshold of ∼400 GeV.

MAGIC-II

The MAGIC (Major Atmospheric Gamma Imaging Cherenkov) Telescope [53] is located in La Palma, Spain, at an altitude of 2200 m. The telescope has a segmented parabolic reflector of 17 m aperture. Its camera has 397 PMTs in the inner region, with 180 slightly larger PMTs in its outer rings. The total FOV of the camera is 3.8°. It has been upgraded to MAGIC-II [54] through the addition

of a second telescope, which is planned to commence operation in the fall of 2008. The separation between the two telescopes is 80 m. The energy threshold of the instrument is 60 GeV for regular operations. This can be reduced to 27 GeV with a special trigger configuration for low energy observations of some sources, such as pulsars.

H.E.S.S.

H.E.S.S. (High Energy Stereoscopic System) [55] is an array of four Cherenkov telescopes located in Namibia at an altitude of 1800 m. Each telescope has a reflector of 12 m diameter, with a total mirror area of 100 m^2. The telescope cameras have 960 pixels covering a large FOV of 5°, which is very useful for sky surveys. The telescopes in the array are located on the corners of a square with 120 m sides. The trigger threshold of the array is ∼100 GeV. Currently, a new telescope is being built, which will be located at the center of the array [56]. This additional telescope will have a large rectangular mirror with a surface area of 596 m^2. The energy threshold with the addition of the new telescope will be in the $40 - 50$ GeV range.

VERITAS

The observations of the Crab Nebula reported in this thesis were made with the VERITAS observatory. Various components of the VERITAS observatory are discussed in detail in Chapter 4; a brief summary is given here. VERITAS is an array of four Cherenkov telescopes located at an elevation of 1270 m on Mt.Hopkins, Arizona, USA. The first VERITAS telescope has been fully operational since early 2005 and VERITAS started stereo mode operations in March 2006 with the addition of the second telescope. The third and fourth telescopes were constructed in the fall and winter of 2006, and scientific observations with the VERITAS four-telescope array began in April 2007. Each telescope in the

array has a Davies-Cotton design reflector of 12 m in diameter, with a total mirror area of 100 m^2. The camera at the focal plane of each telescope has 499 pixels covering a FOV of 3.5°. The telescopes in the array are separated by distances between 35 m and 109 m. The trigger threshold of the array is ∼100 GeV.

1.4.3 Alternative Detectors

Gamma rays can also be detected indirectly on the ground by another technique named "Wavefront Sampling". The successful non-imaging instruments, such as STACEE [57] and CELESTE [58], employ the mirrors of solar research facilities. Such instruments comprise an array of large reflecting mirrors, known as heliostats, which are adjusted to focus the light from different parts of the Cherenkov pool to an elevated collecting station. The trigger system of the instrument records the distribution and arrival times of the photons in the light pool. They select gamma-ray events and infer the properties of the primary gamma ray using the density and temporal distributions of the Cherenkov light on the ground. The large mirror area of such instruments allows for an energy threshold below 100 GeV; however, their sensitivity is not as good as imaging instruments. Currently, no instrument using this technique is operational.

1.5 Gamma-Ray Sources

With the advances in gamma-ray detection instruments in space and on the ground, many different types of gamma-ray sources have been discovered in the last twenty years. It can be said that gamma-ray astronomy has entered a golden age. Currently, 271 sources exist in the current HE catalog, and more than 75 sources are known in the VHE band. A nice review of current VHE sources

can be found in [59]. Figure 1.3 and 1.5 show the current HE and VHE skies, respectively. Each different type of source is shown with a different symbol in the figure. In the next section, the major gamma-ray sources are summarized in two categories: Galactic sources and extragalactic sources.

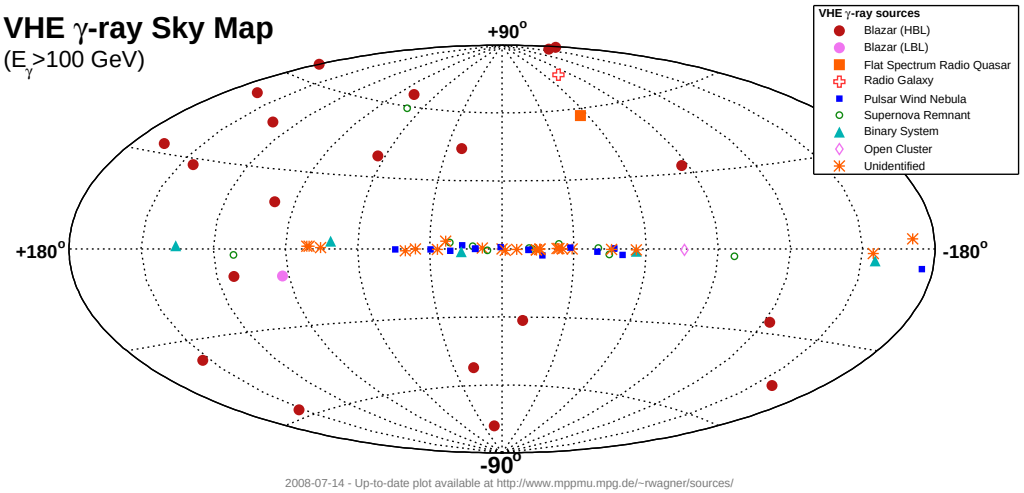

Figure 1.5: The sources in the current VHE gamma-ray sky as of 2008-07-14 are plotted (from http://www.mppmu.mpg.de/ rwagner/sources/). The 23 extragalactic sources are shown together with 54 galactic sources. The different symbols used for each type of the source are listed in the legend.

1.5.1 Galactic Sources

1.5.1.1 Supernova Remnants

Supernova Remnants (SNRs) are formed by the explosion of massive stars when the shock wave of the explosion sweeps up interstellar matter into shells. They are thought to be the sources of cosmic rays up to energies $\sim 10^{15}$eV since their shock waves have the right amount of energy to accelerate protons and other particles to these levels through diffuse acceleration. If they contain a significant

populations of accelerated cosmic rays, gamma rays can then be produced from their interaction with the ambient interstellar matter. SNRs are usually seen as extended sources given the good angular resolution of current detectors.

The correlation of the gamma-ray emission and the emission at other energy ranges, such as X-rays, can be used to test whether the acceleration occurs at the shock fronts. The gamma rays can be produced either by interactions of the leptonic particles with their synchrotron photons or by the interactions of hadronic particles with ambient matter. The accurate measurement of the spectra of the gamma-ray emission from SNRs could distinguish between hadronic or leptonic acceleration. This distinction would test the claim that they are the sources of cosmic rays. Gamma-ray observations can be also used to map the emission regions of these extended sources to determine the acceleration regions. These factors provide substantial motivation to observe SNRs with detectors designed to detect gamma rays.

SNRs are classified into three categories based on whether they have a filled center: Shell type, plerion-type or filled, and composite type. To date, VHE emission from all types of SNRs have been detected. Plerion-type SNRs are an especially highly-populated sub-class of SNRs in the VHE regime.

1.5.1.2 Pulsar Wind Nebulae

Pulsar wind nebula (PWN) are plerion type SNRs. These objects have a rapidly spinning neutron star, a pulsar, in their center and a nebula around it, which has strong non-thermal radio to gamma-ray emission. According to the generally accepted magnetohydrodynamic (MHD) model, the pulsar at the center produces a relativistic wind of electrons and positrons that transports its spin-down energy to the surrounding nebula. The particles in the wind produce synchrotron

emission in radio and X-rays when they interact with the magnetic fields of the nebula. The model predicts that the particles are accelerated to PeV energies via shock acceleration at the termination shocks when the wind meets the interstellar matter at the edges of the nebula. The observed VHE emission from these systems is considered to be due to the interactions of these accelerated particles with their own synchrotron photons via the inverse-Compton process.

To date, 14 sources, the majority of the galactic sources emitting in the VHE band, are identified as PWN type sources. The Crab Nebula, which is the main subject of this thesis, is the prototypical object of this class, and it was the first object discovered in the VHE regime [41]. More discussion of PWNe and the Crab Nebula is provided in Chapter 2 along with the motivation to observe these types of sources.

1.5.1.3 Pulsars

Pulsars are rapidly rotating highly magnetized neutron stars that were first discovered serendipitously in 1968 at radio wavelengths [60]. They emit periodic, non-thermal radiation by converting their rotational energy into dipole radiation. It is believed that pulsars accelerate particles in the charge-depleted gaps near the pulsar where strong magnetic fields exist. These particles radiate curvature and synchrotron radiation from optical to HE gamma rays. Currently, there are three primary models put forward to explain the high-energy pulsed emission from pulsars: the polar cap, outer gap and the slot gap models. They differ in whether the acceleration/emission region is near the magnetic poles of the pulsar star that is inscribed by the last closed lines (polar cap) or close to the light cylinder at the outer magnetosphere (slot gap, outer gap). In all models, the highest energy of the radiation is limited by the pair-production process, either from the interaction

of HE photons with the magnetic fields at the polar caps or by the photon-photon interactions at the outer gaps. In the former case a super-exponential cut-off is expected, while in the latter case, a simple-exponential cut-off is expected in the pulsed emission.

The present catalog of radio pulsars extends to more than 1400 objects. In the HE regime, only six pulsars were identified by the EGRET experiment with no conclusive evidence of a cut-off in their emission at high energies. On the other hand, until very recently, no pulsars have been detected in the VHE range. In September 2008, the MAGIC group reported the detection of VHE pulsed emission from the Crab Pulsar [61] above 25 GeV. This detection could prove to be important in explaining the mechanism behind the HE pulsed emission and in understanding how pulsars accelerate particles in their environments. Furthermore, it might clarify where, and in what conditions, the acceleration occurs, and to what energies pulsars can accelerate particles. Pulsars and pulsed emission are discussed further in greater detail in Chapter 2, Section 2.2.4.

1.5.1.4 Microquasars

A microquasar is a binary system composed of a dense compact object, a black hole or neutron star of a few solar masses, which orbits a large star. Microquasars share common characteristics with quasars in that they both involve a compact object, although on vastly different mass scales, that accretes matter from the nearby star or the galaxy to produce relativistic outflows of particles in the form of jets where particles are accelerated. Thus, microquasars are the smaller versions in our own galaxy of extragalactic quasars. Similar to quasars, microquasars also produce radio emission and high-energy emission from X-rays to VHE gamma rays. These sources show orbital modulation in their VHE emission, indicating

either absorption or periodic emission. To date three microquasars have been detected in VHE energies, LS 5039, LSI+61 303 and Cygnus X-1.

The radio emission from microquasars is generally attributed to synchrotron radiation of accelerated particles in the jets. The VHE emission can be produced by either inverse-Compton scattering of the stellar photons by relativistic particles or by hadronic processes, such as neutral pion decay following interactions of accelerated protons with non-relativistic ions from the stellar wind of the companion star. It is thought that the VHE photons can be attenuated via pair production in the environment of the donor star, redistributing the energy to lower frequencies, down to X-rays.

Microquasars are very important in the study of relativistic jets and particle acceleration. As the closer scaled down versions of quasars, their study could facilitate an understanding of jet formation and the accretion process on a compact object from surrounding matter.

1.5.2 Extragalactic Sources

1.5.2.1 Active Galactic Nuclei

Active Galactic Nuclei (AGNs) are galaxies in which a compact nucleus, a black hole, outshines the rest of the galaxy by up to three orders of magnitude. About 3% of all galaxies are classified as AGN due to their short time-scale variability. AGNs are thought to be powered by accretion of matter onto a super massive black hole. The accreting material forms a disk around the core and produces continuum emission from UV to soft x-rays. AGNs are modeled with two opposite jets of relativistic particles that are aligned perpendicular to the accretion disk, and particles are believed to be accelerated in these jets.

Neither the mechanisms responsible for forming jets in AGNs nor the nature of the particle acceleration in jets, i.e. whether the particle acceleration is due to hadronic or leptonic processes, are known. Observations of AGNs are motivated by the search to answer these questions. Additionally, since they are the farthest sources known at high redshift, they assist in the study of the attenuation of TeV emission by photon-photon absorption due to the extragalactic background light (EBL). Moreover, AGNs have long been suspected to be the sources of UHE cosmic rays. A recent study made by the Pierre Auger cosmic-ray experiment showed that the directions of the highest energy cosmic rays are possibly correlated with the locations of AGNs [22]. Therefore, searching for stronger evidence for AGNs being the source of UHE cosmic rays provides continuing motivation for the further discovery and study of AGNs with VHE gamma rays.

The AGN class can be divided into different types based on their different observational properties. Blazars are AGNs with jets pointing towards us, and many are powerful emitters in the TeV range. The spectral energy distribution of blazars shows a characteristic double peak structure thought to be due to synchrotron and inverse-Compton processes. Blazars are further classified as to whether they exhibit weak (BL Lac) or prominent (Flat Spectrum Radio Quasars, FSRQ) emission lines and whether their synchrotron peak is in the UV to X-rays (High-frequency BL Lacs, HBL) or in the sub-millimeter to optical bands, (Low-Frequency BL Lacs, LBL). The HBLs are more easily detectable in TeV gamma rays. To date most of the detected AGNs (13) in the VHE range are HBL type blazars. Two LBL sources, BL Lacartae and W Comae, and one FSRQ type source, 3C 279, have been discovered so far in VHE gamma rays. Radio galaxies are another different type of AGNs which are very luminous at radio wavelengths and contain jets observable on either sides. To date, one radio galaxy is known at the VHE regime, M87, which confirms that there are other extragalactic sources

emitting VHE radiation besides blazars.

1.5.2.2 Gamma-Ray Bursts

Gamma-ray bursts (GRBs) are the most powerful explosions known in the Universe. They occur at random positions in the sky and are brief, lasting from a few milliseconds to several minutes. However, they produce intense flashes that outshine all other sources of gamma rays combined. GRBs were first detected in the 1960s, but they remain one of the biggest mysteries in astronomy. They are distributed uniformly in all directions in space which supports the idea that they are extragalactic in origin. Since the 1990s, it has been possible to locate their positions with good precision, and observations of their after-glow emission in other wavelengths enable us to measure the distances to many GRBs. These measurements proved that GRBs occur at extragalactic distances.

Converting the observed brightness of GRBs to an intrinsic luminosity given their extreme distances leads to almost inconceivable values. Therefore, beaming almost certainly occurs and is supported by the observations. The leading theories about their nature describe a relativistic fireball, occurring perhaps from the merger of two neutron stars or black holes or from the explosive death of a massive hypernova leading to production of a black hole. The gamma rays may be produced by shock waves created either from material colliding within the jet or from the jet interacting with ambient material.

GRBs are observed in the the X-ray and HE gamma-ray regime by satellite experiments, HETE-2, Swift and BATSE; as yet, however, no detections of them have been made in the VHE range. Observing the VHE emission from these could help answer current questions regarding the nature of GRBs: What types of stars die as GRBs? What determines the duration of the burst? Do more

than one type of phenomena result from various types of GRBs or do they have a unified source?

1.6 Guide to Thesis

The plan for this thesis is as follows: in this chapter, gamma-ray astronomy is introduced and the major astrophysical sources of gamma rays and the gamma-ray detectors are summarized. In Chapter 2, the Crab Nebula and Crab Pulsar are introduced, and the processes giving rise to steady and pulsed emission of very-high-energy gamma rays from nebulae and pulsars are discussed. In Chapter 3, the imaging atmospheric Cherenkov technique which VERITAS utilizes to detect the gamma rays, is explained. Chapter 4 describes the components of the VERITAS observatory. In Chapter 5, the data obtained from the observations of Crab are summarized, and in Chapter 6, the analysis performed on these data is explained. Finally, the results of the spectral and timing analysis of the data collected from the VERITAS observations of the Crab are reported in Chapter 7. The results and the future direction of the research on this subject are discussed in Chapter 8.

CHAPTER 2

Pulsars and Their Nebulae

Pulsar wind nebulae (PWNe) systems are composed of a synchrotron emitting nebula powered by a pulsar (i.e. a rotating compact star). They are created through a Type-II supernova explosion. As a result of the supernova, the core of the progenitor star collapses into a central pulsar star, and the outer material of the progenitor star is thrown off, forming a nebula around the central object. At the early stages of their evolution, PWNe are often embedded in a supernova remnant shell produced from the swept-up interstellar matter by the shock waves of the explosion. The central pulsar star acts as an engine, continuously supplying power to the surrounding nebula through a relativistic wind of particles and magnetic fields which cause the nebula to radiate in all wavelength bands.

The Crab Pulsar and Nebula complex is the best known object of the pulsar wind nebula (PWN) source class. Over the past four decades, 40 to 50 other sources with properties similar to the Crab were identified as members of this class [5]. PWNe systems provide environments where particles are accelerated to high energies in shocks, where energy is carried by the relativistic flows and magnetic fields, and where non-thermal radiation is produced via several different mechanisms. Most of the PWNe discovered to date are in our Galaxy or in the Magellanic Clouds, close enough to be spatially resolved. Thus, they act as convenient laboratories to study these non-thermal acceleration and emission processes, which are common to many high-energy astrophysical sources.

This chapter is organized as follows: the description of the formation of PWNe from supernovae explosions will be given first, followed by a discussion of the characteristics of pulsar stars and their nebulae. Next, the physical mechanisms that lead to the pulsed emission from the central star and to the steady emission of radiation from the nebula will be explained, focusing on the high-energy band of the emission. The chapter will continue with a summary of past observations of the Crab Pulsar and Nebula as a specific PWN object and will conclude with a description of the motivation to observe the Crab in the high-energy gamma-ray band.

2.1 Birth of the PWNe Complex: Supernovae

PWNe are believed to be formed as a result of a supernova explosion. A supernova is an powerful stellar explosion that creates an extremely luminous event at the end of the life of a star. Two different mechanisms can ignite a supernova explosion: Type Ia supernovae are caused when mass of a white dwarf star increases by merger or through accretion processes which raise star's core temperature and eventually end in runaway nuclear fusion. Type-Ib/c and Type-II supernovae, on the other hand, are caused by the collapse of a massive star when its nuclear supply is completely depleted and its nuclear fusion reactions cease. Only the latter type of the explosion creates a central compact star, a neutron star or a black hole, as in the case of the supernova which caused the Crab complex to form.

A Type-II supernova explosion occurs at the end of the life of progenitor stars that have at least a mass of 8 solar masses ($8M_{\odot}$). All stars resist the gravitational collapse of their materials through the thermal pressure produced from the release of energy as a result of nuclear fusion. The process of forming heavier elements

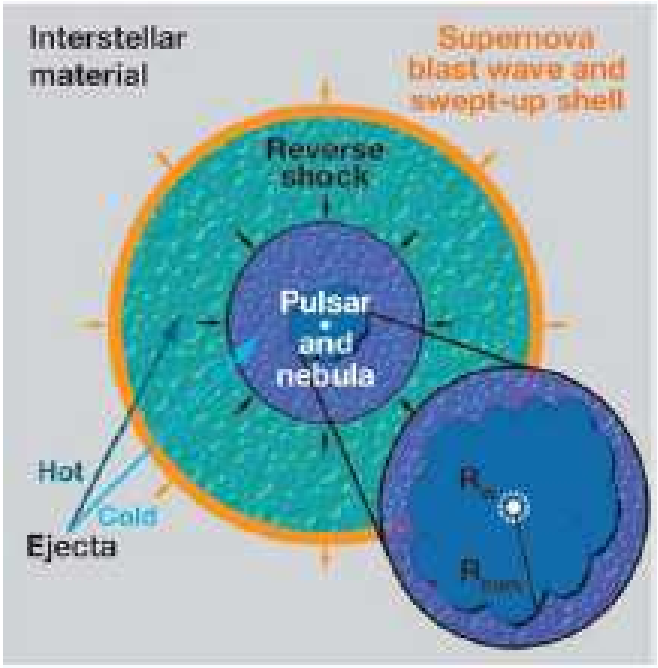

Figure 2.1: The components of a remnant after the supernova explosion are shown with a diagram [5]. The outer orange colored shell formed by the material swept up by the shock wave of supernova expanding into the interstellar medium, the inner shell shows the reverse shock which travels inward and separates the hot and cold ejecta of the explosion, and the newly born PWN complex is shown in the blue region at the center. In the expanded PWN view the radius at which the wind termination shock occurs is shown with R_W and the radius of the nebula is shown with R_{PWN}.

through fusion of the lighter elements continues during the lifetime of the star until the supply of light elements is exhausted. For stars massive enough to cause a Type-II supernova, the end point of this evolution is the formation of iron, the most tightly bound element, at the core of the star after which nuclear fusion in the core is no longer an exothermic process. At this point nuclear fusion ceases and the gravitational pressure in the core exceeds the electron degeneracy pressure, and the core collapses. As a result of the collapse, the temperature in the core rises and photo-disintegration of iron into helium occurs. The helium then disintegrates into protons and neutrons. Protons in turn combine with the ambient electrons to form neutrons and electron neutrinos. Neutron degeneracy pressure prevents further gravitational collapse at the center. However, the outer layers continue collapsing inward and eventually a massive supernova explosion occurs.

The resulting remains of the explosion are a central compact object, either a neutron star or a black hole, and a rapidly moving shock wave of material expanding into the interstellar medium (Figure 2.1). The shock wave sweeps up the surrounding interstellar medium during the free expansion phase, which can last for up to two centuries. The wave then gradually undergoes a period of adiabatic expansion, during which it slowly cools and mixes with the surrounding interstellar medium over a period of about 10,000 years to form a supernova remnant shell. If the mass of the initial star is less than $12M_{\odot}$, the surviving central compact object is an extremely dense neutron star with a typical mass of $M \sim 1.4M_{\odot}$ and a radius $of R \sim 15\,\mathrm{km}$. Only a small fraction of the angular momentum of the progenitor star is carried away by neutrinos and by the ejected matter, so most of the angular momentum is retained by the central neutron star which has a very small radius compared with the progenitor. Conservation of angular momentum means that the neutron star must rotate at a very high

frequency, thus it becomes a pulsar star which emits radiation in a beam that sweeps Earth as it rotates, as in the case of the Crab Pulsar. The material thrown off in the explosion form a diffuse nebula around the central object, such as in the Crab Nebula.

2.2 The Pulsar Star

Pulsars are rapidly rotating, highly magnetized neutron stars which emit non-thermal radiation by converting their rotational energy into dipole radiation.

2.2.1 Connection to Neutron Stars

The first pulsar (PSR 1919+21) was discovered accidentally by Jocelyn Bell, a graduate student working with Antony Hewish, as a periodic signal of unknown origin among the radio data collected from quasi stellar objects using a dipole array. When it was established that its source was of extraterrestrial origin, it was published by Hewish et al in 1968 [60].

After this publication several explanations of the nature of this source were proposed. The two most popular theories argued that the observed pulsating star was either an oscillating white dwarf star or a rapidly rotating neutron star. Both Pacini, in 1967[62], and Gold, in 1968 [63], published the basic theory and the connection with the observations that set out the case for identifying pulsars with rotating neutron stars. They argued that a rapidly rotating neutron star with a strong dipole magnetic field, would act as an very energetic electric generator that emits pulsating radiation from its core and provides energy to produce radiation in a surrounding nebula.

The theory that the vibrations of white dwarf stars were the source of the

pulsed signal could only explain pulsations with periods as short as 0.25 s. On the other hand, neutron stars can rotate fast enough to account for pulsations with periods considerably shorter. The discovery of the short-period pulsar stars Vela and Crab [64], with periods of 89 ms and 33 ms respectively, proved that the pulsar stars were not vibrating white dwarfs, but were neutron stars. A second proof was obtained when the slowdown of the Crab pulsar was discovered [65], which can not be easily explained if the origin is vibrations, but is natural for a rotating object losing angular momentum.

2.2.2 Characteristics of Pulsars

A population of between 10^5 and 10^6 active pulsar stars is expected to be present in the Galaxy, according to a model of the distribution of pulsars [66]. Most of the pulsars are concentrated in the plane of the Galaxy within a layer about 1 kiloparsec thick and within a radial distance of about 10 kiloparsec from the center. Measurements of their motion show that they have high velocities, of the order of 200 km/s moving away from the plane [66]. Similar populations of pulsars are expected to exist in other galaxies, but their detection is not possible with the sensitivity of present radio telescopes. However, X-Ray observations led to the discovery of several pulsars in the Magellanic Clouds.

Observations of isolated pulsar stars have determined that they have periods from tens of ms up to five second [66]. A second class of pulsars, which exists in binary systems, have periods down to 1 ms and are known as "millisecond pulsars". The Crab is a rotation-powered isolated pulsar, thus the focus in this chapter will be on isolated pulsars. The rotation of such a pulsar slows through its lifetime, e.g the slow-down rate of the period for the Crab Pulsar is $\dot{\mathrm{P}} \approx 10^{-13}$ s/s. Thus, the shortest period pulsars are the youngest. The age of a pulsar, T, can

be estimated from the following equation:

$$T = \frac{P}{2\dot{\mathrm{P}}} \tag{2.1}$$

where P is the period and $\dot{\mathrm{P}}$ is the slow-down rate of the period of a pulsar.

The mass of pulsar stars is found to be in the range of $1.2M_{\odot}$ to $1.5M_{\odot}$, from measurements of neutron stars in binary systems. An upper limit for their radius can be calculated from the knowledge of the rotation speed of the fastest pulsars. The balance between centrifugal force and gravity for a sphere of mass M and radius R, rotating with angular velocity Ω and period $P = 2\pi/\Omega$ gives :

$$\Omega^2 R = \frac{GM}{R^2} \tag{2.2}$$

$$R = 1.5 \times 10^3 \left(\frac{M}{M_{\odot}}\right)^{1/3} P^{2/3} \text{ km}. \tag{2.3}$$

Any star that is rapidly rotating may become unstable before the centrifugal limit is reached, thus this equation gives the upper limit on the radius of the pulsar star. The shortest known period for a neutron star is 1.6 ms, for PSR B1937+21, giving an upper limit of < 23 km for the radius [66].

The neutron star core of a pulsar is like a gigantic atomic nucleus, with density similar to ordinary nuclear matter. For the commonly assumed parameters of radius (10 km) and mass ($1.4M_{\odot}$), the mean density of the star is 6.7×10^{14} g cm^{-3} (The density of nuclear matter is 2.7×10^{14} g cm^{-3}). The structure of the neutron star core, as discussed in [66], has two main components: a crystalline solid crust and a liquid interior consisting mainly of neutrons. The outer part of the crust is a very stiff crystalline lattice composed mainly of iron nuclei. Below the surface, the density increases and at a density near nuclear matter, 2.7×10^{14}g/cm^3, the nuclei become unstable and embedded in a super-fluid of neutrons which is superconducting. Some portion of the super-fluid penetrates into the inner part of

the solid crust and moves independently. The transfer of the angular momentum between the two components of the stellar interior may cause abrupt changes in the slowdown rate of a pulsar, which are known as "glitches".

The magnetic field at the poles of pulsars is of the order of $10^{12} - 10^{14}$ Gauss. Such a high-strength magnetic field may seem unreasonable at first, but it can be established easily that these high field strengths are possible by the conservation of magnetic flux during the collapse of the progenitor star [67]. During the collapse the star may be approximated as a good conductor, thus its magnetic field flux, proportional to the field strength of the progenitor star B_{PS} and its surface area, $\Phi \propto BR^2$, should be conserved. From this conservation, one can find the relation between the magnetic field strength of the neutron star, B_{NS}, and of the progenitor star, B_{PS}, as follows:

$$B_{PS}R_{PS}^2 = B_{NS}R_{NS}^2 \tag{2.4}$$

$$B_{NS} = B_{PS}\left(\frac{R_{PS}}{R_{NS}}\right)^2 \tag{2.5}$$

For a typical star of radius $R_{PS} \sim 10^6$ km collapsing into a neutron star of radius $R_{NS} \sim 10$ km, this relation gives that a neutron star magnetic field of magnitude $B_{NS} \sim 10^{12}\,\mathrm{G}$ can be formed from collpase of a progenitor star that has magnetic field of $B_{PS} \sim 100\,\mathrm{G}$.

The magnetic field of a neutron star can also be estimated by assuming that the rotational slow-down energy of the star is dissipated as magnetic dipole radiation. The rotational slow-down energy, $\dot{\mathrm{E}}$, can be written as a function of the observable quantities as follows:

$$\dot{\mathrm{E}} = \frac{d}{dt}\left(\frac{1}{2}I\Omega^2\right) = -(2\pi)^2\left(I\frac{\dot{\mathrm{P}}}{P^3}\right) \tag{2.6}$$

where I is the rotational moment of inertia of the neutron star. For a typical moment of inertia ($I \sim 10^{45}$g cm^2), a radius of 10 km, an observed period ($P \sim$

0.1 s), and a period slow-down ($\dot{\mathrm{P}} \sim 10^{-13}$) of a neutron star, the slow-down rate of the rotational energy can be calculated as $\dot{\mathrm{E}} \sim 10^{36}$ ergs/sec. The magnetic dipole radiation power emitted by a neutron star is given as [68]:

$$\dot{\mathrm{E}} \simeq \frac{2}{3}\left(\frac{B^2 R^6 \Omega^4}{c^3}\right) \tag{2.7}$$

Equating these two quantities, one can find the magnetic field strength of the neutron star with the following equation:

$$B \simeq 3.2 \cdot 10^{19} \sqrt{P\dot{\mathrm{P}}}\ \text{Gauss} \tag{2.8}$$

which gives $B \simeq 10^{12}$ Gauss as a result for the typical values of the quantities involved.

The amount of energy dissipated from the slow-down of the pulsar rotation, is calculated from Eq.2.6 as $\sim 10^{36}$ ergs/sec for the pulsars powering typical young PWN complexes. The observed pulsed emission is small compared with this overall energy loss, most pulsars emit less than 1% of their energy loss in terms of observed radiation. The most significant portion of this energy is emitted as a wind of energetic particles, the pulsar wind. The interaction of this wind with the surrounding nebula is the source of the observed electromagnetic luminosity of the nebula. The transfer of the energy between the pulsar and nebula is discussed in more detail in Section 2.3.3.

2.2.3 Non-Thermal Radiation Mechanisms at Work in PWNe

It is useful to have an overview of the main mechanisms that are involved in the production of high-energy (HE) radiation in PWNe environments, before discussing the physical models that are responsible for pulsed emission from the pulsar and the steady emission from the nebula. Although normal stars shine as a result of the thermal processes in their cores, non-thermal processes are the

main mechanisms for production of the high-energy radiation in environments that are capable of accelerating particles to ultra-relativistic energies.

2.2.3.1 Cyclotron Radiation

When a non-relativistic particle enters in a region where magnetic field is present, it moves around the magnetic field lines in a helical path. The radius of the circular trajectory is determined by the balance between the Lorentz force of the magnetic field and the centrifugal repulsion of the orbiting particle. A particle moving non-relativistically on a curved path in a magnetic field emits electromagnetic radiation at the Larmor frequency, defined by:

$$\nu_L = \frac{eB}{2\pi mc} \tag{2.9}$$

where e and m are the charge and the mass of the particle, respectively, B is the magnetic field strength and c is the speed of light. This type of radiation is called cyclotron radiation. Cyclotron radiation is circularly or linearly polarized, depending on the orientation of the observer relative to the magnetic field direction.

2.2.3.2 Synchrotron Radiation

If a particle in a magnetic field moves at relativistic speeds, it emits synchrotron radiation instead of the cyclotron radiation as it spirals along a magnetic field line (Figure 2.2). Due to the aberration of the particle's dipole radiation by its relativistic motion, this radiation is beamed forward into a cone with opening angle $\alpha \leq \Gamma^{-1}$, where Γ is the particle's Lorentz factor. An observer sees the radiation pulse each time the particle's trajectory is directed toward his line of sight and the pulse is strongly polarized as cyclotron radiation.

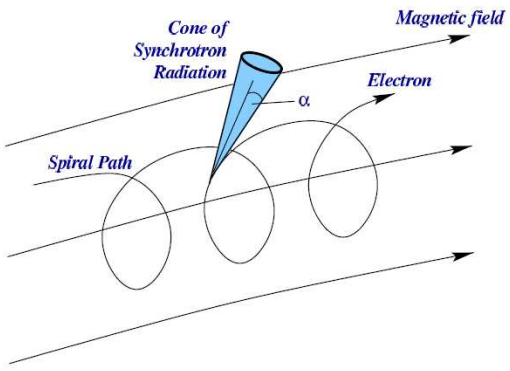

Figure 2.2: The diagram showing the instantaneous cone of the synchrotron radiation emitted by a relativistic electron moving in a magnetic field region.

Synchrotron radiation is emitted with a spectrum that extends to higher harmonics of the Larmor frequency, ν_L, and, for high Lorentz factors, the harmonics are densely packed, resulting in an almost continuous spectrum. The characteristic frequency of the radiation depends on the particle's energy and the magnetic field, and it is given by $\nu_c \sim \Gamma^2 \nu_L$, in terms of the Larmor frequency. The intensity of the total radiated power is maximum at approximately $\nu_m \approx \nu_c/3$. Below ν_m the spectrum is a power law, proportional to $\nu^{1/3}$; above ν_c it falls exponentially as $\exp[-(\nu/\nu_c)]$.

From an astrophysical source in which a population of relativistic electrons is present with energies distributed according to a power law with index α, $N(E) \propto E^{-\alpha}$, the synchrotron spectrum also follows a power law of:

$$P(\nu) \propto \nu^{\beta} \tag{2.10}$$

where the spectral index is $\beta = (1-\alpha)/2$. Synchrotron radiation is the primary non-thermal emission process in astrophysics, and it plays a prominent role in TeV gamma-ray emission through the Synchrotron-Self-Compton process.

2.2.3.3 Curvature Radiation

In regions with very high magnetic field strengths, e.g. in pulsar magnetospheres, particles may be constrained to follow the path of the magnetic field lines very closely, with pitch angle nearly zero. The field lines are generally curved, thus the particles are accelerated transversely during their motion and produce curvature radiation which has very similar characteristics to synchrotron radiation [69]. The critical frequency is similar to the synchrotron radiation and given as:

$$\nu_c = \frac{3c}{4\pi\rho}\Gamma^3 \tag{2.11}$$

where ρ is the radius of curvature of the field lines and Γ is the Lorentz factor of the particle. The spectrum of curvature radiation from a single particle is exactly the same as synchrotron radiation. However, for a population of particles with energies distributed as a power law of index α, the resulting spectrum of the curvature radiation has an index $\beta = (1 - \alpha)/3$, which is different from the case of synchrotron radiation.

2.2.3.4 Inverse-Compton Radiation

In Compton scattering, high-energy photons scatter from low-energy electrons and, as a result, the electrons gain energy from the photons. Conversely, in inverse-Compton scattering, low-energy photons gain energy by scattering from relativistic electrons. The cross-section of the process is approximated by the Thompson-scattering cross section for photons with energy less than the electron rest mass. For photons of MeV energies, the cross-section is given by the Klein-Nishina formula (Equation 2.12), and it is inversely proportional to the photon energy:

$$\sigma_{KN} = r_e^2 \frac{\pi m_e c^2}{E_\gamma}\left[ln\left(\frac{2E_\gamma}{m_e c^2} + \frac{1}{2}\right)\right] \tag{2.12}$$

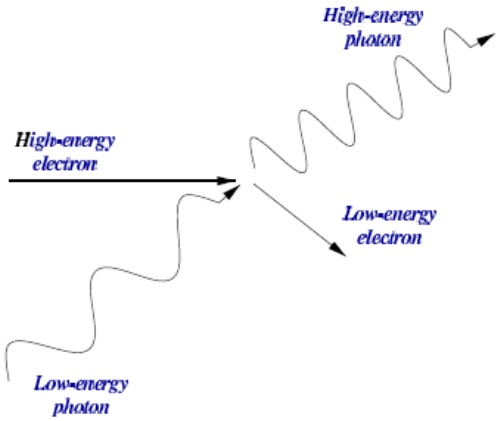

Figure 2.3: Diagram illustrating the inverse-Compton scattering during which a low-energy photon is up-scattered to higher energies by an interaction with a high-energy electron.

where r_e is the classical electron radius, m_e is the mass of the electron and E_γ is the photon energy.

For a population of relativistic electrons with Lorentz factor Γ, and with a power law distribution of energies, $N(E_e) \sim E^{-\alpha}$, the resulting gamma rays will have the characteristic (Thompson) energies of $\Gamma^2 h\nu$ or (Klein-Nishina) energies of $\Gamma h\nu$, where the $h\nu$ is the energy of the initial soft photon. The spectrum of the resulting gamma rays are given as:

$$N(E_\gamma) \sim E_\gamma^{-(\alpha+1)/2} \tag{2.13}$$

The inverse-Compton radiation from a population of high-energy electrons therefore contributes to the total radiative flux from the object and it adds a high-energy component.

In gamma-ray astronomy, the inverse-Compton process is the major mechanism that produces TeV gamma rays from a population of relativistic electrons.

Electrons are accelerated to high energies at shock fronts in SNRs, AGN jets and pulsar environments. Where magnetic fields are present, electrons radiate synchrotron photons, and impart some of their energy to this population of low-energy synchrotron photons by inverse-Compton scattering. This process is known as Synchrotron-Self-Compton radiation, through which both the low-energy photons and the photons with TeV energies originate from the same population of electrons.

2.2.4 Pulsed Emission

The rapidly rotating neutron star core is surrounded by an energetic and electrically charged magnetosphere, which co-rotates with the star. The pulsed emission emerges from processes which occur in the inner magnetosphere, within the radius of the light cylinder. The light cylinder of the pulsar is defined as the region of the magnetosphere which extends out to a radial distance at which the linear velocity of the particles in the plasma approach the speed of light. The region inside the light-cylinder is known as the "near zone". Electric and magnetic fields dominate the dynamics in this "near zone".

Although there are substantial observational data for radio emission from pulsars, the radio emission process has not yet been firmly established. Because the mechanism responsible for the radio beams is not understood and because the radiation is coherent, it has not been possible to describe this emission using a physical model [2]. Currently, there are several possible explanations involving plasma instability or maser action for the source of the coherent radio emission [70]. In this section, the focus of the discussion will be the pulsed emission from optical to HE gamma rays.

All the models explaining the emission from optical to high-energy gamma

rays have their roots in the early standard magnetosphere model of a neutron star by Goldreich and Julian [71]. In this standard model, the neutron star is approximated as a rotating magnetic dipole which induces an electric field both along and across the magnetic field lines. The induced electric field at a radius R, is given for a pulsar with surface magnetic field B, rotating with angular velocity Ω, as follows:

$$E = -\frac{(\Omega \times R) \times B}{c} \tag{2.14}$$

For typical surface magnetic fields of pulsars in the order of 10^{12} G, the strength of the induced electric field exceeds the gravitational value by many orders of magnitude. Thus, the induced electric field is capable of stripping charged particles from the surface of the neutron star. The particles either follow the open field lines passing out of the light cylinder and escape the magnetosphere or they follow the closed field lines filling the magnetosphere of the neutron star with a plasma which co-rotates with the star inside the light cylinder. If the charge density reaches the Goldreich-Julian value,

$$\rho_{GJ} = \frac{\nabla \cdot E}{4\pi} \approx -\frac{\Omega \cdot B}{2\pi c} \tag{2.15}$$

the charges screen the electric field parallel to the magnetic field. The particles redistribute themselves in the magnetosphere in such a way that they short out the electric fields everywhere except for a few locations where the required charge density can not be maintained. One of the reasons for failing to maintain the charge density is that the charged particles flow out along the open magnetic field lines of the light cylinder; this process leaves a charge deficit in some regions inside the light cylinder. In different models these charge depleted gaps develop above the polar caps, or in outer gap regions between the zero-charge-density surfaces and the last closed magnetic lines near the light cylinder. High electrostatic potential, up to 10^{12} V, can be formed in these "gap" regions where charged

particles can be accelerated to ultra-relativistic energies sufficient to generate non-thermal radiation by the processes discussed in Section 2.2.3. The current popular models described in the following sections differ in the location of these regions for accelerating the particles and emitting pulsed radiation.

The accelerated relativistic charged particles in these gaps, influenced by the strong magnetic fields close to the pulsar star, are bound to follow the curved magnetic field lines and radiate curvature radiation up to tens of GeV. Synchrotron radiation is also emitted by the relativistic particles in the regions away from the star surface where the magnetic fields are weaker. Very-high-energy gamma-rays are produced by the inverse-Compton (IC) up-scattering of synchrotron photons or ambient photons of thermal origin. Both the high-energy curvature and IC photons interact further with the magnetic field and produce pairs of electrons and positrons which can lead to pair production cascades where the secondary electrons/positrons can radiate via similar mechanisms.

2.2.5 HE Pulsed Emission Models

Currently, there are three primary models explaining the high-energy pulsed emission from pulsars, the polar cap, outer gap and the slot gap models. They differ in whether the acceleration/emission region is near to the magnetic poles of the pulsar star that is inscribed by the last closed lines (polar cap) or close to the light cylinder at the outer magnetosphere (slot gap, outer gap). A depiction of the acceleration sites for different models are shown on Figure 2.4.

2.2.5.1 Polar Cap Model

In polar cap models [72, 73], the acceleration potential develops along the last closed field lines near the magnetic poles, forming a vacuum gap [74] or a space-

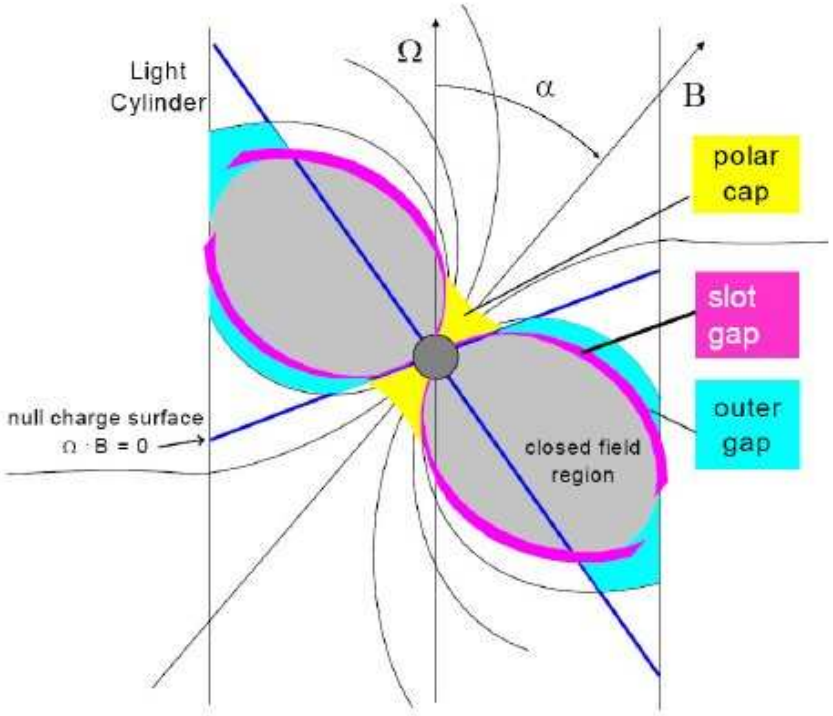

Figure 2.4: The charge deficit regions for acceleration of particles and emission of pulsed radiation are shown for different high-energy models with different colors. The ω shows the rotation axis, and B shows the direction of the magnetic dipole of the star and α is the inclination angle, i.e. the angle between the rotation and magnetic field axes.

charge limited flow accelerator [75]. Particles are accelerated in these gaps and they radiate high-energy curvature and IC photons due to the strong magnetic fields. A cascade of e^+e^- pairs is produced by two processes that repeat each other: pair production from the interactions of the curvature or IC photons with the strong magnetic fields and radiation of additional high-energy curvature or IC photons from the secondary e^+e^- pairs. These e^+e^- pairs are capable of shorting out the acceleration potential, which limits the highest energy of the emitted radiation.

The magnetic pair production attenuation causes a sharp "super-exponential" cutoff in the energy spectrum which is one of the distinct features of polar cap models [76]. An energy spectrum with super-exponential cutoff is given with the functional form $dN/dE = K\ E^{-\Gamma}\exp(-(E/E_{cutoff})^{\alpha})$ where K is the flux normalization, Γ is the photon spectral index of the spectrum, E_{cutoff} is the cutoff energy and α is the strength of the cutoff. The energy of this cutoff is a function of the local magnetic field strength, the pulsar period and the emission altitude, and it lies between 1-20 GeV [1].

Polar cap models can explain the observed double-peaked pulse profiles (See Figure 2.8) at high energies by hypothesizing that the magnetic fields straighten towards the cap center and the emission is reduced in the center region by the absence of curvature radiation. Thus, an emission region of a hollow cone shape is formed around the cap center. For low inclination angles, defined in Figure 2.4, of the pulsar star, an observer situated at an angle to the rotation axis will observe two peaks of emission from the two sides of the hollow emission region as it passes through the observer's line of view on each rotation of the pulsar star. There are two problems associated with the polar cap, the predicted pulse peaks are too narrow and the double-peak profile can be observed only for small inclinations of

the pulsar and at small observing angles [1].

2.2.5.2 Slot Gap Model

In space-charge-limited-flow polar cap models, the acceleration is slower near the last open field line. The slot gap model predicts that a narrow gap forms in these regions, where the particles can not produce sufficient number of e^+e^- pairs to short out the electric field. In these regions the particle acceleration can continue up to high altitudes [77]. Muslimov and Harding [78], improved the slot gap model by including relativistic frame dragging. It is possible to produce wider peaks in the observed pulse profiles with this model, addressing the problem of narrow peaks in the polar cap model. Due to the relativistic phase shifts of the high-altitude emission in this model, it is also possible to observe double-peak pulse profiles at larger viewing angles.

2.2.5.3 Outer Gap Model

In outer gap models [79, 80], the acceleration occurs at the outer magnetosphere near the light cylinder. A charge depleted slab-like region can form between the last closed magnetic field lines, the null surface, and the first open field lines, because the particles that stream out of the gap along the open lines crossing the null surface cannot be replenished from below. The outer gap models can also generate double-peak pulse profiles which may be seen from larger observing angles, but they do not predict any off-pulse emission at all, contrary to the polar cap and slot gap models. Since the magnetic fields are relatively weak in the outer magnetosphere, the highest energy of radiation is limited by photon-photon pair production via the interaction of the high-energy photons with the X-ray photons from the hot neutron star surface. The outer gap model predicts a more gradual

cutoff in the pulsed emission spectrum extending up to 10's of GeVs. Earlier outer gap models predicted a gamma-ray flux at TeV energies due to the IC scattering of high-energy photons with the ambient infrared photons, but this prediction was ruled out experimentally by the observations of atmospheric Cerenkov telescopes.

2.2.6 Predictions of HE Emission Models

2.2.6.1 The Location of Pulsed Emission Sites on Pulsars

The location of the particle acceleration and pulsed emission sites of pulsars is the first issue of debate between the high-energy emission models. Since the accelerated particles radiate their energy quickly, observations of pulse profiles at high-energies have the advantage of mapping the acceleration sites [1]. Thus, reconstruction of the pulse profiles with sufficient sensitivity may help to distinguish between the models.

All the models can, in principle, predict the double-peak shape of the gamma-ray pulse profile, given the overall geometry of the pulsar, i.e. the viewing angle and the magnetic inclination angle. But different models predict different pulse profiles for a set of possible pulsar inclination angles and observation angles, as discussed in the previous section. While the polar cap models can produce narrow double-peak pulse profiles only for small inclination and viewing angles, it is possible to create wider double-peak pulse profiles for the larger viewing angles in slot gap and outer gap models. The outer gap models do not predict any off-pulse emission, in contrary to polar cap and slot gap models. The profiles generated by different models are shown in Figure 2.5. Thus, the study of the individual pulse profiles of various pulsars at high energies is crucial to making a statement on the validity of the different models.

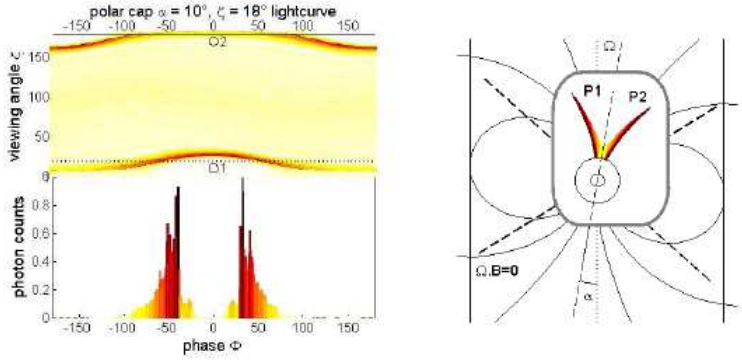

(a) Polar Cap Model

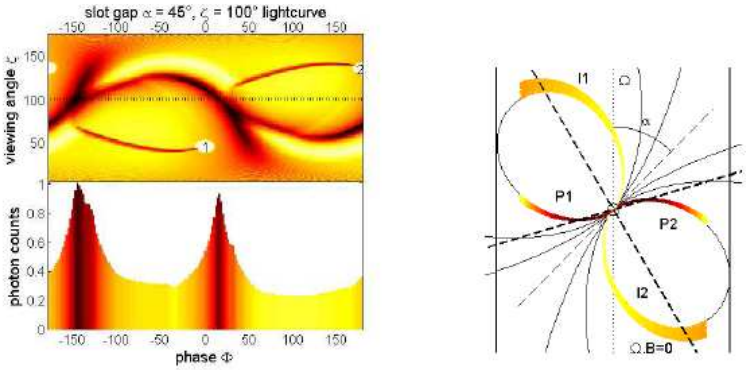

(b) Slot Gap Model

Figure 2.5: Phase plots of the pulsed emission light profiles and sketches of the relevant acceleration regions for typical inclination angles for polar cap and slot gap models are shown [81]. For each model, the diagram on the right shows the predicted acceleration regions for the model with tags, P1, P2, I1, I2, referring to the regions that corresponds the first and second peaks and inter-pulse on the pulse profiles. The upper plots on the left hand sides show how the appearance of the pulse profile changes with the viewing angle. The bottom plots on the left hand sides show the pulse profiles for each model. The regions on the pulse profiles, and viewing angle plots are matched to the acceleration regions that the emission originates using different colors.

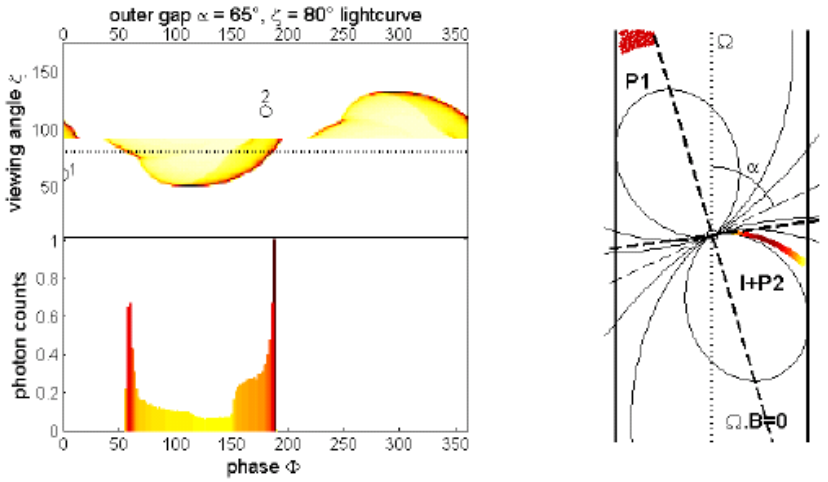

(a)

Figure 2.6: Phase plots of the pulsed emission light profiles and the sketches of the relevant acceleration regions for typical inclination angles for outer gap model are shown [81]. See the caption of Figure 2.5 for further explanations.

Two other open questions relevant to this issue are whether the different models apply to pulsars with different parameters and whether a pulsar's emission mechanism changes from one type to another through its lifetime. A large population of pulsars with sufficient photon statistics to reconstruct sensitive pulse profiles is required to answer these questions.

2.2.6.2 Determining the Shape of Spectral CutOffs

Another way of potentially discriminating between the currently popular models for pulsed emission is to study the spectrum of the pulsed emission. Different models predict different cutoffs in the pulsed emission spectra due to different mechanisms limiting the high-energy emission, as discussed in the previous section. While the polar cap models predict a super-exponential cutoff at energies of a few GeV due to the magnetic pair production in the strong magnetic fields near the surface of the pulsar, the outer gap models allow a softer cutoff extending to 10's of GeV due to the photon-photon pair production. The energy of the cutoffs depend on various pulsar parameters, such as the local magnetic field, the emission altitude and the pulsar period [1].

Although EGRET detected indications of spectral cutoffs in several pulsars, it could not distinguish between a super-exponential cutoff and a simple exponential cutoff. The energy thresholds of the ground-based experiments are higher than the cutoff energy of both models. Thus, it is crucial to study the high-energy spectra from pulsars at GeV energies with a more sensitive space-based instrument, such as FGST, in order to distinguish unambiguously between the predicted spectral shapes.

Figure 2.7 shows the simulated pulsed emission spectra of the Vela pulsar for the polar cap and outer gap models and simulated data from the LAT instrument

of FGST. It can be clearly seen that the predictions of different models for the spectral cutoff energy would be distinguishable with this instrument. The open question of whether any correlation exists between the cutoff energy and the magnetic field strength may also be addressed through spectral studies at gamma-ray energies.

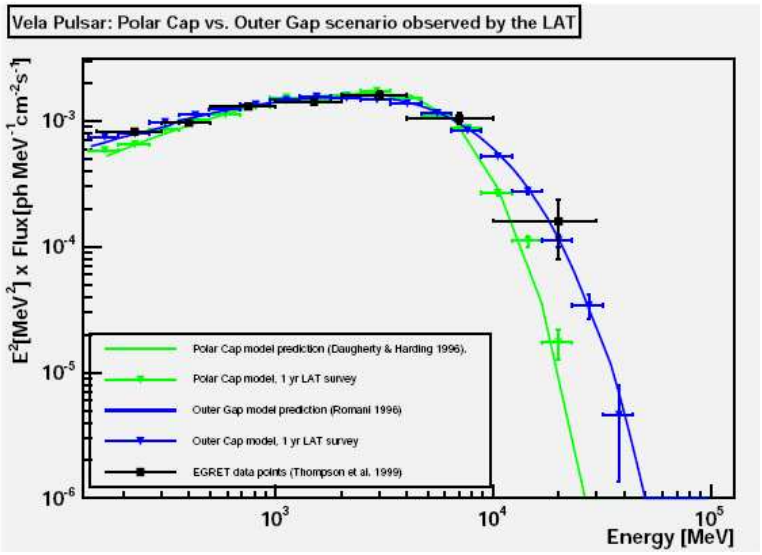

Figure 2.7: The predicted spectra of the Vela pulsar for the polar cap and outer gap models [1] are shown with continuous green and blue lines, respectively. Simulated data points for a 1-year LAT exposure for each model and the observed EGRET data points are also shown with green, blue and black points, respectively.

2.2.6.3 Identifying the Various Radiation Components on the Spectra

All models predict that there are multiple radiation components contributing to the spectra of the high-energy pulsed emission from pulsars. The major radiation components of pulsed emission are curvature radiation from the primary particles,

synchrotron radiation from the pairs, and inverse-Compton scattering of the high-energy electrons from the low-energy photons in the medium. It is expected that the transitions from one component to another happen in the high energy range [1]. Thus observations in the high-energy regime are again important, and it is interesting to find out at what energies these various components are dominant. In order to find the breakpoints of the transitions from one component to another, the pulsed emission spectra need to be measured with good precision. Again it is important to see how the transition energies of different components of the overall spectra change from one class of pulsars to another.

2.2.6.4 Population Studies

It is quite possible that the emission mechanism, acceleration regions, altitude of emission, and the radiation processes contributing to the spectrum depend on different characteristics of the pulsar, such as its period, age or surface field strength [1]. To explore this, it is important to detect a large number of pulsars with different characteristics, with which to look for correlations between their parameters, their multi wavelength profiles, and their spectra.

As an example of the dependency on the period and the magnetic field strength, both the outer gaps and the slot gaps can only exist in younger pulsars, because they rely on sufficient pair production to sustain the gaps. Pulsars with periods larger than 0.3 sec and magnetic fields less then $\sim 10^{12}$ Gauss fall below the "death line" [82].

EGRET pulsars show another example of correlation with age: their spectral hardness increases with age, and, as a result, while the peak of the power spectrum is at hard X-rays for young pulsars, it occurs at high-energy gamma rays for middle-aged pulsars [1, 83]. The ratio of the number of radio-quiet to radio-loud

pulsars is another feature distinguishing between the pulsed emission models. The polar gap model predicts the highest ratio of radio-loud to radio-quiet pulsars, while the high-altitude models predict much lower ratios [1].

2.2.7 VHE gamma-ray Observations of Pulsed Emission

The discoveries by radio, optical and X-ray instruments resulted in a large population of pulsar stars that can be observed in almost all wavelength bands up to gamma-ray energies. The recent Parkes Multibeam survey [84] doubled the number of known pulsars, and X-ray observations of pulsars have advanced quickly since the Chandra X-ray telescope became operational. In the gamma-ray energy band, only six pulsars were detected with high significance by the previous generation satellite experiment, EGRET [83]. Above 100 MeV, the light curves of five pulsars show a double peak structure (Figure 2.8), but the statistics of the data are not good enough to distinguish between the HE emission models based on these profiles. The spectra of these pulsars were measured, and all of them suggested a cutoff around 10 GeV. But EGRET was not sensitive enough to allow for a precise measurement of the cutoff to distinguish between the simple exponential and super-exponential forms predicted by different models.

No pulsed emission from pulsars has been detected by any of the ground-based atmospheric Cerenkov Telescopes operating above 100 GeV. The IC component that is predicted to be observable around the 1 TeV range by some outer gap models has been ruled out [85]. All ground-based experiments report only upper-limits for the pulsed emission [86, 87, 4, 85, 88] to date. The most constraining upper-limit calculated from this measurement is consistent with an estimated cutoff energy of about 27 GeV [87]. Very recently, only the MAGIC group [61] reports a detection of pulsed emission from Crab between 27 GeV and 60 GeV as

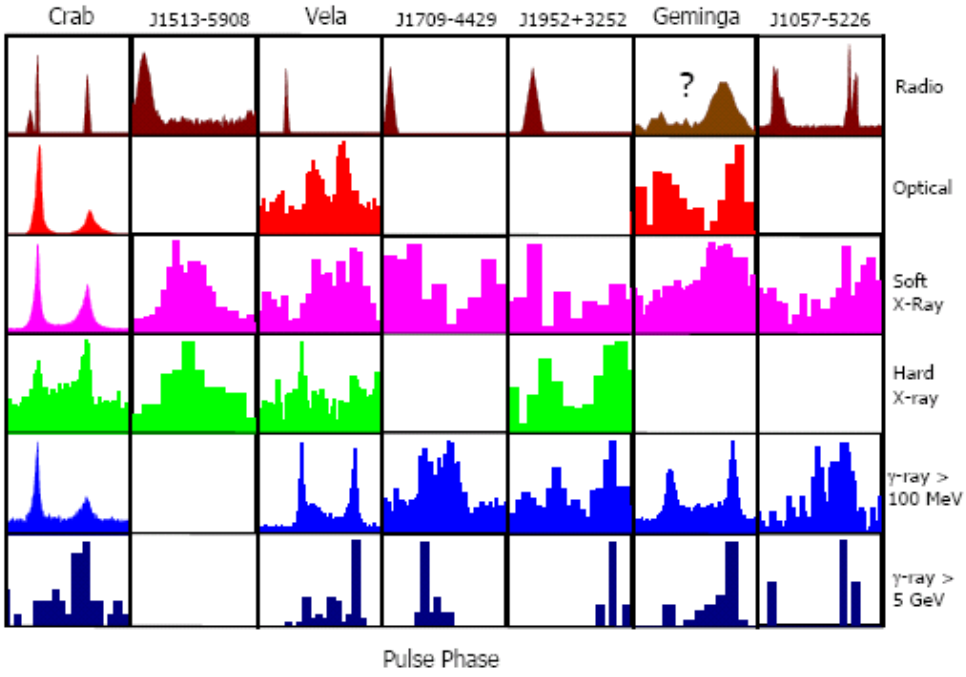

Figure 2.8: The pulse profiles of the seven gamma-ray pulsars in six energy bands [2]. In the last two rows, the pulse profiles of the six pulsars detected by EGRET are given. For all plots the x-axis is the rotational phase of pulsar and the y-axis is the number of events in each phase bin.

a result of their observations concurrent with the work presented in this thesis. It is very important to search for pulsed emission in this energy range to test the MAGIC detection and the predictions of the HE emission models in this energy range.

2.3 Pulsar Wind Nebulae

2.3.1 Regions in a PWN

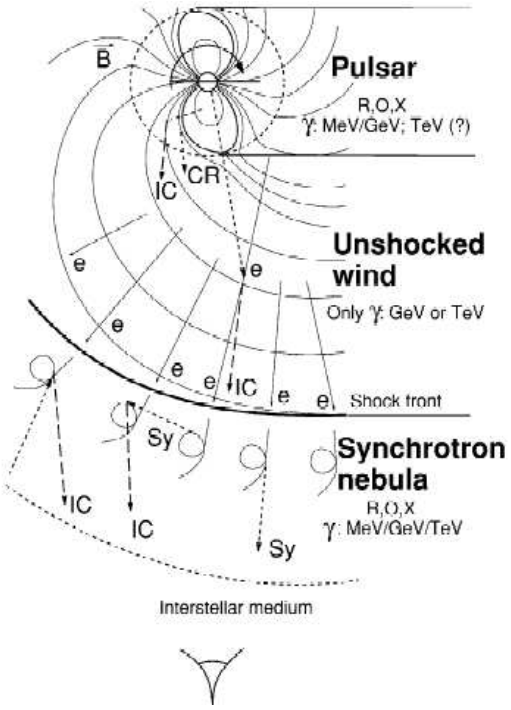

Figure 2.9: A sketch showing the main regions in a PWN complex and the emitted radiation from these regions [3]. Each region is discussed in the text. The sizes of the regions are not drawn to scale on the diagram.

The continuum emission from the nebula is closely coupled to interactions

in the environment of the pulsar. This coupling can be seen more clearly if we consider both the central pulsar and the surrounding nebula collectively as a single entity, a Pulsar Wind Nebula complex. The main regions of the complex, are sketched in Figure 2.9.

The central region of the PWN complex, the pulsar magnetosphere, extends out to the light cylinder. This region has a radius of approximately 10^{-9} pc. The region outside the light cylinder up to the termination shocks is known as the "wind zone". The size of this region is typically around $\sim$ 0.1 pc and the termination shock is located at the outer edge of the wind zone. Beyond the shock, the synchrotron nebula extends for $\sim$ 2 pc up to the outer edge of the remnant. In the following sections, each zone and the interactions in those regions will be discussed separately.

2.3.2 The Central Pulsar: The Energy Source

The necessity of a continuous energy source for a PWN is required to explain the total luminosity of Crab Nebula. The bulk of the observed luminosity from the Crab Nebula is due to synchrotron emission, implying the presence of a population of relativistic electrons in the nebula. However, the electrons producing synchrotron radiation in X-ray energies should lose their energy on time scales of the order of a decade. The fact that the Crab has been shining continuously much longer than this can only be explained through the presence of a powerful energy source that continuously replenishes the electron supply.

It was first showed by Pacini in 1967 [62] and Gold in 1969 [89] that a central pulsar with a slowing-down rotation could provide the necessary energy. In their model, the "magnetic dipole model", the pulsar star is considered as a rotating magnetic dipole producing electromagnetic radiation. As discussed in

Section 2.2.2, it can be shown that the observed luminosity of the nebula can be matched by the magnetic dipole radiation of a slowing-down magnetic dipole.

In the magnetic dipole model, the pulsar has a magnetic dipole moment oriented at an angle α relative to the spin axis of the pulsar. This model does not consider the surrounding material but requires a vacuum pulsar environment. As explained in Section 2.2.4, this is not realistic, and a dense magnetosphere of charged particles surrounds a rotating pulsar. Goldreich and Julian [71] showed that an "aligned rotator model", in which the spin and magnetic axes are parallel, can also produce the same magnitude of pulsar spin-down power in a non-vacuum environment. Their model predicts a strong induced electric field perpendicular to the pulsar surface which can easily strip off charged particles from the surface and carry them into the magnetosphere to form a non-vacuum environment. An additional population of particles is created in this region by the high-energy curvature or synchrotron radiation photons either through their interactions with the magnetic fields through single-photon pair production or with other photons through photon-photon pair production. A more detailed description of the processes in this region was given in Section 2.2.4.

Some of these charged particles, mostly electrons and positrons, are confined into the light cylinder of the pulsar by following the closed magnetic fields and they co-rotate with the pulsar. On the other hand, some of the particles escape from this inner region by following the open magnetic field lines beyond the light cylinder. The result is a "pulsar wind" of relativistic particles, which carries away the kinetic energy and angular momentum from the pulsar and causes it to "spin down". These particles are the main agents that couple the slow-down energy of the pulsar to the nebular emission.

Thus, the central pulsar star is the engine that provides continuous energy

to the surrounding nebula. The main agents, the relativistic wind of particles, that transport this energy to the nebula are first created in the inner pulsar magnetosphere region.

2.3.3 Pulsar Winds: Energy Transport between Pulsar and Nebula

The particles created inside the light cylinder escape from this region along the open magnetic field lines, carrying away the magnetic flux and energy of the central pulsar in the form of an ultra-relativistic, magnetized wind. The angular momentum of the pulsar star is also carried away by the wind, causing the spin down of the pulsar star. The region into which this wind flows, extending up to the termination shock is known as the "wind zone", and it is thought to have a radius of order of the 0.1 pc.

The primary magnetohydrodynamic (MHD) model for the transport of this rotational slow-down energy from the pulsar to a population of relativistic electrons in the outer nebula was first suggested by Rees and Gunn [90] and Kennel and Coroniti [91, 92]. The model considers energy transport by the pulsar wind and by the accompanying magnetic fields. The model starts with a relativistic pulsar wind and treats the wind and the magnetic fields using an MHD approximation. The complete details of the model are beyond the scope of this thesis, and only the main features are explained in this section. A very useful result of the model is the electron and magnetic field distribution for the entire PWN system.

The key feature of this model is that the pulsar wind must be confined within the supernova remnant. The edge of the surrounding remnant is expanding at a speed of 5000 km/s. The ram pressure due to the bulk flow of the pulsar wind calculated by the observed radio synchrotron radiation exceeds this in the un-

shocked wind region. Thus there should be a strong hydrodynamic "termination shock" inside the nebula which slows the bulk flow of the pulsar wind, randomizing the direction of the particles in the wind. By equating the ram pressure of the pulsar wind at the shock radius to the total magnetic and particle pressure within the nebula, Rees and Gunn [90] estimated the location of the termination shock at approximately 0.1 pc from the pulsar.

In almost all models, the wind leaving the pulsar magnetosphere is dominated by the Poynting flux, $F_{E\times B}$, with a much smaller contribution from the particle energy flux, $F_{particle}$ [5]. The magnetization parameter, σ, is defined to represent the ratio of the magnetic flux to the particle energy as follows [92]:

$$\sigma = \frac{F_{E\times B}}{F_{particle}} = \frac{B^2}{4\pi\rho\gamma c^2} \tag{2.16}$$

where B, ρ, and γ are the magnetic field, mass density of particles, and Lorentz factor in the wind, respectively. At the light cylinder, typical values of $\sigma > 10^4$ are expected for the pulsar wind [5]. However, at the end of the wind zone, at the termination shocks, the models require $\sigma << 1$ to meet the flow and pressure boundary conditions [5, 92]. The transfer from a Poynting-dominated flux to a kinetic-dominated flux with Lorentz factors $\sim 10^6$ that occurs in the wind zone is not completely understood, but it is considered to be related to the fast dissipation of the toroidal magnetic field with conversion of its energy into particle acceleration.

This unshocked wind region is under-luminous in X-Rays and lower energies, because the particles move along the magnetic field lines with small pitch angles, thus producing little synchrotron radiation. Bogovalov and Aharonian [93], suggested IC scattering of the relativistic particles on soft photons from either the pulsar or the CMB as a possible source of the gamma-ray radiation from this otherwise invisible region.

2.3.4 The Wind Termination Shock

The relativistic pulsar wind and the frozen magnetic field inflate in a region, the outer edge of which is confined by the expanding shell of the SN. A wind termination shock is formed when the wind meets the more slowly expanding ambient material. At the termination shock radius R_s, the ram pressure of the bulk flow of the pulsar wind is balanced by the total internal pressure of the nebula. Particle travel directions are randomized at the shock, and thus the bulk flow of the wind is converted into thermal energy in this region.

These thermalized electrons diffuse through the nebula and they are responsible for the synchrotron emission observed in the downstream flow. Measurements of the synchrotron spectrum show that the upper end of the emission energy is at around 500 MeV. This cutoff energy of synchrotron emission can be used to estimate the highest energy of the electrons given an average magnetic field of the nebula. For an average B field of $B \approx 3 \times 10^{-4}$ G, the highest energy of electrons is found to be $E \approx 10^{15}$ eV. This energy is higher than the energy of the particles in the wind, which have Lorentz factors $\gamma \approx 10^6$, implying additional acceleration. This acceleration is believed to occur at the termination shock through shock acceleration similar to first-order Fermi acceleration [94].

2.3.5 The Nebular Emission

Downstream, beyond the termination shock at 0.1 pc, the synchrotron nebula fills the region up to the outer edge of the remnant at ~ 2 pc. Thus the nebula is confined by its non-relativistic surroundings at the outer edge and by the termination shock at the inner edge. The bulk of the emission comes from this nebula region. The knowledge of the distribution of the magnetic field in this region is necessary to make statements about the synchrotron and inverse-Compton emis-

sion from this region. The MHD model developed by Kennel and Coroniti [92], which is very successful in predicting the magnetic field distribution across the shock and out to the edge of the remnant, can be used for this purpose.

The nebular emission spectrum is shown for the case of the Crab Nebula in Figure 2.10 [4]. The radiation from the radio band up to 100 MeV is synchrotron emission, and the second peak in very-high-energy gamma rays is due to the inverse-Compton scattering of synchrotron photons on high-energy electrons.

The synchrotron part of the spectrum can be predicted using the knowledge of the magnetic field distribution derived from the MHD model and assuming the electron population in the nebula has a power-law spectral distribution ($dN/dE \propto E^{-\alpha}$) after the shock acceleration. The broad range of the synchrotron spectrum suggests that the electrons have an energy spectrum from $\sim$ 100 MeV up to $\sim$1 PeV. The synchrotron radiation spectrum (thick dashed line in Figure 2.10) may be described by power laws with spectral breaks around 10^{13} Hz, 10^{15} Hz, and 100 keV. The first spectral break at 10^{13} Hz between the radio and optical is predicted to be due to the presence of an older population of electrons which have lost their energy to synchrotron loses over the lifetime of the nebula and have energies between 100 MeV and 100 GeV. The observed emission from the UV to the gamma-ray band, on the other hand, is expected to be due to the "young" electrons that are injected from the wind and that are recently accelerated at the shocks to energies exceeding 1 TeV. The optically emitting electrons below the last spectral break appear as a result of the synchrotron cooling of the TeV electrons [94].

In addition to the synchrotron photons, two other photon fields are considered in the calculation of the IC spectrum shown as the second peak in the figure: the thermal excess radiation (dotted curve in the figure) and the millimeter emission

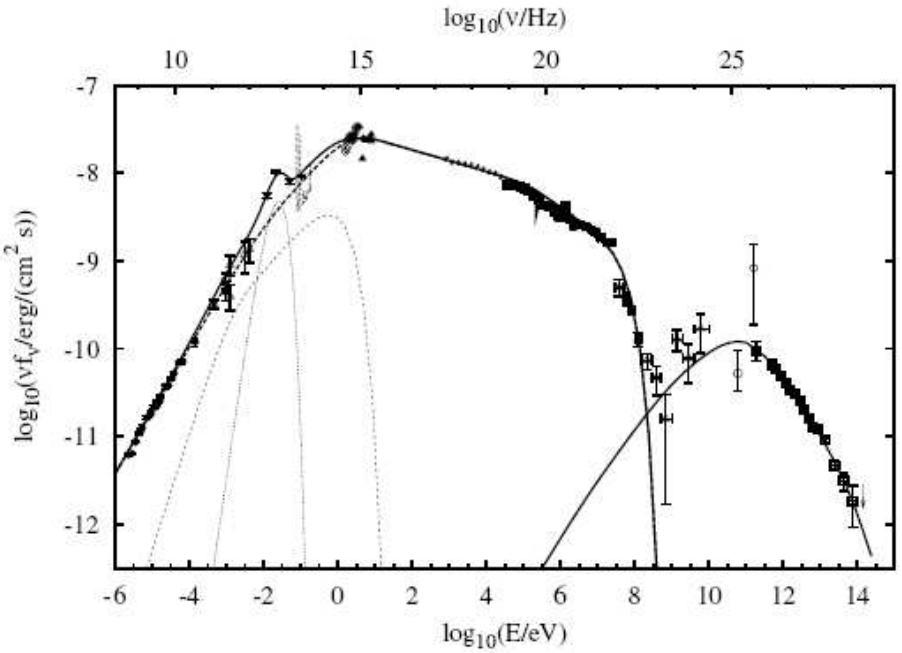

Figure 2.10: The broadband spectrum of the non-thermal emission from the Crab Nebula from radio to very-high-energy gamma rays is shown [51]. The thick-dashed line and the solid line curve on the left hand side correspond to the synchrotron and IC emission, respectively, as calculated using the framework of the MHD model [92]. The thermal excess radiation (dotted line) and the emission at millimeter wavelengths (dashed line) are also taken into account along with the pure-synchrotron photon distribution (thick dashed line) in the calculation of IC radiation spectrum. The emission up to $\sim$100 MeV is due to synchrotron and the emission above that is due to IC processes.

(dashed curve in the figure). The thermal excess radiation is assumed to follow a modified blackbody radiation distribution with a temperature of 46 K and responsible for the small bump in the spectrum around 10^{13} Hz. The success of this two-component (synch+IC) model in fitting the shape and the overall power of the Crab spectrum is impressive, as seen in Figure 2.10.

The spectra of the other PWNe are generally similar to that of the Crab and can be explained by a series of power-law distributions. In the radio band, the spectra are hard, with indices, α, between 0 and 0.3. At high frequencies the spectra soften, and in the X-ray band they are very steep, with $\alpha > 1$ [94].

Shortly after it was shown that the continuous spectrum of the Crab Nebula was due to synchrotron radiation, Gould [95] predicted that high-energy gamma rays would be produced by inverse-Compton scattering of relativistic electrons on the soft photons in the nebula. Later, the detection of the Crab Nebula emission at TeV energies was first made by the Whipple collaboration in 1989 [41].

The first satisfactory model calculation of the IC component of the Crab Nebula was carried out by De Jager and Harding in 1992 [96] and many others used this model for explaining the gamma-ray emission from the Crab above 100 GeV. The target photon fields for IC scattering can be the cosmic microwave background radiation, photons from thermal radiation, or as in the case of the Crab Nebula, the synchrotron radiation of the relativistic particles themselves (SSC-Model). The IC spectrum calculations use the distribution of the magnetic field from MHD calculations and the measured synchrotron emission to derive the energy spectra of the electrons. The IC flux at a given energy is then obtained with the IC production rate, by integrating over the spatial distribution of the photons and the relativistic electrons and their energies.

In a reverse approach, one can use the model of the IC and synchrotron spec-

tra to derive the mean nebula magnetic field strength and its spatial distribution, and then the PWN's particle content and an independent estimate of the magnetization parameter, σ, can be obtained [96]. The estimated values of B_{PWN} and σ as calculated by De Jager and Harding [96], are in good agreement with those derived from the MHD model of the Kennel and Coroniti [92].

2.4 Crab Pulsar and Nebula

The Crab Nebula is one of the most extensively studied objects in astrophysics due to its strong and stable emission over 21 decades of frequency. It is a pulsar wind nebula, a remnant of the supernova explosion which occurred in 1054 AD. as recorded by Asian and native American astronomers. After the supernova explosion that formed the Crab, it reached a maximum apparent magnitude of approximately -5, bright enough to be visible in the daytime. Its brightness slowly dwindled, but it remained visible to the naked eye for a period of 21 months. Currently its absolute brightness magnitude is around -3 and its apparent brightness is +8.4.

At the center of the nebula lies the Crab Pulsar, a rotating neutron star, which emits pulses of radiation from radio waves to gamma rays with a period of 33 ms. It is considered as the prototype member of the "plerion" class of supernova remnants with a filled center. The Crab Pulsar and Nebula complex is located at a distance of about 6,300 light years (2 kpc) from Earth, at a right ascension of 05h 34m 31.97s and at a declination of +22°00' 52.1", in the constellation of Taurus. The nebula has a diameter of 6 ly and it is expanding at a rate of about 1,500 kilometers per second. It can be contained in an 6×4 arcmin ellipse in the optical band.

2.4.1 Observations of the Crab Nebula

The Crab Nebula was first observed in 1731 by Jon Bevis and independently rediscovered by Charles Messier in 1758 who placed it in the Messier Catalog as the nebula M1. The name "Crab Nebula" is given by Lord Rosse in 1844, after its tentacle-like structure depicted in his drawings. In 1949, the radio astronomers Bolton, Stanley and Slee [97] identified the Crab Nebula as a radio source, making it the first non-solar system radio source to be identified with a known optical object. The radio flux was higher than the optical flux so the continuum radiation could not be explained by thermal radiation. The continuum emission was first explained by Shklovsky in 1953 [98] to be synchrotron emission. Later it was observed that the nebula generated optical, radio and X-ray radiation such that its brightness should fade away within a few years. This showed that an energy source must continuously supply energy into the nebula and led to the discovery of the Crab Pulsar.

It was suggested by Gould in 1965 [95] that since the Crab Nebula is a source of synchrotron radiation, due to IC scattering, it could also be a source of VHE photons. Since the synchrotron spectrum of Crab nebula implies the presence of electrons with energies up to $\sim 10^{15}$ eV, IC emission in the TeV range was also expected. The detection of the Crab Nebula in TeV gamma rays was first made by the Whipple Collaboration in 1989 [41] using the atmospheric Cherenkov technique, although before that there were many unsuccessful attempts. The Crab Nebula was thus the first gamma-ray source to be firmly detected by ground-based experiments. After this detection, more than a dozen other groups have detected and confirmed a steady TeV gamma-ray signal from the Crab Nebula.

There is a good agreement between the spectral measurements of the different groups operating at TeV energies. The Crab Nebula is considered as the

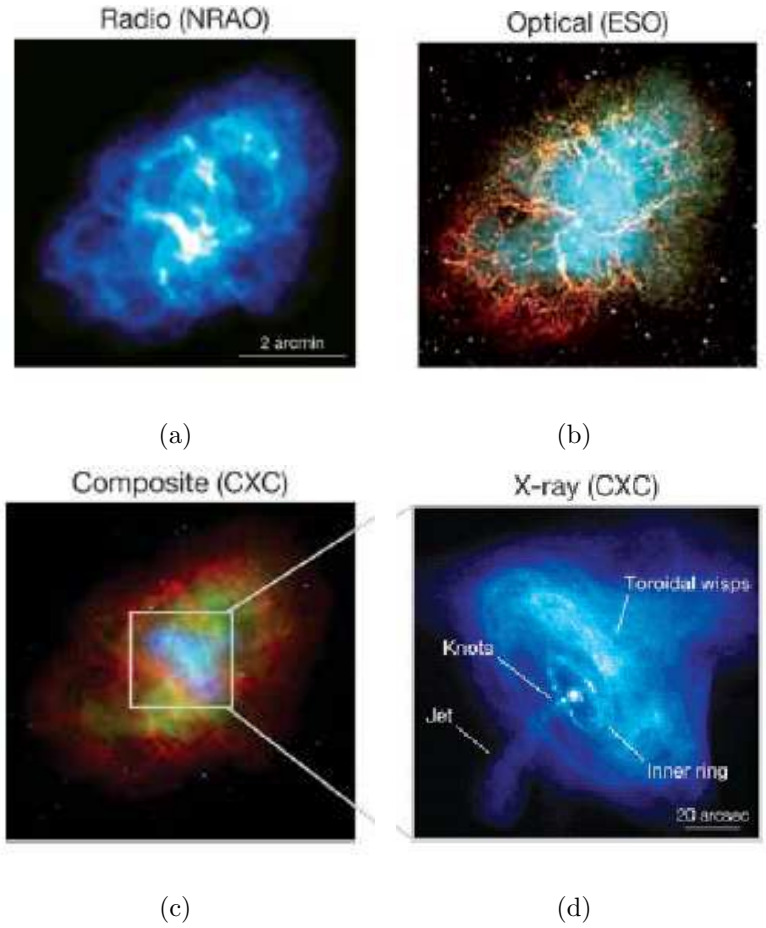

Figure 2.11: Images of the Crab Nebula in different wavelengths are given [5]. (a) The radio emission from the Nebula. (b) The optical synchrotron emission (blue-green) and the emission from the filaments (red). (c) The composite image of radio (red), optical (green) and X-ray(blue) emission. (d) The X-ray emission from the Nebula. Note that the scales of the first three images are the same and larger than the scale of the last image, as shown.

"standard candle" in VHE gamma-ray astronomy due to its strong and steady emission. All the data between 300 GeV and 10 TeV, where most of the spectral measurements are reported, are consistent with a single power law spectrum with a photon index of ∼2.5.

The spectrum of the IC-component of the nebular emission at GeV energies was measured by the EGRET experiment. This energy region is of special interest because it is where the transition from synchrotron emission to IC emission is expected to occur. The spectrum measured by EGRET shows a clear spectral hardening above 0.1 GeV as expected above the synchrotron cut-off, and its shape up to 5 GeV appears to be in reasonable agreement with the synchrotron-self-Compton model. But the level of the EGRET flux is higher than the expectations, which may be an indication of additional gamma-ray component.

The Crab Nebula is the strongest steady source of VHE gamma rays known in our Galaxy. The Crab is a strong VHE gamma-ray source because of its unusually high spin-down luminosity of its pulsar at 5×10^{38} ergs. The average magnetic field in the nebula is also high, $\sim 10^{-4}$ G, and this causes rapid cooling of the relativistic electrons. As a result, the size of the synchrotron nebula decreases with increasing energy because the higher the energy of a particle the faster it loses energy by synchrotron emission. The lifetime of the radio emitting electrons is larger than the age of the nebula, therefore, they fill the whole nebula. The optically emitting electrons have smaller lifetimes, thus the nebula is smaller in optical wavelengths. The X-ray emitting electrons lose their energy in only a few years, thus the X-ray image is the smallest in angular size and covers the region very close to the light cylinder of the pulsar [94]. This is consistent with the central pulsar being the source of the radiation emitted from the nebula. On the other hand, since the synchrotron spectrum does not extend to the gamma rays,

but gamma rays are produced by IC scattering of the same population electrons after the shock region, the gamma-ray emission comes from the outer nebula.

2.4.2 Observations of the Crab Pulsar

The presence of a pulsar star as the energy source to the Crab Nebula was first suggested by Pacini in 1967 [62]. The actual discovery of the Crab Pulsar (PSR B0531+21), was made first in the radio band in 1968 [64]. This was followed by optical and X-ray detections.

The pulsed gamma-ray emission from the Crab Pulsar was first reported by various balloon [27, 28, 99] and by the satellite experiments SAS-2 [100] and COS-B [101, 102] in the energy range between 1 MeV and 1 GeV.

The current highest energy pulsed emission detection was made by the EGRET experiment on board CGRO [6]. The pulsations have been seen up to an energy of 5 GeV with no conclusive evidence for pulsed emission above this energy. The pulse profile of the Crab Pulsar at the highest energies, has two fairly narrow peaks, separated in phase by about 0.4 cycles, with a small amount of inter-pulse emission between them. The broader second peak contains about 54% of the flux of the first peak. Figure 2.12 shows the pulse profile of the Crab Pulsar reconstructed from EGRET data above 100 MeV. The energy spectrum of the pulsed emission between 50 MeV and 10 GeV was fitted to a double power law with index of -4.89 ± 0.66 below $\sim$50 MeV, hardening to -2.05 ± 0.04 above $\sim$100 MeV [103]. The data points are shown in Figure 2.13, the existence of any cutoff above 5 GeV is inconclusive due to the error on the highest energy point.

Above 100 GeV, no detection of pulsed emission has been clearly established by any ground-based experiment. So far, only upper-limits have been reported by these experiments: Whipple at $\sim$ 250 GeV [86], STACEE at 190 GeV [104],

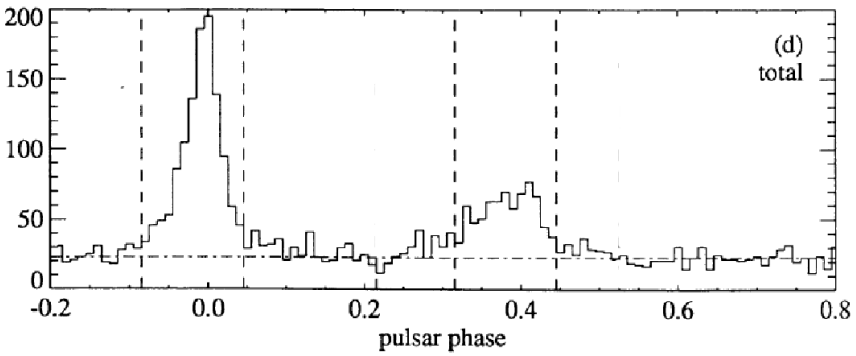

Figure 2.12: The pulse profile of the Crab Pulsar detected by EGRET above 100 MeV [6]. The x-axis is the rotational phase of the pulsar relative to the phase that main peak of the radio emission occurs, y-axis is the excess number of photons detected over the steady emission.

CELESTE at 60 GeV [87], HEGRA at 548 GeV [4] and HESS at $\sim 400 GeV$ [85]. The most constraining few of these upper limits can be seen on Figure 2.13. Very recently, only the MAGIC group [61] reports a detection of pulsed emission from Crab between 27 GeV and 60 GeV as a result of their observations concurrent with the work presented in this thesis.

2.4.3 Significance of Observations of the Crab with VERITAS

As seen from the Figure 2.10, there is an observational gap in the energy spectrum of the steady emission from the Crab Nebula, in the energy region around 100 GeV, where the peak intensity of the IC-emission is expected. This is due to the fact that the past satellite experiments are limited by photon statistics at energies above a few GeV and the previous-generation ground-based experiments have energy thresholds around 400 GeV and are limited by the background below that energy. The FGST sensitive to the gamma rays up to 300 GeV, will fill

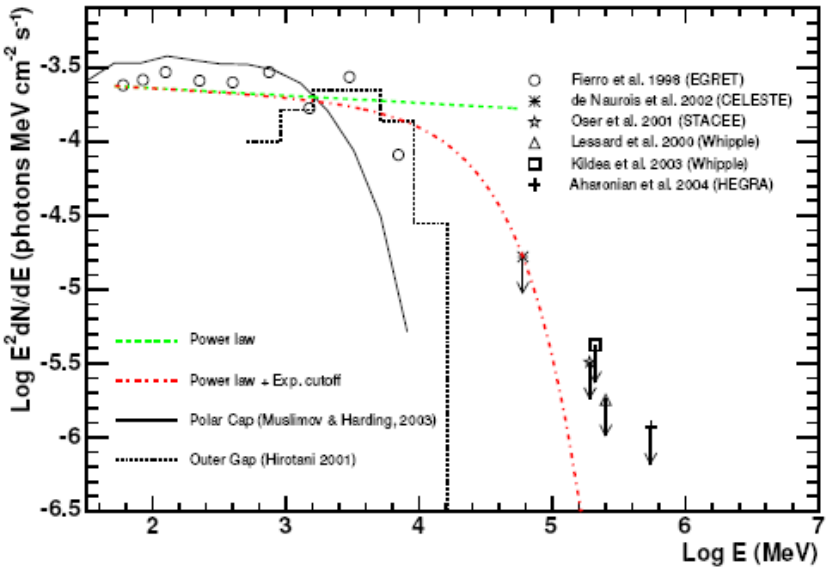

Figure 2.13: The EGRET data points are shown with the curves in the form of simple power law (green dashed) and power law with the exponential cutoff (red dot-dashed) fitted to the points. The prediction of the outer gap model (dotted line) and polar cap (solid line) model are also shown. The various upper limits attained from the observations of ground-based telescopes are shown with different symbols as listed in the legend.

this observational gap. The current generation ground-based experiments, such as VERITAS, has lower energy thresholds of around 100 GeV and considerable sensitivity near this energy. Thus, it is very interesting for VERITAS to observe the Crab Nebula and to measure its spectrum as near to the IC-peak as possible. The goal is to verify that the spectrum flattens near the peak region, deviating from the power law seen above 300 GeV as expected from the models.

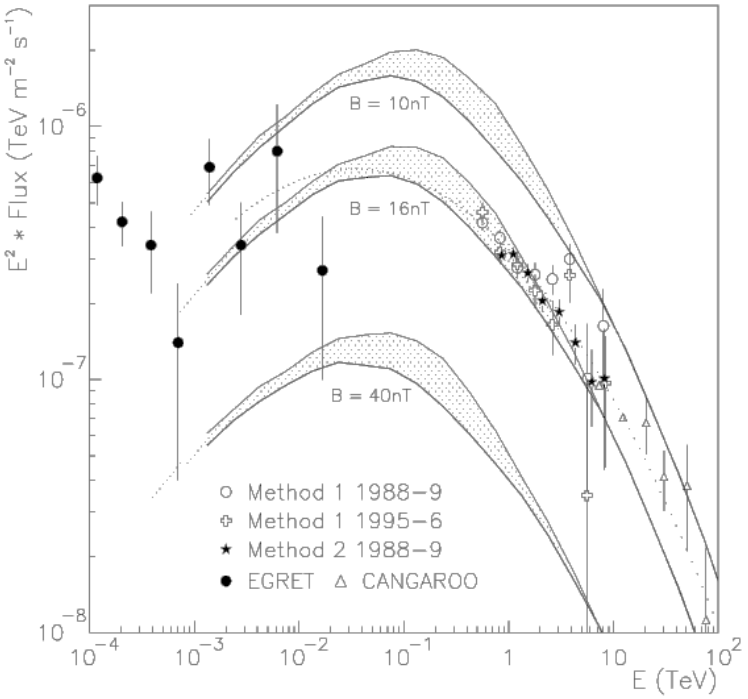

Figure 2.14: The spectrum of the Crab Nebula measured by the Whipple [7] and EGRET [8] experiments are compared with the predicted IC spectrum [9] for three different magnetic field strengths [7].

As described in Section 2.3.5, the IC gamma rays may be a sensitive probe of the magnetic field of the Crab Nebula. Various attempts have already been made to determine the magnetic field from the TeV flux levels. Figure 2.14 shows the comparison of the spectrum measured by Whipple and EGRET to the model

of Atoyan and Aharonian [9], for three magnetic field values. The data is best fit by a mean magnetic field value of 1.6×10^{-4} Gauss, which is well below the equipartition value of 3×10^{-4} G [7]. A further detailed measurement of the IC-spectrum along with the knowledge of the synchrotron spectrum will help in modeling the magnetic field distribution more completely and improve the current models.

The pulsed emission from the Crab Pulsar is seen at all wavelength from the radio band to GeV energies. Yet, various open questions regarding the high-energy pulsed emission, such as the locations of the acceleration regions in the pulsar environment, cannot be answered with the current available data. The current models for high-energy pulsed emission can be distinguished by the determination of the cut-off energy of the pulsed emission. The cut-off energy is expected in the region between 10 GeV to 100 GeV from the predictions of these models. It is expected that the FGST, which is sensitive to energies up to 300 GeV with good photon statistics, will detect the cutoff of the pulsed emission in the gamma-ray range and answer this important open question in pulsar physics. Until the launch of FGST, any determination or constraint on the cut-off energy by the current generation of ground-based experiments is important. These are the main motivations for observations of the Crab and the search for pulsed emission by VERITAS.

CHAPTER 3

The Ground-Based Detection of Gamma Rays

3.1 Introduction

Gamma rays represent the highest energy radiation of the electromagnetic spectrum. They are created by non-thermal processes initiated by the most extreme conditions at various astrophysical sources in the universe. Since gamma rays are uncharged, they travel through space without changing their direction, thus preserving the information about their origin. Detection of gamma rays is an essential probe to these extreme environments which are the natural laboratories capable of accelerating particles to very high energies.

Gamma rays are not attenuated significantly while they propagate through space, but their flux decreases with increasing energy mostly due to the intrinsic acceleration mechanisms of their sources. It is possible to detect gamma rays directly from space. However, due to the energy dependency of their flux, the small collection areas of space-based detectors place an energy limit of $<300\,\mathrm{GeV}$.

Unfortunately, since the Earth's atmosphere absorbs gamma rays, it is not possible to directly detect γ-radiation on Earth where we can build detectors with large collection areas. Fortunately, gamma rays initiate extensive air showers in the atmosphere and the cascade of the particles in these showers produces Cherenkov radiation which carries the information from the primary gamma ray. This enables one to use the atmosphere itself as a part of a detector and one can

detect this brief Cherenkov flash from the ground over the background of night-sky light using a suitable instrument. Unfortunately, cosmic rays also generate similar showers and therefore they form a significant background to the detection of gamma rays on the ground. One needs to study the differences between the air showers of gamma rays and cosmic rays to come up with a technique to distinguish gamma rays from the cosmic-ray background. In the 1980's, the Whipple Collaboration proved that the imaging atmospheric Cherenkov technique (IACT) makes it possible to extract the gamma-ray signal from the cosmic ray background to detect a gamma-ray source with high significance. Since then, this technique has been successfully used to detect gamma-ray sources in the energy range of 100 GeV to 10's of TeV, bringing this unexplored very high energy (VHE) window to the reach of science.

In this chapter, the propagation and the detection of gamma rays in space is first discussed. Then the interaction of gamma rays and the production of extensive air showers are explained. This is followed by the description of the production of Cherenkov radiation by these showers and the differences between gamma-ray showers and cosmic-ray showers. In the final section, the properties of a telescope to detect this Cherenkov radiation are summarized and the imaging atmospheric Cherenkov technique is introduced.

3.2 Propagation of Gamma Rays In Space

Gamma rays are uncharged, and that is why after they are emitted from the sources of their origin they are not affected by magnetic fields throughout their travel in space. Thus, they travel without changing their direction. Since their trajectories point directly back to their sources, unlike the distribution of cosmic rays, the flux of gamma rays is not isotropic.

The dominant interaction gamma rays may have through space is photon-photon pair production, $\gamma_{\mathrm{VHE}} + \gamma_{\mathrm{Bg}} \rightarrow e^+ + e^-$, if they come across a suitable energy photon of the intergalactic background on their way to Earth (Figure 3.1). The energy of the intergalactic background photon that allows this process can be found for the peak cross section of the process through Equation 3.1, where E_{VHE} and E_{Bg} are the energy of the VHE and intergalactic background photons, respectively. θ is the collision angle between the two photons, m_e is the mass of the electron, and c is the speed of light.

$$E_{VHE}E_{Bg}(1 - cos\theta) \sim 2(m_e c^2)^2 = 0.52(MeV)^2 \tag{3.1}$$

For gamma rays, intergalactic optical/IR photons can be significant absorbers that attenuate the gamma-ray signal. This is one of the limitations for the farthest distance to which VHE gamma-ray telescopes can detect sources. On the other hand, given a known intrinsic spectrum of VHE gamma rays from a particular source, the attenuation properties of them can be used to probe the intensity of the intergalactic background light.

The principal interaction of a gamma ray above 10 MeV with matter is electron and positron pair-production in the presence of an atomic nucleus, $\gamma\,(+\,Nucleus)$ $\rightarrow e^- + e^+\ (+\,Nucleus)$ (See Figure 3.1). Since the momentum of the initial photon must be conserved as well as its energy, the pair-production cannot occur in empty space out of a single gamma ray, but the presence of matter, a nucleus, is required to take up some of the initial momentum. For this process, the initial gamma ray needs to have at least an energy of twice of the electron rest mass, ($h\nu > 2m_e c^2 \sim 1.02\,\mathrm{MeV}$).

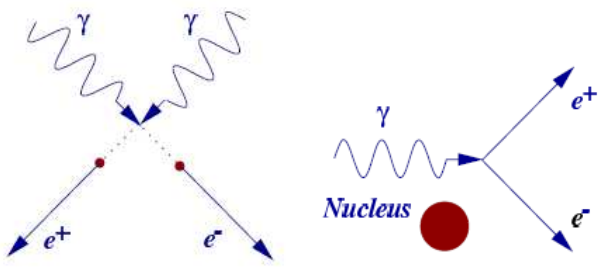

(a) (b)

Figure 3.1: Interactions of a gamma ray - I. (a) Photon-photon pair production occurs when a VHE gamma-ray interacts with a suitable energy, optical or infra-red, photon. (b) Single-photon pair production in the presence of matter.

3.3 Interactions of Gamma Rays and Cosmic Rays with the Atmosphere

3.3.1 Gamma-Ray Induced Air Showers

The Earth's atmosphere is opaque to any high energy radiation from space, in particular to gamma rays and cosmic rays above energies of 10 MeV. As discussed in the previous section, the main interaction of a gamma ray with matter, air molecules in this case, is the pair production mechanism in the presence of a nucleus (Section 3.2 and Figure 3.1). The mean free path of a gamma ray in the atmosphere can be given in units of g cm^{-2}, which include the effect of the density of the atmosphere, and it is $\sim$ 37.7g cm^{-2} for the density of atmosphere at standard temperature and pressure (STP). This means that upon entering into the atmosphere a gamma-ray is absorbed, producing an electron-positron pair within this distance which corresponds to $\sim$30 km above sea level.

The resulting electron-positron pair further interacts with the ambient nu-

clei via bremsstrahlung, producing more gamma rays while the energy of the pair is reduced by $1/e$ in one radiation length (Figure 3.2). The cross-section and the radiation length of the bremsstrahlung process is very similar to that of pair production. The emitted photons via this process still have enough energy to pair-produce into secondary electrons which again lose energy via bremsstrahlung while producing more photons. These two processes repeat themselves many times resulting in an extensive air shower of the electromagnetic type until the average energy of the particles in the shower is reduced to below the energy level of $\sim$83 MeV necessary for bremsstrahlung. At this point, known as the shower maximum, the exponentially-growing cascade reaches its maximum particle content which is of the order of 10^3 particles for a 1 TeV gamma ray.

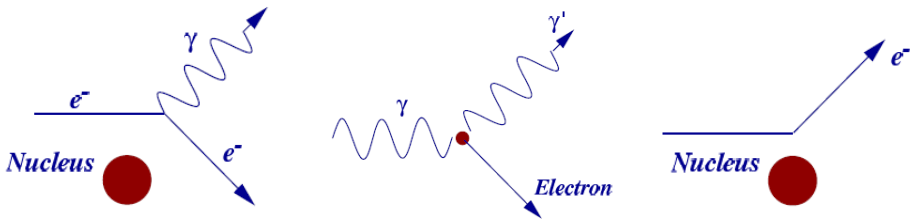

(a) Bremsstrahlung. (b) Compton Scattering. (c) Coulomb Scattering.

Figure 3.2: Interactions of a gamma ray - II. Each interaction is explained in the text (Section 3.3.1).

After shower maximum, the dissipative processes start to reduce the total energy in the shower. Compton scattering is the main process by which photons lose their energy. The electrons lose their energy through ionization and Coulomb scattering (Figure 3.2). Compton scattering is the scattering of a photon from a free electron and its cross-section is dominant at energies around < 10 MeV. Ionization occurs when a free electron in the cascade inelastically collides with the bound electron of a nucleus and removes it from its orbit. Coulomb scatter-

ing occurs between two charged bodies, a free shower electron and a nucleus in our case. A part of the initial energy of the electron is imparted to the nucleus during the reaction, causing the free electron to lose energy. All these processes are electromagnetic in nature. As a consequence of the low transverse momentum of the secondary electrons, the shower is strongly beamed along the direction of the primary gamma ray. Coulomb scattering is the only process that spreads the shower out which allows one to detect this shower over a considerable area (typically $3 \times 10^4 \mathrm{m}^2$) on the ground. The schematic diagram of the shower generation can be seen in Figure 3.3.

Many particles in the shower travel faster than light in air due to their relativistic energies. As described in Section 3.4, from the point of the initial interaction to until the energy of the particles falls below the energy of $\sim$21 MeV which happens well after shower maximum, the particles emit Cherenkov radiation. For a gamma ray of < 10 TeV initial energy, the secondary particles created in the shower lose their energy and the shower is dissipated well before it reaches the ground. It is due to this Cherenkov radiation from the shower that it is possible to detect the initial gamma ray indirectly using the IACT.

3.3.2 Cosmic Ray Induced Air Showers

Cosmic rays also produce extensive air showers which have a similar cascade structure as gamma-ray showers when they enter the atmosphere. These cosmic-ray showers form the major background to the gamma-ray signal detected on the ground. Fortunately, those hadron induced showers have some distinguishing characteristics that produce different distributions of the emitted Cherenkov light than gamma-ray showers.

The two principal interactions of a proton in the atmosphere are the ionization

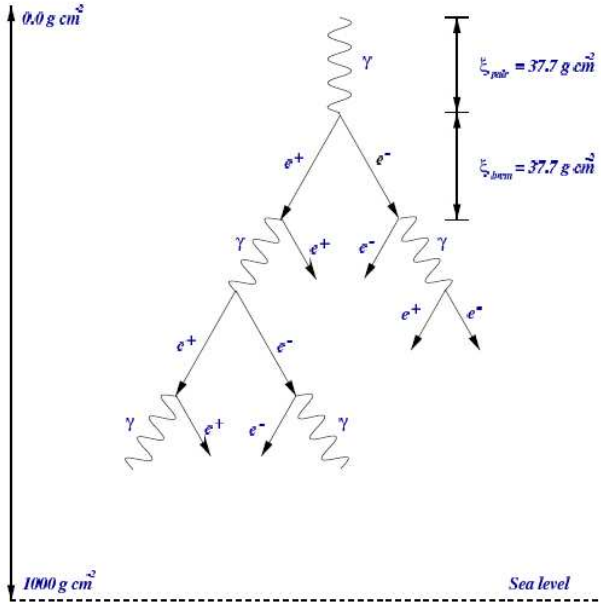

Figure 3.3: Schematic diagram of the generation of a gamma-ray induced extensive air shower [10]. The number of particles in the shower multiplies by alternating pair-production and bremsstrahlung processes at each radiation length of approximately $37.7\,\mathrm{g\,cm^{-2}}$ until shower maximum is reached. See Section 3.3.1 for more details.

collisions with the electrons of an air molecule and the nuclear collisions with air nuclei. The energy loss and the scattering angle of the incident cosmic ray in the ionization collision is not substantial enough to contribute to the shower development. Thus we can ignore the effect of this interaction.

On the other hand, during nuclear collisions, the primary cosmic ray loses a considerable amount of its energy and may produce a few secondary hadrons as an outcome. The surviving primary hadron and each of the secondary hadrons can be energetic enough to continue to have the same interaction with air nuclei, producing a cascade of hadronic particles. Due to the large momentum of the primary cosmic ray, these hadrons keep the strong directionality of the initial particle. This cascade is referred to as the "nucleonic component" of the hadronic air shower.

During the nuclear interactions, if the interacting hadron has an energy greater than $\sim$1 GeV, charged and neutral pions are also produced until the initial hadron's energy falls below that threshold energy. The neutral pions decay into gamma rays almost instantly (with a lifetime of $\sim 0.83 \times 10^{-16}$ seconds), via the decay channel $\pi^0 \rightarrow 2\gamma$. The resulting gamma rays initiate electromagnetic sub-showers via the same mechanisms discussed in the previous section.

The charged pions, on the other hand, decay into muons with a lifetime of $\sim 2.6 \times 10^{-8}$ via the decay mechanism $\pi^{\pm} \rightarrow \mu^{\pm} + \nu_{\mu}(/\bar{\nu_{\mu}})$. These muons form the "muonic component" of the hadronic shower. Muons are weakly interacting, although they eventually decay into electrons, and due to their relatively long lifetimes, they live down to ground level where they form another type of background to the gamma-ray showers.

The three component nature of a cosmic-ray shower can be seen in Figure 3.4 compared to a gamma-ray shower (Figure 3.3). The lateral spread of cosmic-ray

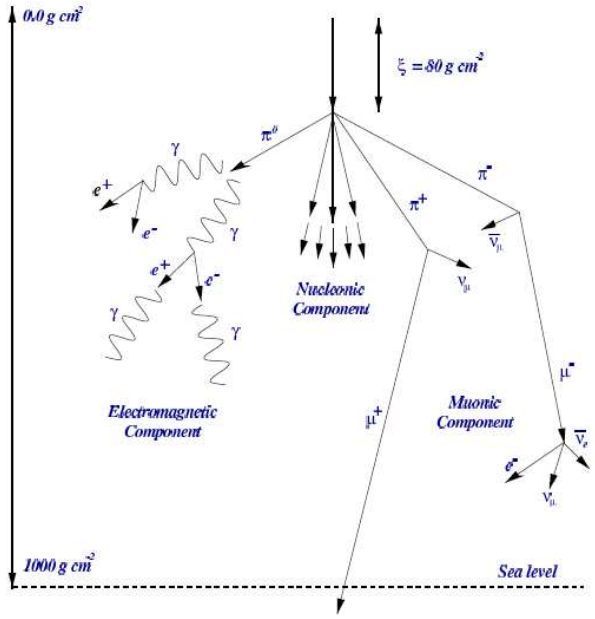

Figure 3.4: Schematic diagram of a cosmic-ray induced extensive air shower; three different components are labeled. See Section 3.3.2 for more details. ([10]).

showers is larger than that of gamma-ray showers, mainly because the transverse momentum imparted to pions is significantly larger than the transverse momentum imparted to an electron-positron pair from a gamma-ray. The relevant quantity here is the ratio of the mass of the pion to the electron mass, $m_\pi/m_e \sim 300$. Since a cosmic-ray shower has a three component nature, it is also more irregular than a gamma-ray shower. These characteristics are quite useful in distinguishing gamma-ray showers from the large background of cosmic-ray showers.

3.4 Cherenkov Radiation from Air Showers

As discussed in the previous sections, the shower maximum of an extensive air shower occurs in the atmosphere well above the ground. After that, the shower particles decay or are absorbed by the atmosphere before they reach the ground. Fortunately, many of the charged particles in the shower cause the generation of Cherenkov radiation because they travel faster than the speed of light in air. The Cherenkov radiation from all the particles adds up coherently and it reaches the ground in a cone of light centered around the axis of the extensive air shower. It can be detected as a short flash of considerable intensity over the night sky background as a signature of the primary gamma ray or cosmic ray. In this section the production of the Cherenkov radiation and its properties are discussed.

3.4.1 Production of Cherenkov Radiation

When a charged particle travels in a dielectric medium with a relativistic speed greater than the speed of light in that medium, the medium emits a radiation known as Cherenkov radiation. This radiation is an analog of the sonic boom jets produce when they travel at speeds faster than sound in air. During its travel in

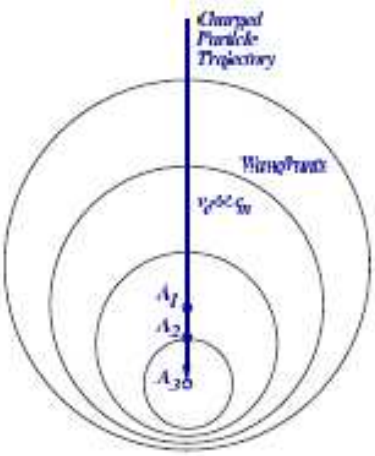

(a) For $v_p << c_m$, the electromagnetic field waves can not interfere and no coherent radiation is emitted.

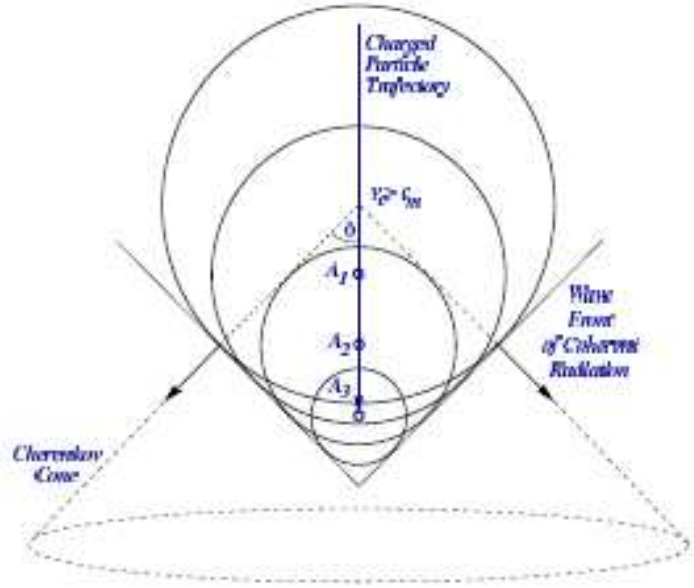

(b) When $v_p > c_m$, the wavefronts interfere constructively and the Cherenkov radiation is emitted in a cone relative to the axis of the particles trajectory.

Figure 3.5: Diagrams illustrating the production of Cherenkov Radiation.

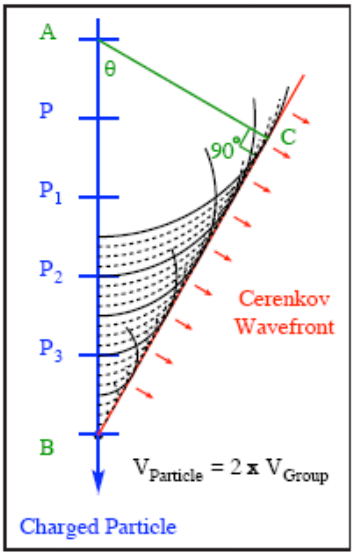

Figure 3.6: The Cherenkov angle can be deduced from the diagram using simple geometric arguments. See the text for explanation of the derivation.

the medium, a charged particle polarizes the nuclei along its path, causing them to oscillate as they return to their equilibrium position. For low particle velocities the polarized electromagnetic fields cancel each other, but for relativistic speeds the polarized electromagnetic fields interfere constructively, causing a coherent radiation to be emitted at a critical angle, θ_c, to the trajectory of the particle as depicted in Figure 3.5 [105].

One can deduce the Cherenkov relation, the condition that should be met for the production of this radiation from Huygen's principle, as shown in Figure 3.6. During the time the particle travels from point A to B with velocity $v_p = \beta c$, the radiation emitted by the medium at point A reaches point C traveling with the speed of light in the medium, $c_m = c/n$ where n is the refractive index of the medium. The angle of the emitted radiation to the particle trajectory can be

written as:

$$\cos\theta_{\rm c} = \frac{{\rm c_m}\Delta t}{v_{\rm p}\Delta t} = \frac{1}{\beta n} \tag{3.2}$$

The angle θ is called the Cherenkov angle of the medium, and it is a maximum when $\beta = 1$:

$$\theta_{\rm max} = \cos^{-1}\frac{1}{n} \tag{3.3}$$

The minimum velocity the particle should have for the production of Cherenkov radiation in a medium of refractive index n can be also deduced from the same equation (3.2) as $\beta_{min} = 1/n$. This corresponds to a threshold energy E_{min} given by:

$$E_{min} = \frac{m_0 c^2}{\sqrt{1-\beta_{min}^2}} \tag{3.4}$$

where the m_0 is the rest mass of the particle.

In the atmosphere, with a refractive index of $\sim$1.0003 (at sea level), the Cherenkov angle is θ_c $\sim$1.4° and the threshold energy for an electron to cause Cherenkov radiation production is about 21 MeV. At higher altitudes, the air density, and thus the refractive index of the air, is lower. Therefore the Cherenkov angle is narrower at the beginning of the shower.

The number of Cherenkov photons emitted per path length (dx) per frequency interval ($d\lambda$) for a charged particle with charge Ze is given by [105]:

$$\frac{{\rm d^2N}}{{\rm d}x{\rm d}\lambda} = \frac{2\pi\alpha Z^2}{\lambda^2}\left(1 - \frac{1}{\beta^2 n^2(\lambda)}\right) \tag{3.5}$$

where α is the fine structure constant and $n(\lambda)$ is the frequency-dependent index of refraction. For electrons, this can be integrated to obtain the number of photons emitted in the frequency range (λ_1, λ_2) over a distance l:

$${\rm N} = 2\pi\alpha l\left(\frac{1}{\lambda_2} - \frac{1}{\lambda_2}\right)\left(1 - \frac{1}{\beta^2 n^2(\lambda)}\right) \tag{3.6}$$

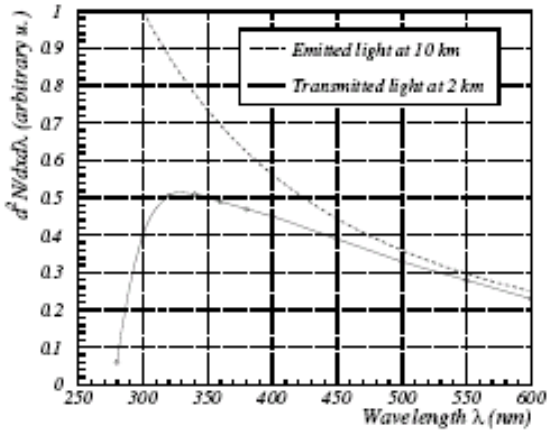

Figure 3.7: The intrinsic spectrum of Cherenkov radiation and the spectrum of the transmitted Cherenkov radiation is plotted. The x-axis is the wavelength of the radiation and the y-axis is the number of Cherenkov photons emitted per path length (dx) per frequency interval ($d\lambda$).

One can see from Equation 3.5 that the number of Cherenkov photons emitted is proportional to $1/\lambda^2$. There are various processes that can absorb the higher energy photons like Rayleigh scattering, Mie scattering and ozone absorption. As a result, the bulk of Cherenkov emission produced in the atmosphere is in the ultra-violet (UV) and blue parts of the spectrum. In a Cherenkov telescope, the wavelength dependency of the reflectivity of the mirrors and the quantum efficiency of the PMTs further alter the spectrum of the detected Cherenkov photons from their intrinsic spectrum (Figure 3.7).

3.4.2 Properties of Cherenkov Radiation from Extensive Air Showers

In an extensive air shower all particles with energies above the Cherenkov energy threshold produce Cherenkov radiation. For highly relativistic particles where

$\beta \sim 1$, the number of Cherenkov photons is constant for all energies (see Eq. 3.6). Thus the total amount of Cherenkov light produced is proportional to the total number of the electron-positron pairs produced in the entire shower. In this sense the intensity of the Cherenkov light is a calorimetric measurement since the total Cherenkov light yield is proportional to the primary particle's energy.

The Cherenkov angle, the angular spread of the Cherenkov radiation generated to the direction of travel of the relativistic particle, varies with the particle's energy and the refractive index of the medium, as shown in Equation 3.2. Since the refractive index of the atmosphere changes with altitude, the Cherenkov angle also varies with the emission height as seen in Figure 3.8(a). As the Cherenkov angle changes with the emission altitude, the radius of the Cherenkov cone when it hits the ground is also dependent on the emission height as shown in Figure 3.8(a).

The characteristic angle for sufficiently energetic particles is about 0.9° at the height of shower maximum (∼8 km) and 1.3° at mountain altitude. If all particles in the extensive air shower traveled along the shower axis, the result of this would be a ring of light on the ground with a radius of ∼125 m centered on the shower axis (Figure 3.8(b)). But the EAS has a lateral extent mainly due to the multiple Coulomb scattering of the electrons in the shower. The Cherenkov light from all the scattered particles adds up, smearing out the light pool on the ground to give a uniform, smooth circle.

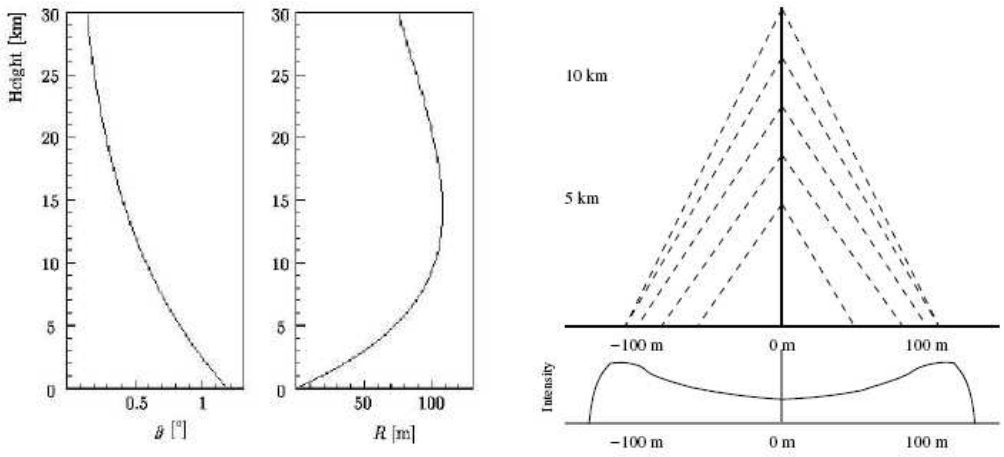

(a) (b)

Figure 3.8: Various parameters of the Cherenkov light emitted from an extensive air showerare shown. (a) The dependency of the Cherenkov angle, θ, and the Cherenkov ring radius, R, on the height of shower maximum is shown in the plots on the left and right, respectively [106]. (b) The intensity of Cherenkov light on the ground is given in the bottom plot. When the light produced at different emission points along the shower axis, it adds up as shown in the diagram on the top [107].

3.5 Differences between Gamma-Ray and Cosmic-Ray Air Showers

Since cosmic rays form a significant background to the detection of gamma-ray showers, it is important to study the differences between the showers produced by these particles and exploit those differences to come up with an effective rejection technique to significantly reduce the background of cosmic-ray showers while keeping most of the signal of gamma rays. A detailed discussion of the differences between the gamma-ray and cosmic-ray showers can be found in Hillas' review paper [108].

The most important difference between a gamma-ray and cosmic-ray shower is the total Cherenkov light yield produced. For a gamma-ray shower, all of the primary particle energy goes into the secondary electron-positron pairs, all of which contribute to the total Cherenkov light produced. For cosmic-ray showers on the other hand, a proportion of the energy goes into the muonic and hadronic components of the shower. Since muons are highly penetrating and heavier than electrons, they can carry significant amount of energy but produce relatively little Cherenkov light. The same is true for heavy hadrons. In addition, in cosmic-ray showers some of the initial energy goes into neutrinos which produce no Cherenkov radiation at all. The net result is that an EAS initiated by a cosmic ray has less Cherenkov light than a shower initiated by a gamma ray with the same initial energy.

The longitudinal spread of the showers, more specifically the distribution of the points of Cherenkov emission, is different in the two cases. Gamma-ray showers are initiated at higher altitudes than cosmic-ray showers due to the smaller mean path length of a gamma ray in the atmosphere ($\sim 37\text{g/cm}^2$) compared to

protons ($\sim 80 g/cm^2$). On the other hand, cosmic-ray showers penetrate deeper into the atmosphere, on average, than gamma-ray showers. During the development of the shower, while a gamma-ray initiated shower remains compact and uniform about the shower axis, a cosmic-ray shower suffers greater spread and lack of uniformity.

Cosmic-ray and gamma-ray showers are also different in their lateral density profiles. In gamma-ray showers, the initial energy is distributed evenly among all of the secondary particles which are electrons, positrons and photons. None of these particles acquires a large transverse momentum; thus they travel in small angles relative to the primary particle's original direction. The resulting Cherenkov photon density on the ground is uniform, circular, and centered about the shower core. On the other hand, in a cosmic-ray shower, the hadronic nuclear collisions can generate pions with large transverse momentum. Each of these particles with high transverse momentum create independent sub-showers of various energies which cause multi-cored and overlapping rings of Cherenkov light on the ground. The cosmic-ray showers also have a longer, more penetrating tail due to a larger number of particles, like muons, reaching to the ground. Therefore the lateral profile of the Cherenkov light from these showers is more diffuse and spread out. Thus when the Cherenkov light from these sub-showers reaches the ground, the result is an irregular lateral density of photons consisting of individual arcs and patches of light. This multi-cored nature of cosmic-ray showers is useful in distinguishing them from gamma-ray showers (See Figures 3.9 and 3.10).

When focused on the focal plane of a telescope with a multi-pixeled camera, the shower images again keep the general characteristics of the shower profile. The gamma-ray images have compact and uniform elliptical shapes while the

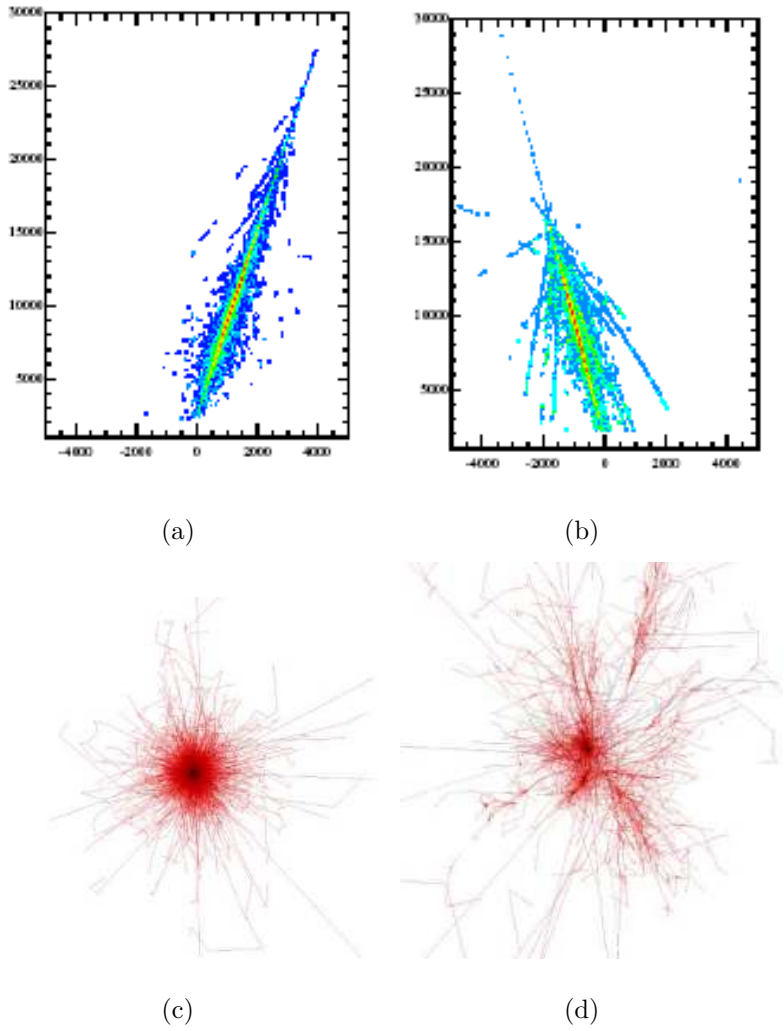

(a) (b)

(c) (d)

Figure 3.9: Comparison of the longitudinal and lateral development of a gamma-ray and a cosmic-ray shower [106, 11] from simulations. (a) Longitudinal view of a 1 TeV gamma-ray shower. (b) Longitudinal view of a 1 TeV proton shower. In these plots the x-axis is the distance on the ground from an arbitrary point and the y-axis is the height above the sea level in meters. (c) Lateral view of a 100 GeV gamma-ray shower. (d)Lateral view of a 100 GeV proton shower.

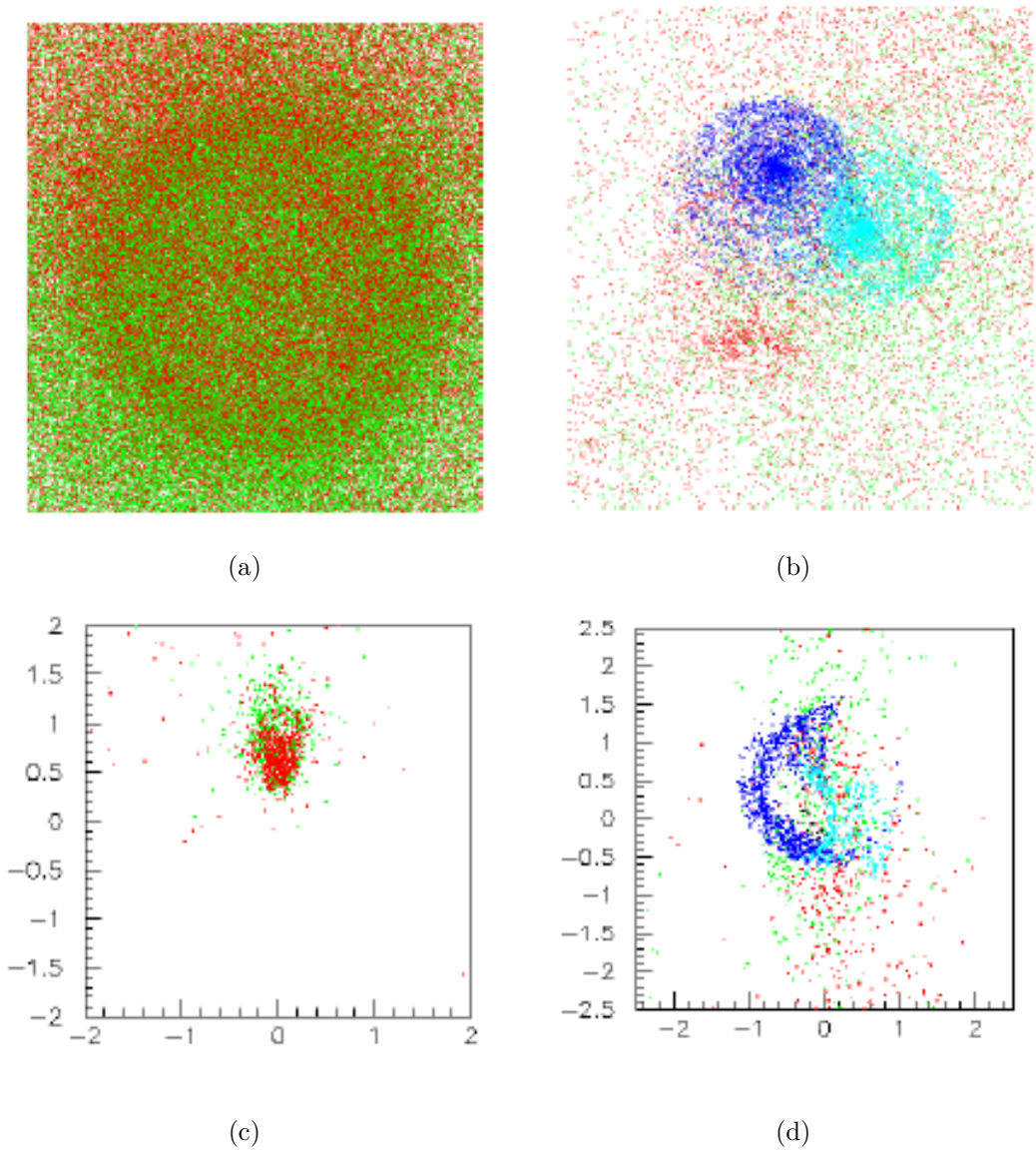

Figure 3.10: Comparison of the Cherenkov light pool on the ground and the image in the camera of a gamma-ray and a cosmic-ray shower from simulations [10]. (a)Cherenkov light pool of a 500 GeV gamma-ray shower on the ground. (b) Cherenkov light pool of a 150 GeV proton shower on the ground. (c) Image of a 500 GeV gamma-ray shower in a telescope camera. (d) Image of a 150 GeV proton shower in a telescope camera.

proton images are irregularly shaped and non-uniform. Also muon rings appear often in the images of proton showers (See Figure 3.10). Moreover, the orientation of the images for gamma-ray showers are pointed towards the source direction while the images for cosmic-ray showers are randomly oriented.

3.6 Imaging Atmospheric Cherenkov Technique

Cherenkov radiation has been known since the work of Cherenkov [109], Frank and Tamm [110] in 1937 (which eventually led to the 1958 Nobel Prize). The first successful observation of Cherenkov radiation from extensive air showers in the night sky was made in 1953, only after the development of the photomultiplier tube [111]. The generation of Cherenkov radiation from secondary particles in an extensive air showers makes it possible to indirectly detect the primary gamma ray or cosmic ray, since neither the primary particle nor the secondary particles from the air shower reach the ground. Its application to gamma-ray astronomy was first proposed in 1963 by Jelley and Porter [112]. However, the first solid detection of a gamma-ray source was achieved by the Whipple Collaboration in 1989, only after they developed the imaging technique (Figure 3.11) [41]. Since then many other experiments use this technique to successfully distinguish between gamma-ray and cosmic-ray showers produced by a primary particle with energy in the range 100 GeV to tens of TeV. With this technique a variety of other gamma-ray sources have been detected.

3.6.1 A Cherenkov Telescope

The essence of the technique to detect gamma rays indirectly is to take a snapshot of the Cherenkov light from the shower in a high resolution camera at the focus

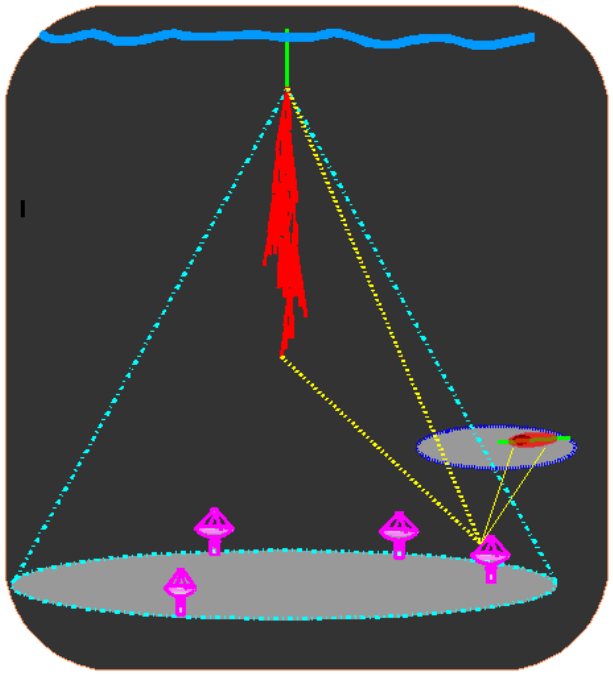

Figure 3.11: A diagram showing the concept of an array of Cherenkov telescopes in the Cherenkov light pool of a shower imaging the shower on their focal plane. The height the Cherenkov radiation starts is $\sim 10 - 20\,\mathrm{km}$ above the sea level, the radius of the Cherenkov light pool on the ground is $\sim 125\,\mathrm{m}$.

of a telescope with a large optical reflector. The telescope to be used to collect the Cherenkov light from these showers must have some key specifications as discussed by Weekes [19]. First of all the detector must be placed at high altitudes in order to get closer to the shower maximum where most of the Cherenkov light is emitted. The Cherenkov photon intensity is rather low (approximately 50 photons per square meter within 100 m of shower axis from a 1 TeV gamma-ray shower), thus the detector must have a large reflector pointed to the source direction to collect as much of the Cherenkov light as possible and focus it to the camera plane.

To use the imaging technique effectively, the instrument must have a good angular resolution. This can be achieved by having as large a number of pixels as possible in the camera. Since the Cherenkov light is peaked towards the ultraviolet end of the spectrum, having a significant response at these short wavelengths is another requirement. Using photomultiplier tubes (PMTs) with a bi-alkali photo-cathode is ideal for sensitivity in the UV and blue bands where the peak of the Cherenkov emission is observed. The field of view of the camera must be as large as to at least contain the angular extent of the shower light, which is on the order of 1°. For large impact distances of showers, the positions of the centroids of the images are farther away from the center of the field of view. Thus an even larger field of view is useful to obtain images of showers. Although the larger angular field of view is useful to get more distant showers and it increases the collection area of the detector, it is a disadvantage at the same time since it entails accepting more background night-sky light.

Next, one needs to pick out the Cherenkov light from these showers from the fluctuations of the night-sky light. The Cherenkov light duration in a gamma-ray shower is on the order of a few nanoseconds. In order to record the Cherenkov

pulse, the integration time of the detector must be matched to this intrinsic duration of the light flash. This requires a fast response trigger and high-speed electronics to record the collected information. Detecting coincident Cherenkov pulses from multiple points in the camera or from multiple detectors separated by some distance on the ground is very helpful in rejecting the background due to statistical fluctuations of the night-sky light or due to local muons, keeping the trigger rate and dead-time of the detector manageable.

Lastly, one can estimate the energy of the primary particle from the total intensity of the detected light since the total Cherenkov light is a calorimetric measure of the primary energy. In order to do that, the detector must be calibrated to have a uniform response for its individual pixels over the camera, which records the light from different points of the shower.

3.6.2 Imaging Technique

Once the Cherenkov light from gamma-ray and cosmic-ray showers is detected, the next challenge is to distinguish gamma-ray showers from the large background of cosmic rays. Using a Cherenkov telescope equipped with a camera composed of an array of photomultiplier tubes to detect the Cherenkov light from different parts of the shower, one can get a crude image of the shower. The Cherenkov light is emitted along a small cone about the shower axis. Typically the point the shower axis intersects with the ground, the shower core, is at a large distance from the detector, so the Cherenkov cone projects as an elliptical image in the focal plane of the detector (Figure3.12). This elliptical image has a different shape and orientation for gamma-ray and cosmic-ray initiated showers due to the differences in their development.

First of all, due to the isotropic arrival directions of cosmic rays, their images

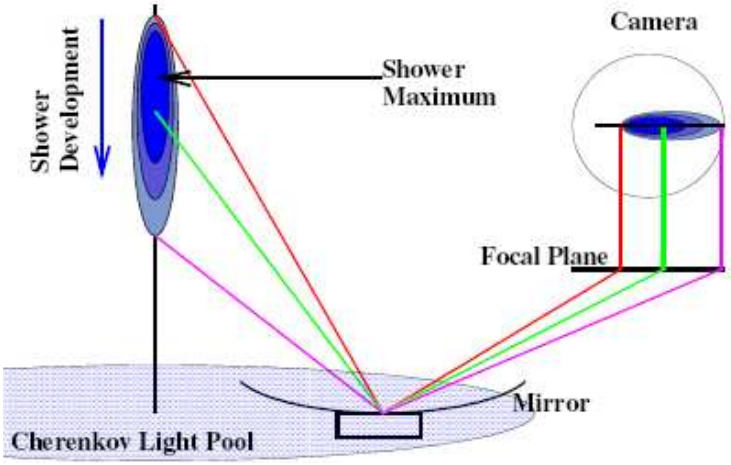

Figure 3.12: Imaging a vertically incident extensive shower in the focal plane of a telescope in the Cherenkov light pool of the shower [11].

do not have any preferred direction in the camera. On the other hand, since the telescope can be pointed to the direction of point sources that emit gamma rays, gamma-ray images are pointed towards the center of the field of view. In addition to the orientation, shape parameters like length and width also provide means of rejecting cosmic-ray events. Because of the smaller spread of gamma-ray showers, the images of them tend to be narrower and elongated in the camera compared to wider and shorter cosmic-ray images. Because of the uniform nature of gamma-ray showers, the gamma-ray images tend to be symmetric around the projection of the shower axis on the camera, while the images of multi-cored cosmic-ray showers are not symmetric. Exploiting these differences forms the core of the imaging technique. Even with a crude imaging technique one can remove 99.9% of the background cosmic-ray showers while retaining more than a third of the actual gamma-ray signal.

Hillas was first to use a moment-based analysis to fit the image of a shower

to an ellipse and parametrize it to define six independent parameters: alpha, distance, length, width, centroid, and size (Figure 3.13)[18]. The details of this parametrization is given in Chapter 6 and a full description of the moment fitting technique may be found in [113]. These parameters reflect the physical characteristics of the shower which differ between a gamma-ray and a cosmic-ray shower. The simulations of gamma rays and cosmic rays then can be used to define regions in this parameter space where gamma rays concentrate. These regions can be identified and utilized by defining certain event selection criteria capable of keeping a large fraction of gamma-ray events while discarding the majority of the background cosmic-ray events to obtain the best signal to background ratio.

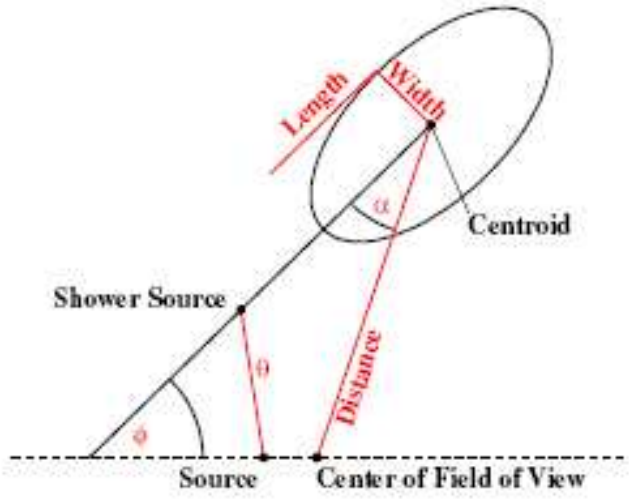

Figure 3.13: The Hillas parameters are shown in the diagram [11]. The parameters are described in Chapter 6.

After the event cuts have been applied, the incident direction of candidate gamma-ray events can be determined from the shower orientation. The primary particle's energy can be estimated using look-up tables created by simulations dependent on the impact distance and size parameter of the event.

The next important advance in the imaging technique, stereoscopic imaging, is the concept of using multiple telescopes to view a single extensive air shower simultaneously. It was first used by the HEGRA collaboration using a 5-telescope array. Stereoscopic observations have several advantages, the first one being the better quality of reconstruction of the shower parameters. While there is an ambiguity for the shower direction in single-telescope imaging, with stereo imaging of the shower one can use simple geometrical arguments to unambiguously determine the shower direction by intersecting the major axes of each image in the camera plane. This improves the angular resolution of the detector significantly. While it is not possible to find the core position in a single-telescope imaging without using look-up tables from simulations, one can use a similar concept of intersecting the major axes of the images on the ground to find the actual core position of the shower. The knowledge of the shower core position, along with the size information, also improves the energy reconstruction resolution dramatically.

A second advantage of stereoscopic observations is to be able to add one more level to the trigger requirement, which is the coincident detection of a shower by multiple telescopes to record an event. Since the rejection of false triggers due to night-sky or local muons can be done in hardware, this enables the detectors to be sensitive to lower energy showers while keeping the rates and dead-time of the system manageable.

Lastly, using simultaneous images recorded in several cameras, one can use more complex event selection mechanisms to achieve very powerful rejection of background showers from cosmic rays, local muons, and night-sky fluctuations. Calculation of the stereoscopic shower parameters and their application are discussed in more detail in Chapter 6.

CHAPTER 4

The VERITAS Observatory

The "Very Energetic Radiation Imaging Telescope Array System" (VERITAS) is an array of four 12 meter diameter Cherenkov telescopes designed to observe astrophysical gamma rays in the energy range from 100 GeV to tens of TeV. The VERITAS observatory is located at an elevation of 1270 m on Mt. Hopkins, south of Tucson, Arizona, USA. The first VERITAS telescope became fully operational in early 2005 and VERITAS started stereo-mode operations in March 2006 with the addition of the second telescope. The third and fourth telescopes were constructed in the winter of 2006, and the scientific observations with the VERITAS four telescope array began in April 2007.

The four VERITAS telescopes share a common design which is similar to their predecessor, the Whipple 10 m Cherenkov telescope [42]. Initially, it was planned to place the telescopes in a filled-triangular (Mercedes star) configuration with a baseline of 80 m. Due to problems acquiring the primary site, the telescopes were eventually deployed at the base camp of the Fred Lawrence Whipple Observatory (FLWO) with a configuration allowed by the space available on this site. The current configuration of the VERITAS array, where the telescopes are separated by distances between 35 meters to 109 meters, can be seen in Figure 4.1. The telescopes are tagged with an ID, T1, T2, T3 and T4. These IDs are shown in the figure next to each telescope.

This chapter presents a detailed description of the components of the individ-

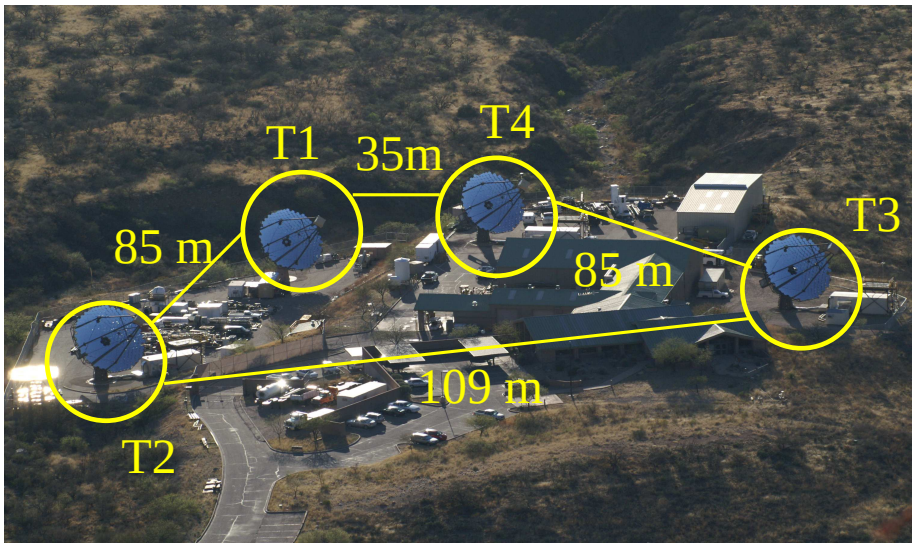

Figure 4.1: A photograph of the VERITAS array. The distances between the telescopes are shown. The telescopes are tagged with an ID, T1, T2, T3 and T4 shown next to each telescope, to use in referring to a specific telescope.

ual VERITAS telescopes. We start with introducing the mechanical and optical components of the telescopes in Section 4.1, followed by the description of the camera components in Section 4.3. The VERITAS Trigger and Data Acquisition systems are discussed in more detail in Section 4.4 and Section 4.5, respectively. This chapter concludes with a summary of the calibration procedures being used on the instrument in Section 4.6.

4.1 The Positioner and Optical Support Structure

The mechanical structure of an individual VERITAS telescope is similar to the Whipple 10 m telescope [42]. It uses a custom-designed, steel space-frame optical support structure (OSS) mounted on a commercial altitude-azimuth positioner. The 12 m diameter reflectors of the telescopes are formed by individual mirror

facets attached on the OSS and the camera is carried on the quadruped arms of the OSS at a focal distance of 12 m.

4.1.1 Positioner

The positioner is an off-the-shelf unit (Model PG-4003) manufactured by RPM-PSI (Northridge, California). The positioner is capable of achieving pointing accuracies of 0.01°[114]. It has a design slew speed of 1°/s in both elevation and azimuth, but it is driven at 0.3°- 0.5°for safety reasons. It is controlled by an Ethernet interface to a tracking computer, and the telescope pointing information is logged to the VERITAS database at a rate of $\sim$ 4 Hz during data taking. The positioner is designed to be safe to operate at wind speeds up to 20 MPH.

4.1.2 Optical Support Structure

The OSS was designed by M3 Engineering (Tucson, Arizona) and fabricated by Ambel Steel (Chandler, Arizona). The Davies-Cotton configuration [115] is used for the design of the OSS and mirrors due to its advantages over other designs. The main advantage of the Davies-Cotton design is that it allows segmented mirrors, each facet spherical and identical, which makes for straight forward fabrication, replacement and alignment of facets. This design offers smaller off-axis aberrations than a parabolic reflector so that it has good image quality out to a few degrees from the optical axis. The only disadvantage of the design is that it is not isochronous, which means the reflector introduces a time spread into the light pulse. The f-number is a parameter for an optical system which expresses the ratio of the aperture (diameter) of the optical system to its focal length. Optical aberrations are reduced with a higher f-number while the time spread introduced into the reflected rays decreases with a lower f-number. An f-number of f/1.0 was

chosen for VERITAS telescopes because it provides the best optical quality while keeping the optics-induced time spread roughly equal to the intrinsic spread of the Cherenkov shower.

The weight of the OSS, the mirror segments and the camera (a total of $\sim$350 kg) is balanced by the use of a mechanical by-pass to direct the load to a set of counterweights at the back of the OSS. The weight of the system causes some flexure in the OSS which depends on the elevation. The optical distortions due to this flexure take two forms: blur and decentering. Blur is the RMS width of an image of a point source formed by all the mirror facets. The decentering is the movement of the mean of the image centroid from the center of the focal plane [116]. In the following section, the corrections to the mirror alignment and positioner tracking needed to minimize these distortions are discussed.

4.2 The Mirrors

Each telescope has a segmented spherical reflector, composed of 350 separate hexagonal mirror facets covering an area of $\sim$110 m^2 (Figure 4.2). The hexagonal design allows for a closer packing to cover the maximum possible area as compared to circular facets. Each mirror has a radius of curvature of 24 m $\pm$ 1%. They are arranged on a spherical surface of 12 m radius and attached to the OSS via a triangular frame which isolates the facets from the OSS flexure. Adjustment screws allow the alignment of each facet to obtain better quality images.

The mirror glasses are provided from the vendor DOTI (Round Rock, TX) and they are cleaned, aluminum coated, and anodized at the on-site facility at the FLWO. They then undergo acceptance testing of their optical quality. Their performance exceeds the VERITAS requirements: $>$ 90% of the reflected light

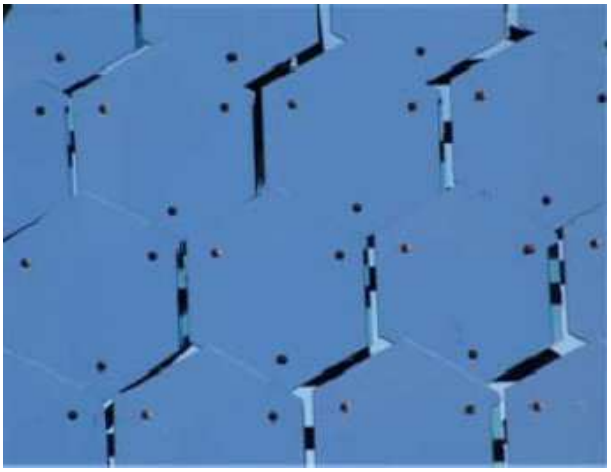

Figure 4.2: A photograph of the hexagonal mirror facets of Telescope 1 of VERITAS.

from a point source falls in a 10 mm circle located at the radius of curvature. The reflectance curve is shown on Figure 4.3(b), where it can be seen that the reflectance exceeds 90% at 320 nm and is $> 85\%$ from 280 to 450 nm [12].

The desirable optical parameters of the reflector of a Cherenkov telescope should be specified in relation to the characteristics of a gamma-ray shower. For a gamma-ray source at the center of the field of view (FOV), the average distance of the image centroid from the center is $\sim 0.85°$, and the image has a RMS width and length of about 0.14°and 0.25°, respectively [117]. The reflector should have sufficient resolution to record image structure on this scale. The resolution is limited by the optical distortion blur, which is represented by the "point spread function" (PSF) of the system. The PSF is defined as the width of the Gaussian fit to an image of a bright star on the focal plane recorded by a CCD camera. The PSF can be improved by optical corrections described in the following section. The point spread function of each telescope is 0.06° at an observing elevation of 70°, after applying optical corrections, which is well under the PMT size of the

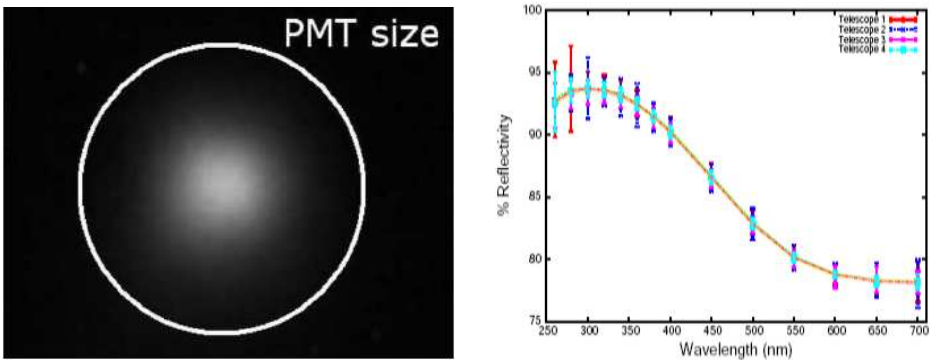

(a) (b)

Figure 4.3: (a) The image of a star reflected onto the focal plane of VERITAS. The white circle is the VERITAS PMT size of 0.15°. (b) VERITAS mirror reflectivity curve [12].

VERITAS camera (Figure 4.3(a)) [12].

4.2.1 Alignment of Mirrors and Optical Corrections

The individual mirror facets are aligned so that they act like a single spherical mirror focusing the reflected rays to a single focal point. The mirror alignment is done using a laser-based alignment tool placed at the radius of curvature (2 x focal distance) of the spherical reflector. A helium-neon laser beam is reflected from each individual mirror facet, and the mirror facet is rotated by the adjustment screws until the return laser beam coincides with the original laser beam from the alignment tool. The mirrors, aligned in this fashion, converge the light coming from a source at infinity to the focal plane of the reflector on the camera. The mirror alignment is done at least once a year for each telescope.

Even after the mirror alignment, the reflected image suffers from two different optical distortions mainly due to the flexure of the OSS, as explained in

Section 4.1.2. Optical corrections are applied to reduce these distortions to a minimum. Well defined images improve the angular resolution of the telescope.

The optical distortion in the form of decentering can be corrected for by a series of adjustments to the telescope pointing using the azimuth and elevation drives of the telescope positioner. The adjustments are a series of spherical rotations, known as T-Point corrections, which when applied, re-center the source image in the camera. They are calculated by pointing the telescope to a star for which the exact location is known. The image of the star is reflected on a screen at the focal plane, and the pointing of the telescope is adjusted iteratively until the image is centered in the FOV. The process is repeated for a series of stars at different elevations and a set of ten parameters are calculated which model the required correction to the pointing as a function of elevation. These corrections are then applied to the positioner by the tracking program during observing.

The optical distortion in the form of blur is represented by the "point spread function" (PSF) of the system. The RMS spread of the PSF can be reduced, by using a correction technique known a bias-alignment. The PSF is elevation dependent due to the changes of the OSS flexure at different elevations. It can be corrected by intentionally mis-aligning the mirrors at the stow position so that the OSS flexure causes them to return the correct alignment at the desired elevation. Sixty-five degrees is chosen to be the elevation at which the best focus is achieved. For a more detailed discussion of alignment procedures, one can refer to [118]. Figure 4.4 shows improvement of the PSF after the bias-alignment is applied.

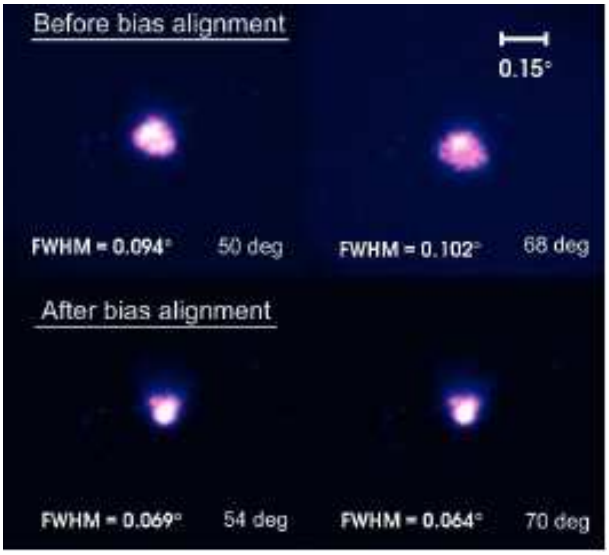

Figure 4.4: The improvement in the focusing of the images from bias alignment is shown by comparison of before (top) and after (bottom) bias alignment [118]. Each star image is taken at different elevation levels, as shown in the panels.

(a) (b)

Figure 4.5: (a)The front face of the Telescope 2 camera of VERITAS is shown displaying the packing of 499 pixels. (b)The same camera is shown with the light cone layer added.

4.3 Camera

The VERITAS cameras are located at the focal plane of each reflector at a distance of 12 m from the mirrors. Each camera has a total field of view of 3.5°, and it contains an array of 499 photomultiplier tubes (PMTs). The PMTs are packed in a hexagonal grid to minimize the dead space between them, which results in a 0.15° angular spacing between the centers of two adjacent PMTs. A plate of light cones is attached on the front face of the camera to concentrate the light onto the active region of the PMT photo-cathodes. The high voltage (HV) for the tubes is provided by a commercial power supply which allows the HV applied to each tube to be controlled individually. Each PMT has a preamplifier integrated into its base to amplify the signal from its last anode before the signal travels to the trigger electronics along a long cable. The camera also holds the monitoring hardware for the anode currents of the PMTs and charge injection hardware that can inject calibrated charge pulses into the signal chain.

The cameras are installed in a focus box, a light-tight and waterproof structure, which is supported by a hexapod structure to precisely adjust the position and tilt of the focal plane. The focus boxes are equipped with a garage-style shutter which is kept closed during daytime to protect the PMTs from UV exposure.

The Figure 4.5 shows the camera face with, and without, the light cones. In the following subsections, all components are discussed in more detail.

4.3.1 Light Cones

A plate of reflective light cones is placed in front of the PMT array to concentrate the light onto the active region of the PMT photo-cathodes. It consists of 499

molded plastic cones glued onto a machined Delrin plate (Figure 4.5(b)).

The cone shape is a hybrid design with a hexagonal entrance window evolving to a Winston cone at the exit. This design reduces the dead-space between PMTs by 25%, directing the light impinging on the space between the PMTs to the sensitive area of the photo-cathodes. The inner surface of each cone has an evaporated aluminum coating with a protective over-layer giving a $> 85\%$ reflectivity above 260 nm. The light cones help to shield the PMTs from ambient background light that does not come from the mirrors by limiting the acceptance angle of PMTs to the solid angle subtended by the telescope mirrors. Thus, the use of the light cones increases the light collection efficiency, and in turn the collection area, significantly. The light collection efficiency, which is the percentage of the light that arrives on the sensitive area of the PMT photo-cathodes relative to the total amount of light that shines on the camera, is measured to increase from 55% to 75% as a result of the light cones. For more discussion, one can read [119, 120].

4.3.2 Photomultiplier Tubes

To detect a gamma-ray induced air shower, the response time of the photon counting detector used should match the intrinsic temporal width of the shower, which is 3-4 ns. Thus a low noise, high gain, fast response (rise time < 2.5 ns) detector is required if the temporal behavior of the shower is to be studied. For a fast enough detector, one can also minimize the charge integration gate for the signal to reduce the contamination of the background light to the signal. This has the effect of increasing the signal-to-noise ratio and reducing the energy threshold of the detector. Currently only photomultiplier tubes (PMTs) meet these requirements [117].

For the VERITAS cameras, Phillips Photonis XP2970/02 model PMTs with 10 dynode stages with a bi-alkali photo-cathode are used. The model has a 28 mm (1 1/8 inch) diameter which allows packing with an angular distance of 0.15° between PMT centers on the camera.

The quantum efficiency (QE) is an important parameter characterizing a PMT which is a measure of the probability of a photo-electron being released if the photo-cathode is struck by an electron, ie. the efficiency of the photoelectric effect at the PMT photo-cathode. The QE depends on the material of the photo-cathode and the wavelength of the original photon. PMTs used on a Cherenkov Telescope like VERITAS, are chosen to have the maximum possible efficiency at the characteristics wavelengths of Cherenkov radiation. Typical quantum efficiency of the VERITAS PMTs is $\sim 25\%$ at wavelengths relevant for Cherenkov radiation (~ 320 nm); one can see its wavelength dependency in Figure 4.6.

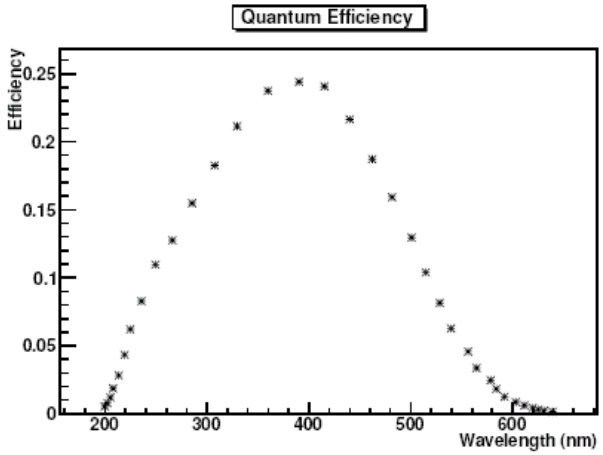

Figure 4.6: The wavelength dependency of the quantum efficiency of the VERITAS PMTs [11].

Currently the VERITAS PMTs are running at a gain of $\sim 2 \times 10^5$. For this PMT gain, the anode currents are typically $3\mu A$ for dark fields (like Mrk 421)

to $6\mu A$ for bright fields (like the Crab Nebula). This corresponds to a night-sky photo-electron background rate of 100-200 MHz at each PMT.

4.3.3 High Voltage System

The HV for the PMTs is provided by a multichannel modular commercial power supply (model CAEN SY1527/A1932.) Two crates of this model are used which hold a total of 11 modules. Each module controls 6 sectors of 8 channels each. Thus powering off a sector effects an 8 channel array. On the other hand, while the power is on, this system is capable controlling the voltages applied to each PMT individually within 1 Volt precision up to 1500 Volts. This way, it is possible to adjust the PMT gains and to reduce the current draw when a bright star image falls directly on a specific PMT.

The HV on each PMT is set by a control program through an Ethernet interface. The voltages can be set manually from a graphical interface of the program, or the program can read the voltages from the VERITAS database. The program can also automatically change the voltage of each channel depending on the monitored level of the anode current. When the HV's of the PMTs are first turned on at the start of an observing night, the HV program reads the preset voltages from the VERITAS database, for a pre-determined flat-fielded gain of each PMT. During observing, the program automatically changes the HV of a channel to suppress it when, for example, a star passes into the field of the view. Another situation that needs automatic response of the control program is when a car passes by with headlights on or when somebody mistakenly directs a flash light towards the camera. This case is recognized by the control program when a large number of tubes register a high current at the same time, and the entire camera is switched off automatically. The observers can also manually suppress

the voltage of any PMT from the graphical user interface program, for example, when a certain channel is broken or noisy.

During the 2- and 3-telescope operation of VERITAS in 2006-2007 season, the pixel suppression conditions were such that a pixel was suppressed immediately if its anode current exceeded $80\mu A$ and was suppressed after 9 seconds if its anode current was above $50\mu A$ during that time. Additionally, if the anode currents of three adjacent pixel's exceeded $20\mu A$, they were also suppressed immediately. If more than 20 pixel's currents all exceeded 80 uA at the same time, the whole camera was powered off.

The program logs both the measured HV values and anode currents to the VERITAS database (DB) once a minute, and any changes to the set HV are logged immediately. These records in the DB are used during offline analysis of the data to determine the active PMTs during the observing.

4.3.4 Preamplifiers

High-bandwidth preamplifiers, integrated at the bases of the PMTs, are used to amplify the signals from the anodes of each PMT before the signal proceed through a $\sim$50 m RG-59 coaxial cable to the counting house, which contains the trigger and data acquisition (DAQ) electronics. The signals coming from each PMTs is AC coupled at the input of the preamps to remove any bias current mainly due to the average night-sky brightness that the tube is exposed to. At the input of the DAQ electronics, a small (pedestal) current is reintroduced to facilitate the measurement of the negative fluctuations from the mean sky brightness. The pre-amplifier has a large bandwidth, 300 MHz, in order to reproduce the pulse shapes for fast Cherenkov pulse rise times. After traveling through the cable, a delta-function input signal has a rise time (10% to 90%) of 3.3 ns and

a width of 6.5 ns. Under normal operating conditions, the PMT gain combined with the preamplifier amplification factor of 6.6 gives a pulse height of 2.4 mV for a single photo electron at the other end of the cable [119]. The signal after the cable should match the FADC input voltage range of 0 to -1.65 V. The 50 m cable attenuates the signal by 25%, so the dynamic range of the pre-amplifiers is 0 to -2.2 V. With the single pe conversion factor, this implies a dynamic range of $\sim$ 900 photo-electrons for the preamplifiers. The preamplifier also provides a direct dc output for monitoring the anode-current with the current monitor system.

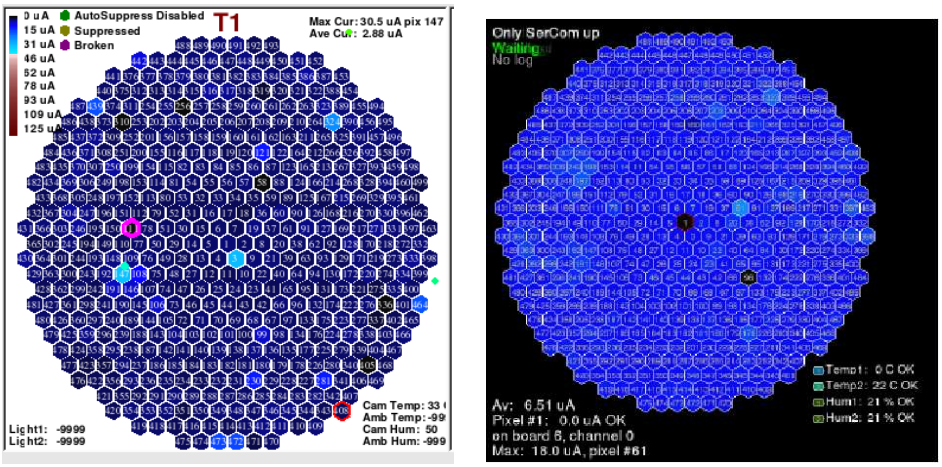

(a) (b)

Figure 4.7: (a) A screen-shot of the HV program GUI for one telescope. The color scale shows the currents on the pixels. The color coded brackets represent the status of a pixel. The stars in the FOV are shown by green filled circles. (b)The screen-shot of the current monitor program GUI (for a different run and telescope). The blue color scale shows the currents of each PMT. The central pixel and pixel 96 were turned off in this run. Figure is from [119].

4.3.5 Current Monitor System

The anode current of a PMT is proportional to the light that falls on its photo-cathode. But there is an upper limit on the currents a PMT can tolerate, above which permanent damage can occur. Thus, it is important to monitor the PMT anode currents to identify the situations described on the HV section that cause high currents which may damage the tubes. Monitoring the PMT currents over a long period of time also helps to detect long term changes in the tube performance which depends on the total charge deposited on its photo-cathode over its lifetime.

Current monitoring is accomplished by a custom built system which reads the anode currents using the electronics on the camera connected to the preamplifier DC output, which is, in turn, connected via a fiber-optic link to the electronics in the control room. The electronics inside the camera box are 16 FPGA-controlled circuit boards with 32 channels on each board. These channels can be used to read and transmit the PMT currents or data from environmental sensors. The current readout precision is $0.5\mu A$ with a dynamic range of $0\mu A - 125\mu A$ [119].

The monitored currents are displayed in the GUI of the current monitor control program. The currents are shown with a color scale for each PMT, and the observer can read the exact current values by clicking on any PMT on the pixel map displayed (Figure 4.7(b)). Summary information, such as the maximum current and the pixel number showing that current and average current, is also listed on the GUI. The current monitor program logs the currents to a local file on a disk and communicates them to the HV control program to use in determining the situations to suppress the voltage for a PMT.

The performance of the camera electronics can be affected by environmental factors like temperature or humidity. These factors are especially important for PMTs subjected to very high voltage during their normal operation. High

humidity or temperature can result in irreversible damage to the circuit, similarly temperature changes affect the PMT gains and the PMT noise. Thus, camera fans are installed in each focus box to provide extra circulation. There are also humidity and temperature sensors in the camera connected to the current monitor system that are displayed in real-time.

4.3.6 The Charge Injection System

The capability of injecting calibrated charge pulses into the signal chain is very useful for the purposes of calibration, testing, and diagnostics of the full data acquisition (DAQ) electronics following the PMTs. It is especially convenient for testing the DAQ during non-observing conditions like daytime which forbids use of the PMTs. The Charge Injection (QI) system provides a set-up that sends a programmable charge directly into the PMT base.

The system consists of a central QI circuit board inside each camera that is fanned out to individual PMT bases. A Programmable Pulse Generator (PPG) is connected to the fan-out/mask board attached to each of the 16 current monitor boards. The generator provides pulses with an adjustable frequency, a programmable output width, and an adjustable amplitude. It is also possible to specify certain patterns of pixels the signal is sent to. All these capabilities are controllable by the observer via command-line scripts or via the GUI of the charge injection program [119].

The QI system can be used for various purposes such as studies of triggering efficiency using different trigger patterns, cross-talk between the channels, miswired/mislabeled channels, and the dead-time.

4.4 Trigger

Cosmic rays produce extensive air showers generating Cherenkov radiation quite similar to gamma rays. The fluctuations in the night-sky background or local muons may also produce signatures that look like a gamma-ray induced event. The main limitation in recording all instances in which the telescope array is hit by Cherenkov light is that it takes some time to record each event and during this time the system is effectively dead and unable to record other events. Thus a careful design of the trigger is necessary to act as a selection mechanism in hardware to recognize and record candidate gamma-ray events with a high efficiency, while rejecting events from night-sky fluctuations or local muons to keep the trigger rate manageable. Moreover to be sensitive to as low an energy as possible, the VERITAS electronics should trigger at low PMT threshold levels. Running the system at thresholds that are below the level of night-sky fluctuations causes very high trigger rates, so one needs to develop additional levels of trigger to distinguish the noise from real events. To limit the overall trigger rate and to keep the data acquisition dead-time to an acceptable level, while being sensitive to lowest possible energy regime at the same time, a three level trigger scheme was developed for VERITAS.

4.4.1 Level One Trigger

The first level (L1) trigger of VERITAS acts at the single pixel level. The amplified signal of the PMT is applied to a Constant Fraction Discriminator (CFD), the threshold of which is programmable. The trigger signal is generated as a logic pulse if the input signal voltage passes the pre-determined threshold value. The output width of the logic pulse is programmable between 4-25 ns.

Precise timing of the output logic pulse carrying the trigger information is desirable in order to reduce the coincidence time of the next level trigger, which in turn is useful to reduce the energy threshold. This is the main reason for the choice of a CFD over a conventional simple threshold discriminator which has a larger jitter in its output pulse timing. The determination of trigger time by the CFD works by splitting the input signal from the PMT in two. One copy of the signal is delayed and inverted, while the other copy of the signal is attenuated. A zero-crossing discriminator (ZCD) is formed by summing these two signals, and the trigger time is the point at the zero crossing of the summed signal. See Figure 4.8 for the block diagram of the CFD circuit.

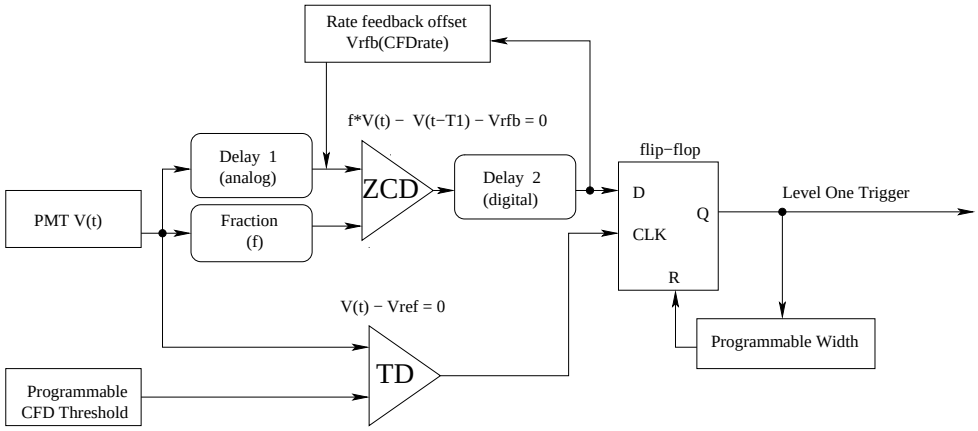

Figure 4.8: Block diagram of the VERITAS CFD circuit [13].

The ZCD is sensitive to the noise conditions, and the night-sky background will introduce a jitter in the trigger time. In order to reduce this jitter, a small constant offset is added to the ZCD, suppressing its noise trigger rate. Applying a large offset minimizes the jitter in the trigger decision but involves increasing the decision time. Thus an optimum offset should be chosen depending on the noise level. But the NSB changes by up to a factor of four, depending on the pointing of the telescope. To determine the optimum ZCD offset value coupled

to different ZCD trigger rates, a novel circuit, the rate feedback (RFB) loop, is added to the standard CFD design. The RFB automatically adjusts the ZCD offset, and, in turn, the effective threshold, when the noise level rises. As a result of this dynamic adjustment of the ZCD offset, the NSB triggers are suppressed further. The strength of the RFB coupling between the noise level and the ZCD offset is programmable. The jitter of the CFD trigger time is less than 1 ns and the slew time is in the range of 0.6-0.9 ns for NSB values between 0.4-0.8 photoelectric/ns.

More detailed discussion on the VERITAS CFD design can be found in [13]. The VERITAS CFDs nominally operate at a 50 mV threshold, with a 10-12 ns output trigger signal width and with a RFB value of 60 mV/MHz during 2 and 3 telescope array observations.

4.4.2 Level Two Trigger

The second level (L2) of the VERITAS trigger acts at the telescope level using the L1 triggers from each pixel as input. It is basically a pattern selection trigger (PST) that is programmed to recognize the gamma-ray like events formed by a certain pattern of L1 pixel triggers, eg. three nearest neighboring pixels triggering in a certain coincidence time interval. In this way, the L2 trigger can discriminate (in hardware) between the compact images of gamma-ray initiated showers which trigger a group of adjacent pixels and background events caused by night sky noise or after-pulsing which trigger pixels at random locations in the camera.

The VERITAS PST [121] has two main components, an ECL signal splitter and 19 pattern selection modules with programmable pattern look-up memory. The pixel trigger pulses from 463 CFDs (some of the outermost CFDs are excluded from contributing to the L2 trigger) are copied by the ECL signal splitter

module and organized into 19 overlapping patches of 59 pixels. These signals are then redirected to 19 separate pattern selection modules. The pattern selection modules contain memory chips which can be pre-programmed to recognize pixel patterns using a look-up table. If a pre-set multiplicity of pixel trigger signals overlap by at least 5 ns (which is the time required to sum these signals and evaluate the result using a comparator), the patterns of these pixels are captured and compared to the patterns stored in the memory look-up. If a positive match is found, a telescope trigger is sent to the third level of the trigger (L3).

The timing of the L2 trigger is taken from a delayed copy of the signal from the comparator. The time jitter in the circuit is on the order of 5 ns, thus an L1 pulse width of at least 10 ns is required to guarantee 100% L2 trigger decision efficiency.

Figure 4.9(a) shows the telescope level trigger rate with respect to different first level trigger thresholds for two different pattern trigger conditions. For single telescope operations, VERITAS nominally uses a pattern trigger which requires three nearest neighbor pixels to trigger, each with a threshold of 6-7 photo-electrons ($\sim$70 mV) within a 10-12ns interval to issue the telescope trigger pulse.

4.4.3 Level Three Trigger

The last level (L3) of the VERITAS trigger operates at the array level based on a geometry-adjusted multiplicity condition on the telescope triggers consistent with the simultaneous observation of an air shower by multiple telescopes. At low energies the background is dominated by the night-sky fluctuations and local muons. Although the majority of the NSB triggers can be rejected by a two level trigger, the background due to local muon events are irreducible by a single

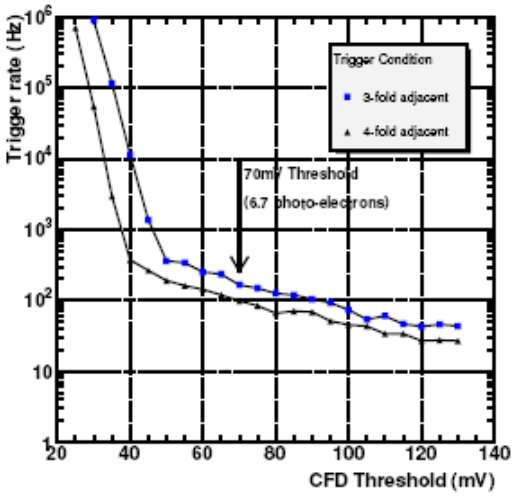

(a)

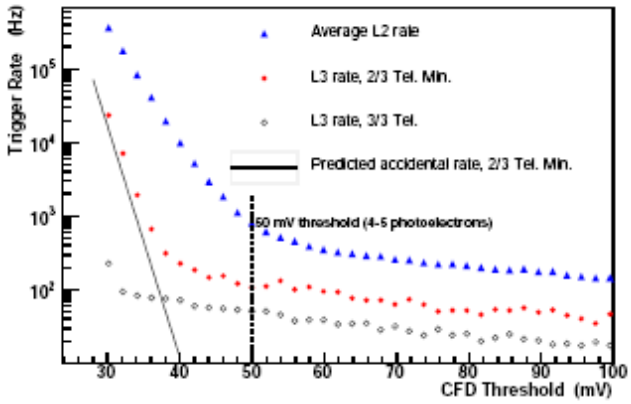

(b)

Figure 4.9: The trigger rates with respect to first level (CFD) trigger thresholds for (a) the single telescope operations for the different pattern trigger conditions [114] and (b) array operations for two different telescope multiplicities [15]. The average L2 trigger rate is also shown with blue.

telescope, since the Cherenkov light from muons with large impact parameter to the telescope produce quite similar images to gamma-ray showers. Fortunately, the Cherenkov cone of local muons can only trigger a single telescope in most cases, which can be rejected using an array level trigger. This additional level of trigger enables us to reduce the CFD thresholds into the regime where otherwise the single telescope triggers would swamp the trigger rate. Thus with a three level trigger, the energy threshold of the instrument can be reduced and the sensitivity of the detector can be increased significantly.

The L2 triggers from each telescope are transmitted to the central L3 location via optical fibers which link a transmitter-receiver pair of Digital Asynchronous Transceiver (DAT) modules at each side. The same modules are also used for communication of the event number and event type. More detailed discussion for these modules can be found at [14]. The DAT modules consist of two 6U high, single width VME modules, one of them is the transmitter unit, DAT-TX, and the other one is the receiver unit, DAT-RX, which are connected by fiber optic link over a distance of 150 m. The modules are VME controllable through a Field Programmable Gate Array (FPGA) unit on board. The conversion of the electrical signals to optical signals and back is achieved using the Infineon 1.25 Gbits/s parallel optic link (PAROLI2) consisting of a 12 channel, 850 nm VCSEL driven transmitter and a PIN diode-array receiver. The use of the fiber optic connection maintains the signal integrity, but it is not possible to send asynchronous signals directly through that connection. To overcome this problem, the asynchronous signals are modulated by a 25 MHz clock signal. This is achieved by encoding the incoming signals with the clock through an exclusive OR (XOR) gates on the FPGA boards at the transmitter. Then this encoded signal and a copy of the clock signal are optically transmitted to the receiver. The XOR gates on the receiver side are applied in an inverted manner to recover the original input signal.

Figure 4.10 shows how the encoding and recovery works at both sides. Using the asynchronous method, the dead-time associated with the use of sequential logic is avoided.

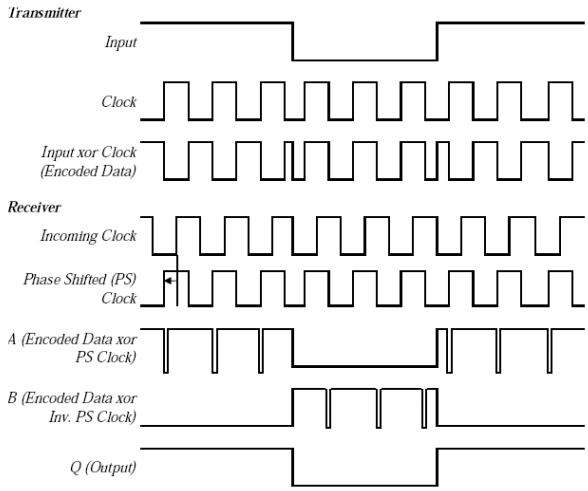

Figure 4.10: The depiction of the XOR encoding at the transmitter and receiver side of the DATs [14]. Details can be found in the text.

After receiving the L2 triggers from each telescope, the L3 trigger electronics process them to identify the events that trigger each telescope simultaneously accounting for the delays caused by the geometrical layout of the array. The core of the L3 hardware consists of two custom built VME modules, the Pulse Delay Module (PDM), and the Sub-Array Trigger Board (SAT), and a commercial GPS clock. The illustration of the L3 trigger system's interface with other systems can be seen in Figure 4.11. A more detailed discussion on the array trigger system can be found on [15].

The PDM unit is responsible for delaying the L2 signals from each telescope according to the telescope location in the array and its pointing to account for the wavefront orientation. The delays needed to adjust the signal transmission

time differences due to the locations of the telescopes in the array are constant and compensated exactly by the PDM delay lines using the measurements of the precise location of each telescope. The second component of the delays are due to the different arrival times of the Cherenkov wavefront on individual telescope reflectors. They depend on the pointing of the telescopes and are constantly changing as telescopes track a source across the sky. These delays are calculated using the current pointing of the telescopes updated every five seconds. The telescope pointings are recorded to the VERITAS DB by the tracking computer and polled by the level 3 trigger program to use in this calculation.

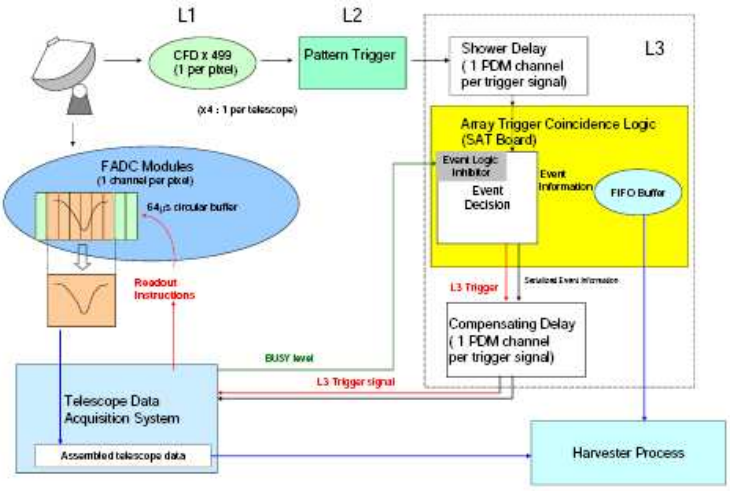

Figure 4.11: Illustration of the trigger system's operation and interface with the DAQ [15].

The SAT module is then responsible to determine whether a pre-determined array trigger condition occurs if a multiple of these delay adjusted L2 signals falls in a certain coincidence gate, and it issues the array trigger to command the DAQ to record the event. To achieve this, SAT converts the arrival times of the delay corrected L2 signals into digital time-stamps via 1.25 ns resolution time-

to-digital converters (TDCs) and buffers them. The coincidence logic algorithm, which is pre-configured by a programmable pattern look-up table, then searches the time-stamped buffers until a programmed coincidence pattern is found in a programmed time window. The coincidence time window can be programmed in the range of 1-125 ns, and the shortest possible window is limited by the residual spread of the delay-corrected L2 trigger arrival times (which is on the order of 20-25 ns). Currently, the VERITAS array is operated in a conservative coincidence time window of 100 ns.

After the trigger decision is made, the array trigger sends an L3 trigger logic pulse to command the DAQ system to record the event by the FADC modules(see section 4.5 for info on FADCs). The FADC modules continuously digitize the PMT signals into a circular memory buffer depth of 8 μs. Only approximately a 50 ns portion of this buffer actually represents the PMT signals due to a particular event. When the DAQ system receives the L3 trigger, the start point of this portion of the memory buffer is located earlier by a time interval that corresponds to the time it took to make the array trigger decision after the receipt of the L2 trigger. Thus, the DAQ look-backs by this amount of time to record the relevant portion of the memory buffer for the triggered event. The SAT board guarantees that the look-back time is always constant by applying additional delays to pad the actual array trigger decision time to the pre-programmed fixed look-back time with respect to the timing edge of the L2 trigger signal from each telescope. Thus the L3 trigger signals sent to each telescope are adjusted to have a timing edge which is a fixed amount later than the timing edge of the L2 trigger generated at each telescope. The telescopes that do not participate in the event decision (and thus that have no L2 signals) can be still commanded to record the event information in a forced-readout mode by sending an L3 trigger with a time edge determined by other telescopes.

During the the FADC readout, the DAQ system at each telescope inhibits the array trigger coincidence logic by raising a BUSY level. The SAT also self-vetoes for 10 μs after an event decision, in order to allow for L3 signal propagation to the telescopes. Thus, the total dead-time of the system is the combination of this L3 trigger propagation time and the time between the issue of its BUSY signal by the first telescope until the last telescope withdraws the BUSY signal. The dead-time due to the DAQ of each telescope overlaps largely and is $\sim 400\mu s$. The dead-time of the trigger system is monitored by using a 10 MHz reference clock and a set of 32-bit scalars on the SAT boards. As expected, since the dead-time occurs only during the readout of L3 triggered events, the dead-time scales linearly with the array trigger rate, reaching $\sim 6-8\%$ at 150-170 Hz and $10-11\%$ at 225 Hz [15].

4.5 Data Acquisition

The VERITAS data acquisition (DAQ) also operates in three levels, VME crate-level DAQ, telescope-level DAQ and array-level DAQ. The VME DAQ controls the readout of the FADC Board channels on each VME crate, the Event Builder controls and merges the data from all VME crates at each telescope, and the Harvester collects the event information from each telescope and the central array trigger and merges them into complete array events. The Figure 4.13 at the end of this section shows the interactions of all components of the VERITAS DAQ system. In this section, all components are discussed separately. More detailed discussion can be found on [16].

4.5.1 FADC Boards

The custom built Flash Analog-to-Digital Converter (FADC) boards [122] are the front end of the DAQ chain and form the centerpiece of the VERITAS DAQ. After passing through the pre-amplifiers, the PMT signal produced at each pixel of the camera is fed into a Flash-ADC (FADC) channel which digitizes the signal and buffers it continuously with a 500 MHz sample rate (ie. each sample has 2 ns time width) into a circular memory depth of $8\mu s$. The digitization stops when the array trigger signal is received. At that point, the pre-programmed portion of the FADC memory is recorded by the VME DAQ program representing the digitized version of the Cherenkov pulse relevant to the triggered event. During the 2- and 3-telescope operation of the VERITAS array in the 2006-2007 season, a 24 sample width of the FADC buffer was recorded, and the look-back times were pre-programmed for each channel corresponding to the amount of the constant delay of the L3 trigger signal with respect to the L2-trigger edge produced by each telescope.

Each FADC channel has an 8-bit dynamic range, but also employs an automatic gain switch which is engaged when the signal to be digitized exceeds the default dynamic range. In those cases, the analog signal is delayed and passed through a lower gain channel, and a scaled digitized trace of the pulse is produced in the memory buffer following the truncated saturated pulse. This auto-ranging capability extends the dynamic range of FADCs from 256 to 1500 digital counts.

The digitized Cherenkov pulse waveform of the FADC preserves the information on the shape and time structure of the pulse which allows the use of digital signal processing methods to measure the total charge and the time edge of the pulse, giving the capability to reduce the adverse effect of the noise on these measurements. Recording the Cherenkov pulse waveform in 2ns time intervals

for a time span greater than the wavefront duration allows one to see the propagation of the wavefront across the pixels of the camera. Figure 4.12(b) shows a FADC trace of a Cherenkov pulse recorded by a pixel in the camera and on Figure 4.12(c) the time gradient of the propagation of the wavefront across the camera is clearly seen.

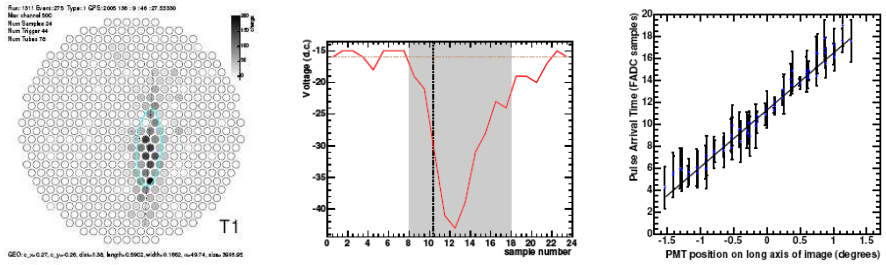

(a) (b) (c)

Figure 4.12: (a)The charge distribution across the camera for a cosmic-ray event. (b) The FADC trace for a pixel in the image. The dashed line indicates the estimated arrival time for this pulse. (c) The Cherenkov pulse arrival time distribution across the camera along the long axis of the event image of (a) [114].

4.5.2 VME Data Acquisition

VME Data Acquisition System (VDAQ) serves as an interface between the five VME crates that control the pulse digitization of the FADCs and the Event Builder system that merges the event fragments from those separate VME crates. The FADCs for each telescope are deployed in four VME crates, and each VME crate has a single Clock Trigger Board (CTB). The fifth crate is an auxiliary crate which holds the master CTB and the GPS clock for the telescope.

The VME DAQ controls the initialization of the crates at the start of the acquisition process. During the initialization, the memory map of the modules

on each VME crate are generated and various configurable features of the FADCs and the CFDs are set. The most important of the configurable parameters include the CFD threshold levels and output pulse widths, the FADC look-back times, and the size of the FADC buffers to be recorded. After the initialization, VDAQ processes wait for the arrival of the L3 trigger signal to initiate the data read-out.

At the receipt of the L3 trigger signal, each FADC channel locates the portion of their memory buffer relevant to the event and records this portion of the trace into their on-board buffer RAM awaiting the VME read command. At that point, the VME CPU initiates an A32/D32 chained block transfer (CBLT) which is a type of DMA transfer designed to handle the variable-length data distributed over the number of FADC modules in the crate. In this way, the data are read from the first to the last board using a chained block transfer. VME DAQ program then merges the data from all crates into an event piece and transfers them to an event building computer via the Scalable Coherent Interface (SCI). The recorded data are buffered at each of the VDAQ machines and transferred in blocks to the Event Builder via the SCI system.

During the read-out, the CTB on each VME crate raises a BUSY flag when the subsequent triggers cannot be processed. The master CTB combines the busy levels from each crate into a single telescope BUSY level and sends this BUSY signal to the array trigger to inhibit the generation of subsequent L3 triggers. After the readout is complete on each crate, this signal is cleared.

Along with the L3 trigger, the VDAQ also receives additional event information as a serialized signal (event mask) that contains a unique event number for the event and the type of trigger. This event mask is also copied to each crate and encoded into the event fragments from each crate to allow the synchronization of the data by the Event Builder program.

4.5.3 Event-Builder

The Event-Builder program acts as the telescope level data acquisition and it is responsible to form the telescope events. It receives the event fragments from the VME DAQ from each VME crate of the telescope via SCI connection and combines them together into telescope-level event information. It then writes the data to the local disk and sends them to an array DAQ program, the Harvester, via GBit Ethernet to be integrated with the data from other telescopes.

The Event-Builder software is written in C++ and is multi-threaded. Typically, five threads are active during data acquisition: Communications, SCI Buffer Acquisition and Parsing, Event Building, Disk Writer and Network Writer. The actual event building process starts by transfer of the event fragment buffers from the VDAQ via the SCI Buffer Acquisition Thread. The SCI Buffer Parser thread then parses the memory blocks, extracts the individual event pieces tagged by unique event numbers and stores them in memory. Once the all pieces of an event from each crate are in memory, the Event Building thread merges them together to form a complete single telescope event. These events are buffered and once roughly 160 kBytes of events are accumulated, the Disk Writer and Network writer threads dispatch them onto a local file and to the Harvester, respectively.

4.5.4 Harvester

The array level data acquisition is the responsibility of the Harvester process. It is a single eight-core machine that collects the data from the telescopes and the array trigger to integrate them into an array event. It runs a variety of real-time sanity checks on the data to make sure that all the telescopes are read out according to the event mask on the array-trigger information. The Harvester then saves the merged data buffers to its local RAID disk in real time. The

data is saved using a custom format named VERITAS Bank Format (VBF). In that format, the user has access to all the telescope events and the array trigger information for any event given the unique event number.

The VBF has been designed for portability, high performance in reading and writing, compactness, and extensibility. After the run is finished, a customized compression algorithm is applied to the data file to further compress it.

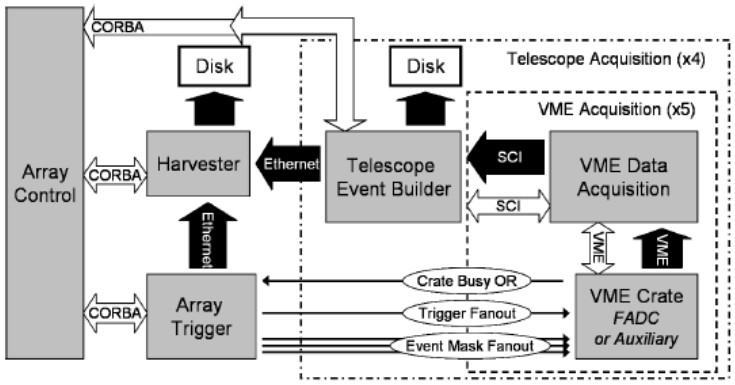

Figure 4.13: Illustration of the components and interactions of the VERITAS DAQ System [16].

4.5.5 Array Control

The observer interacts with the VERITAS Trigger and DAQ software through a Graphical User Interface (GUI) of the central array control software. This software interfaces to various systems and it has the capability to initialize, start and stop all the VERITAS trigger and DAQ systems.

The array control interface to the L3, Event Builder and Harvester systems involves initialization of the systems and starting and stopping the hardware for individual observing runs. These systems also communicate back to the array

control to send the run status information during an active run and the run statistics at the end of the run. The array control software uses this information to provide the observer with diagnostic information on the run such as trigger rates, data size, the number of corrupt events, the dead-time and the available hard disk space. All communications in both directions are achieved through the use of the CORBA (Common Object Request Broker Architecture) protocol.

4.6 Calibration of the Instrument

4.6.1 Bias Curve Measurements

The operating trigger parameters must be chosen to give best sensitivity to the lowest energy showers, while maintaining a stable trigger rate with an acceptable level of dead-time. To determine the optimum trigger parameters, special runs, bias curve runs, are taken to map the dependence of the system trigger rates to several trigger parameters. During these runs, scans on a particular parameter are performed while other configuration parameters are kept constant.

In all cases, the L2 and L3 trigger rates have almost a level plateau with respect to the CFD thresholds in the trigger regime where the air-showers dominate the total rate. There is a break point below which the accidental triggers due to night-sky background fluctuations dominate and the rates increase rapidly (Figure 4.9(b)). At the optimum configuration, the break point is at the lowest possible CFD threshold at which the trigger rates are constant. A stringent trigger configuration could have a break point at significantly lower thresholds, but the cosmic-ray rate, thus in turn gamma-ray rate detectable at the higher thresholds reduce, too. The standard bias curve measurement is the scan of the CFD thresholds for a constant configuration of CFD widths, L2 and L3 multiplicity.

During the single telescope operation of VERITAS, a CFD threshold of 70 mV that corresponds to approximately 6-7 photo-electrons was chosen as the optimum operating point with a three nearest-neighbor multiplicity requirement of the L2 trigger. During 2- and 3- telescope VERITAS operations, the operating CFD threshold was reduced to 50 mV, corresponding to 4-5 photo-electrons, with the same L2 requirement and with a 2 out of 2-telescopes or a 2 out of 3-telescope trigger multiplicity requirement in a 100 ns coincidence window of L3 trigger.

4.6.2 Nightly Laser Runs

The response of each of the 499 pixels on the telescope camera to the same amount of simultaneous light illumination is not equal in terms of the total charge produced at each channel and the start time of the pulse on each FADC trace. It is important to have an equal amount of charge produced in all channels for the same amount of light to be able to sum up the charges in each camera to estimate the total light content of the shower. The simultaneity of the start times of the pulses on the FADC traces for a simultaneous light illumination is required to be able to measure the time gradient produced on the image while the Cherenkov wavefront sweeps over the camera.

The time spread of the pulses is mainly due to the cable length differences from the PMT to the FADC channels. The time differences between the start times of the digitized pulses on different FADC channels can be calculated for a simultaneous light illumination and this correction can be applied to each channel signal during the offline analysis of regular data runs. The inhomogeneity in the amount of charge produced on each channel depends on the quantum efficiency of the photo-cathode and the gain through the photomultiplier stages of the PMT. There is a simple relation between the high voltage applied to a PMT and the

gain of the PMT with a known number of dynodes. For VERITAS PMTs this relation is $G \sim V^{7.5}$ to obtain a gain of G for an applied voltage of V. Thus the relative gain of a channel with respect to other channels can be adjusted by varying the applied high voltage accordingly. The relative gain of all channels for a constant intensity of light can be equalized by applying varying voltages to each of the PMTs according to that relation to cancel out their differences. This process is called flat-fielding the camera.

Both of the above procedures requires a simultaneous illuminations of all channels in the camera with a constant intensity light. A laser system is employed in VERITAS for these purposes. A five minute constant-intensity laser run is taken at the start of each observing night to measure and monitor the relative gains, the results of which are used in the offline analysis.

VERITAS laser system uses a nitrogen laser with wavelength of 337 nm and a pulse length of 4 ns. The beam is directed into a dye which fluoresces at 400 nm and the beam is sent through neutral density filters arranged in sequential wheels which vary the transmission of the beam in the range of 0.02%-100%. It is then divided approximately equally among 10 optical fibres. Four of them are routed to opal diffusers located on the optical axes of each telescope, at a point 4 m in front of the PMTs. The diffuser produces a uniformly spread beam such that all the pixels in the camera receive an equal amount of light irrespective of their locations on the camera. One fibre is connected to a photodiode which can be connected to an oscilloscope or to a spare FADC channel to monitor the intensity of the beam. Another fibre connected to a PIN diode is used to provide an external trigger to the trigger system. This allows triggering the telescope at light levels which would not normally generate a trigger. A more detailed discussion of the VERITAS laser system can be found on [123].

4.7 Observing Modes

A few different observation configurations are available to a IACT: PAIRS mode, TRACKING mode and WOBBLE mode. These configurations are different from each other in their approaches to the background estimation.

PAIRS Mode: In this observing mode, a candidate or known gamma-ray source is tracked for 28 minutes by pointing the telescopes such that the source is at the center of the FOV. This run is referred as the ON run, and the data recorded during this run are used to estimate the gamma-ray and the background flux from this FOV of the sky while a source is present. Two minutes after this run, an OFF run is taken tracking the same line in the sky pointing to a position separated from the source position by 30 minutes in Right Ascension. The data recorded during this run is used to estimate the background flux from this region of the sky in the absence of a candidate gamma-ray source. The underlying assumption is that the background rate from an equal elevation and azimuth sky regions, ON and OFF regions, are the same and both observations are made in equal sky conditions. Therefore, this mode is only suitable for best and stable weather conditions. One drawback for this method is that it doubles the required observing time, spending half the observing time not looking at the source for background estimation. On the other hand, it gives the best background estimation for a candidate source the position of which is not accurately known, has large positional error box or has extended emission in the FOV.

TRACKING Mode: In this observing mode, the sky is observed only with the source at the center of the FOV, and the background flux is estimated from the same FOV using a scaling factor and the candidate gamma-ray events whose estimated directions are not consistent with the source position. The scaling factor should be determined from the data collected from a region of sky where

no source is present. This mode is suitable for bad weather observations when it is impossible to take a matching OFF run. However, since the background estimation is not accurate, only observations of a known gamma-ray source at the center of the FOV is appropriate with this method.

WOBBLE Mode: When stereoscopic observations are available using more than one telescope, the source position and shower core can be determined with a better accuracy. This allows estimating the background with sufficient accuracy from the same FOV with the source. In the observing mode, the telescopes are pointed such that the source is located at an offset distance in declination or right ascention from the center of FOV. The background is estimated from the sky regions in the same FOV at the same offset distance from the center as the source. In order to avoid any bias due to a particular direction of offset, the same number of runs are taken where source is located at the same offset distance alternately to the north, south, east and west directions in the equatorial coordinate system. The only drawback of this mode is that the source is not at the center of the FOV where the sensitivity of the instrument is highest. However, this is a small price to pay compared to the PAIRS mode which requires double the exposure time.

The VERITAS instrument uses WOBBLE mode for regular observations. The offset distance of the source location from the center of FOV is determined using simulations of the detector response and using test observation runs to compare the data analysis results for the highest sensitivity.

4.8 The Crab Optical Pulsar Hardware

The large reflector area of a VERITAS telescope enables us to perform optical monitoring of an astrophysical object by measuring the intensity of the light focused on the central PMT. In order to attempt the detection of the VHE gamma-ray emission from the Crab Pulsar, it should first be proven that the detector has time stamping capability with sufficient precision to record the arrival time of each event. For this purpose, the optical pulsed signal from the Crab Pulsar is detected using a special hardware set-up involving the electronics dedicated to the central pixel and the GPS clock of VERITAS telescope T2.

For these special optical runs, the electronics connected to the central pixel, to a pixel located in the first ring of pixels around the central pixel, and to a pixel located at the outer camera close to the edge are configured to count the number of single photo-electrons recorded by their PMT which is proportional to the intensity of the optical light focused on it. The pixel in the first ring of pixels around the central pixel is read out by this set-up to check to see if there is any spill-over of the signal focused in the central pixel, and the pixel at the outer edge is read out to verify that any signal in the central pixel is due to the focused optical light rather than a feature of the background. In order to do this, the threshold of the CFD connected to the central pixel is configured at the single-photoelectron level to produce a trigger pulse each time a photon arrives at the central pixel. The central pixel line is directed from the standard electronics chain after the CFD output and routed to a VME counting module (CAEN V830) to record the number of photons during a continuous series of integrating windows of 50 μs. This integration window is sufficiently small compared to the period of the Crab Pulsar, and it provides 660 singles rate measurements per Crab Pulsar phase. Figure 4.14 shows the diagram of the hardware set-up.

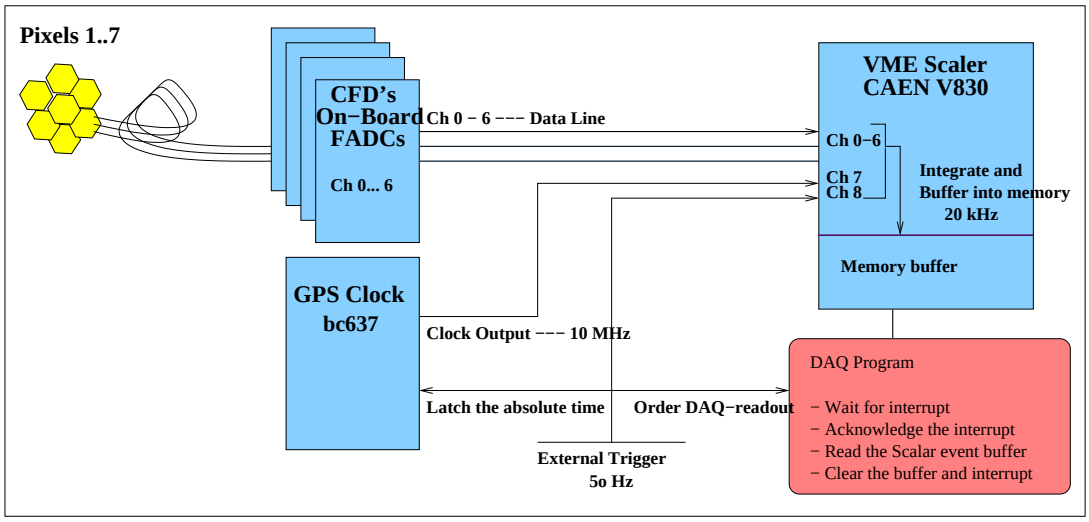

Figure 4.14: The diagram of the hardware set-up to detect the optical pulsed signal is shown. The set-up is explained further in the text.

The V830 unit is capable of recording the number of counts "on-the-fly" which means that there is no dead-time between the integrating windows, i.e. they are contiguous. The 10 MHz clock signal ticks from GPS are also counted during each integrating window with the V830 unit. Since the recorded time windows are contiguous in the memory buffer, these clock ticks can be reliably used to interpolate the absolute time of each integrating window, during which the intensity level is measured, within a precision of 100 ns. Figure 4.14 shows the timing diagram of the optical pulsar set-up.

In order to associate each sampling of the light intensity with absolute time stamps, the GPS clock should be latched and recorded at the start of each integrating time window. Unfortunately, the speed of the VME read-out limits how fast the DAQ can be run to latch the clock and record the light intensity. This directly limits the duration of the integrating windows if each time window start needs to be latched. In order to work around this difficulty, the GPS times are

latched and the DAQ readout is performed with a lower frequency and the event buffer memory of V830 is used to store the intensity and duration of multiple time windows between each DAQ readout cycle. The DAQ cycle period is chosen as 20ms to buffer ~ 400 integrating windows on each cycle. During the first pass offline analysis, the 10MHz clock ticks are used to interpolate the absolute time to each intensity sampling. As a check, the sum of the 10 MHz clock ticks are compared with the absolute time differences between contiguous DAQ cycles. If the difference between them is greater than 300 μsecs, the whole buffer is removed from the data for which the temporal analysis is applied.

Timing Diagram

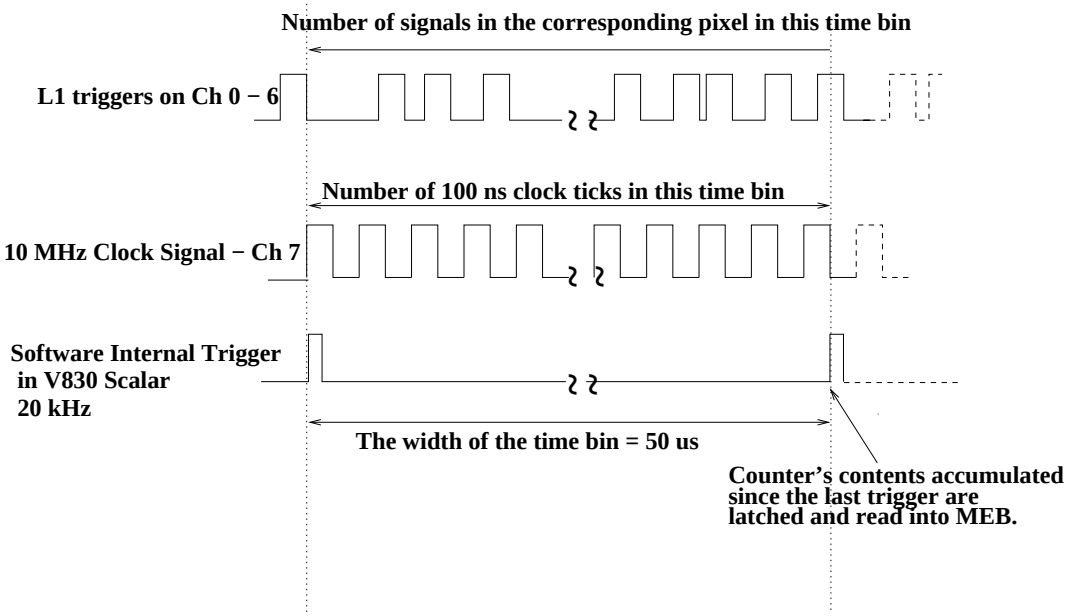

Figure 4.15: The timing diagram of the optical pulsar hardware is shown for one time window in the event buffer memory of the V830 unit. In one time window, the scalar channels connected to the pixels read the L1 triggers, and the channel connected to the 10MHz clock reads the number of 10 MHz clock ticks. The internal trigger signal of the V830 unit is also accumulated in another scalar channel to define the start of each time window. The set up is explained further in the text.

CHAPTER 5

The Crab Observations

From 2006 to 2008, the Crab Nebula was observed extensively during the 2-,3- and 4-telescope phases of VERITAS. The 2-telescope VERITAS array is comprised of telescopes referred to as T1 and T2 in Figure 4.1, the 3-telescope array includes telescopes T1, T2 and T3, and the 4-telescope array includes telescopes T1, T2, T3 and T4. In this chapter, the Crab data set used in the analysis is presented.

The observations of the Crab Nebula were made for various purposes. First and foremost, the Crab is an interesting and important scientific target. In addition, the Crab Nebula is the standard candle in TeV astronomy, and it is a natural choice as the primary observing target to test the detector in the engineering phase. Various engineering tests were made using the Crab observations for this purpose at each VERITAS commissioning phase. The availability of separate data sets for different detector configurations is very useful in testing and comparing the results to determine the optimum sensitivity of the detector. However, utilization of data for scientific purposes requires a uniform configuration. Therefore, a data set that possesses a stable detector configuration was selected for each VERITAS commissioning phase to use in the analysis reported in this thesis.

At this step, it is important to remove the particular runs that are affected adversely by non-ideal environmental or hardware conditions. The uniformity of external conditions is ensured by applying a run quality selection on these data

sets. In Section 5.3, the quantities that are used to assess the quality of the data runs are discussed. The final data set chosen for each phase of VERITAS is used in spectral and timing analysis after this selection. This final data set is listed in Section 5.2.

5.1 Standard Detector Configuration

After various configurations were tested and the resulting data were compared, a final standard detector and observing configuration was selected for each commissioning phase. The data sets used in the present analysis were selected from the data recorded using the standard configuration at each VERITAS commissioning phase. As a result, three independent data sets were identified and used in the analysis and the results are reported separately for each: 2-Telescope data set (2T), 3-Telescope data set (3T), and 4-Telescope data set (4T). The various settings in this standard configuration are summarized in this section.

In Table 5.1, the settings of the CFD parameters are listed for each data set. The CFD output pulse width is different between T1 and the other telescopes because the L2 systems on the latter telescopes have a slightly different design.

For all three data sets, the multiplicity condition of the L2 system is set to require that at least three nearest neighbor pixels trigger within the coincidence window of the system. The coincidence window is the same as the CFD pulse width given in Table 5.1.

For all data sets, the array trigger (Section 4.4.3) is configured to require at least two telescopes to trigger within a 100 ns coincidence window. With this configuration, both telescopes participate in the trigger of an event during the 2-telescope phase, 2 or 3 telescopes participate in the trigger during the 3-telescope

CFD Settings			
Data Set	Threshold (mV)	RFB (mV/MHz)	Pulse Width (T1/T2/T3/T4) (ns)
2-Telescope	50	60	9-10/ 12-13
3-Telescope	50	60	10/13/13
4-Telescope	50	100	10/13/13/13

Table 5.1: The CFD settings in the three final data sets are listed. Each CFD parameter is explained in the text.

phase and 2, 3 or 4 telescopes were triggered during the 4-telescope phase. In all phases, the force-readout mode was activated in the array trigger system. This mode ensures that all telescopes are read out if an event triggers the system, irrespective of its participation in the trigger.

Data for all sets were collected in the WOBBLE observing mode (Section 4.7) with a source offset distance of 0.5 degrees. Data were collected in 20-minute duration runs.

5.2 Crab Data Set

The Crab was observed with the 2-telescope array of VERITAS in November 2006 with the standard configuration summarized in Section 5.1. The Crab observations with three telescopes were conducted between December 2006 and February 2007, and the Crab observations with four telescopes were made between September 2006 and March 2008. The Crab was observed for a total of 721 minutes ($\sim$12 hours) with two telescopes, 694 minutes ($\sim$11.6 hours) with three telescopes, and 1198 minutes ($\sim$20 hours) with four telescopes.

The data recorded with the standard configuration at each VERITAS commissioning phase are listed in Tables A.1, A.2 and A.3 for the 2-, 3- and 4-telescope data sets, respectively, in Appendix A. Each table lists the data recorded, the run numbers of the Crab data, and the corresponding laser run number used in the calibration of these data. The tables also list the duration of each run, the source offset distance and direction from the pointing direction, and the mean elevation of the source during the run. The RMS of the FIR temperature (Section 5.3.2) during the observations, the L3 rate and its RMS, and the elevation-adjusted L3 rate are given. Finally, each run is subject to a run quality selection, as explained in Section 5.3. If the run failed the selection criteria, it was tagged by an "X".

5.3 Run Quality Diagnostics

Certain conditions can deteriorate the sensitivity of the instrument and may lead to low quality data. In order to identify and reject poor quality data, a data-quality selection based on various quantities was used.

5.3.1 Hardware and Observing Problems

One of the obvious reasons for low quality data is the presence of a problem in some system of the detector. Similarly, observer errors may cause unacceptable configurations. Fortunately, these problems have visible real-time effects that observers notice right away. In those cases, the observing run is usually aborted and a notice is entered in the observing log.

In order to avoid including data taken in spite of hardware problems or observer errors, all observing logs were reviewed and any runs tagged with such errors were removed from the final data set. Similarly, any run with durations

less than the expected 20-minute length were rejected.

5.3.2 FIR

The main cause of low quality data is poor weather, which causes irregular scattering or absorption of the Cherenkov light, resulting in array-trigger rate instabilities. A far-infrared (FIR) pyrometer connected to one of the telescopes is used to detect cloud cover by continuously measuring the temperature of the night sky to obtain an assessment of the weather conditions at the VERITAS observatory. While the absolute value of the FIR temperature depends on external conditions, such as ambient temperature, humidity or elevation, the RMS variation of the measured FIR temperature provides a good indicator for determining unstable weather conditions. When the weather is not stable, possibly due to patchy clouds in the sky, the FIR temperature and the array trigger rate exhibit large variations. The weather is rated from A to D depending on the RMS of FIR temperature as shown in Table 5.2.

The Crab data sets were selected such that runs with an FIR RMS above 0.3°C, (i.e. worse than B-rated weather), were rejected.

Weather Rating with FIR RMS				
FIR RMS (°C)	< 0.1	$0.1 - 0.2$	$0.3 - 0.4$	> 0.5
Weather Rate	A	B	C	D

Table 5.2: The rating of the weather conditions depending on the RMS of the measured FIR temperature. See the text for the discussion of FIR temperature.

5.3.3 Trigger Rates

Instability in the array trigger rate increases the systematic uncertainties in the measurement of the gamma-ray flux from a source. It was found that the stability of the array trigger rate correlates strongly with the irregularities of the weather conditions. Additionally, the absolute value of the L3 trigger rate may decrease from its expected value (for a given array configuration, multiplicity condition and observing elevation) due to a number of reasons; e.g. a high dead-time of the system or cloud cover in the sky. In order to remove the adverse effects of unstable trigger rates, runs were rejected if the absolute value of the array trigger rate was less than 80% of the expected rate, or if its fractional RMS variation was higher than 10%.

The expected L3 rate for 2-, 3- and 4-telescope array configurations for a source at zenith is needed for this purpose. The L3 rates depend on the observing elevation; therefore, they need to be adjusted for their elevation before their use in any selection criteria. Since the effective area of the detector changes with respect to elevation by a factor proportional to the cosine of the zenith angle, the change of the L3 trigger rate with zenith angle was also approximated by a cosine(zenith angle) factor to first order. The array trigger rate of each run was adjusted by this factor, and the expected rate for an array configuration was estimated by averaging the adjusted array trigger rate of runs taken at maximum available zenith angle.

In Figure 5.1, the L3 trigger rates adjusted by the observing elevation and the RMS of the FIR temperatures during 38 3-telescope observing runs with duration longer than 5 minutes are shown. It can be seen clearly that for the runs during which the FIR RMS temperature was more than 0.3°C, indicating C-rated or worse weather, the L3 trigger rates were less than 80% of 180 Hz, the expected 3-

telescope trigger rate of observations at the zenith. Additionally, for those cases when the weather conditions were not stable, the trigger rate exhibited large variations as shown by the error bars on the points.

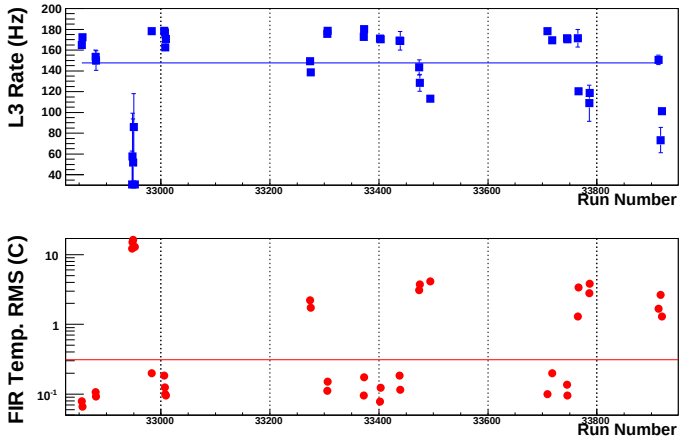

Figure 5.1: The L3 trigger rates (top panel) and FIR temperature RMS (bottom panel) for 38 3-telescope Crab runs with a duration longer than 5 minutes are shown. The runs with L3 rate higher than the minimum L3 rate (shown by the horizontal line on the top plot), and with the FIR temperature RMS less than the maximum FIR temperature RMS (shown by the horizontal line on the bottom plot) are accepted in the analysis data set.

5.4 Quality Selected Crab Data set

After the quality selection described above was applied to the Crab data set, a final data set was chosen for each phase for use in the analysis. The selected data from the Crab observations corresponds to 660 minutes (11 hours) with 2 telescopes, 420 minutes (7 hours) with 3 telescopes and 720 minutes (12 hours) with 4 telescopes. These data sets will be referred as 2T, 3T or 4T, corresponding

to each VERITAS phase.

Various quantities for the 2-, 3- and 4-telescope data sets are summarized in Table 5.3.

Data Set	N_{Tels}	Date	N_{Runs}	Obs.Time (hours)	⟨Zn Angle⟩ (°)	L3 Rate @Zn (Hz)
2T	2	11/2006 - 11/2006	33	11.0	15.5	110
3T	3	12/2007 - 02/2007	21	7.0	13.4	180
4T	4	09/2007 - 03/2008	36	12.0	14.8	273

Table 5.3: A list of various quantities for the three data sets from the VERITAS observations of the Crab Nebula. The second column lists the number of telescopes in the array, the third column lists the time period during which the data were recorded, and the fourth column lists the number of observing runs (of usually 20 mins in duration). The total observing time, the average zenith angle of the source during the observations, and the expected elevation adjusted system trigger (L3) rate at zenith for each data set are given in the fifth, sixth and seventh columns, respectively.

5.5 Simulations

Monte-Carlo simulations of gamma-ray initiated air showers and of the VERITAS detector are essential in many areas of VERITAS operation and data analysis. In general, during the design and engineering phase of VERITAS, simulations were useful in understanding the detector response to gamma rays and cosmic rays to improve the design of the detector and to compare the detector's performance to the simulated ideal world. Additionally, simulations provide various inputs to the offline analysis of data.

For the Crab data analysis described in Chapter 6, the simulated gamma-ray showers and simulated detector response were used in two places: to build lookup tables to estimate the expected Hillas parameters and the energy of a gamma-ray shower triggering the detector, and to calculate the effective area of the detector depending on the energy of the gamma-ray shower and the observation zenith angle. The simulation set that provides these inputs to the present analysis has two components: the CORSIKA [124] air shower simulation package for the extensive air shower simulations and GrISUDet [125] for the simulation of the VERITAS detector.

For simulations of extensive air showers, CORSIKA version 6.5021 was used with the hadronic interaction models QGSJet II-03 for primary particle energies above 500 GeV and FLUKA at lower energy levels. The EGS4 model was used for the electromagnetic interactions, and the Bernloehr package was used for the IACT simulations [126, 127]. The U.S. standard atmosphere model, US76 was used in calculations for the atmospheric properties.

The CORSIKA package generates simulated events according to input particle type, energy range and spectral index. For each event, it produces the distribu-

tions of the Cherenkov photons on the ground. Only the Cherenkov photons that pass through the detector mirrors are recorded. The gamma-ray and proton showers are simulated in an energy range of 50 GeV to 50 TeV. The gamma-ray events are simulated with a spectral index of -2.5 in order to match the energy spectrum of the Crab Nebula above 350 GeV, and proton air showers are simulated with a spectral index of -2.7. Gamma-ray air showers are simulated for seven zenith angles, 0°, 20°, 25°, 30°, 35°, 40° and 45°, and all proton showers are generated at a 20° zenith angle. The azimuths of showers are randomized between 0° and 360°. The shower cores (Section 6.5.3) of both gamma-ray and proton events are scattered randomly on a circular area 750 m in radius. In order to increase the statistics, the core location of each gamma-ray and proton shower is randomized; each gamma-ray shower is re-used ten times and each proton shower is re-used twenty times. The number of simulated gamma-ray showers is 1.5×10^6 for each zenith angle except for the 0° zenith set, which has 7.5×10^5 showers. The number of proton showers is 6×10^6 for the 20° zenith angle set. These represent the number of showers before they are re-sampled to use more them than once.

The VERITAS detector is simulated using the GrISUDet package. This package uses the CORSIKA output of Cherenkov photons striking the mirrors of the telescopes as input. As another input, a detector configuration file must be provided, which includes the parameters of the VERITAS detector, such as the PMT quantum-efficiency, mirror reflectivity, trigger settings, etc. The GrISU program performs three processes on the input photons: it traces the Cherenkov photons through the optical system, it calculates the response of the camera and electronics, and it applies the trigger criteria. More information on the detector parameters can be found in [126]. The GrISUDet program produces simulated FADC traces at each pixel for each simulated event which trig-

gers the detector. The output of the GrISUDet package is saved in the same standard VBF format (Section 6.1) as the real data. This makes it possible to treat the simulation data in exactly the same manner as the real data. In order to cover a wider range of sky noise from extra-galactic viewing conditions to moderate moonlight with a single simulated data set, the noise level is added to the simulated data in the analysis stage. All gamma-ray simulation sets are passed through GrISUDet simulations for each of the seven wobble offset distances of 0.0°, 0.25°, 0.5°, 0.75°, 1.00°, 1.50°and 1.75°. Seven different noise levels are simulated with values of 100, 150, 200, 250, 300, 350 and 400 photo-electrons/ns/m^2/sr covering different sky brightness levels for observations. As a result, 7 (zenith angles) $\times$ 7 (source offset distances) $\times$ 7 (noise levels) = 343 sets of simulated data are used.

CHAPTER 6

Data Analysis

The ultimate goal of observing an astrophysical object with VERITAS is to make a statement about its properties: to find out whether it is a significant source of gamma rays, to determine the stability or variability of the gamma-ray flux from the source over time, to obtain the energy spectrum of the gamma rays from the source, to resolve the morphology of the source, etc. Obtaining this information from observations requires application of various analysis methods on the recorded data. The main strength of the imaging atmospheric Cherenkov technique is the ability to effectively extract the gamma-ray signal from the excessive cosmic-ray background through offline image processing and to successfully reconstruct the properties of the detected gamma-ray signal.

In order to reconstruct the energy spectrum of the nebular emission from the Crab Nebula and to search for the pulsed emission from the Crab Pulsar, the data collected with VERITAS from the observations of the Crab were analyzed and the results are reported in this thesis. In this chapter the analysis methods used to obtain those results are described.

A number of offline analysis packages have been independently developed for the analysis of VERITAS data to guard against systematic errors being introduced in the analysis. The VERITAS collaboration policy requires that each result must be confirmed by the standard offline analysis package, the "VERITAS Gamma-ray Analysis Suite (VEGAS)" [128] and by at least one independent

secondary analysis. The results presented here are obtained using the VEGAS analysis package, and they are confirmed by other collaboration members using other analysis packages summarized in [129]. Most of the methods described in this chapter are common to each of those independent analysis packages.

The analysis performed on the data consists of many steps in which various methods can be used to attain the desired information. The first step is to determine the most basic parameters that represent the signal measured at each pixel: the charge and arrival time of the signal. Section 6.2 discusses the trace analysis that determines these parameters by evaluating the recorded FADC traces. The next step is to calibrate the data as explained in Section 6.3. Calibration is done by determining the parameters that represent the hardware response of the instrument and unfolding the response from the recorded data. The third step is to combine the photon yields recorded by each pixel to form the image of the event as seen at each telescope. These images are then parameterized as described in Section 6.4 and combined to reconstruct the development of the shower in the atmosphere. From this information, we infer the properties of the primary gamma ray: its direction, its projected impact point on the plane perpendicular to its direction, and its energy. The procedures to calculate these properties are explained in Section 6.5. Finally, a data selection algorithm, or a set of "cuts", is applied to extract the gamma-ray events from the background of cosmic rays (Section 6.6), and the rate of background events surviving these cuts is estimated using one of two different methods described in Section 6.7. Once the gamma-ray signal and surviving background rate are determined, it is then possible to estimate the significance of the detection of the source (Section 6.8), to reconstruct its energy spectrum (Section 6.9) and to search for a pulsed signal from the source (Section 6.10), using the methods explained in the respective sections.

As a member of VEGAS development group, I wrote a large part of the code in the calibration step of the analysis for the VEGAS package. Additionally, I did the first extensive test of the spectrum analysis code and provided feedback about its functionality, usability, failures and additional feature requirements during its development. Furthermore, I developed the timing analysis code using an available barycentering library and provided its interface to the VEGAS package.

6.1 The VERITAS Data

The online VERITAS data is recorded in a custom format, "VERITAS Bank Format (VBF)", which holds all event-by-event information recorded by the detector. In this format, all data relevant to a single detected Cherenkov shower are contained in an "array event" structure. These array events consist of an "array trigger" and a number of "telescope event" structures for each telescope participating in the observation.

An "array trigger" possesses the top-level information of the event including an unique event number in the run, the GPS time of the event arrival, a code describing the type of trigger which caused the event to be recorded, along with various other information such as the ID and number of telescopes that participated in the event trigger, the dead-time information, etc.

A "telescope event" possesses the actual data recorded at each telescope. A large fraction of a telescope event consists of the FADC traces (Section 4.5.1, 6.2) that represent the signal collected on each pixel of each telescope. The rest of the data are the information on the configuration of the various components of the telescope regarding the particular event that is recorded, e.g. the high/low gain switch of the FADC channel, etc.

All the events from a single observing run, typically of 20 min duration, are stored in a single compressed file named uniquely by a run number. A typical run file recorded by the 4-telescope VERITAS array is ∼5 GBytes in size.

6.2 FADC Trace/Pixel Analysis

When photons strike the pixels (Section 4.3.2) of a telescope camera, they are converted by the PMTs into electrons, producing a pulse, the total charge of which is proportional to the number of photons hitting the PMT photo-cathode. These signal pulses are digitized at 500 MSamples/s rate by an FADC dedicated to each channel, as explained in Section 4.5.1. The digitized data is a series of signal amplitudes in successive 2 ns time bins recorded starting some time before the trigger to include the time the light hit the pixel, covering and extending over the duration of the PMT pulse. The recorded series of signal levels for a subsequent number of time bins forms the "FADC trace" or the "waveform" (see Figure 6.1). The signal level at each time bin is recorded in units of digital counts (d.c.). The conversion from the d.c. to photo-electrons (p.e.) is determined by the average of the PMT voltages of a telescope (See Section 6.3.3).

The total charge deposited in the PMT pulse, which is proportional to the total number of photo-electrons detected, and the arrival time of the signal at each pixel are the relevant quantities describing the signal due to the detected light. The recorded FADC trace from each pixel is evaluated as explained in the following sections to obtain these quantities.

6.2.1 Signal Window Determination

The Crab data, and indeed most of the VERITAS data, is recorded using a 24 sample long FADC trace, covering a time window of 48 ns duration bracketing the signal pulse generated on each pixel. The duration of a Cherenkov signal is about 8-10 ns, including the time spread due to the mirror and electronics. Each PMT records light from the night-sky background (NSB) and the Cherenkov photons from the shower during this time. Thus, an FADC trace contains the charge deposited due to the background light, which is present during its whole duration, and the charge from a Cherenkov signal which is present only in a $\sim$10 ns portion. In order to minimize the contamination from the NSB to the total charge, it is important to find the exact portion of the trace into which the Cherenkov signal is deposited. This portion is called the "signal window" or "integration window" (Figure 6.1).

Thus, we need to determine the first sample of the trace in which the signal is present and the number of subsequent samples over which to integrate the trace in order to maximize the ratio of the Cherenkov signal to the NSB. One additional complexity is that the signal from an extensive air shower does not arrive at each pixel at the same time. A gradient in the arrival times of the light on the pixels over the camera, depending on the direction of the shower, must be accounted for. Thus, if a common integration window is going to be used for all pixels, one should ensure that the integration window is wide enough to cover the shift of the signal window over the recorded trace of each pixel in the camera.

Various methods are used to determine the signal window. The simplest method is to use a single integration window located at the earliest start position of the signal for all pixels of a telescope for all events. This window is made wide enough to cover the shift of the pulse due to the time gradient of the shower

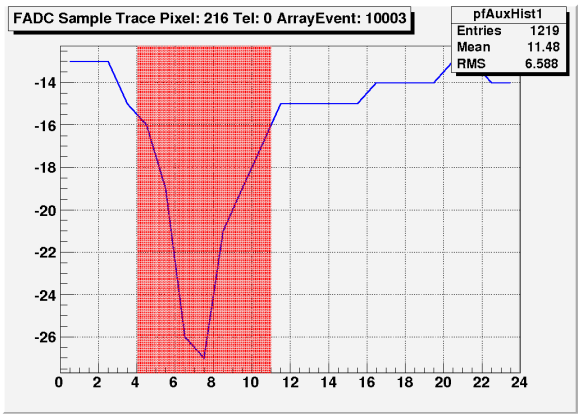

Figure 6.1: A typical FADC trace is shown. The x-axis is the sample number of the FADC trace and the y-axis is the amplitude of the recorded signal pulse in digital counts (d.c) at each sample. The shaded region shows the integration window used to determine the charge deposited by the Cherenkov shower on this pixel.

arrival at each pixel. To determine the correct position of the start point of the integration window, a number of events in the run are examined and the start time of the pulse from each channel is sampled separately for each telescope. Only pulses which have a charge greater than a pre-determined lower limit are taken into consideration to ensure that the sampled pulses are due to Cherenkov light and not due to the fluctuations of the NSB. The number of events used for this sampling is large enough to guarantee a good statistical sampling without significantly increasing the analysis run time. The mean start time of the pulse is determined from these samples for each telescope and the integration window for the telescope is chosen to start 4 ns before this point and to cover the width of the distribution. A seven sample (14 ns) integration window width was determined to be wide enough to cover the duration of the pulse and to account for the shift

of its start with respect to the common start position.

A more complex method uses a "sliding window" to determine the charge integration window. This method has the advantage that a narrower window can be used that is better matched to the intrinsic spread of a PMT pulse due to Cherenkov light. In this method, a different start time for each channel for every event is chosen, depending on the pixel's position on the gradient line of the shower arrival direction, i.e. depending on the arrival time of the light at each pixel. In this method, two analysis iterations are made. The first analysis uses a wide standard integration window to yield a set of image parameters from which the time gradient of the image on the camera is calculated. Then, on a second iteration, the same analysis is repeated using a narrower integration window, adjusted for each channel in the image to account for the time gradient. This method is relatively slow, since each event is analyzed twice.

Similar to the "sliding window" method, other methods have been used which do not require knowing the direction of time gradient in advance and in turn do not require a second iteration of the analysis. In one such method, the peak of the pulse on the FADC trace is determined. The integration window is located starting a certain number of time bins before the position of the peak. Since the peak shifts with the location of the pulse in the trace, this method automatically determines the correct location of the signal in the trace.

The standard configuration of the VEGAS analysis package, used throughout this work, utilizes the first method. The default option for the number of events to determine the window start time is 10,000. The width of the integration window used is seven samples (14 ns).

6.2.2 Charge Integration

The most simple method to estimate the total charge deposited in a pixel by the Cherenkov light is to integrate the portion of the digitized pulse contained within the window described above. The charge deposited in the trace is calculated by summing the signal levels from each sample in the integration window. This method is the standard for the VEGAS analysis and is used for the Crab analysis reported here.

More sophisticated methods have been suggested in which the digitized pulse is fitted to a continuous function representing the PMT pulse and the charge is calculated by integrating the area under this fitted function.

6.2.3 Timing Determination

The start time of the pulse recorded at each channel, T_0, represents the arrival time of the signal at a pixel. It is defined as the time on the leading edge of the pulse at which the pulse reaches half of its peak value after subtraction of the pedestal baseline (see Section 6.3.1 for the calculation of the pedestal baseline).

6.3 Data Calibration

The data recorded by VERITAS consists of the Cherenkov signals of interest convolved with the instrumental response corresponding to the various systems of the detector. It is crucial to accurately characterize the response of the instrument and to remove the hardware dependency from the recorded signal. This calibration procedure is the first step of the data analysis. The primary calibration parameters are the pedestal levels contributing to the charge collected by each channel, the time shift that the hardware introduces on the signal arrival

times at each pixel and the gain of each channel when converting a fixed number of photons to a charge. Additionally, during the calibration procedure, the status of each pixel during data collection is assessed and the badly behaving pixels are removed from the image of an event to insulate the analysis from their adverse effects.

6.3.1 Pedestal Removal

The average NSB brightness always produces a steady current through the PMTs. On the short time scales measured by VERITAS (during the 14 ns integration window), significant positive or negative fluctuations are present in the charge contributed by the NSB. In order to decide whether a detected level of light is likely due to an actual Cherenkov signal or whether it is within the range of expected fluctuations of the NSB, it is necessary to measure the distribution of the NSB fluctuations in the absence of a Cherenkov signal.

The AC coupling of the VERITAS preamplifiers removes the steady NSB current before the signal is sent to the FADCs and it puts the baseline of the signal to zero. Since the FADCs only record signals of a single polarity, it would be impossible to measure the positive fluctuations of the NSB unless this baseline value is artificially shifted away from zero. In order to see both the negative and the positive fluctuations in the night sky brightness, a constant negative offset of approximately 13 digital counts per FADC sample, known as the "pedestal", is put into the signal before it is digitized. This offset defines the "mean pedestal level" applied on the digitized trace of the PMT signal, and the NSB fluctuations are measured relative to this negative offset. In order to obtain the portion of the detected light due to the Cherenkov shower, the value of this offset, the "mean pedestal", and the level of its fluctuations, referred to as the "pedvar", are

calculated in the absence of a Cherenkov signal. It should be noted that the name "pedvar" is misleading; despite its name, the "pedvar" is defined as the width, i.e. the RMS value, of the NSB charge distribution instead of the "variance" of the distribution which the name seems to suggest.

In order to measure the mean pedestal and the fluctuations in the NSB, the telescopes are triggered artificially at a constant rate to record the sky brightness on each pixel in the absence of an actual Cherenkov signal. These artificially triggered events are saved as a special type, "pedestal" events, among the regular events triggered by actual Cherenkov light. During the calibration step of the offline analysis, these pedestal-type events are used to estimate the contribution of the injected pedestal and the fluctuations of the NSB for each pixel. The FADC traces recorded during these events are integrated to calculate the charge deposited by the NSB and the distribution of the calculated charge in each event gives the "mean pedestal" and the "pedvar".

6.3.1.1 Calculation of the Mean Pedestal

The injected pedestal level, the "mean pedestal", on the FADC channel of each pixel is constant during a run and during an event. Thus, in order to calculate the mean pedestal level for a pixel, the distribution of the charge deposited is built using all pedestal events collected during the whole run, in order to minimize the statistical uncertainty. For the same reason, the largest integration window, i.e. the whole duration of the FADC trace, is used to calculate the charge. The "mean pedestal level" is then calculated per sample by dividing the mean of the charge distribution by the number of samples in the integration window.

6.3.1.2 Calculation of the Pedvar

The "pedvar" of a pixel is calculated from the width of the pedestal charge distribution for that pixel. The pedvar is different for each pixel since each pixel sees a different portion of the sky at a given time. It also depends on the size of the integration window used to calculate the charge, therefore, it is calculated for each possible integration window size that might be used in the analysis (Figure 6.2(b)). The total width of the FADC trace is large enough so that it is possible to use different portions of the FADC trace to extract multiple independent pedvar estimates from one pedestal event. For example, from a standard 24-sample FADC trace, one can calculate three different pedvars for an integration window width of seven samples using the samples [0-6], [7-13], [14-20] while the last three samples are left unused.

The VERITAS FADCs use a 125 MHz clocking signal to write 4 bytes into a pipeline burst RAM for each channel. It was found that this clocking adds a periodic noise to an FADC trace at every four samples [11]. Depending on the location and the width of the integration window and the phase of the noise, such periodic noise can bias the pedestal calculation. In order to minimize the systematic error caused by this noise, the start of the integration window is chosen randomly on the FADC trace of each pixel for each event.

The pedvars also have a dependency on time. As a telescope follows a target, the background stars in the field move through the pixels of the camera changing the NSB levels in the pixels. Thus, the NSB levels are monitored continuously during the course of an observing run. A high rate of the artificial pedestal events is desirable to obtain the high statistics needed to estimate the NSB level accurately on each channel at every instant. However, recording the additional pedestal events inflates the dead-time of the system. A pedestal rate of 1-3 Hz

is chosen as the optimum rate to trigger the VERITAS telescopes during normal data taking.

Given the size of the VERITAS PMTs, it can be calculated that the projection of a star moves through one pixel in approximately three minutes, which is therefore the approximate time scale on which the sky brightness is changing for a channel. Therefore, the charge deposited by the pedestal events on each pixel of each telescope are accumulated separately for each three minute interval of the run. The width of the charge distribution accumulated at such three minute windows gives the time dependent "pedvar".

Figure 6.2(a) shows the pedestal charge distribution of pixel 261 of Telescope 3 accumulated from the pedestal events recorded in the first three minute interval of Run 38200. The mean of the distribution gives the "mean pedestal", the injected voltage offset on the pixel, and the width of the distribution gives the "pedvar", the level of NSB fluctuation of the sky projected on this pixel. In Figure 6.2(b), the charge distributions for the same pixel in the same run obtained for different integration window sizes are shown. It can be seen that the mean pedestal per sample is the same but the width of the distributions, i.e. the pedvar, is different for each integration window size.

Figure 6.3 shows the distribution of the mean pedvars for all the channels in the camera of Telescope 3, between the minutes 3 and 6 in a Crab observing run. The pedvars shown are calculated with an integration window size of 7 samples (same as Figure 6.2(a)).

6.3.2 FADC Timing Calibration

The arrival time of a signal detected on a pixel, T_0, measured from the FADC trace of its PMT pulse (Section 6.2.3), does not depend only on the timing gradient

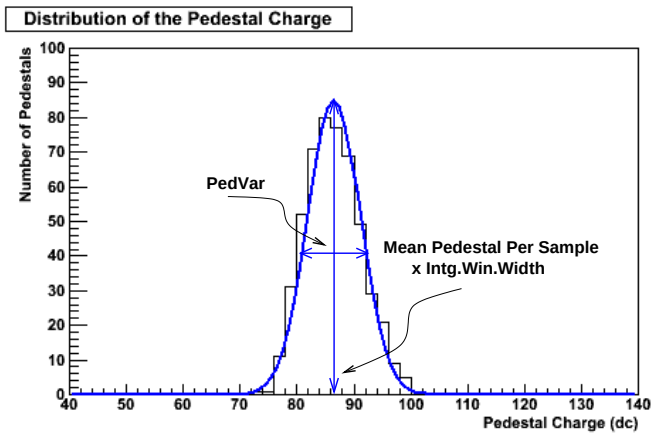

(a)

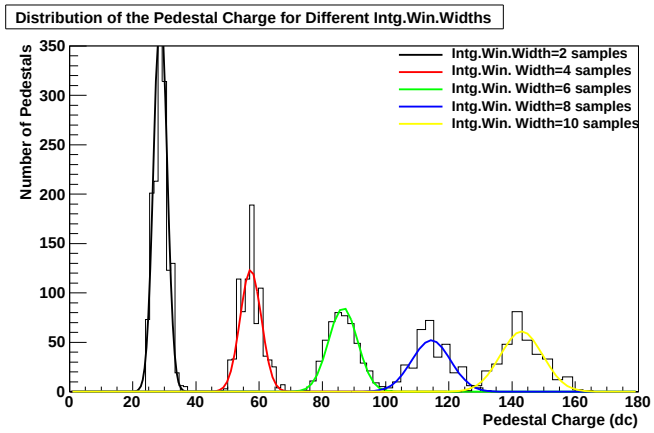

(b)

Figure 6.2: (a) A distribution of the pedestal charge (Pixel 261 of Telescope 3 from Run 38400) for an integration window width of 7 samples is plotted. The "mean pedestal per sample" and "pedvar" are shown. (b) The same distribution obtained for different integration window sizes from 2 samples to 10 samples (left to right) is shown. The dependency of the pedestal variances on the integration window width is evident. On the other hand, the mean pedestal for each integration window is a constant mean pedestal per sample multiplied by the integration window width.

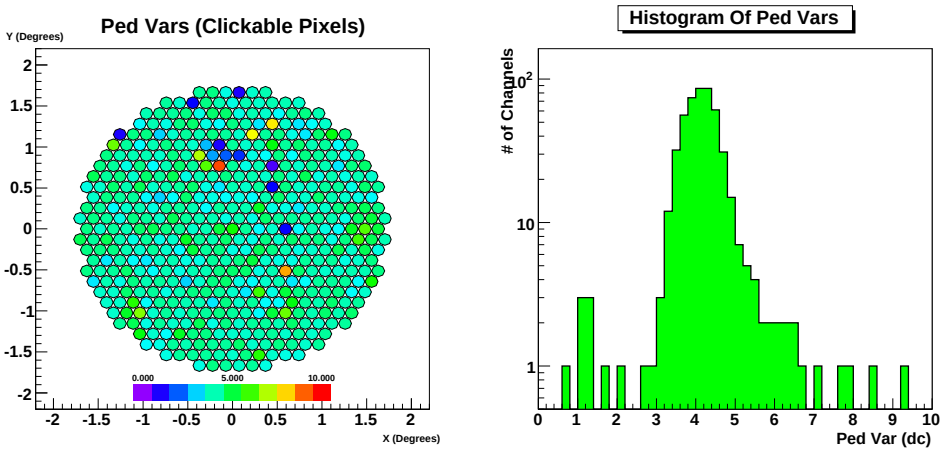

(a) (b)

Figure 6.3: (a) The mean pedvar on each pixel is shown by the color scale for the camera of Telescope 3 between minutes 3 and 6 in a Crab observing run, Run 38200. The color scale shows the mean pedvar in units of d.c. (b) The distribution of the mean pedvars of all the channels in the same camera in the same time slice and from the same run as in (a) is plotted.

of the Cherenkov shower on the camera due to the inclination of the shower direction. In fact, T_0 values for different pixels in the camera are not aligned even for a flash of light simultaneously illuminating all pixels. This is because the start times of the PMT pulses are shifted slightly due to differences in cable length and delays introduced by the HV and the electronics between the PMT and the FADC channel of the pixels.

These arrival time differences introduced by the hardware on different channels, referred as T_{offset}, are measured using laser flashes which simultaneously illuminate all pixels during specialized "laser runs" taken each night (see Section 4.6.2).

The T_{offset} value of a channel is defined as the average difference between the start time of a pulse on that channel and the arrival time of the event. We define the arrival time of the event, T_{event}, as the average arrival time of the signal over the pixels in the camera as follows:

$$T_{event} = \frac{1}{N} \sum_{i=1}^{N} (T_0)_i \tag{6.1}$$

where $(T_0)_i$ is the arrival time of the signal for each channel i and N is the total number of channels in the camera. The time difference between the arrival time of the signal at a channel i and the arrival time of the event is then given by:

$$\Delta t_i = (T_0)_i - T_{event} \tag{6.2}$$

The hardware dependent time offset of a channel i, $(T_{offset})_i$ is then obtained from the mean of the Δt_i distribution for a large number of events M:

$$(T_{offset})_i = \frac{1}{M} \sum_{event=1}^{M} (\Delta t_i)_{event} \tag{6.3}$$

The T_{offset} values for each channel are calculated as described from the specific laser run each night, and during the analysis of an observing run these values are

removed from the recorded arrival times of signals at each channel to get the actual arrival time of the Cherenkov light independent of the hardware factors.

Figure 6.4(a) shows the distribution of Δt_i values for a single channel, Channel 224 of Telescope 4, measured from the laser events of a typical laser run, run 38186 taken on 12/04/2007. The mean value of this Δt_i distribution, 0.22 ns, is the time shift introduced by the hardware on the signal detected on this pixel. It is desirable to have a sharp Δt_i distribution, i.e. a small RMS, in order to accurately estimate the time shift introduced by the hardware. Figure 6.4(b) shows the T_{offset} values for each channel in camera of Telescope 4, and Figure 6.4(c) shows the distribution of T_{offset} for all the channels on the same camera measured from the same run. It can be seen from the figure that the typical time shifts introduced by hardware are less than ± 2 ns, i.e. one FADC sample.

6.3.3 Relative Gain Calibration

For an ideal camera, each pixel produces the same amount of charge compared to other pixels for an equal intensity light illumination. For this ideal camera, the amount of charge recorded at the FADC channel of each pixel is directly proportional to the number of photons detected and it is possible to sum the charges recorded on each channel to get a total charge that is proportional to the total light from the Cherenkov air shower. The PMT voltages, on which the gain of the PMT depend strongly, are adjusted approximately once per season to set an equal response to an equal number of photons detected at each pixel. This determines the overall ratio of the photo-electron to the FADC digital counts. For 2007-2008 observing season, one d.c. corresponds to approximately 4.3 to 5.3 p.e. depending on the average PMT voltages of each telescope.

However, PMT aging, dirt accumulation on the PMT faces and other internal

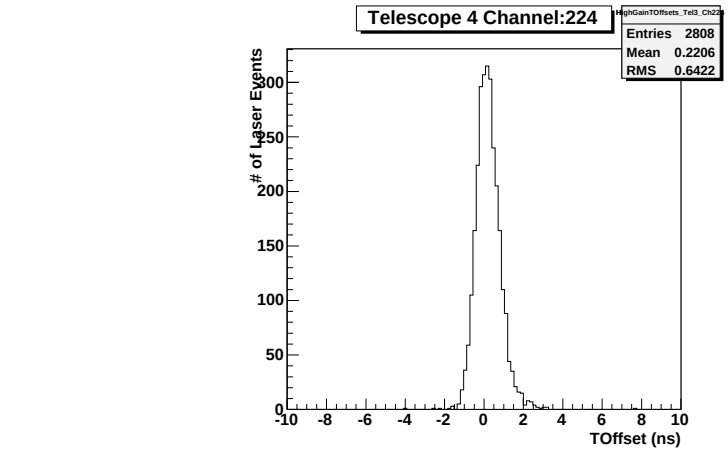

(a)

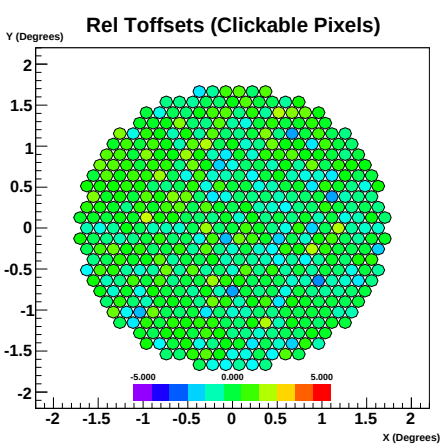

(b)

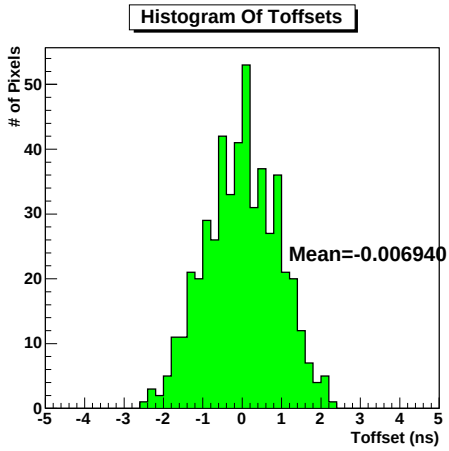

(c)

Figure 6.4: (a) The distribution of Δt_i for a single channel, Channel 224 of Telescope 4, measured from the laser run, Run 38186, taken on date 12/04/2007 is shown. (b) T_{offset} of each channel is given by the color scale for the camera of Telescope 4 from the same laser run. (c) The distribution of T_{offset} of all the channels in the same camera measured from the same run is shown. See text for the definition of these quantities.

electronic and external environment factors change the PMT response on a night to night basis and break the homogeneity in the charge response of the pixels. As a result, the same amount of light will result in a different amount of charge deposited on each channel. This effect is corrected for by measuring the difference in the response of each channel for an equal intensity of light illumination provided by the laser events during special laser flashes taken nightly.

The difference in the response of a channel with respect to other channels for the same amount of the light can be characterized as follows: the average charge deposited on one channel during an event, $\langle Q_{evt} \rangle$, is calculated by averaging the charge deposited over all the channels in the camera for that event:

$$\langle Q_{evt} \rangle = \frac{1}{N} \sum_{i=1}^{i=N} Q_{i,evt} \tag{6.4}$$

The relative charge of a channel i in an event evt, $(Rel.\, Q_i)_{evt}$, is defined as the ratio of the charge detected on that channel to the average charge detected in the camera for the same event:

$$(Rel.\, Q_i)_{evt} = \frac{Q_{i,evt}}{\langle Q_{evt} \rangle} \tag{6.5}$$

For each channel, the "relative gain" is calculated for a large number of laser events, say M, as the mean of this relative charge distribution:

$$(Rel.\, Gain)_i = \frac{1}{M} \sum_{evt=1}^{M} (Rel.\, Q_i)_{evt} \tag{6.6}$$

A relative gain value close to 1.0 is desirable to ensure equalized response from each channel.

Figure 6.5(a) shows the distribution of the relative charges for a typical channel, Channel 220 of Telescope 4, measured from the laser events of a typical laser run, Run 38186 taken on 12/04/2007. The relative gain of that channel is

5.5% higher than 1.0, the value expected from an ideal flat-fielded camera. Figure 6.5(b) shows the relative gain distribution of all channels for Telescope 4, for the date this laser run is taken. A tighter distribution means better homogeneity in the hardware response of the pixels in the camera, i.e. a better flat-fielded camera. It should be noted that the y-axis scale is logarithmic. Figure 6.5(c) shows the distribution of the mean relative gain for all the channels of the same camera measured in the same run. It can be seen from the figure that the typical relative gain of all pixels is less than 10% higher or lower than 1.0.

6.3.4 Pixel Status Assessment

In a given run, there are always some pixels that are either turned off or are malfunctioning. These pixels do not have a meaningful trace or a correct amount of deposited charge, and they should be removed from the analysis. These channels can be identified by using the distributions of signals recorded during the run and by using the monitor information from the database (DB). The identification of these pixels is done during the calibration step of the analysis before the reconstruction of the shower image in the camera.

A pixel may be turned off manually or automatically by the HV system if the projection of a bright star falls on it during observations. The status of pixels are logged to the DB by the HV system and read in during the calibration step of the analysis in order to tag the inactive pixels for removal. If a pixel is inactive for an unknown reason, its pedvar is close to zero which provides another signature to identify it even if it is not logged by the HV system. Additionally, a pixel may be malfunctioning for a number of reasons that are mostly hardware related, e.g. a bad PMT/base connection, a missing PMT, etc. A malfunctioning pixel tends to be noisy and its pedvar is significantly larger than the average pedvar of the

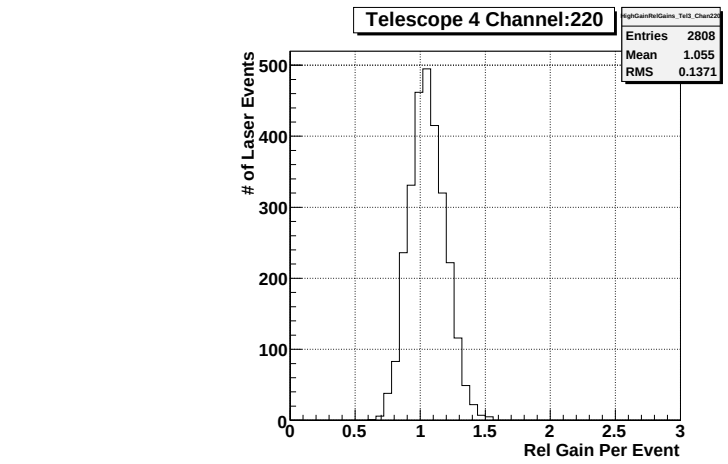

(a)

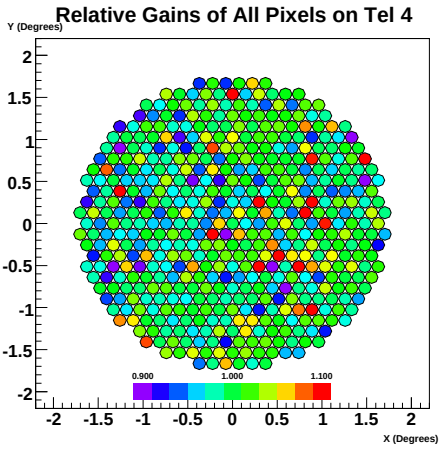

(b)

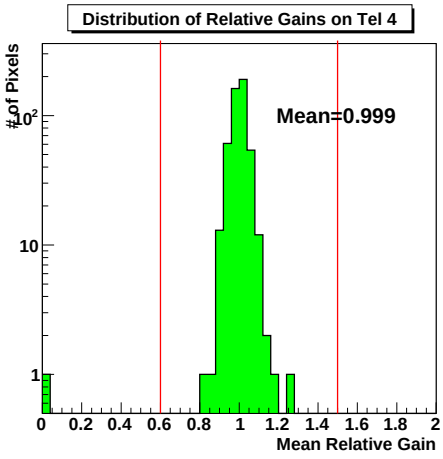

(c)

Figure 6.5: (a) The distribution of "Relative Charge" of a typical channel, Channel 220 of Telescope 4, measured from the laser run 38186 taken on date 12/04/2007 is plotted. (b) The relative gain of each channel is given by the color scale for the camera of Telescope 4 from the same laser run. (c) The distribution of the relative gains of all the channels in the same camera measured from the same run is shown. The red lines show the acceptable range of relative gains.

pixels in the camera.

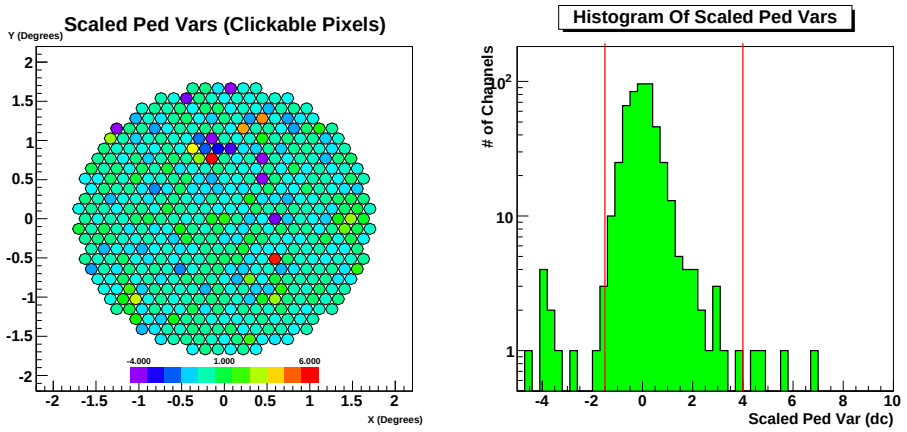

(a) (b)

Figure 6.6: (a) The mean scaled pedvar of each channel is shown by the color scale for the camera of Telescope 3 between minutes 3 and 6 in a Crab observing run, run 38200. (b) The distribution of the mean scaled pedvars of all the channels in the same camera in the same time slice and from the same run as in (a) is plotted. The red lines show the scaled pedvar region defined as normal, the channels outside this region are deemed as outliers and removed from the analysis.

In summary, in addition to the logged monitor information in the DB, the pedvar distributions of the pixels provide additional information to allow the identification of misbehaving pixels. These pixels are removed from the analysis to avoid their adverse effects. Figure 6.6 shows the distribution of the pedvars for the pixels of Telescope 3, during the first three minutes of the run. To identify the outliers from the normal behaving pixels, a criterion on the scaled pedvar, as defined in the following equation, can be used:

$$\text{Scaled pedvar} = \frac{\text{pedvar} - \langle \text{pedvar} \rangle}{\sigma_{\text{pedvar}}}$$

In Figure 6.6, the scaled pedvar distribution corresponding to Figure 6.3 is

shown. When these two figures are compared, it can be seen that the definition of scaled pedvar does not change the place of a channel in the pedvar distribution, but it provides a convenient way to assess pedvars with a scale independent of the mean value of the pedvars. On the right panel of Figure 6.6, towards the top of the camera, a cluster of channels are seen with a dark blue color corresponding to a very low pedvar. The HV for this cluster of pixels is turned off due to the projection of the bright star zeta-Tau falling on them. A few noisy channels distributed over the camera with reddish colors are also seen. A few isolated channels distributed over the camera with dark blue color are the pixels manually turned off due to a bright star or a hardware problem. On the left panel of Figure 6.6, the distribution of the scaled pedvar and the defined region of acceptable pedvar values, $-1.5 <$ Scaled Pedvar < 4.0, are shown.

Similarly, another scaled quantity based on the relative gain is calculated to remove the pixels with outlying relative gain values to have a better flat-fielded camera. The cut applied on the relative gain is $-3 <$ Scaled Relative Gain < 3.

6.4 Single Telescope Parameterization

Once the signal strength in each channel is established after the signal calibration, the images of the Cherenkov shower on each telescope camera are identified and parameterized. Image pixels are identified through a "cleaning" procedure, and the parameterization of the images is done by calculating the moments of the light distribution following a procedure first suggested by Hillas [18].

6.4.1 Cleaning

Cleaning is done in two steps to identify the collection of pixels which represent the image of the Cherenkov shower on each camera and to remove the pixels that contain noise-induced charges.

First, the pixels which contain an integrated charge greater than 5.0 times their pedvar are selected as "Picture Pixels", and any pixels adjacent to a picture pixel and having at least 2.5 times their pedvar are tagged as "Boundary Pixels". Secondly, isolated picture pixels, with no neighboring picture or boundary pixels, are removed from the image. The collection of remaining pixels is defined as the image of the Cherenkov shower. The effect of the cleaning for a gamma-ray, a cosmic-ray and a muon event is shown in Figure 6.7.

6.4.2 Hillas Parameterization

The resulting images are then parameterized by calculating the first and second moments of the light distribution on the image using the location, the x and y coordinates in degrees with respect to an origin at the camera center, of each pixel in the image with respect to the center of the field of view and the registered signal strength, s, in the pixel (Figure 6.7). The following parameters, first suggested by Hillas [18], characterize the shape and orientation of the image and they can be derived from the moments of the image: *Distance*, *Width*, *Length*, *Miss*, *Azwidth*, *Asymmetry*, *Alpha*, *Size* and *Frac3*. A full description of the moment fitting technique can be found in [113]. All parameters are defined in Table 6.1 and the geometrical representation of some are shown in Figure 6.8.

The first six of these parameters are independent of each other and calculated directly from the second moments of the image. *Alpha* is calculated by combining

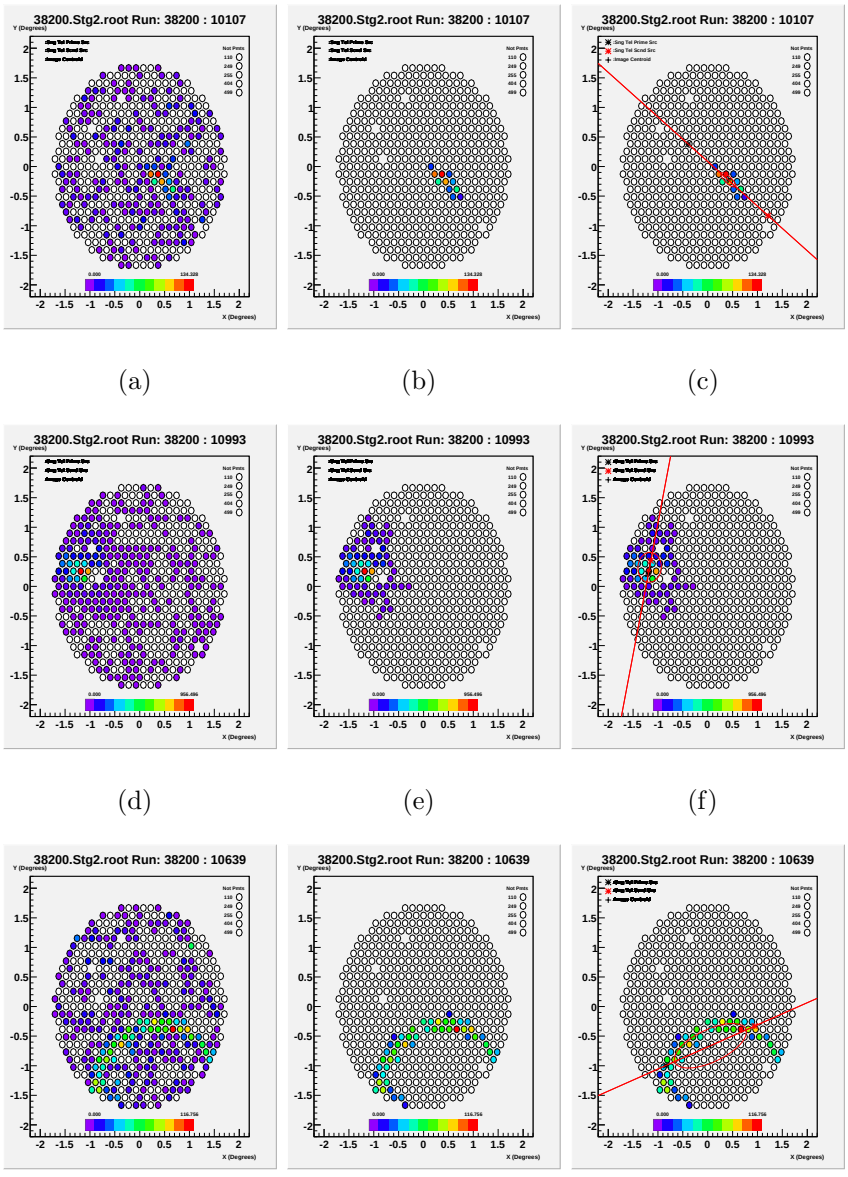

Figure 6.7: The images of the events caused by three types of primary particles are shown in the figure before and after the cleaning procedure in the left and middle columns, respectively. The first and second moments used to calculate the Hillas parameters are illustrated by an ellipse shown in the right column. The line passing along the major axis shows the reconstructed shower direction of the primary particle by single telescope analysis. (a-c) A gamma-ray event. (d-f) A cosmic-ray event. (g-i) A muon event.

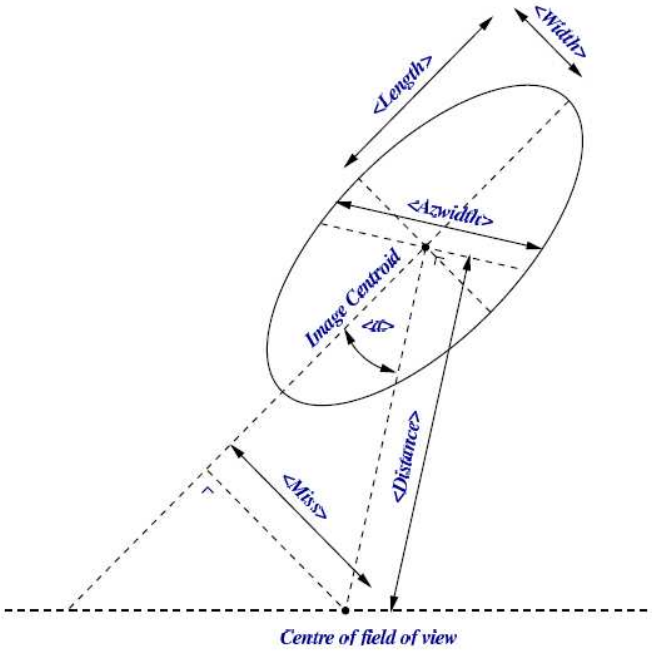

Figure 6.8: A depiction of the Hillas Parameters for an ellipse fitted to a Cherenkov image [17]. Each parameter is explained in the text.

Miss, and *Distance* and the last two parameters are calculated from the signal strength s on each pixel. The total signal from all the pixels in the cleaned image, *Size*, is a measure of the total light produced by the shower, which in turn depends on the energy of the primary particle. The parameter *Frac3* corresponds to the trigger threshold of the detector.

Simulations of gamma-ray and cosmic-ray showers can be used to identify a region in phase space that gamma-ray-like showers tend to occupy. Hillas predicted that by specifying that each image should have at least four of its parameters within this region, it would be possible to efficiently discriminate between gamma-ray and cosmic-ray images. This criterion is central to the single telescope analysis for the discrimination of gamma rays and cosmic rays.

For stereo analysis, the Hillas parameters are used to select good-quality images to use in the reconstruction of the shower parameters, as described in the following subsection. In this analysis, the parameters, *Distance*, *Width*, *Length*, and *Size* are used for this purpose.

6.5 Stereo Parameterization

In this step, the images of each telescope camera are combined to obtain the shower level information for the primary gamma ray. The shower parameters, the arrival direction of the shower and the position of the projected impact point on the plane perpendicular to the pointing direction, the *Shower Core*, are reconstructed from individual images using simple geometrical techniques [130]. The energy of the shower and the "mean scaled width" and "mean scaled length" parameters are calculated using lookup tables generated from simulations of gamma-ray showers and the detector. The last two parameters have proven to be very

Parameter	Definition
Distance	Distance from the centroid of the image to the center of the field of view.
Width	RMS spread of the light along the minor axis of the image.
Length	RMS spread of the light along the major axis of the image.
Miss	Perpendicular distance between the major axis of the image and the center of the field of view.
Azwidth	RMS spread of the light perpendicular to the line connecting the image centroid with the center of the field of view; a measure of the width and pointing.
Asymmetry	Measure of the asymmetry in the light distribution along the major axis of the image. Gamma-ray images should have a cometary shape with their light distributions skewed towards their source position.
Alpha	Angle between the major axis of the ellipse and a line joining the centroid of the ellipse to the center of the field of view.
Size	Total charge in all of the pixels in the image, corresponding to the total light content of the image.
Frac3	Percentage of the total light content of the image contained in the three pixels with the highest signals.

Table 6.1: The definitions of the Hillas Parameters from [18] are summarized.

useful in distinguishing gamma-ray showers from cosmic-ray showers.

6.5.1 Event Quality Selection

Before proceeding to shower reconstruction, each telescope image is tested against image quality selection criteria to ensure the robustness of the reconstruction. This stage is capable of using any cuts based on the image parameters to select good telescope images. For the standard analysis, the image quality selection is based on the N_{Pixels} in the image, the *Size* and *Distance* of the image as listed in Table 6.2. Figure 6.9 shows distributions of these parameters for a typical 4-telescope Crab observing run, run 38063. (It should be noted that more than 99% of recorded events are background events due to cosmic rays or NSB light.) The image selection cuts listed below are not utilized to discriminate between a gamma-ray or a cosmic-ray event, but they are used to remove images that would cause erroneous reconstruction of the shower parameters either because the images are too faint (small size), have no clear shape (small number of pixels), or are detected at relatively large impact distances and thus are truncated at the edge of the camera (large image distance).

After the images are removed based on the image selection, the event quality selection cuts are imposed. An event is rejected completely if less than two telescope images are left for reconstruction or if only two telescope images are left where the major axes are approximately parallel to each other (the angle between the two axes is $< 10^{\circ}$). In this stage it is also possible to select or remove events with images present from a specified telescope (or a telescope combination). For the 4-telescope data set, the events triggered only by the T1 and T4 combination are removed at this stage, since these events are dominated by the accidental coincidences of small showers due to the short baseline between

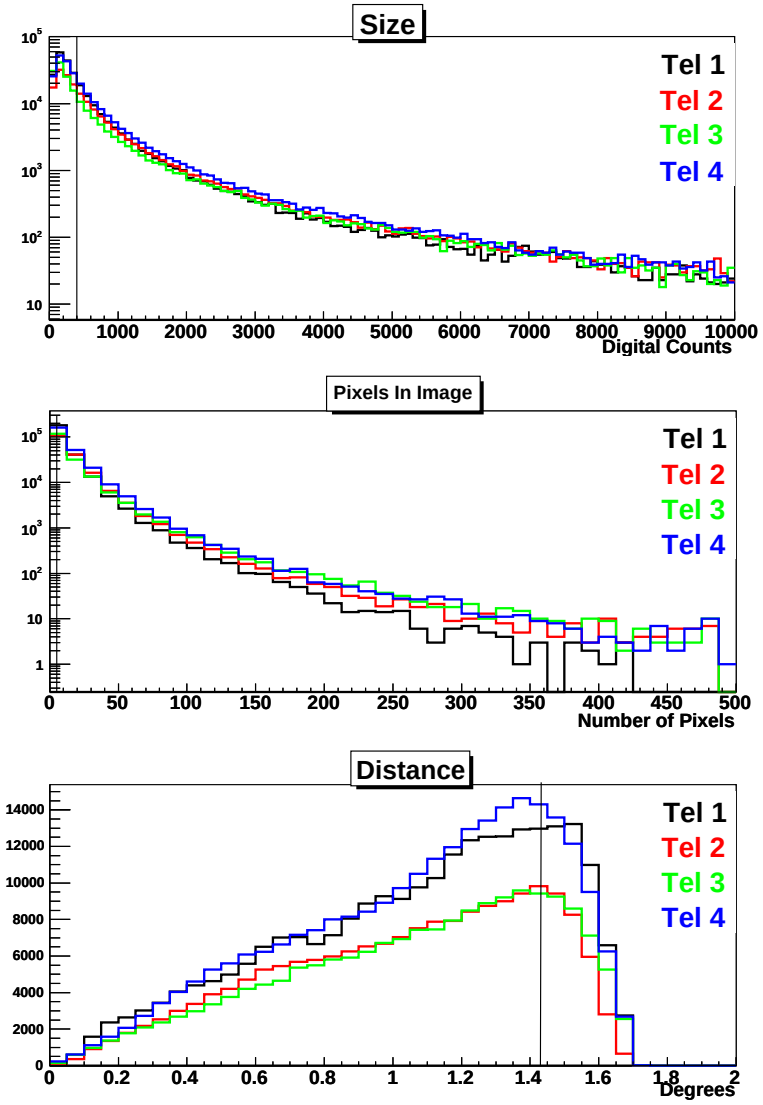

Figure 6.9: The distributions of three Hillas parameters, *Size*, N_{Pixels} and *Distance*, that are used in the event quality selection are plotted for a typical 4-telescope Crab observing run, Run 38063. (It should be noted that more than 99% of events recorded are background events due to cosmic rays or NSB light). The vertical lines show the lower limit (for parameters *Size* and N_{Pixels}) or the upper limit (for *Distance*) of the acceptable range.

the T1 and T4 telescopes. Finally, after the core position is reconstructed, a cut on the impact distance of the shower is applied to remove the showers with large impact distances to avoid their bias in the calculation of the mean scaled parameters. Those cuts are also listed in Table 6.2 along with the cut efficiencies for simulated gamma rays and for the background events detected in a typical Crab observing run, run 38063. After all cuts, the reconstruction efficiency of the shower direction and shower core (see following sections) is 38.4% for simulated gamma rays and 18.7% for background events. Similarly, the reconstruction efficiency of the mean scaled parameters and energy is 36.6% and 16.9% for simulated gamma rays and background events, respectively. It is clear from the comparison that, these quality cuts remove a higher percentage of background events than the gamma-ray events, and thus, they improve the signal to noise ratio.

6.5.2 Shower Direction Reconstruction

In the field of view of the telescopes, the major axes of the images recorded on each telescope camera intersect in the region of the arrival direction of the primary particle. Thus, the shower arrival direction is obtained by finding a point, in the camera plane, that minimizes the weighted perpendicular distance between that point and the major axis of each image. The weight is given by the image *Size*. The shower direction reconstruction for 2-, 3-, and 4-telescope images is shown in Figure 6.10.

The degree to which the reconstructed shower direction is consistent with the position of the target being observed can be represented by another parameter, θ^2, which is the square of the angular offset between the reconstructed shower direction and the true direction of the target. A cut on the distribution of θ^2 is

	Image Quality Selection			
	Size	N_{Pixels}	Distance	
Cuts	> 400 dc	≥ 5	[0.0 °, 1.43°]	
Eff.(γ)	43%	69%	90%	
Eff. (Bg)	28%	52%	86%	
	Event Quality Selection			
	Tel. Comb.	Num. Tels	Min. Angle	Impact Distance
Cuts	No T1T4	>= 2	10°	10 km
Eff.(γ)	94.6%	44.6%	99.3%	98.2%
Eff.(Bg)	95.7%	24.1%	98.9%	98.3%

Table 6.2: The standard image quality selection cuts used in the analysis are given in upper panel. All parameters are defined in the text. The percentage of telescope images surviving each cut (cut efficiency) is given for simulated gamma rays at 20° zenith angle and for the background events (from Crab run 38068) in the second and third rows, respectively. In the lower panel, the event quality selection cuts applied to the recorded events after the image selection cuts are shown. For the last two rows, the first column is the events triggered by the allowed telescope combinations, the second column is the minimum number of telescope images required in the event, the third column is the minimum angle between the major axes of images if only two image are present in the event and the fourth column is the maximum impact distance of the shower core to each telescope. The last two rows list the percentage of events survive each cut for simulated gamma-ray events and for background events detected in a typical Crab run, run 38063.

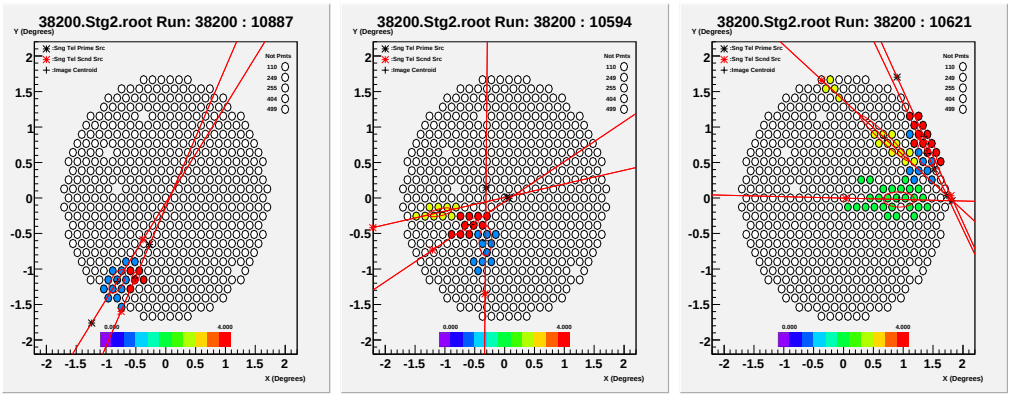

(a) (b) (c)

Figure 6.10: The intersection of the major axes of the images in the camera plane for 2-, 3-, and 4-telescope events are shown in (a), (b), and (c), respectively.

very useful for rejecting background events originating from positions away from the position of the target object.

6.5.3 Shower Core Reconstruction

The position of the *Shower Core* is determined by finding the point in the plane perpendicular to the reconstructed shower direction, the mirror plane, that minimizes the weighted perpendicular distance to the projected major axes of all selected telescope images. The estimate of the shower energy depends on the distance in this plane of the shower core to each telescope, and thus accuracy in the shower core reconstruction is crucial for achieving good energy reconstruction.

The shower core position reconstruction for 2-, 3-, and 4-telescope images is shown in Figure 6.11.

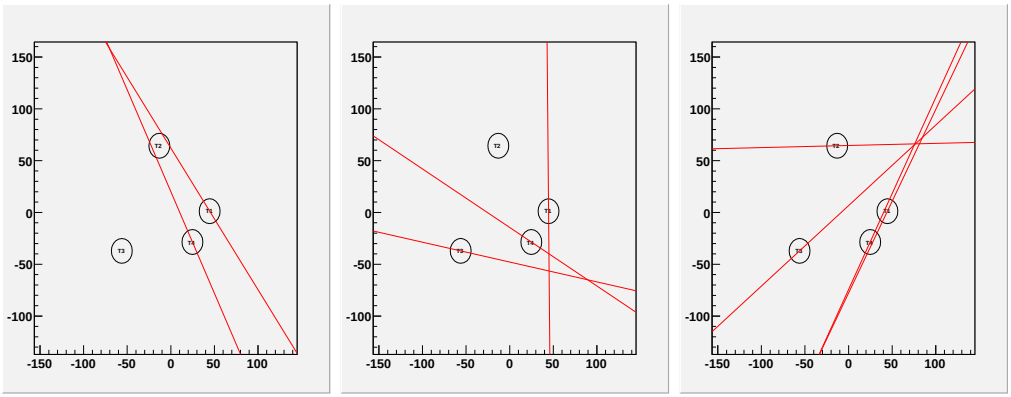

(a) (b) (c)

Figure 6.11: The reconstruction of the shower core position through the intersection of the major axes of the images in the mirror plane for 2-, 3-, and 4-telescope events are shown in (a), (b) and (c), respectively, for the same events shown in Figure 6.10. The red lines are the major axes of each telescope image projected in the mirror plane.

6.5.4 Mean Scaled Parameters

Two shower level shape parameters, the *Mean Scaled Width* and *Mean Scaled Length*, are useful to discriminate gamma-ray events from the background due to cosmic-ray events. These mean scaled parameters (MSPs) are obtained using the single-telescope image parameters *Width* and *Length*, and using simulation-based lookup tables to provide the expected values of the parameters depending on the impact parameter and the *Size* of the image. The lookup tables used in estimation of the MSPs are generated corresponding to five dimensions of observing conditions: the zenith angle and azimuth angle of the observation, the offset distance of the source location from the pointing direction, the NSB noise level for the sky region in the field of view (FOV) and the telescope ID, as explained in Section 6.5.6. The definition of a MSP used in this analysis follows the prescription found in [131] and is given by:

$$MSP = \frac{1}{N_{tel}} \sum_{i=1}^{N_{tel}} \frac{p_i}{\bar{p}_{sim}(Size, r)} \tag{6.7}$$

where p_i is the parameter to be scaled (*Width* or *Length*) for telescope i and $\bar{p}_{sim}(Size, r)$ is the mean value of that parameter corresponding to the impact distance, r and image size,*Size*, of the event obtained from the appropriate lookup table for the observing state of the event. A similar definition for the calculation of the MSPs, as in [132], has been studied and found to yield comparable performance.

In Figure 6.12, the MSW and MSL parameter distributions are shown for gamma rays obtained from simulations of the 4-telescope VERITAS array and from the excess events of the 4-telescope Crab data set. The same distributions are also shown for the background events obtained from the same Crab data set for comparison. A clear difference in the shape of these distributions between the

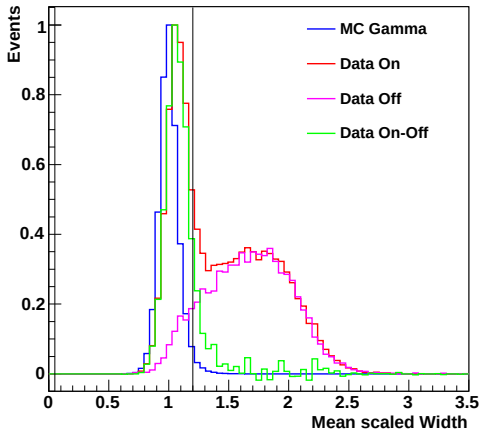

(a)

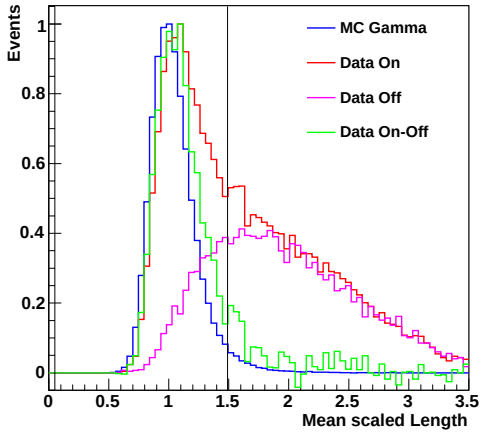

(b)

Figure 6.12: The MSW and MSL distributions are shown in (a) and (b), respectively, for simulations of gamma rays (blue), for the events identified as gamma rays from the direction of Crab (On, red), as background (Off, pink) and as the excess gamma rays from the direction of the Crab (On−Off, green) in the 4-telescope Crab data set. See Section 6.8 for the selection of On and Off events. The vertical lines show the value of the cut used on the corresponding parameter to separate the gamma-ray events from the background events. See text for further discussion.

gamma-ray and background events is evident, and this difference is exploited to distinguish between gamma-ray and background events in the data. Additionally, these figures show that the simulations of gamma rays and data reasonably match each other.

6.5.5 Energy Reconstruction

An energy is estimated for each telescope image that passes the image quality selection using the energy lookup tables (Section 6.5.6) similar to those used for the determination of the scaled image parameters. The energy of the primary particle, the shower, is calculated as the average of all individual telescope image energy estimates weighted by their $Size$. Figure 6.13 shows an example of the lookup table for the Energy of an image in Telescope 2 for an event at 20° zenith, 180° azimuth angle and a pedvar value of 6.43dc corresponding to a sky noise level of 200 photo-electrons/ns/m^2/sr. For each bin in impact distance and log(Size), the color scale shows the estimated log(Energy(GeV)) for the image.

The fractional error in the reconstructed energy can be calculated for simulated events using the following definition:

$$\Delta_E = \frac{E_{Rec} - E_{True}}{E_{True}} \tag{6.8}$$

where E_{True} is the true energy and E_{Rec} reconstructed energy for the simulation event.

The energy bias, (ε_{Bias}), is defined as the mean value of the fractional error in the reconstructed energy. This quantity is useful to define a safe energy range, in which the energy estimation can be trusted. Reconstruction of the energy spectrum from a source is performed over the safe energy range. Further discussion of the determination of the safe energy range is given in Section 7.2.

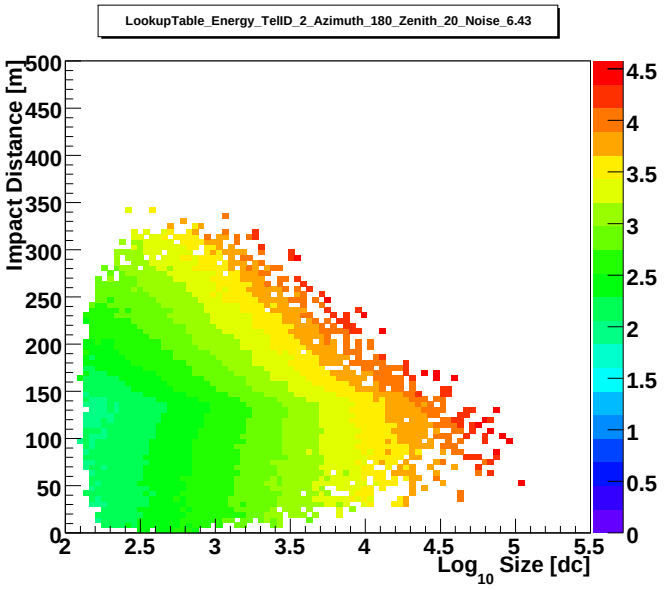

Figure 6.13: Graphical representation of the data in the lookup table which is used to estimate the energy of an image on Telescope 2, using the impact distance and the size of the event for a noise (pedvar) level of 6.43 dc and an observation direction of Zenith=20°, Azimuth=180°. The color scale gives the estimated log(Energy(GeV)) at each bin.

The energy bias as a function of the true energy for four zenith angles and for a source at 0.5° offset from the pointing direction is shown in Figure 6.14. The energy bias is positive and gets larger for lower energies close to the threshold, due to a selection effect where events with energies reconstructed too high are selected. The bias is negative and its absolute value gets larger for higher energies, because the images of high energy events are truncated at the edge of the camera FOV, and thus their energies are reconstructed lower than their true energies.

The width of the Δ_E distribution gives the energy resolution of the detector. The energy resolution defines the minimum energy bin width of any resolvable energy structure, therefore, it is taken into account in the selection of the optimum

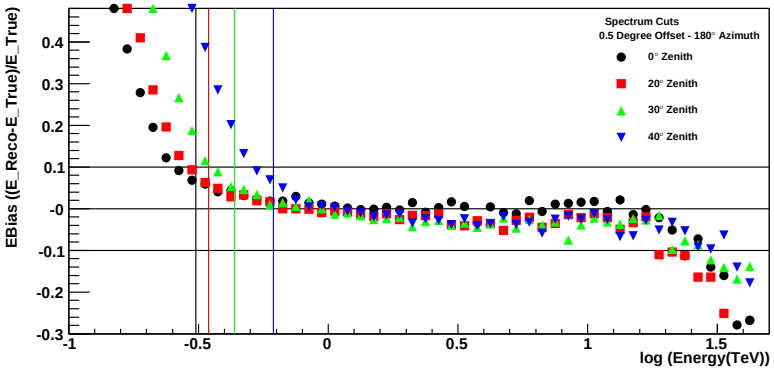

Figure 6.14: The energy bias is shown for the full 4-telescope array of VERITAS as a function of the simulated true energy for zenith angles 0° (circles), 20° (squares), 30° (triangles) and 40° (inverted triangles), obtained from simulations analyzed with the standard cuts. The vertical lines show the lower edge of the safe energy range for each zenith angle above which the energy bias is less than 0.10.

binning for spectral analysis (Section 7.2).

Figure 6.15 gives the energy resolution of VERITAS obtained from gamma-ray simulations of a source at 20° zenith angle. The energy resolution depends on the energy. In order to avoid the effect of the energy bias, the events in Figure 6.15 are selected above 0.340 TeV for which the bias is less than 0.10. The width of the fitted Gaussian distribution is 19%.

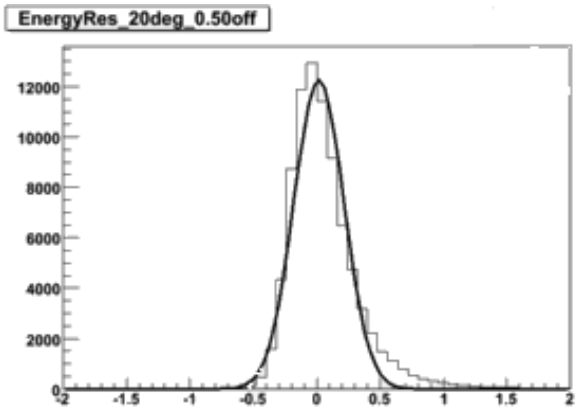

Figure 6.15: The distribution of the relative error in the reconstructed energy is given for simulations of the 4-telescope VERITAS array observations of gamma-ray events with energy above 0.340 TeV at 20° zenith angle. The width of the fitted Gaussian distribution gives the energy resolution as 19%.

6.5.6 Lookup Tables

In order to estimate the value of the image parameters *Width*, *Length* and *Energy*, used in calculation of the shower parameters, MSL, MSW and the shower energy, discussed in the previous sections, lookup tables for the image parameters are generated using detailed simulations of gamma-ray showers and the detector response (Section 5.5). Each lookup table contains the estimate of

an image parameter as a function of the logarithm of the image *Size* and the impact parameter (which is the distance from the shower core to the telescope). The tables are filled with the true impact parameter of the simulated shower, and for the analysis of the real data, the reconstructed impact parameter is used to find the parameter of interest from the table.

For each image parameter to be estimated, separate lookup tables are generated in five different dimensions corresponding to the five observing parameters of the event: the zenith angle and the azimuth angle, the offset distance of the source from the pointing direction, the ID of the telescope and the NSB noise level. In any dimension, if a lookup table is not available for a given value of the observing parameter, the program interpolates between the two closest lookup tables to obtain the estimate of the parameter in question. The interpolation is linear in noise, in offset distance, and in cos(Zenith Angle) of the event. No interpolation is done for the azimuth angle of the event, but the azimuth=0° lookup table is used for event azimuth angles in the range of -90° to 90° and azimuth=180° lookup table is used for event azimuth angles in the range of 90° to 270°. Clearly, no interpolation is needed for the telescope ID.

For each parameter to be estimated, 343 lookup tables are generated for seven zenith angles between 0° and 45°, for seven source offsets from the pointing direction between 0° and 1.75°, and for seven noise levels from 100 to 400 pe/ns/m^2/sr which cover the range of sky noise from extra-galactic observations to moderate moonlight.

6.6 Gamma Hadron Separation

A set of cuts based on the shape and orientation of the shower is used to select gamma-ray-like events pointing back to the source and to reject the events due to cosmic rays. The cuts used in the standard analysis are based on the *mean scaled Length*, the *mean scaled Width*, and θ^2. The accepted ranges of those parameters in the selection criteria to classify an event as gamma-ray-like are listed in Table 6.3.

	Gamma-Hadron Separation		
Cuts	θ^2	MSW	MSL
Std	< 0.025	[0.05, 1.2]	[0.05, 1.49]

Table 6.3: The cuts used to select the gamma-ray events are listed in the table. The various quantities are defined in the text.

This standard set of cuts is chosen to minimize the value of the ratio R_{bg}/R_{γ}^2 for the 4-telescope Crab data set, where R_{bg} is the rate of background events and R_{γ} is the rate of gamma-ray events from the source. This ratio is proportional to the time required to detect a certain flux level from a source at a selected significance level. This method of optimization is most suitable to find cuts that give the highest sensitivity of the detector to detect weak sources.

The optimization to get the highest sensitivity of the array tends to favor the inclusion of higher energy events and the exclusion of lower energy events, since the selection criteria are more efficient at higher energies. Therefore, for the analysis of a target expected to have low energy emission, such as the pulsed emission, the cuts selected with this method may not be suitable because they are too restrictive. See the Section 6.10, where the timing analysis for the search

of pulsed emission is discussed for which a more relaxed cut set is used.

6.7 Background Estimation

The level of contamination of gamma-ray-like cosmic-ray events reconstructed in the region of the source must be estimated. The number of excess events above this background level can then be used to calculate the statistical significance of the detection of gamma-ray emission and can be used to estimate the gamma-ray flux from the source. Two different methods of background estimation, as discussed in [132], are used and compared for consistency: the *reflected background region model* and the *ring background region model*.

6.7.1 Reflected Background Region Model

Assuming that the cosmic ray distribution across the field of view is azimuthally symmetric around the center of the FOV, the background event level in the region of the source can be obtained from a similar region at a symmetric location with respect to the center of the field of view. In order to benefit from greater statistics, it is also possible to estimate the background from multiple regions located at equal distances from the center. These regions are located as far as possible from the source location so as to minimize possible gamma-ray contamination (See Figure 6.16(a)). Similarly, the background regions overlapping with similar sized regions around bright stars in the FOV are excluded from the analysis to avoid the bias introduced by the stars. The reflected background region estimation model is not applicable to a source at the center of the FOV and is most suitable for point-like or limited-extension sources observed in wobble observing mode (Section 4.7). Since the background estimate is derived from the events in the

same run, systematic effects due to variations in weather or detector performance are reduced. However, it should be noted that this method is subject to possible systematic effects resulting from camera or field of view inhomogeneities.

6.7.2 Ring Background Region Model

With the ring region background estimation model, there is no restriction on the observing mode, and it is especially useful in survey analysis when the source position and extension are not *a priori* known. The background estimate is derived for any trial source position from an annulus around the source region (See Figure 6.16(b)) having an inner radius chosen large enough to eliminate any gamma-ray contamination from the putative source. Since the ring covers points that have different offsets with respect to the center of the camera compared to the source position, a relative event rate, or *acceptance*, correction has to be applied to normalize each background count. Additionally, any part of the ring that overlaps a previously known gamma-ray source or a bright star needs to be excluded from the background estimate.

6.8 Source Detection

In order to find out whether an object being observed is a source of gamma rays, one needs to determine the excess gamma-ray events above the level of background coming from the source direction. Then, one determines the significance of the excess compared to the background level.

In calculating the gamma-ray event excess, the first step is to select candidate gamma-ray events by applying the shape cuts (MSW/L cuts), as explained in Section 6.6. Among these events, those with orientations consistent with the

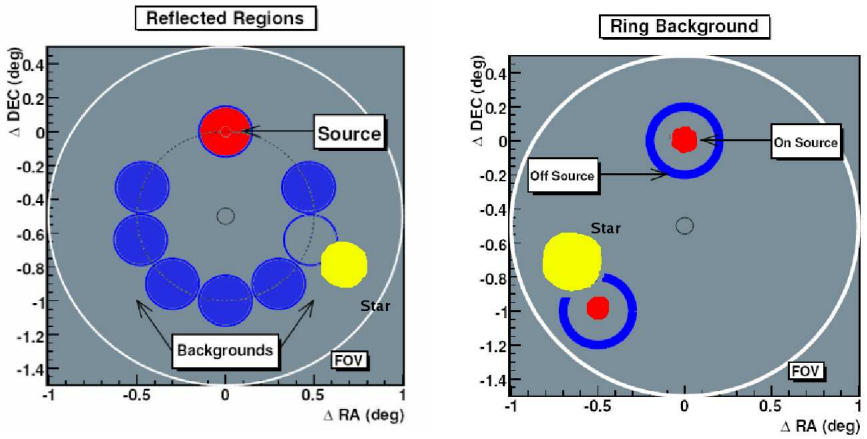

(a) (b)

Figure 6.16: (a) The location of the source and background regions on the sky for the *reflected background region* model (Section 6.7.1). The small circle in the center is the direction to where the telescopes point and the red circle is the source region, located at an offset from the pointing position. The blue circles are the background regions located at the same offset as the source region from the pointing position. The yellow circle is the exclusion region around a star, and the overlapping background region shown with an empty blue circle is not used in the background estimation. The white circle shows the FOV of the camera. (b) The location of the source and background regions for the *ring background region* model (Section 6.7.2). For this model, the source position may not be known *a priori*. For every point in the FOV, the source events are integrated from the small circular region around that point (red circle in the figure) and the background events are integrated from the annulus around it (blue annulus). A second trial source position is also shown. The part of the annulus overlapping with the yellow exclusion region of a bright star is not used for background estimation of the corresponding trial point at the center. The trial point which gives the highest significance of detection determines the source position. (Images are from [11]).

source location in the sky (within a region of size θ^2) are classified as N_{ON} events. The next step is to estimate the gamma-ray event contamination in that region due to background events, N_{OFF}. N_{OFF} are the number of events reconstructed within the various background regions as determined by either of the models explained in previous section. The background estimation model also provides the normalization of the source to background events, α. Essentially, α is the ratio of the effective exposure integrated in observing time and area of the source region to that of the background regions. Once these parameters are known, the excess number of events are given as:

$$N_{Excess\gamma} = N_{ON} - \alpha N_{OFF} \tag{6.9}$$

The normalization parameter α depends on the observing mode and background estimation model. For the pairs mode, the observed source (ON) and background (OFF) regions are at identical positions in the FOV, but separated in time. Thus, α is the ratio of the total time spent observing the on and off regions:

$$\alpha_{pairs} = \frac{\mathrm{T_{ON}}}{\mathrm{T_{OFF}}}$$

In the reflected and ring background estimation models, the background regions and the source region do not coincide in position in the camera, and α depends on the "acceptance" of the camera. The acceptance of a point in the camera is the relative number of candidate gamma-ray events detected at that point compared to the total number of events detected. To first order, the acceptance of the camera is a function only of the radial distance from the center of the camera, i.e. it is azimuthally symmetric. In the reflected background model, all background regions are located equidistantly from the center of the camera, and therefore, the exposure of a background region is identical to the source region.

Thus, α is simply the inverse of the number of background regions, N:

$$\alpha_{Reflected} = \frac{1}{N}$$

However, for the ring background model where the background region is an annulus around the source position, the acceptance of the camera is not uniform across the background ring. Thus, the acceptance must be calculated for every point in the camera (see Figure 7.3(c) for a 2D map of acceptance), and α is the ratio of the integrated acceptance of the source region to the integrated acceptance of the background region:

$$\alpha_{RBM} = \frac{\int_{\text{source}} \epsilon(r)\text{dA}}{\int_{\text{bg ring}} \epsilon(r)\text{dA}}$$

where $\epsilon(r)$ is the acceptance of a point at position r in the camera and dA is the area element in the camera plane.

Once N_{ON}, N_{OFF} and α are determined, the significance of the excess events is given by the Equation 6.10 [133]:

$$\sigma_{detection} = \sqrt{2}\left\{ N_{ON}\, ln\left[\frac{1+\alpha}{\alpha}\left(\frac{N_{ON}}{N_{ON}+N_{OFF}}\right)\right] + \right.$$
$$\left. +N_{OFF}\, ln\left[(1+\alpha)\left(\frac{N_{OFF}}{N_{ON}+N_{OFF}}\right)\right]\right\}^{1/2} \quad (6.10)$$

Using the same information, the gamma-ray rate from the source, R_γ, is calculated as:

$$R_\gamma = \frac{N_{ON} - \alpha N_{OFF}}{\text{T}} \pm \frac{\sqrt{N_{ON} + \alpha^2 N_{OFF}}}{\text{T}} \quad (6.11)$$

where T is the total observing time, corrected for the dead-time.

6.9 Spectrum Reconstruction

Reconstruction of the gamma-ray flux from a source is a two step process. First, the energies of each candidate gamma-ray event coming from the source (ON) and background (OFF) regions are reconstructed. The energy reconstruction is explained in Section 6.5.5. Then, the events from the ON and OFF regions are binned in energy separately. The minimum width of the energy bins is selected by the energy resolution of VERITAS, given in Section 6.5.5.

In the next step, the differential flux in each energy bin, E_i, is calculated using the formula:

$$\frac{dN}{dE}(E_i) = \frac{1}{\Delta t \Delta E_i} \left\{ \sum_{j=1}^{N_{ON,i}} \frac{1}{A'_{eff}(E_j, \theta_j)} - \alpha \sum_{k=1}^{N_{OFF,i}} \frac{1}{A'_{eff}(E_k, \theta_k)} \right\} \tag{6.12}$$

where Δt is the total live time and ΔE_i is the width of the i'th energy bin. The first sum is for all gamma-ray events detected from the ON region with energies in energy bin i, and the second sum is for all gamma-ray events detected from the OFF region with energies in energy bin i, normalized by the acceptance factor α. $E_{j,(k)}$ are the reconstructed energies of events j, (k), and $\theta_{j,(k)}$ is the zenith angle of the source when events j, (k) are recorded. The term $A'_{eff}(E_j, \theta_j)$ is the effective area of the detector, for an event with energy E_j and zenith angle θ_j, which includes the acceptance and the finite energy resolution of the detector.

The effective area of the detector representing the detector acceptance is calculated from simulations as follows: a number of gamma-ray events, $N_0(E, \theta)$, are simulated according to a given spectral energy distribution and are randomly distributed to arrive into a sufficiently large area, $A_0(E)$ around the detector. The number of events that trigger the detector and survive the reconstruction and event selection cuts, $N_{tr}(E, \theta)$, is recorded. The effective area of the detector

for an event of zenith angle θ and energy E is given as:

$$A_{eff}(E,\theta) = \frac{N_{tr}(E,\theta)}{N_0(E,\theta)} A_0(E) \tag{6.13}$$

The finite energy resolution of the instrument is taken into account in Equation 6.12 by using a modified effective area, A'_{eff}, which includes the response function of the energy reconstruction, the energy resolution function (Figure 6.15). Its value depends on the assumed spectrum since the collection area has to be averaged over a finite energy bin width and the effects of the energy resolution will lead to spill-overs where events will migrate from one energy bin to another. In practice, the A'_{eff} is computed using Equation 6.13, weighting the events according to an incident power law spectrum with a differential spectral index β and using the reconstructed energy, E_{recon}, instead of the true simulated energy, E_{true}. In order to avoid an iterative calculation of the modified effective area, the energy spectrum of the simulated events should roughly match the energy spectrum of the source in consideration. Fortunately, due to the relatively good energy resolution of achieved by VERITAS ($\sim$20%), A'_{eff} depends only slightly on the assumed differential spectra index.

For this analysis, the simulated events are distributed assuming a power law with a spectral index β of 2.45 which is reasonably consistent with previous measurements of the Crab Nebula.

Similar to the lookup tables generated for the event reconstruction, the effective area is parameterized by four different event parameters: the zenith angle and the azimuth angle of the source, the offset distance of the source from the pointing direction and the average noise present. Effective areas are generated for seven zenith angles between 0° and 45°, two azimuthal directions between 0° and 180°, nine offset distances between 0.0° and 2.0°, and seven different NSB noise levels between 100 and 400 photo-electrons/ns/m^2/sr. If in any dimension

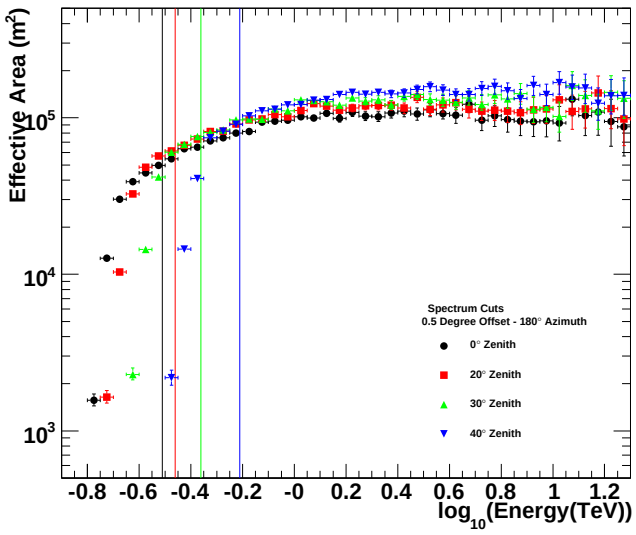

Figure 6.17: The effective areas of the VERITAS instrument are shown as a function of the reconstructed energy for zenith angles of 0°, 20°, 30° and 40°, obtained from simulations of the 4-telescope array. The vertical lines show the safe energy thresholds for the spectral analysis as defined in the text.

an effective area curve is not available for a given value of the event parameter, the program interpolates between the two closest curves to obtain the effective area. The interpolation for the effective area in the gamma-ray energy is linear in log(E).

The effective area of VERITAS as a function of E_{recon} for a source at four different zenith angles, calculated using the cuts listed in Table 6.3, is shown in Figure 7.6, for a source in the south direction, 90° < azimuth < 270°, and at a 0.5° offset distance from the pointing position, for an average noise level of 200 photo-electrons/ns/m^2/sr.

This simple unfolding method to determine the energy spectrum does not

correct for the energy bias, shown in Figure 6.18(a). In order to avoid the adverse effects of the bias, it is necessary to define a safe energy range, as in [132]. The lower limit of this energy range, the safe threshold energy, is defined as the energy 10% higher than the energy of the lowest bin in the bias histogram for which the bias is less than 10%. The safe threshold energy calculated from the energy bias curve (Figure 6.14) for each zenith angle is shown by the vertical lines in Figure 7.6. Table 7.2 lists the safe thresholds for each zenith angle. The upper end of the safe energy range can be defined in a similar way using the highest energy bin with a bias less than 10%. In most cases, the highest energy is limited by statistics and defined by the requirement of at least 2σ detection in each bin.

6.10 The Timing Analysis

To search for pulsations in the data, a timing analysis is performed on the detected gamma-ray-like events. In order to select the gamma-ray-like events from the direction of the source, the standard analysis is applied to the data. Since the pulsed signal from the Crab Pulsar is expected to concentrate in the lowest possible energy region to which VERITAS is sensitive, i.e. below 100 GeV, a set of relaxed cuts is used to retain the low energy events in the data. The cuts used for this specific analysis are discussed in Section 6.10.1. In the timing analysis, the event arrival times are the primary information. These times need to be converted to the pulsar rotation phase relative to a known reference phase. This calculation is known as epoch folding and it is explained in Section 6.10.2. In the process, the event arrival times are transformed to the time at the barycenter of the Solar System to account for the motion of the Earth, as explained in Section 6.10.3. Finally the detected events are plotted with respect to the pulsar phase to obtain the pulse profile from the data (Section 6.18(a)). This pulse

profile is used to search for any periodic excesses to determine the existence of a pulsed signal from the source.

6.10.1 Event Selection Criteria

As discussed in Chapter 2, the pulsed emission from the Crab is expected to be in an energy region lower than 100 GeV, which is at the lowest edge of the energy range VERITAS is sensitive to. Therefore, it is important to retain throughout the analysis the events with as low as energy as possible. Since the detector sensitivity increases at higher energies, the standard analysis cuts listed in Table 6.2, especially the *Size* cut, remove most of those events. Hence, it is necessary to relax (or remove) the *Size* cut to retain low energy events. Moreover, the timing analysis contains a very efficient cut, the *phase* of the event, to distinguish between a random cosmic-ray event and a gamma-ray event emitted from the pulsar at the specific phases that pulsed emission is expected. At low energies, the shape cuts, MSW and MSL, are not effective in discriminating between gamma-ray and cosmic-ray events. Therefore, to retain low energy events, we do not apply shape cuts on mean scaled parameters and only a direction cut on θ^2 is applied. The angular resolution of the detector degrades for lower energy events, and thus a wider θ^2 cut is required. The cuts listed in Table 6.4 are utilized to select the candidate gamma-ray events to use in the timing analysis. The use of these relaxed cuts is found to increase the candidate gamma-ray events by a factor of ~ 30 compared to using the cuts of the standard analysis.

6.10.2 Epoch Folding

Once the gamma-ray-like events from the direction of the source are identified, the periodicity in the data can be tested with a variety of methods. For data

	Event Quality Selection			Gamma-Hadron Separation		
Cuts	Size	N_{Pixels}	Dist	θ^2	MSW	MSL
Plsr	> 0 dc	≥ 5	[0.0 °, 1.43°]	< 0.04	No cut	No cut

Table 6.4: The cuts used to select the gamma-ray events for the timing analysis are listed in the table. The event selection parameters are defined in Section 6.4 and the gamma-hadron separation parameters are defined in Section 6.5.

with low signal-to-noise ratio or for unevenly sampled data, the epoch folding technique is the most suitable method since it permits combining data taken over large periods of time. In the epoch folding method, the arrival time of each event is converted to a relative rotational phase of the pulsar using a reference phase determined from observations made at other wavelengths. Then, it is possible to combine all the data in phase, irrespective to the temporal separations among them.

If the frequency, f, or the period P of a pulsar is known, the relative rotational phase, ϕ, corresponding to an event arrival time T, relative to a reference time T_0, can be calculated as follows. Most pulsars slow down, as explained in Chapter 2; accordingly, a time dependent frequency and period, f(T) and P(T), are used in the calculations:

$$\phi(T) - \phi(T_0) = \int_{T_0}^{T} \frac{dT}{P(T)} = \int_{T_0}^{T} f(T)\, dT \tag{6.14}$$

The time dependent frequency of a pulsar can be approximated by its Taylor series around a reference time, T_0:

$$f(T) = f(T_0) + \dot{f}(T_0)(T - T_0) + \frac{1}{2}\ddot{f}(T_0)(T - T_0)^2 + ... \tag{6.15}$$

The Crab pulsar frequency (on 15 June 2008) is 29.747 Hz and its frequency derivative is $3.720 \times 10^{-10} s^{-2}$ [134]. Since the frequency derivative is very small

compared to the frequency, it is clear that the terms above the first order can be neglected for time differences on the order of a month, i.e. for $\sim 2.5 \times 10^6$s.

Thus, the phase of a pulsar corresponding to an event arrival time T can be obtained by combining the last two equations:

$$\phi(T) = \phi(T_0) + f(T_0)(T - T_0) + \frac{1}{2}\dot{f}(T_0)(T - T_0)^2 \tag{6.16}$$

In order to calculate the phase using Equation 6.16, T_0, the precise emission time of a particular pulse with a known corresponding phase is required. Generally the reference time, T_0, is taken as the mean arrival time at the Solar System Barycenter (SSB) of a particular radio pulse. For this use, the Jodrell Bank radio observatory [134, 135] publish the arrival times of the first radio pulse corresponding to the main peak in the pulse profile ($\phi(T_0) = 0$) to arrive after midnight on the 15th day of each month, along with the calculated frequency of the Crab Pulsar and its frequency derivative at this time.

Due to the Earth's movement around the Sun, the event arrival time T at the detector and the reference time T_0 at the SSB are not comparable times. Instead, the event arrival time T at the detector must be converted to the time at the SSB to correct for the time of flight difference of a photon from the pulsar to VERITAS relative to the SSB. Furthermore, the time systems giving the time at the detector and at the SSB should be the same. Corrections for these effects are known as the barycentering corrections explained in the next section.

6.10.3 Barycentering

The barycentering correction that needs to be applied on the event arrival times has two stages. The first is to convert between the time systems of the arrival times of gamma-ray events and the reference pulse, and the second is to account

for the time-of-flight difference a photon experiences due to the distance between the observatory and the SSB.

The event arrival times at the detector are measured in Coordinated Universal Time (UTC), but the reference times, T_0, are given in Barycentric Dynamical Time (TBD) at the SSB. To convert between these time systems, the following time definitions are used:

UTC (Universal Time, Coordinated): This is the time displayed by the GPS clocks and the event arrival times at the detector are measured in this time system. It is the mean solar time at the Royal Observatory, Greenwich. Most UTC days contain exactly 86,400 seconds. However, since the mean solar day is slightly longer than 86,400 seconds, every so often an extra "leap second" is added on the last day of a year to account for the total extra length of all the mean solar days since the previous leap second. UTC is derived from International Atomic Time (TAI). From 1972 onwards UTC ticks at the same rate as TAI, with a difference of leap seconds.

TAI (Temps Atomique International): TAI is a high-precision atomic time standard that measures proper time on Earth, and it is the primary terrestial time standard. It is a weighted average of the time measured by various atomic clocks around the world. TAI differs from the UTC by the leap seconds since 1972, in addition to 10 seconds initial difference at the start of 1972. As of Feb 2007 when the Crab optical pulsar data are taken, the difference, UTC - TAI, is +33 seconds and the next leap second is scheduled to be added on December 31st, 2008.

T(D)T (Terrestial -Dynamical- Time): TT is the modern astronomical standard for the time on the surface of the Earth. TT is a theoretical ideal; its measurement is approximated by the International Atomic Time (TAI) + 32.184

seconds. In 1991, its name was redefined by removing "Dynamical" from it.

TBD (Barycentric Dynamical Time): TBD is the same time system as TT, except for the relativistic corrections to move the origin to the SSB. This correction takes account of the time dilation when calculating orbits of planets in the Solar system. The correction between TT and TBD amounts to as much as $\sim \pm 1.6$ ms and it is periodic in time with an average of zero. This time system is used for calculating the planetary motions and to calculate the position of Earth with respect to the SSB for the barycentering time-of-flight corrections explained next. The arrival time of the reference radio pulse from the Crab pulsar is also given in this time system by the Jodrell Bank Observatory.

Using these definitions, the barycentering correction due to the time system transformation is given as:

$$T_{TBD} = T_{UTC} + \Delta_{TAI-UTC} + \Delta_{TT-TAI} + \Delta_{TBD-TT} \tag{6.17}$$

As of February 2007, this correction amounts to:

$$\begin{aligned} T_{TBD} &= T_{UTC} + 33.000\,000s + 32.184\,000s + (-0.000\,435)s \qquad (6.18) \\ &= T_{UTC} + 65.184\,435s \end{aligned}$$

$$(6.19)$$

The second component to the barycentering correction is the time-of-flight correction. The acceleration of isolated pulsars, such as the Crab, relative to the SSB is sufficiently small that in calculating the phase of the pulsar rotation from the event arrival times, the SSB can be assumed to be in an inertial frame. The movement of the Earth, on the other hand, introduces time-of-flight delays similar to the Doppler shift between the photons from the pulsar depending on the Earth's relative position at the time of detection (Figure 6.18). This Doppler-like

shifts between the event arrival times are corrected for by converting the event arrival times at the detector to arrival times at the SSB.

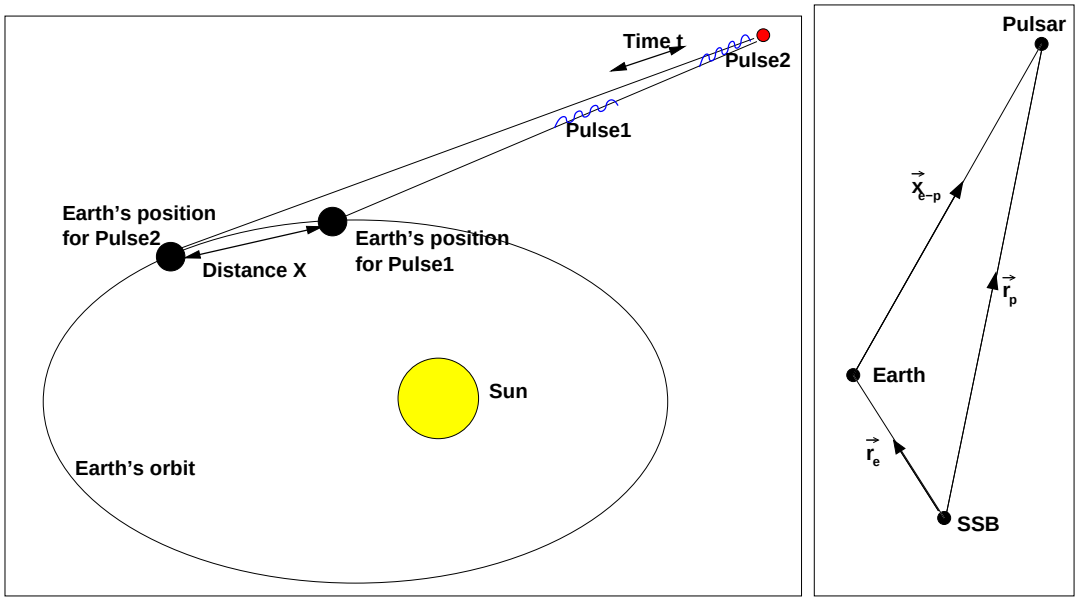

(a) (b)

Figure 6.18: (a) The figure shows the additional distance X a pulse coming some time t later than than another pulse needs to travel due to the Earth's movement around the Sun. (b) The geometry of Equation 6.21 is illustrated. See the text for details.

The time of flight corrections can be divided into two parts: the correction for the distance between the SSB and the Earth's center and the correction for the distance between the Earth's center and the VERITAS location. The former is the major contribution to the barycentering correction. The time delay introduced in the photon arrival time between the SSB and the center of the Earth can be calculated using the schema in Figure 6.18(b). As shown, $\vec{r_p}$ is the distance vector from the SSB to the pulsar, $\vec{r_e}$ is the distance vector from the SSB to the Earth-center, and $\vec{x}_{e-p}$ is the distance vector from the Earth-center to the

pulsar. It should be noted that the schema is not drawn to scale and $r_e \ll r_p$. With this relation, one can approximate that the vectors $\vec{r_p}$ and $\vec{x}_{e-p}$ are parallel. Therefore, one can write the path length difference as a regular subtraction and neglect the terms in $O\left(\left(\frac{r_e}{r_p}\right)^2\right)$:

$$\begin{aligned}
\Delta r &\equiv r_p - x_{e-p} \\
&= r_p - \sqrt{r_p^2 - 2\vec{r}_p \cdot \vec{r}_e + r_e^2} \\
&\simeq r_p - r_p \left\{ 1 - \frac{1}{2} \left[2(\hat{r}_p \cdot \hat{r}_e)\frac{r_e}{r_p} + \left(\frac{r_e}{r_p}\right)^2 \right] + O\left(\left(\frac{r_e}{r_p}\right)^2\right) \right\} \\
&\simeq (\hat{r}_p \cdot \hat{r}_e) r_e \qquad (6.20)
\end{aligned}$$

$$(6.21)$$

With this approximation on the path length difference, the resulting time-of-flight delay is given by:

$$\Delta_{SSB \to Earth} = \frac{\Delta r}{c} \simeq \frac{\hat{r}_p \cdot \vec{r}_e}{c} \qquad (6.22)$$

The position of the Earth-center relative to the SSB, $\vec{r_e}$ in Equation 6.22, at the event arrival time, T_{TBD}, in the TBD system is obtained from the JPL DE200 Planetary and Lunar Ephemeris [136, 137]. Using the Crab pulsar position, RA:$05^h\ 34^m\ 31^s.973$ and Dec:$22°00^m52^s.061$ in J2000.0 coordinates, to calculate $\hat{r}_p$, one can obtain the $\Delta_{SSB \to Earth}$ which can be as large as 500 s for the position of Earth on its orbit around the Sun where it is farthest from the Pulsar.

The second part of the time-of-flight correction is due to the distance between the Earth-center and the position of the observatory on the Earth surface. This correction requires the geocentric coordinates of the observatory (x,y,z) and the zenith angle of the pulsar at the time of the observation, and it is given by:

$$\Delta_{Observatory \to Earth} = \frac{1}{c} r_0 cos(Z) \qquad (6.23)$$

where r_0 is the distance from the observatory to the Earth-center and Z is the

zenith angle of the source. r_0 is found by measuring the observatory's geodetic coordinates (Longitude, Latitude, Altitude) with a GPS receiver and converting to the geocentric coordinates using the SlaLib routine slaGeoc (v2.4-0,[138]).

To summarize in one equation the total barycentering correction to the event arrival times is given as:

$$T_{TBD}@SSB = T_{UTC} + \Delta_{TAI-UTC} + \Delta_{TT-TAI} + \Delta_{TBD-TT} + \\ + \Delta_{Observatory \rightarrow Earth} + \Delta_{Earth \rightarrow SSB} \quad (6.24)$$

6.10.4 Pulse Profile

The pulse profile is simply a histogram of the pulsar rotation phase calculated for each detected event. In order to reconstruct the pulse profile, each event arrival time at the detector in the UTC system, T_{UTC}, is converted to an arrival time at the SSB in the TBD time system, $T_{TBD}@SSB$, using the barycentering correction in Equation 6.24. The closest reference time T_0 to the event arrival time at the SSB is chosen from the Crab ephemeris data published by Jodrell Bank observatory [134]. The pulsar phase corresponding to the corrected event arrival time is calculated using Equation 6.16. The calculated phase for each event is histogrammed. This histogram is called as the phaseogram, or the pulse profile of the pulsar.

Using the pulse profile of the pulsar in other wavelengths, one can define phase ranges where periodic excess is expected in the gamma-ray energy range. Any pulsed signal excess is searched for in these phase regions and the background level, which is usually the steady emission from the surrounding nebula, is taken from the remaining phase range. The pulse profile of the Crab Pulsar as detected by EGRET for energies above 100 MeV is shown in Figure 6.19. The phase regions

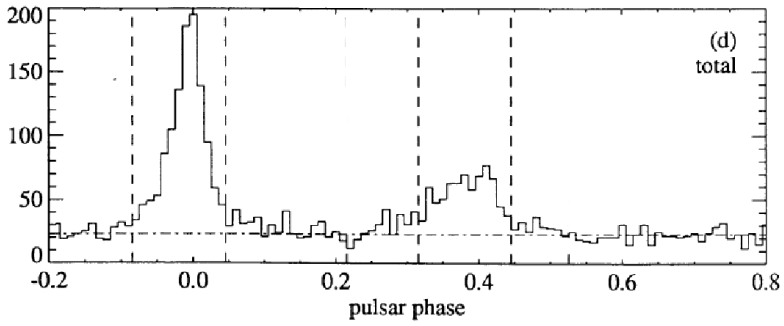

Figure 6.19: The pulse profile of the Crab Pulsar as detected by EGRET above 100 MeV is shown. The peak gamma-ray pulsed emission regions, between the phases [-0.08, 0.05] and [0.32,0.45], are shown with the dashed lines around the two peaks.

around the main peak and the inter-peak, between the phases [-0.08, 0.05] and [0.32,0.45], respectively, are chosen as the pulsed signal region. The background level to the pulsed signal, which is the steady emission from the Crab Nebula, is estimated from the rest of the phase regions.

CHAPTER 7

Results

7.1 Detection of the Crab Nebula

The three data sets, 2T, 3T, and 4T, collected during the Crab observations during the 2-, 3- and 4-telescope operation phases of VERITAS were analyzed separately to calculate the detection level of the Crab Nebula by VERITAS. First, the analysis procedures discussed in Sections 6.2 to 6.6 were performed on the data and the candidate gamma-ray events in each data set were selected using the standard event selection and gamma/hadron separation cuts. The event selection (Section 6.5.1) is based on the image parameters, $Size$, N_{Pixels} and $Distance$, which are defined in Section 6.4. The gamma/hadron separation (Section 6.6) depends on the shape parameters of shower, MSW and MSL, the calculation of which are explained in Section 6.5. The directional cut θ^2 is used to define the size of the source and the background regions used in estimating the number of gamma rays due to the source or the background. The acceptable regions of these cuts are listed in Tables 6.2 and 6.3.

Second, the candidate gamma-ray events due to the source, "On" events, and due to the background, "Off" events, were determined using two independent analyses corresponding to two different background estimation models: the reflected background region model and the ring background region model (Section 6.7). In the last step, the significance of the excess gamma-ray events from the

direction of the Crab Nebula was calculated separately for three data sets.

The Crab Nebula was strongly detected during all operation phases. The detection level is consistent using either of the background estimation models. In the following subsections the detection results using both background estimation models are discussed, and they are summarized in Table 7.1.

7.1.1 One-Dimensional Analysis

In order to estimate the background level from the direction of the Crab Nebula using the reflected background region model, a source region and background regions with a radius of 0.158°, corresponding to a cut (of 0.025) in the θ^2 parameter in Table 6.3, were used. The locations of the background regions were determined as described in Section 6.7.1. The regions around the bright stars were excluded to avoid their effect in the background estimation; as a result, three to five background regions were used depending on the location of the star Zeta-Tau during each observing run in the data set.

In Figure 7.1, the number of gamma rays detected within each annulus of width $\delta\theta$ around the position of the Crab Nebula, along with the average number of gamma rays detected from the background regions is plotted as a function of the square of the radius of the annulus. The square of the angular distance is used so that each bin corresponds to a constant solid angle on the sky. The total number of counts to the left of any value of θ^2 on the plot represents the integrated number of gamma rays inside a circular region of radius θ. In the figure, the red curves show the distribution of the candidate gamma-ray events selected by the shape cuts (MSW/L) in the "On" region. The blue curves represent the normalized distribution of candidate gamma-ray events selected by the shape cuts in the "Off" region. The definition of the "On" and "Off" regions according to

the reflected background region model are given in Section 6.7.1. The vertical lines show the size of the source and background regions. The excess gamma-ray events from the direction of the Crab Nebula is evident in the plots shown for data from 2-, 3- and 4-telescope operations. The significance of the gamma-ray event excess and the corresponding gamma-ray rate from the Crab Nebula, obtained using the reflected background region model for each phase of VERITAS is shown in Table 7.1.

7.1.2 Two-Dimensional Analysis

In order to check the consistency of the detection level with a different background estimation model, the background level around the Crab Nebula was also estimated using the ring background region model (Section 6.7.2) for each data set. As a first step, the distributions of the directions of all candidate gamma-ray events selected by the shape cuts were plotted on a two-dimensional (2D) sky map in the FOV. Such a distribution for the 4-telescope data set is plotted on a 2D map centered on the position of the Crab Nebula in Figure 7.2.

A search region size of 0.158° was used as the source region for each trial point in the FOV and a ring of inner radius of 0.5° and outer radius of 0.8° around this trial point was used as the background region. The integrated number of "On"and "Off" events (See Section 6.7.2 for the determination of On and Off events according to the ring background model), corresponding to the number of events reconstructed within the source region and background ring for each trial point, respectively, were plotted on a 2D sky map. These maps for the 4-telescope data set are shown in Figure 7.3(a) and 7.3(b). The normalization parameter *alpha*, was calculated for each trial point as explained in Section 6.8 using the acceptance map determined from the same data set. Figures 7.3(c) and

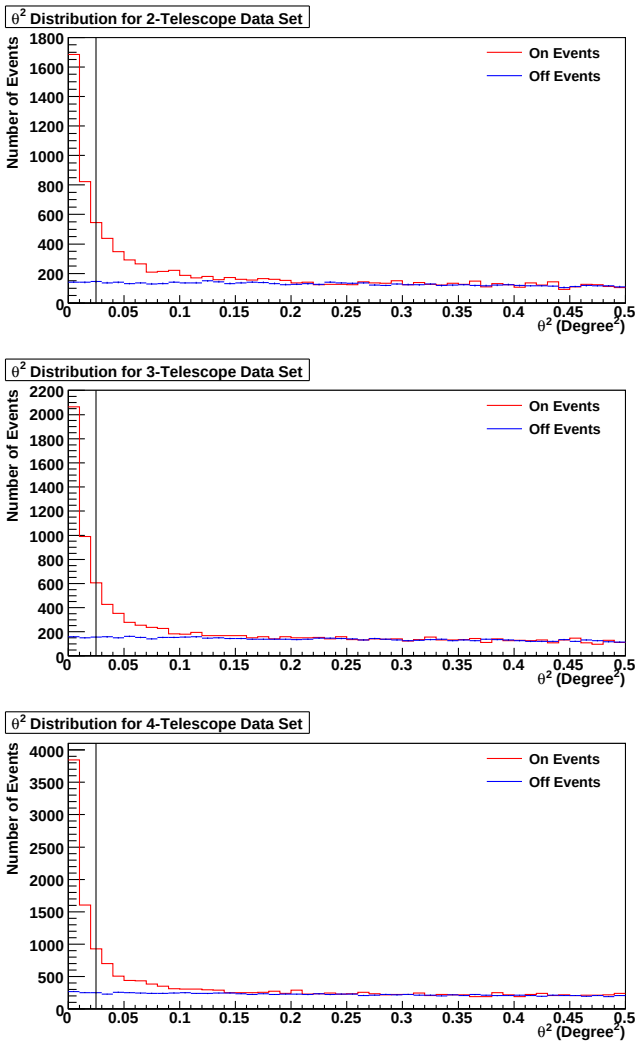

Figure 7.1: The distributions of the candidate gamma-ray events after shape cuts (MSW/L) are plotted as a function of the square of the angular distance, θ^2, between the shower arrival direction of each event and the Crab Nebula position (On) and between the shower arrival direction of each event and the center of the background regions (Off) for the 2-telescope (top), the 3-telescope (middle) and the 4-telescope (bottom) data set. The vertical lines illustrate the size of the source and background regions used in the analysis. See the text for further explanations.

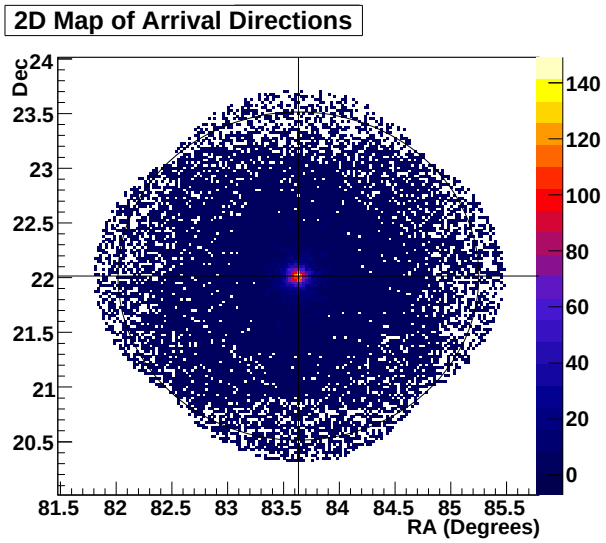

Figure 7.2: The distribution of shower arrival directions of the candidate gamma-ray events selected by the shape cuts (MSW/L) is given in a 2D sky map centered on the position of the Crab Nebula for the 4-telescope data set. The color scale corresponds the number of gamma-ray events in each bin of size $0.025^\circ \times 0.025^\circ$. It should be noted that gamma-ray events plotted in this map are not classified as On or Off events yet. On the next step, the On and Off regions defined according to the ring background model are determined for this map for each trial point in the sky and the number of events in those regions are integrated using the distribution of the events in this map.

7.3(d) show the maps of the camera acceptance and the normalization parameter for each point in the FOV.

Using these quantities, the number of "Excess" gamma-ray events at each point in the FOV was calculated as described in Section 6.8. The 2D sky map of "Excess" gamma-ray events obtained from the 4-telescope data set is given in Figure 7.3(e). The significance of the excess was then calculated at each point using Equation 6.10. The significance map for the 4-telescope data set is given in Figure 7.3(f). The significance was calculated the same way for the 2- and 3-telescope data sets and shown in Figures 7.4(a) and 7.4(a), respectively.

7.1.3 Discussion

A gamma-ray rate of 3.9 gamma rays/min is detected from the Crab Nebula with a statistical significance of $20.3\sigma/\sqrt{hr}$ from the 2-telescope data set, and a rate of 7.7 gamma rays/min is detected with a significance of $28.9\sigma/\sqrt{hr}$ from the 3-telescope data set. The detection level with the full VERITAS array of 4 telescopes is 8.3 gamma rays/min with a significance of $30.4\sigma/\sqrt{hr}$. These results were obtained with the standard cuts listed in Table 6.3 which gives a conservative estimate of the VERITAS sensitivity and the reflected background region model was used to estimate the background. Use of the ring background model gives comparable sensitivity. The Table 7.1 lists the results of the analysis for the three Crab Nebula data sets obtained using the two independent background estimation methods.

The gamma-ray rate detected by VERITAS increased by almost a factor of two, and the significance increased by a factor of $\sqrt{2}$, from the 2-telescope to the 3-telescope array. The addition of fourth telescope improved the sensitivity only slightly. This is due to the short baseline of 35 m, imposed by space constraints,

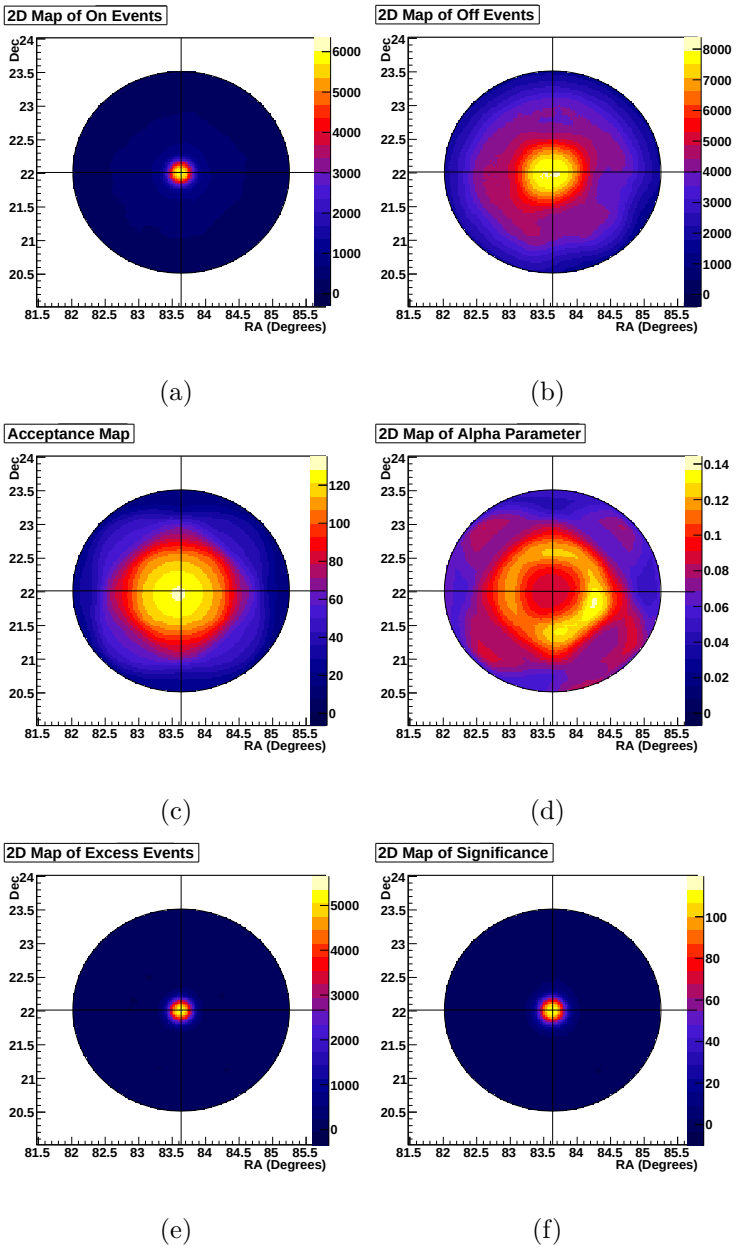

Figure 7.3: The following quantities relevant to analysis using the ring background model (Section 6.7.2) for the 4-telescope data set are shown for each point in a 2D sky map centered on the position of the Crab Nebula: (a) The number of "On" events. (b) The number of "Off" events. (c) The camera acceptance. (d) The normalization parameter α. (e) The number of excess events. (d) The significance of the excess events. The 3.5° diameter circle is the size of the VERITAS FOV.

Data Set	Live Time (min)	Excess (events)	Significance (σ)	γ-ray Rate (γ/min)	Sensitivity ($\sigma/\sqrt{(}h)$)
	Reflected Background Region Analysis				
2T	628	2456	65.59	3.91 ± 0.086	20.27
3T	386	2984	73.22	7.73 ± 0.153	28.87
4T	640	5293	99.21	8.27 ± 0.122	30.38
	Ring Background Region Analysis				
2T	628	2446	73.00	3.90 ± 0.085	22.56
3T	386	3049	84.31	7.90 ± 0.153	33.24
4T	640	5312	112.65	8.30 ± 0.122	34.29

Table 7.1: The results of the analysis performed on 2-, 3-, and 4-telescope data sets selected from the Crab Nebula observations of VERITAS are listed for two independent background estimation methods: the reflected background region model and the ring background region model. The columns list the data sets, the total live time, the number of excess events, the significance of the detection, the gamma-ray rate from the Crab Nebula, and the significance attained in one hour, respectively.

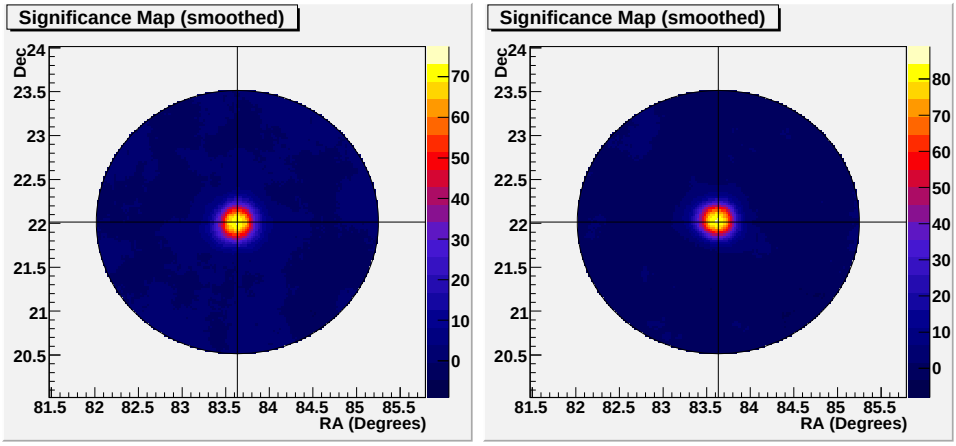

(a) (b)

Figure 7.4: The significance of the excess events from the 2- and 3-telescope data sets are shown for each point in a 2D sky map centered on the position of the Crab Nebula on the left and right panels, respectively.

between the fourth telescope and the first telescope. Basically these two telescopes act as a single telescope with a larger reflector. However, the addition of the fourth telescope with a short baseline could help to lower the energy threshold of VERITAS and special trigger schemes are currently being tested to optimize the sensitivity at low energies.

7.2 Differential Energy Spectrum of the Crab Nebula

The energy spectrum of the Crab Nebula was measured for each data set recorded during the 2-, 3- and 4-telescope operation phases of VERITAS. The method for the evaluation of the energy spectrum of a source is discussed in Section 6.9.

In order to select the candidate gamma-ray events for the measurement of the differential flux from the Crab Nebula, the same cuts used in the detection

analysis are utilized. For spectral analysis, the ring background region model for background estimation is less suitable than the reflected background region model since the acceptance of the camera may not be uniform as a function of energy. Therefore, the reflected region model is used.

The energy of each candidate gamma-ray event is estimated as discussed in Section 6.5.5. The mean fractional error in the reconstructed energy, the relative energy bias as defined in Equation 6.8, is calculated from simulations as a function of the true energy of a gamma-ray event. The relative energy bias curves for each VERITAS commissioning phase, for four zenith angles covering the zenith angle range of the Crab observations, are shown in Figure 7.5. These curves are used to define the lowest energy, "the safe energy threshold", above which the energy reconstruction is trustworthy. Gamma-ray events with energies reconstructed below the determined safe energy threshold are not used in the reconstruction of the energy spectrum.

The safe energy threshold is defined as being 10% higher than the energy of the lowest bin that has a relative energy bias less than 10%. The threshold energy is shown by vertical lines for each zenith angle of observations at each phase in Figure 7.5. Table 7.2 lists the safe energy threshold for four zenith angles determined from these curves.

For an observing run with an arbitrary zenith angle, the safe energy threshold is not determined by an interpolation between the curves, but it is taken from the first available energy bias curve that corresponds to a zenith angle larger than the maximum zenith angle of the run. This method gives a conservative threshold compared to the interpolation method, and the bias that might be introduced by the interpolation over the bias curves in an energy range that may not be completely trustworthy is avoided. For a data set of multiple runs with

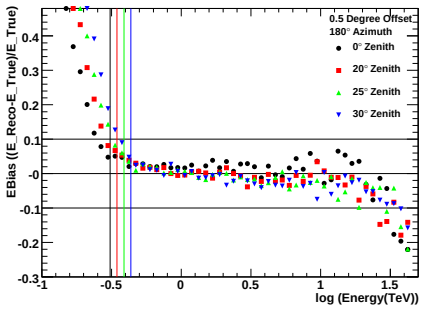

(a)

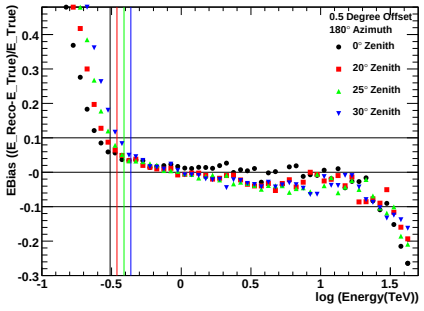

(b)

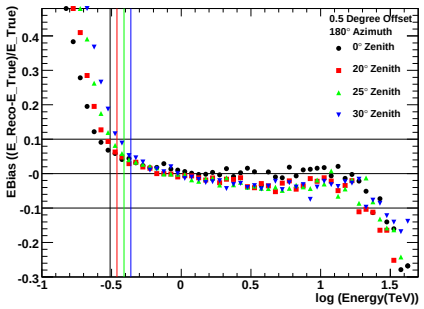

(c)

Figure 7.5: The relative energy bias curves for four zenith angles covering the zenith angle range of the Crab observations are shown for the 2-telescope (a), 3-telescope (b), and 4-telescope (c) data sets. The vertical lines show the safe energy threshold for each phase at the corresponding zenith angle of observations. See text for the discussion of the safe energy threshold.

different zenith angles, the lowest energy bin in the spectrum is determined by the maximum zenith angle of an observing run which has the lowest mean zenith angle in the data set. For the three Crab data sets used in the spectral analysis, the observing run with the lowest mean zenith angle in each data set has a mean zenith angle of 10° and a maximum zenith angle of 11°. Thus, the safe energy threshold of 0.35 TeV is determined by the energy bias curve for a zenith angle of 20° from the available curves that are for zenith angles of 0°, 20°, 25° and 30°.

The upper end of the safe energy range can be determined similarly as 10% lower than the energy of the highest bin that has a relative energy bias less than 10%. But for all data sets, the highest energy bin of the spectrum is limited by the low statistics of the gamma-ray events in those bins. Thus, the upper end of the energy range in the spectrum is set as 6 TeV by the requirement of a minimum 5σ detection in each energy bin, or a minimum of two On and Off events in each energy bin.

Zenith Angle (°)	Safe Energy Threshold (TeV)
0	0.31
20	0.35
25	0.39
30	0.45

Table 7.2: The lower end of the safe energy range is listed for four zenith angles covering the zenith angle range of the Crab Nebula observations. These thresholds are obtained from the relative energy bias curves given in Figure 7.5, as explained in the text. It was found that the safe energy thresholds are the same for all VERITAS commissioning phases.

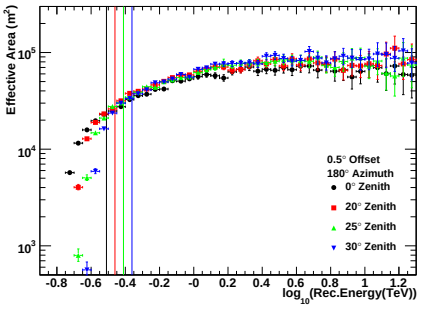

(a)

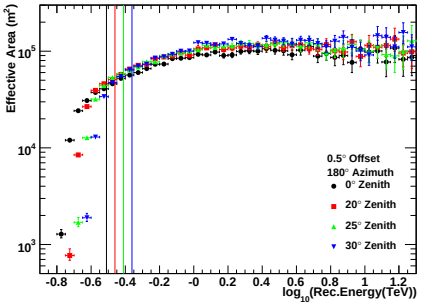

(b)

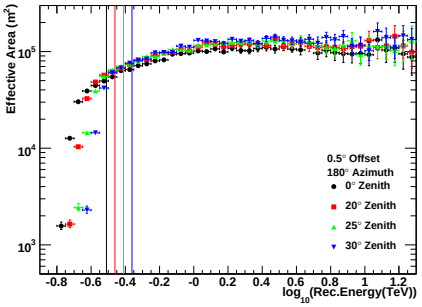

(c)

Figure 7.6: The effective area curves as a function of the reconstructed energy, for four zenith angles covering the zenith angle range of the Crab observations, are shown for the 2-telescope (a), 3-telescope (b), and 4-telescope (c) data sets. The vertical lines show the safe energy threshold for each phase at the corresponding zenith angles of observations. See text for the discussion of the safe energy threshold.

The effective area of the instrument is necessary in order to measure the flux of gamma rays from a source. The effective area of VERITAS is calculated from simulations as explained in Section 6.9 for the 2-, 3- and 4-telescope phases of VERITAS. Figure 7.6 shows the effective area curves as a function of the reconstructed energy, i.e. the modified effective areas, for four zenith angles of observations for each phase of VERITAS. These curves are obtained from simulations of south-facing ($90^\circ <$ azimuth angle $< 270^\circ$) observations, with the pointing direction at a 0.5° offset from the source location and with an average noise level of 6.43 dc, corresponding to the azimuth range, pointing offset, and average noise level of the Crab observations. Figure 7.7 shows the comparison between the effective areas of the three phases of VERITAS. It can be seen that the effective area changes by approximately a factor of two between the 2-telescope and 3-telescope phases but it is almost the same for 3- and 4-telescope operation. This is confirmed by the comparable gamma-ray rate obtained from the Crab Nebula observations at these phases (Section 7.1).

The common definition of the energy threshold of an atmospheric Cherenkov telescope is the energy for which the differential rate curve is a maximum. The differential rate curve is formed by folding the effective area curve of the instrument with the expected gamma-ray flux from the source. The energy threshold calculated from this definition is slightly lower than the safe energy threshold defined earlier, therefore, clearly a significant amount of gamma-ray signal is present below the safe energy threshold. Figure 7.8 shows the VERITAS effective area curves at each phase, for a source at a 20° zenith angle and a southern azimuthal direction, at an 0.5° offset from the pointing direction, calculated for the standard analysis cuts folded with a unit flux with a spectral slope of -2.5, which is the approximate differential photon index of the Crab Nebula spectrum. It was found that the energy threshold of VERITAS is the same for the 2-, 3- and

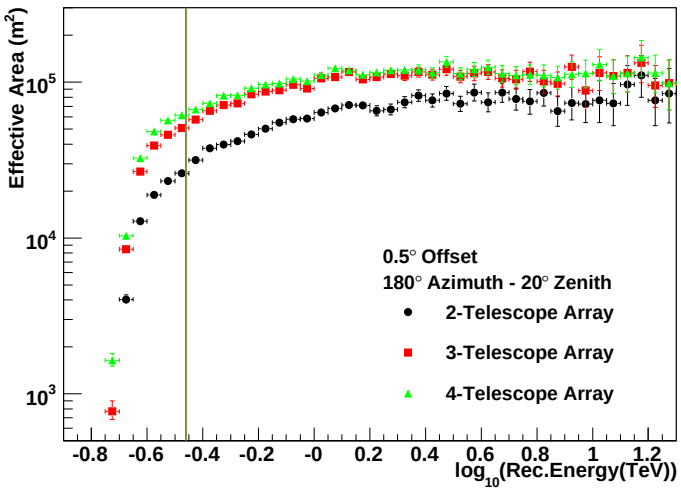

Figure 7.7: The comparison of the effective area curves for the 2-, 3- and 4-telescope VERITAS commissioning phases, for the observation of a source at 20° zenith angle, in the south azimuth range (90° < azimuth < 270°), in a region of sky with an average noise level of 6.43 dc. The symbols used for the effective area curve for each phase are given in the legend. The vertical line shows the safe energy threshold (0.35 TeV) for each phase for 20° zenith angle of observations.

4-telescope phases (0.27 TeV), whereas the safe energy threshold is 0.35 TeV.

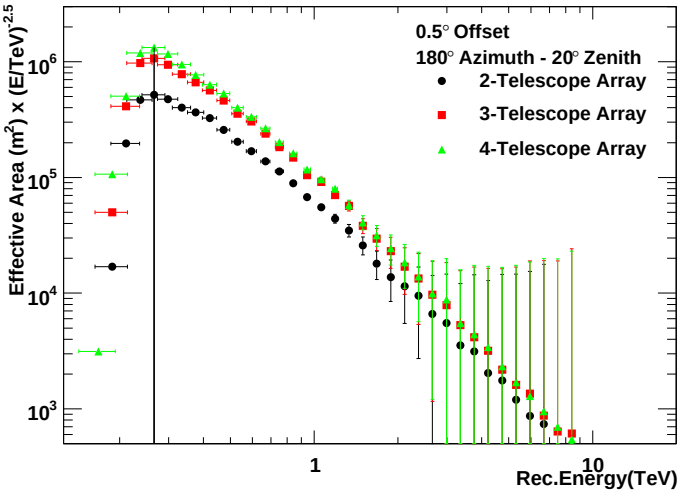

Figure 7.8: The VERITAS effective area curves for each phase folded with a unit flux with a differential spectral slope of -2.5, which is the approximate photon index of the Crab Nebula spectrum, are shown, for the observation of a source at 20° zenith angle, in the azimuth range 90° < azimuth < 270°, in a region of sky with an average noise level of 6.43 dc, and at an 0.5° offset from the pointing direction. The symbols used for each curve are given in the legend. The peaks of these curves define the standard energy threshold of the instrument and the vertical line shows the standard energy threshold (0.27 TeV) for each phase.

Once the effective area of the detector is known, the detected gamma-ray events from the "On" and "Off" regions are binned by their reconstructed energies and the flux of the excess gamma rays in every energy bin is calculated following Equation 6.12 for each data set. The energy resolution of VERITAS defined in Section 6.5.5 and given in Figure 6.15 determines the minimum bin width in the differential energy spectrum. Accordingly, the calculated flux of the gamma rays

is binned in log(E) space using 36 bins in the range $-1.5 < \log(\mathrm{E}/1\mathrm{TeV}) < 1.5$ corresponding to a bin width of 20%.

Figure 7.9 shows the measured energy spectrum of the Crab Nebula using the 2-, 3- and 4-telescope data sets. The data points are fit between 350 GeV and 6 TeV by a simple power law in the form of

$$\frac{\mathrm{dN}}{\mathrm{dE}} = I_0 \left(\frac{E}{1\,TeV} \right)^{-\Gamma} \tag{7.1}$$

The minimum energy bin in the fit is defined by requiring the safe energy threshold discussed above and the maximum energy bin is defined by requiring a statistical significance greater than 5 standard deviations or having at least two On and Off events in each bin.

The fit results for the energy spectrum measured from the data set of each phase are given as follows:

- Simple power law fit to the 2-telescope data set:
  - $I_0 = (2.97 \pm 0.09_{\mathrm{stat}} \pm 0.65_{\mathrm{sys}}) \times 10^{-7}$ TeV^{-1}m^{-2}s^{-1},
  - $\Gamma = (2.37 \pm 0.04_{\mathrm{stat}} \pm 0.17_{\mathrm{sys}})$
- Simple power law fit to the 3-telescope data set:
  - $I_0 = (3.48 \pm 0.10_{\mathrm{stat}} \pm 0.77_{\mathrm{sys}}) \times 10^{-7}$ TeV^{-1}m^{-2}s^{-1},
  - $\Gamma = (2.36 \pm 0.04_{\mathrm{stat}} \pm 0.17_{\mathrm{sys}})$
- Simple power law fit to the 4-telescope data set:
  - $I_0 = (3.19 \pm 0.07_{\mathrm{stat}} \pm 0.70_{\mathrm{sys}}) \times 10^{-7}$ TeV^{-1}m^{-2}s^{-1},
  - $\Gamma = (2.40 \pm 0.03_{\mathrm{stat}} \pm 0.17_{\mathrm{sys}})$

Apart from the statistical errors, the measurement of energy spectra by cosmic-ray or gamma-ray experiments suffer from rather large systematic errors. One reason for this is the lack of methods (e.g. test beams) to calibrate the entire instrument in combination with the development of an extensive air shower in the atmosphere. Instead, the detector systems are calibrated in pieces, and simulations are used in modeling the physical processes or the detector response. With these limitations, currently the best approach is to estimate the systematic errors due to various components separately and to add these individual errors in quadrature to estimate a total systematic error [139]. The individual sources of systematic error are discussed in the next section. Combining the individual systematic errors, the total systematic error on the flux is estimated as $\pm 22\%$ and on the spectral slope as ± 0.17.

7.2.1 Estimation of Systematic Errors

Various independent factors introduce systematic error in the energy reconstruction and in the absolute flux and the photon index of the measured spectrum. The dominating factors include uncertainties due to the models used in simulations, uncertainty in various aspects of the detector response, the variability of environmental conditions and the effects of different analysis methods.

Model Assumptions in Simulations: The uncertainties due to the models used in the simulations are mainly in the atmospheric modeling and in the shower interaction models. The deviation of the real density distribution from the standard atmospheric model used in the simulations, seasonal and daily variations in the atmospheric temperature and pressure, and insufficient knowledge of the atmospheric extinction value cause these uncertainties. To first order, the effects of these factors do not change with the energy of the gamma-ray and thus they

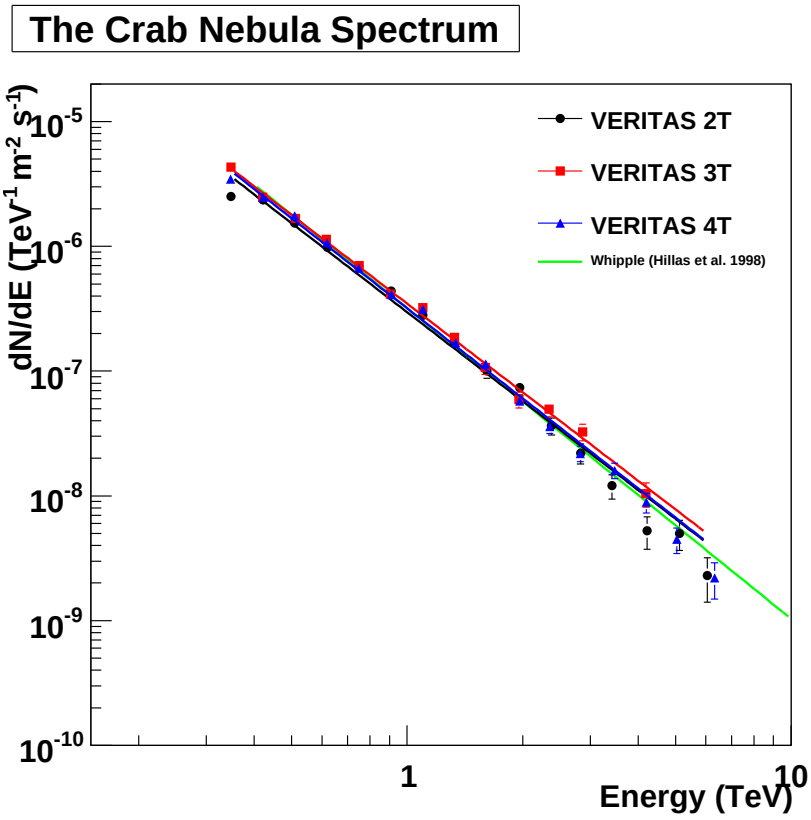

Figure 7.9: The measured energy spectrum of the Crab Nebula using the data sets 2T, 3T and 4T. The lines show a simple power-law fit to the data points for each data set between 350 GeV and 6 TeV. The green line is the measurement by the Whipple experiment [7] for comparison.

introduce an error on the flux but not on the index. We estimate the systematic error on the flux due to these factors as $\pm 10\%$ [132]. The modelling of shower interactions differ from one simulation package to another, which leads to differences in the estimation of the total Cherenkov light generated from gamma-ray and cosmic-ray initiated showers. This difference leads to an incorrect estimation of the photon collection efficiency by simulations and in turn an incorrect estimation of the effective area of the instrument (which results in a shift on the flux level). We estimate the error on flux due to this as $\pm 1\%$ [132].

Uncertainties in the Detector Modeling: The systematic errors due to the detector modeling stem from insufficient measurements, or lack of direct measurement methods, of certain parameters, or from daily variability of some parameters based on the environmental conditions. The systematics due to the detector parameters can be grouped into a few classes. The optical parameters, such as changes in mirror reflectivity, the mirror alignment effects on the point spread function, contribute to the systematic error on the absolute flux. We estimate that the systematic error on the flux due to these are approximately $\pm 5\%$. The most critical contributions to the systematic error in the detector modelling come from the uncertainities in the overall photon collection efficiency. The variations in the photon collection efficiency are a combination of many small effects, such as insufficient knowledge or variations in the light cone efficiency and the effects of its geometry, the angular effects of the PMT surface and the cathode non-uniformity, the spread in the PMT quantum efficiency, the gain variations in the first dynode of PMTs, and the variable number of inactive pixels in the camera. These factors change the overall scale of the $Size$ of the detected events, and they thus cause an under/overestimation of the energy of the event and the effective area of the detector. Since these parameters also change with the energy scale, they effect both the absolute flux and the photon

index of the spectrum. We estimate the systematic error due to the photon collection efficiency on the flux is ±15% and on the photon index is ±0.1. The last group of detector parameters that contribute to the systematics is the trigger modelling. The trigger inefficiencies in the detector due to the dead-time in different components of the trigger system, the threshold level variations in the CFDs and other electronics, and FADC variations affecting the pulse shape and size are in this group of effects. These effects contribute to uncertainty in the event rate and in turn to approximately a ±3% error in the flux. In principle, these factors change the energy threshold, and thus they affect the photon index as well, but due to the analysis cuts, the reconstructed event's energy is much higher than the trigger threshold. Thus, the systematic error on the photon index due to trigger inefficiencies is negligible.

Variability of Environmental Conditions: Run-by-run variations in the detected gamma-ray rate are mainly due to the atmospheric and environmental conditions. The various data sets that can be formed with different run quality selection give slightly different measurements of both the flux and the spectral slope. Comparable to the run-by-run gamma-ray rate differences, the systematic error on flux due to this is estimated as ±5% and on the spectral slope as ±0.1.

Effects of the Offline Analysis: The event reconstruction methods, the selection and gamma/hadron separation cuts in the analysis, and the background estimation, have an effect in the reconstruction losses and in the wrong assignment of events depending on their energy. Thus the analysis introduces a systematic error into the flux and the photon index. There is no simple method to cross-check the error range of the reconstruction efficiency and a reasonable guess is made. The systematic error due to these effects is estimated as ±10% on the flux and ±0.1 on the photon index.

Combining all these various sources of systematic errors gives an overall systematic error on the flux as $\pm 22\%$ and on the spectral slope as ± 0.17.

7.3 The Detection of Optical Pulsed Emission From the Crab Pulsar

Before any periodic modulation is searched for in the gamma-ray emission from the Crab Pulsar, it is necessary to show that the time resolution of VERITAS is sufficiently precise to detect pulsed emission at the Crab Pulsar period of 33 ms. Additionally, it is also necessary to prove that the temporal analysis employed for this search is capable of detecting periodicity in a signal in which periodic modulation is known to exist.

For this purpose a special optical pulsar set up (explained in Section 4.8) was integrated in the hardware of telescope T2 to detect the optical pulsed emission from the Crab Pulsar. The optical data were recorded in a few $\sim$10 minute special runs during which time the data were directed to a separate data acquisition (DAQ) program independent of the regular VERITAS DAQ. Table 7.3 lists the three optical runs that were used in the analysis. The recorded optical data were analyzed with the temporal analysis discussed in Section 6.10.

An optical photon travels without any interaction in the atmosphere (i.e. without creating an EAS in the atmosphere). It can be detected directly by a Cherenkov telescope which focuses all the photons collected by its reflector onto its camera. The optical signal is focused onto the central pixel with possible spill-over onto the first ring of pixels around the central pixel, depending on the PSF and the pointing accuracy of the optical system of the telescope. The optical pulsar set up records the signal from the central pixel and from the first ring of

Run Number	Start Time (UTC)	Duration (mm:ss.ns)
061220-1	2006-12-20 07:03:30.426486900	9:50.615072600
061222-2	2006-12-22 06:15:07.922373700	8:49.592192500
061222-3	2006-12-22 06:29:55.994680700	11:09.394174700

Table 7.3: The list of special runs taken with the optical pulsar set up and used in the analysis. The start time of each runs is given in the UTC time system with the format of year-month-day hour: minute: second. nanoseconds. The duration of each run is given in minutes: seconds .nanoseconds format. The precision of the GPS clock is ±100 ns. The total exposure time of these three runs is approximately 30 minutes.

pixels around it. The signal from a pixel close to the edge of the camera is also recorded to verify that any periodic excess signal on the central pixel is due to the optical pulsed emission rather than a feature of the background.

The pulse profile of the recorded optical signal is reconstructed as explained in Section 6.10.4. Figure 7.10 shows the pulse profile obtained from the analysis of the data of Run 061222-2 plotted with respect to the phase of the Crab Pulsar rotation covering two complete ranges of phase. The signal detected on the central pixel of the T2 camera, on a pixel (pixel 4) in the first ring of pixels around the central pixel, and on pixel 131, which is located close to the edge of the camera, are shown in the first, second and third rows, respectively. The left-hand-side panels show the pulse profile of the detected signal before the barycentering correction is applied. The right-hand-side panels show the pulse profile of the detected signal after the barycentering correction is performed on the data. On the right-hand-side panel of the first row, a periodic excess signal can be seen

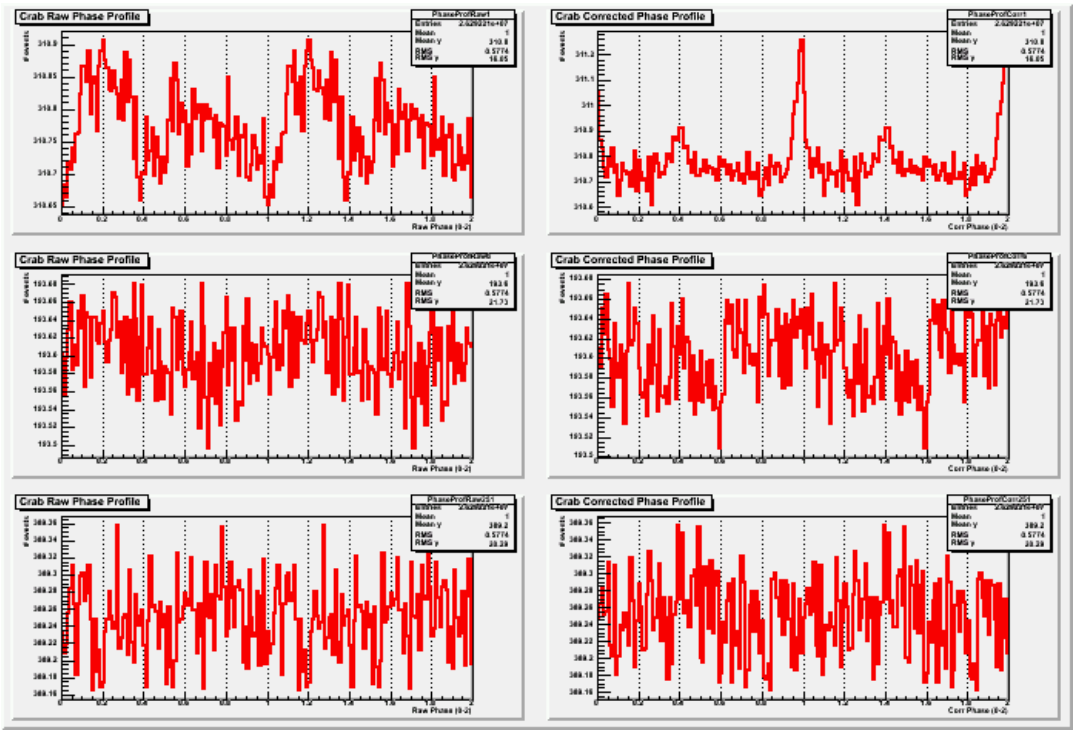

Figure 7.10: The pulse profile of the detected optical signal obtained from the analysis of the data of Run 061222-2 is plotted with respect to the phase of the Crab Pulsar rotation over two complete ranges of phase. The signal detected on the central pixel of the T2 camera, on a pixel in the first ring of pixels around the central pixel, and on an outer pixel located close to the edge of the camera, are shown in the first, second and third rows, respectively. The left-hand-side panels show the pulse profile of the detected signal before the barycentering correction is applied. The right-hand-side panels show the pulse profile of the detected signal after the barycentering correction is performed on the data. A clean signal of pulsed emission is seen on the central pixel but no periodic excess is seen on pixels away from the center. See the text for further discussion.

in the data recorded on the central pixel around the phase intervals [-0.08, 0.05] and [0.32, 0.45] corresponding to the main peak and inter-peak of the well-known Crab pulse profile. A periodic excess is even evident before the barycentering correction is applied (left-hand-side panel of the first row), although the peaks are not as well defined and focused. No periodic excess is seen on pixels away from the center. This indicates that most of the focused optical signal is contained in the central pixel and the leakage of the signal to the surrounding pixels is negligible. Having no pulsed excess in the data recorded from pixel 251 proves that the excess in the central pixel is indeed due to the optical signal rather than the manipulation of background by the temporal analysis program.

The three runs listed in Table 7.3 are combined after the barycentering correction is applied. Figure 7.11 shows the phase plot of the signal obtained by combining the data. It clearly shows the main and inter pulses of the optical pulsed emission.

The detection of the periodic optical signal confirms that our online time stamping and our offline temporal analysis are capable of detecting the 33 ms pulsed emission and that we can reconstruct the double-peaked phase structure of the Crab Pulsar successfully.

7.4 The Search for Gamma-Ray Pulsed Emission from the Crab Pulsar

The angular resolution of VERITAS is not sufficiently small to resolve the Crab Pulsar in the Crab Nebula. Therefore, the signal recorded from observations of the Crab Nebula includes the contribution from the Crab Pulsar emission. The gamma-ray emission from the Pulsar can be extracted from the steady signal

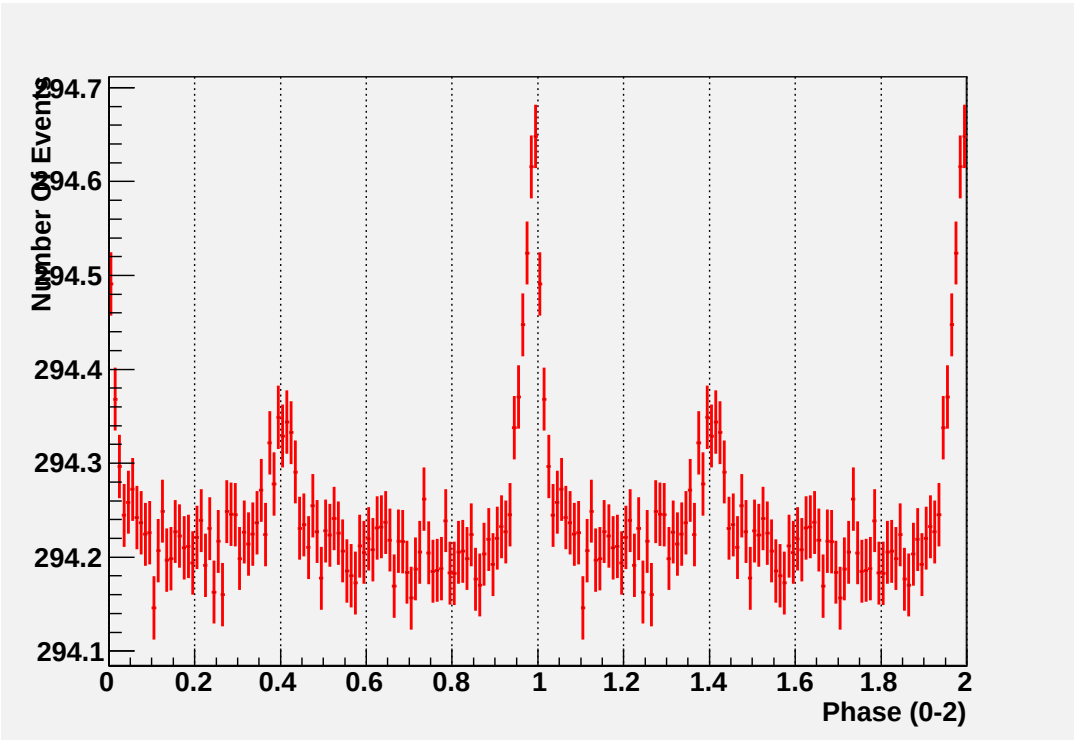

Figure 7.11: The pulse profile of the detected optical signal obtained from the analysis of the combined data set listed in Table 7.3 is plotted with respect to the phase of the Crab Pulsar rotation covering two complete ranges of phase. The main and inter pulses of the optical pulsed emission are clearly seen.

of the Crab Nebula only if the signal detected exhibits a periodic modulation at the frequency of the Pulsar. Any periodic excess in the signal can be then used to measure the pulsed emission spectrum from the Crab Pulsar to provide information about the VHE pulsed emission mechanisms at work near the pulsar surface. A non-detection of a periodic excess in the detected gamma-ray signal would give an upper limit on the pulsed emission cut-off energy which could restrict the high-energy pulsed emission models.

With this goal, the temporal analysis discussed in Section 6.10 is performed on the data collected by VERITAS to search for a periodic modulation in the VHE gamma rays. Since the pulsed emission is expected only at the lowest energies to which VERITAS is sensitive, more relaxed event selection cuts and a wider θ^2 cut (listed in Table 6.4) were used to enhance the acceptance of low-energy events. The binning of events by phase acts to separate the signal and background, and no further gamma/hadron separation cuts are applied.

These loose cuts increased the overall number of candidate gamma-ray events by a factor of $\sim$12 relative to the standard analysis. In Figure 7.12, the effect of using loose cuts on the effective area of the 4-telescope VERITAS array is seen as a higher acceptance of lower energy events compared to the effective area obtained with the standard cuts. In Figure 7.13, the effective area curve obtained with the looser cuts folded with a power law spectrum with an index of 2.5 is shown in comparison to the curve obtained with the standard cuts. As seen from the peak position of this curve, the energy threshold of the instrument with these loose cuts is 0.17 TeV compared to the standard energy threshold of 0.27 TeV.

After the event selection, a timing analysis is performed using the arrival times of candidate gamma-ray events to calculate the barycentering correction and the corresponding pulsar rotation phase separately for the events reconstructed in

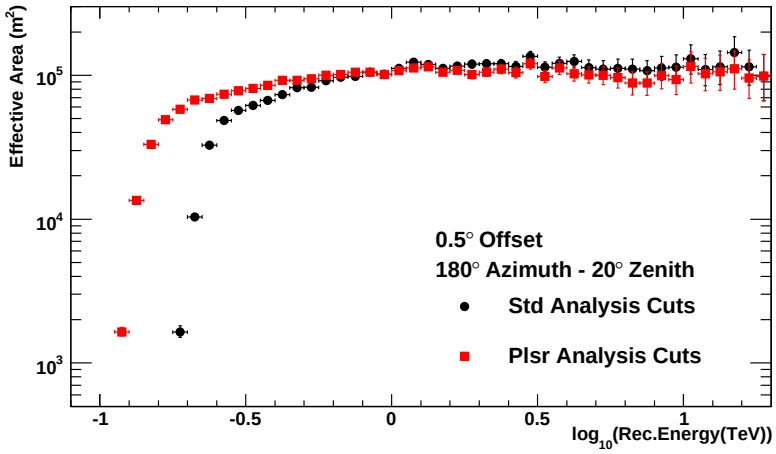

Figure 7.12: The effective area of the 4-telescope array of VERITAS obtained using the looser analysis cuts is shown in comparison to the effective area obtained using the standard analysis cuts. Both curves are for a source at 0.5° offset from the pointing direction, observed at a zenith angle of 20° and in the southern azimuthal range.

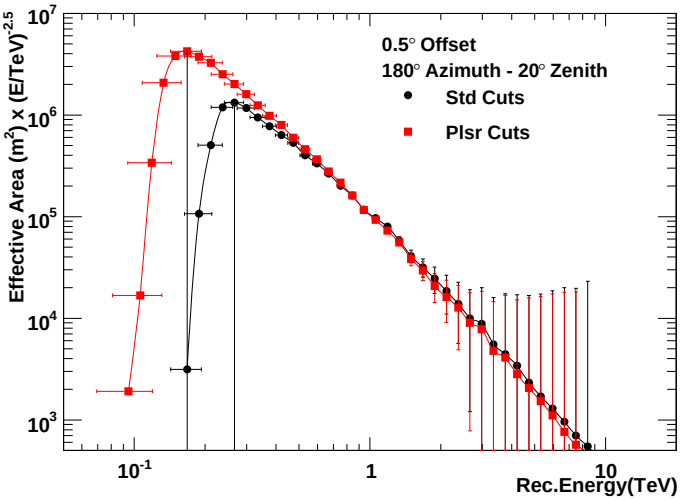

Figure 7.13: The effective area of the 4-telescope array of VERITAS obtained using the looser analysis cuts folded with a power law spectrum with an index of 2.5 is shown in comparison to the effective area obtained using the standard analysis cuts. The peak positions of both curves, which denotes the energy threshold of the detector for looser cuts and standard cuts, are shown with the vertical lines. Both curves are for a source at 0.5° offset from the pointing direction, observed at a zenith angle of 20° and in the southern azimuthal range.

the source region and in the background region. Two pulse profiles at the period of the Crab Pulsar are obtained from the source and background regions.

In Figure 7.14, the phase histogram of the signal from the source region and the estimated background are shown for the 2-telescope data (top) and 3-telescope data (middle) and 4-telescope (bottom) data obtained with the pulsar cuts. The significance of the pulsed excess is calculated by assuming the pulse shape as seen in the EGRET energy range, with a defined pulsed emission region between the phases $[-0.06 - 0.04]$ and $[0.32 - 0.43]$ for the main pulse and inter-pulse regions respectively. The remaining phase regions are used to estimate the background for the pulsed emission. No evidence for pulsed emission is seen. The large difference in the levels of the gamma-ray events from the source region (red) and from the background regions (blue) is the excess gamma-ray events due to the steady emission of the Crab Nebula.

An upper limit on the pulsed emission flux and on the fraction of the pulsed emission relative to the steady signal is then calculated using the method of Helene [140], assuming Gaussian statistics for the excess events, at a 95% confidence level. The upper limits are calculated from the pulse profiles using the standard analysis cuts obtained similar to the case using the pulsar cuts. This made it possible to quote the limits conventionally at the standard energy threshold of the detector.

These upper limits on the excess events are used to obtain the integral flux upper limits on the pulsed emission. The collection area of the standard analysis cuts are used in the process assuming a power law spectrum and a photon index of 2.5 for the pulsed emission. The integral upper limit on the pulsed emission from the Crab Pulsar using the 4-telescope data set is $< 4.35 \times 10^{-12} cm^{-2} s^{-1}$, using the 3-telescope data set is $< 8.17 \times 10^{-12} cm^{-2} s^{-1}$ and the upper limit for

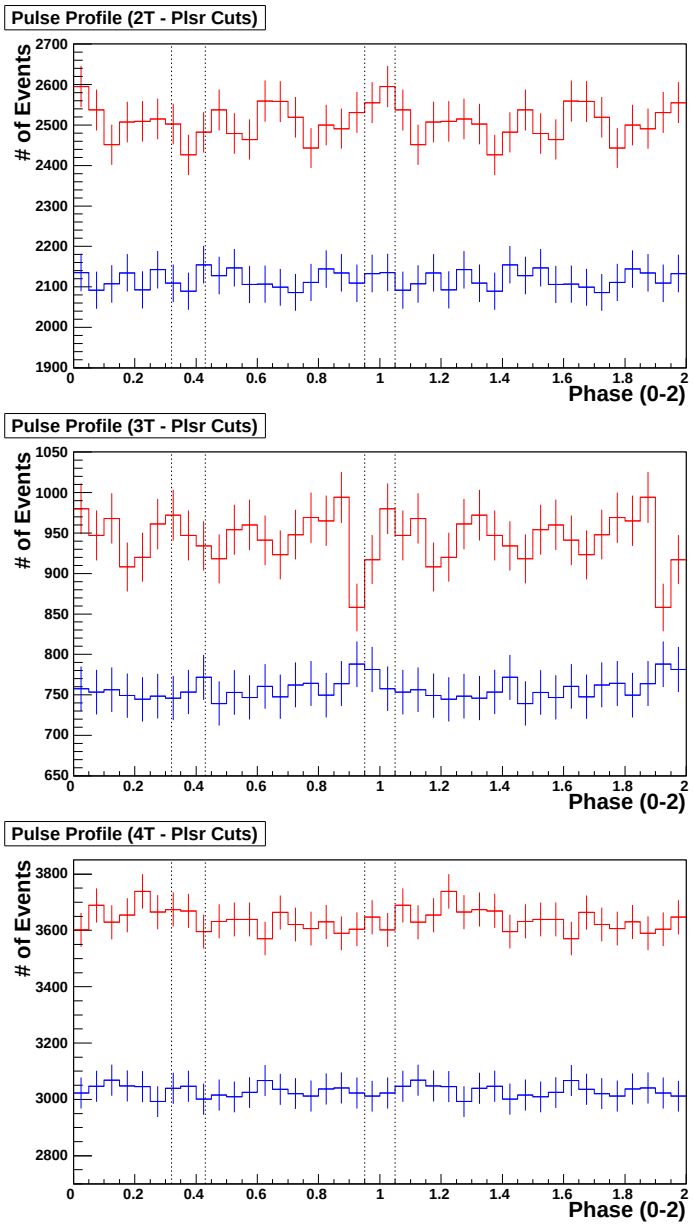

Figure 7.14: The phase histogram of the gamma-ray signal from the source region (red) superimposed on the estimated background from the background regions (blue) for the 2-telescope (top), 3-telescope (middle) and 4-telescope (bottom) data obtained with the pulsar cuts described in the text.

the 2-telescope data set is $< 3.58 \times 10^{-12} cm^{-2} s^{-1}$ as plotted on Figure 8.3. All flux upper limits are calculated above the VERITAS energy threshold of 0.24 TeV for observations at 15° zenith angle which is the approximate average zenith angle of the Crab in all three data sets.

The cutoff energy of the pulsed emission corresponding to an integral upper limit is calculated assuming a break in the energy spectrum of the pulsed emission as described by an exponential cutoff. The measured pulsed spectrum by EGRET below 10 GeV [103] is extended with this cutoff and equalized to the calculated flux upper limits as follows:

$$F(E, E_{CutOff})_{UL} = F(E)_{<10\,GeV,\,EGRET} \times exp\left(-\frac{E}{E_{CutOff,\,UL}}\right) \qquad (7.2)$$

where $F(E, E_{CutOff})$ is the integral flux of the assumed cutoff spectrum, $F(E)_{<10\,GeV}$ is the measured integral flux of pulsed emission from the Crab Pulsar by EGRET, and E_{CutOff} is the cutoff energy. The most constraining integral flux upper limit, obtained from the 2-telescope data, is used to derive the upper limit on the cutoff energy as < 50 GeV.

CHAPTER 8

Summary and Interpretation of the Results

In this thesis, the following main results are reported from our studies using the data collected from the Crab Nebula and Pulsar with VERITAS:

- The strong detection of the Crab Nebula in all commissioning phases of VERITAS.
- Measurement of the differential energy spectrum of the Crab Nebula at each operation phase of VERITAS and the test of any deviation of the measured spectrum from a simple power law shape.
- The detection of the optical pulsed emission from the Crab Pulsar.
- Upper limits on the pulsed emission flux from the Crab Pulsar above an energy of $\sim$170 GeV and upper limits on the cut-off energy of the pulsed emission.

8.1 Detection of the Crab Nebula

The Crab Nebula has been detected strongly during each commissioning phase and with the complete 4-telescope array of VERITAS. The detected gamma-ray rate from the Crab Nebula is $3.9 \pm 0.1\,\gamma$/min with a total significance of 65.6σ during the 2-telescope phase; $7.7 \pm 0.2\,\gamma$/min with a total significance of 73.2σ

during the 3-telescope phase; and $8.3 \pm 0.1\,\gamma$/min with a total significance of 99.2σ during the 4-telescope phase. The improvement of the detected gamma-ray rate and the significance of detection are consistent with the estimated increase of the effective area of VERITAS with the addition of the third and fourth telescopes.

The detection level of the Crab, the standard candle of VHE astronomy, with the full array of four telescopes can be used to derive the sensitivity of VERITAS. We define the sensitivity as the time required to detect a point source of similar spectral slope to the Crab, observed at 0.5° offset from the camera center and at the zenith angle corresponding to the average zenith angle of the Crab observations. It was found that with the 4-telescope array, four hours of observations at a zenith angle of 12° are required to detect a point source with a flux of 5% of the Crab Nebula at the 5 standard deviation level. Figure 8.1 shows the time required for a 5 standard deviation detection as a function of signal strength in terms of the Crab flux.

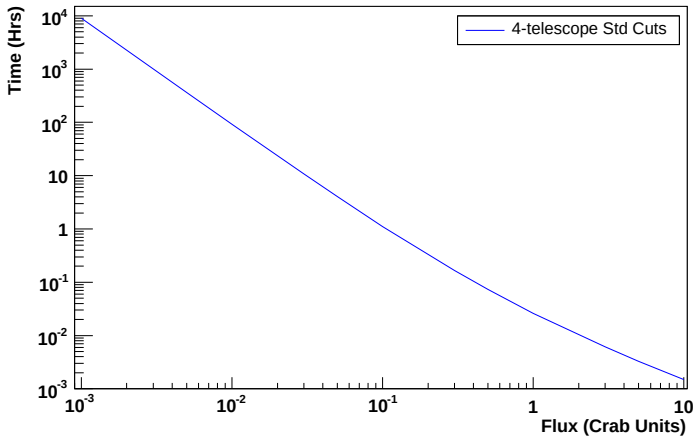

Figure 8.1: The time required for VERITAS to detect a point source of a certain signal strength, observed at the zenith angle corresponding to the average zenith angle of the Crab observations (12°).

8.2 Differential Energy Spectrum of the Crab Nebula

After the presence of a gamma-ray signal in the data was established, the differential flux of the gamma-ray emission from the Crab Nebula was measured with 2-, 3- and 4-telescope data sets. The flux points were calculated in the safe energy region of 0.36 TeV to 6.00 TeV, determined from energy bias and photon statistics considerations, and the points are fitted by a simple power law. A simple power law fit to the 2-telescope data gives $\mathrm{dN/dE} = (2.97 \pm 0.09) \times 10^{-7}$ $(\mathrm{E/1\ TeV})^{-(2.37+/-0.04)}$ $\mathrm{TeV^{-1}m^{-2}s^{-1}}$. The measured spectrum from the 3 and 4-telescope data sets are $\mathrm{dN/dE} = (3.48 \pm 0.10) \times 10^{-7}$ $(\mathrm{E/1\ TeV})^{-(2.36+/-0.04)}$ $\mathrm{TeV^{-1}m^{-2}s^{-1}}$ and $\mathrm{dN/dE} = (3.19 \pm 0.07) \times 10^{-7}$ $(\mathrm{E/1\ TeV})^{-(2.40+/-0.03)}$ $\mathrm{TeV^{-1}m^{-2}s^{-1}}$, respectively. The measured spectrum of the Crab Nebula extends more than a decade in energy and three decades in flux.

The energy production mechanisms in the Crab Nebula system and the resulting broadband emission spectrum of the Crab Nebula is discussed in Chapter 2. The continuum emission of the Crab Nebula, shown in Figure 2.10, is predominantly produced by non-thermal processes via synchrotron and inverse Compton radiation, covering the energy range from radio to VHE gamma rays. The synchrotron origin of the emission from radio to a few MeV was first proposed by Shklovsky [98] and was experimentally demonstrated by polarization measurements [141]. The broad range of the synchrotron spectrum up to multi-TeV energies implies the presence of electrons accelerated up to PeV energies at the termination shocks of the Nebula. These PeV electrons are considered to radiate via inverse Compton scattering to produce the VHE gamma-ray emission of the Crab Nebula above 1 GeV up to, and beyond, 50 TeV with detectable flux levels for space- and ground-based experiments sensitive in this energy range.

Detailed models of the VHE gamma-ray emission due to inverse Compton

scattering have been discussed by Atoyan & Aharonian [9, 4] and de Jager & Harding [96]. The model by Atoyan & Aharonian [4], takes into account three seed photon populations from which the electrons scatter: synchrotron photons radiated by the same electron population, far-infrared photons from thermal emission and cosmic background radiation photons. In order to extract the underlying electron spectrum, they used the observed broadband spectrum of the Crab Nebula and assumed an average constant magnetic field within the nebula. The photon densities are calculated using the measured size of the nebula at different wavelengths and assuming a radial density profile following a Gaussian distribution. The predicted IC-spectrum from this model is shown with a thick dashed line in Figure 8.2.

The differential flux points calculated from the data for each commissioning phase of VERITAS are also shown in Figure 8.2 along with measurements by various other experiments. In the energy range of our measured spectrum between 300 GeV and 10 TeV, all results are in good agreement with each other and with our measurements within the systematic errors. This confirms that the VERITAS detector, a new gamma-ray instrument, performs as expected and successfully measures the differential spectrum of a gamma-ray source during each commissioning phase and with the complete array. This also confirms that the energy reconstruction methods used in the spectral analysis are successful in reconstructing the energy spectrum from a gamma-ray source. All measurements are in reasonable agreement with the IC emission model as well. This agreement indicates that the IC-model under consideration explains reasonably well the VHE emission from the Crab Nebula.

A softening in the Crab spectrum at high energies is predicted by the IC-model of Atoyan & Aharonian [4]. A steepening in the spectrum of the Crab

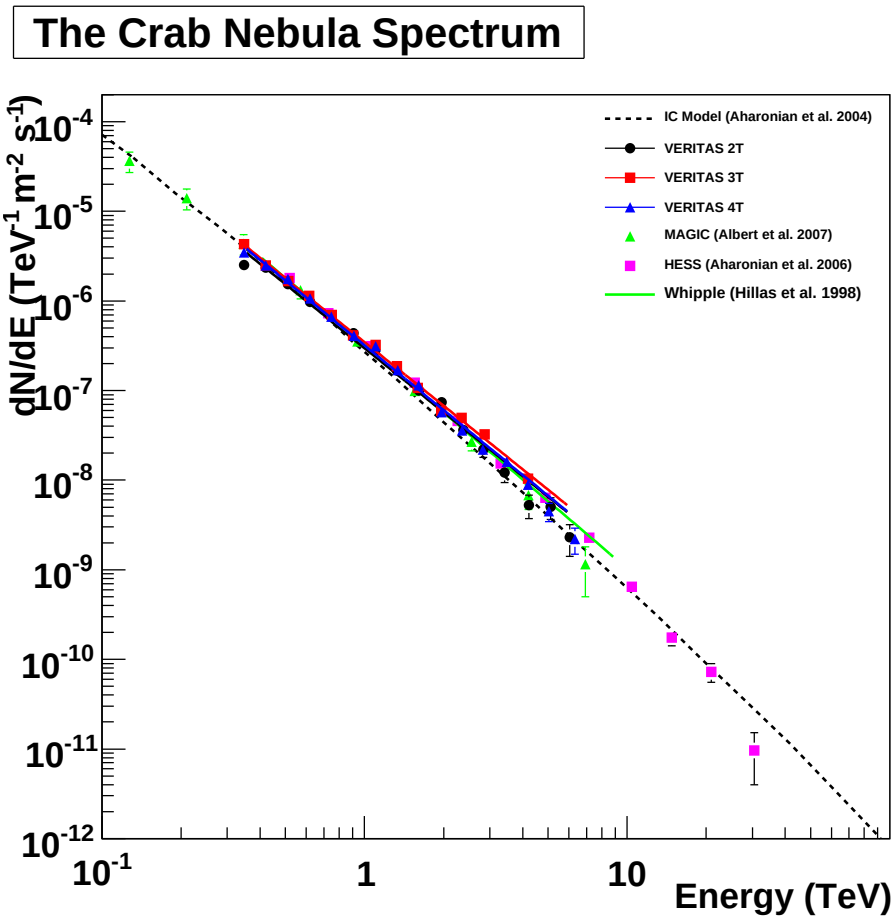

Figure 8.2: The measured differential flux from the Crab Nebula with the 2-telescope(black circles), 3-telescope (red squares) and 4-telescope arrays (blue triangles) of VERITAS are shown in comparison with previous measurements by other groups and the predicted spectrum by the inverse Compton emission model of [4]. The model prediction is given by the thick dashed line. The additional data points show the measurements by MAGIC (green triangles), HESS (pink squares), and the power-law formula reported by Whipple (green line).

Nebula was reported by the HEGRA and HESS experiments above 10 TeV in accordance with the model. We attempted to test this result using the spectral measurements by VERITAS. The highest energy in the measured spectrum of the Crab Nebula by VERITAS of 6 TeV was obtained from the 4-telescope data set, limited by the statistics of the detected gamma rays. Although a power law fit with an exponential cut-off gives a better χ^2 than a simple power law fit, both fits are comparable within the statistical and systematic errors of the measurement. In conclusion, it became clear that we need more data, preferably at larger zenith angles, in order to make a statement in the energy region above 10 TeV.

According to the same model, the spectrum is expected to harden below $\sim$200 GeV. So far, only the MAGIC experiment has sufficient sensitivity in this energy range to measure the differential spectrum of the Crab in order to test this prediction. Their measurements [139] exhibited the expected flattening in the spectrum around 100 GeV, and they estimated the position of the IC-peak at $\sim$77 GeV. Since the relative energy bias in the energy reconstruction achieved by VERITAS below 350 GeV is greater than the safe limit of 0.10, it was not possible to reconstruct the differential flux spectrum in this energy range to test this prediction and confirm the MAGIC result.

In order to gain sufficient sensitivity with VERITAS in the energy range less than 350 GeV for differential spectral reconstruction, various improvements are needed. As shown in Chapter 7, the energy threshold of the instrument is $\sim$270 GeV for observations at the average zenith angle, 20°, of the Crab data set as opposed to the safe energy reconstruction threshold of 350 GeV. Thus, an improvement in the energy reconstruction methods to achieve a smaller energy bias will allow spectral reconstruction down to $\sim$270 GeV. Furthermore, as shown with the pulsar analysis, it is possible to detect gamma rays with energies

as low as ∼150 GeV with VERITAS using relaxed analysis cuts, because the trigger threshold of the instrument is well below the spectral analysis threshold of 350 GeV. On the other hand, in this region, the gamma/hadron rejection power is not as efficient without additional background rejection criteria, such as the timing information for pulsed emission. Thus, in order to become more sensitive in this region, improved background rejection methods or the rejection of background events in hardware using special trigger configurations are necessary.

8.3 Upper Limit on the Pulsed Emission from the Crab Pulsar

Since the first detection of the Crab Pulsar was made in the radio band [64] in 1968, the pulsed emission from the Crab Pulsar at a period of $33\mu s$ has been detected from radio to HE gamma-ray energies up to a few GeV by various experiments. The current highest energy detection of the pulsed emission is made by EGRET at around a few GeV with no conclusive evidence of a cut-off in the emission. Various open questions, such as the acceleration mechanisms in the pulsar environment that give rise to HE pulsed emission, the location of the acceleration regions near the pulsar, and the highest energy that pulsars can accelerate particles, can not be answered with the currently available data. Currently, there are three popular HE pulsed emission models, the polar cap, the outer gap and the slot gap models, discussed in Section 2.2.4, that attempt to explain the HE pulsed emission. These models can be distinguished by the determination of the shape and the energy of the cut-off in the pulsed emission in the region between 10 GeV to 100 GeV.

With this motivation, a periodic modulation was searched for at the fre-

quency of the Crab Pulsar. A timing analysis was performed on the extracted gamma-ray events from the data sets collected during each commissioning phase of VERITAS. A relaxed cut set was used to accept events with energies as low as the trigger threshold of VERITAS in the region above 100 GeV. The analysis energy threshold achieved with these cuts was 0.18 TeV. An excess was searched for in the reconstructed pulse profile of the gamma-ray signal in the phase regions where EGRET detected the main and inter-peaks of pulsed emission. No significant excess was found in any data set. An upper limit on the flux of pulsed emission was calculated using the method of Helene [140] for each data set at the standard energy threshold of 0.26 TeV, using the standard analysis cuts. Additionally, assuming that the power law spectrum of the Crab Pulsar measured by EGRET is attenuated by an exponential cut-off in the GeV energies, an upper limit of < 50 GeV on the cut-off energy was determined. This cut-off does not distinguish between the models but strongly disfavors earlier claims by the outer gap models [142] of a strong TeV pulsed emission component due to IC scattering of the soft pulsed photons by the unshocked wind particles.

In the past, various ground-based experiments have searched for pulsed emission from several pulsars, as well as the Crab Pulsar, with no significant detection. In September 2008, MAGIC collaboration announced the detection of pulsed emission from the Crab Pulsar [61] above 25 GeV up to 60 GeV. Figure 8.3 shows the current upper limits on the pulsed emission from the Crab Pulsar as determined by various experiments and by this work. Currently, the most constraining upper limit on the cut-off energy is 27 GeV as determined by the Celeste [87] experiment and the earlier MAGIC publication [139].

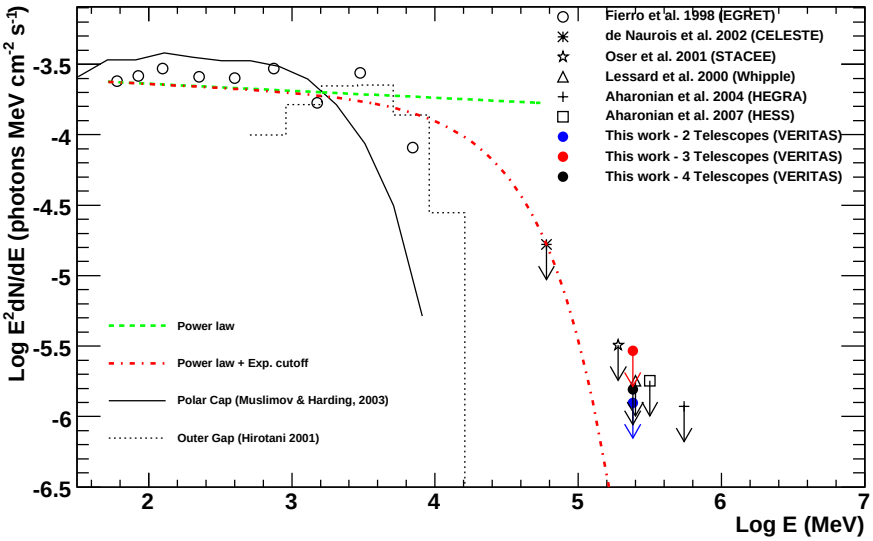

Figure 8.3: The integral flux upper limits on the pulsed emission from the Crab obtained from the 2-, 3- and 4-telescope data set are shown with filled circles along with the results from other experiments.

8.4 Future Directions for the Studies of Pulsed Emission from Pulsars

A future detection of the pulsed emission from the Crab Pulsar and observation of its cut-off energy could be possible by VERITAS or by any ground-based experiment, if the energy threshold of the instrument is reduced below 100 GeV. Although the atmospheric Cherenkov technique is challenged by the excessive background levels and by less efficient background rejection techniques in this energy range, special trigger configurations can be utilized to achieve additional background rejection. Having a larger mirror area also reduces the energy threshold by increasing the detected number of low energy signal photons by a larger fraction than the background photons. Currently, various studies are being made within the VERITAS collaboration to achieve a larger mirror area by exploiting the short baseline between telescopes T1 and T4. Additional tests are being made to reduce the energy threshold of VERITAS by employing special trigger configurations that have larger acceptance for low energy events at the hardware level compared to the standard trigger configuration.

Alternative to the ground-based detectors, the energy region below 100 GeV is now accessible by the current space-based telescope, FGST [24]. The main instrument of FGST, the Large Area Telescope (LAT), is a pair conversion telescope designed to detect gamma rays from 30 MeV to 300 GeV. The predicted high sensitivity of the LAT offers a very good opportunity to study high-energy pulsed emission from pulsars. It is estimated that the LAT will detect more than a hundred new gamma-ray pulsars, and thus it will significantly increase the current number of gamma-ray pulsars. It is hoped that many of the open questions of the pulsar physics can finally be answered by LAT measurements of the pulse profiles and the spectral characteristics of a large number of pulsars. Some of the

studies on pulsed emission from pulsars that will be possible with FGST data are discussed below.

8.4.1 Resolving the Puzzle on Location of Pulsed-Emission Sites

All the models, in principle, can predict the double-peak shape of the gamma-ray profile, given the overall geometry of the pulsar, i.e. the viewing angle and the magnetic inclination angle. But there are some differences between the predictions as discussed in Chapter 2. In summary, the polar cap models can produce narrow double-peak pulse profiles for only small inclination and viewing angles, and conversely, it is possible to create wider double-peak pulse profiles for the larger viewing angles in the slot gap and outer gap models. The outer gap models do not predict any off-pulse emission in contrary to the polar cap and slot gap models. LAT observations will lead to sufficient sensitivity in the pulse profiles of pulsars to resolve these differences and we should be able to make a statement about which model is responsible for the observed pulse profile.

8.4.2 Identify the Spectral Characteristics

We will be able to get much better photon statistics from a given pulsar because of the 30 times better sensitivity of the LAT compared to EGRET. Thus, it will be possible to apply additional harder event selection criteria to the data to select a phase-dependent sample and still have enough statistics. This will enable us to measure the spectrum separately for the pulsed emission from the pulsar and for the steady emission from the nebula. Application of the knowledge of the measured spectrum from the ground-based experiments in the overlapping energy region with FGST will give us the crucial information about the level of the steady emission flux. Thus, it will be also possible to measure the level of

the pulsed emission spectrum on the off-pulse regions by subtracting the steady emission from the total flux. Using the measured spectrum of the pulsed emission, one can study the shape of the cutoff in the spectra to distinguish between the pulsed emission models. FGST will be able to measure the spectrum with sufficient sensitivity to distinguish between the spectral cutoffs of the simple-exponential and super-exponential shapes. While the former shape argues for high-altitude emission models, a super-exponential cutoff favors polar cap model. The better sensitivity and energy resolution possible by LAT observations will also enable the detection of transitions in the pulsed spectrum. Additionally, the LAT can measure phase-resolved spectra with error bars five times smaller than EGRET [2]. The much improved statistics will enable measurements of spectral components and cut-offs as a function of phase and allow more detailed comparison with model predictions. In summary, the combination of the low-energy sensitivity of the LAT instrument in the 10-100 MeV range which will allow detections of breaks in the primary spectrum and the LAT's high energy sensitivity above 10 GeV which will allow observation of cut-offs in the spectra are ideal to answer many of the pressing questions.

8.4.3 Population Studies

FGST observations will provide a substantial increase in sensitivity to allow for the detection of many new pulsars. Increasing the number of available laboratories where we can study various aspects of pulsar physics may be the most significant result from pulsar observations with FGST. The large number of detected pulsars will not only help us to resolve current puzzles of pulsar physics, it will also make it possible to do population studies on different properties of pulsars. The ratio of the radio-quiet to radio-loud pulsars obtained from the large

number of FGST detected pulsars will give us an important diagnostics between the polar cap and outer gap models.

Although both models expect that more radio-quiet pulsars will be discovered, the outer gap models expect a larger ratio of radio-quiet to radio-loud pulsars. Detection or non-detection of gamma-ray pulsars older than 0.5 Myr will be another crucial test for the current models. Although the polar cap models predict that all pulsars are capable of pulsed emission at some level, the outer gap models predict a "death line" of pulsed emission between young and old pulsars depending on the period and surface magnetic field. The larger population of pulsars detected with FGST will also show if there is a correlation between spectral hardness and age. EGRET data indicated a trend among the six gamma-ray pulsars it detected: the peak of the power spectrum moves from hard X-rays to high energy gamma-rays for the middle age pulsars. LAT observations will show if similar trend persists among a higher number of pulsars.

APPENDIX A

Crab Data Set

The data recorded with the standard configuration at each VERITAS commissioning phase are listed in Tables A.1, A.2 and A.3 for 2-, 3- and 4-telescope data sets, respectively. In the first three columns, each table lists the date the data were recorded, the run numbers of the Crab data, and the corresponding laser run number used in the calibration of these data. The following four columns list the duration of each run, the source offset distance and direction from the pointing direction, and the mean elevation of the source during each run. The RMS of the FIR temperature during observations, the L3 rate and its RMS, and the elevation-adjusted L3 rate are listed in columns 7 to 10. Finally, each run is subject to a run quality selection, as explained in Section 5.3. In columns 10 to 14, if the run failed the selection criteria, it was tagged by an "X" according to the reason it was removed from the final selected data.

Table A.1: 2-Telescope data set recorded with the final configuration. The quantities on the columns are explained in the text.

Date	Run Number	Laser Run	Duration (min)	Pointing (°)	Mean Elevation (°)	FIR RMS (°C)	L3 Rate (Hz)	L3 Rate RMS (Hz)	L3/ cos(Zn) (Hz)	Dur <20 min	FIR RMS >B	Bad Hardware	Do Not Use
11/19/06	32341	32328	20	N 0.5	71.35	0.1 - A	103.90	1.90	109.65				
11/19/06	32342	32328	20	S 0.5	75.69	0.1 - A	103.64	1.53	106.95				
11/19/06	32343	32328	20	E 0.5	78.81	0.1 - A	102.47	1.38	104.46				
11/19/06	32344	32328	20	W 0.5	80.26	0.1 - A	100.98	1.21	102.46				
11/19/06	32345	32328	20	N 0.5	79.72	0.1 - A	102.32	1.25	103.99				
11/19/06	32346	32328	20	S 0.5	75.08	0.1 - A	101.97	1.33	105.53				
11/19/06	32347	32328	20	E 0.5	69.89	0.1 - A	102.66	1.11	109.33				
11/19/06	32348	32328	20	W 0.5	64.43	0.1 - A	101.02	1.43	111.99				
11/20/06	32374	32368	20	N 0.5	67.35	0.2 - B	102.57	1.17	111.14				

Continued on next page

Table A.1 – continued from previous page

Date	Run Number	Laser Run	Duration	Pointing	Mean Elevation	FIR RMS	L3 Rate	L3 Rate RMS	L3/ cos(Zn)	Dur <20 min	FIR RMS >B	Bad Hardware	Do Not Use
11/20/06	32375	32368	20	S 0.5	71.03	0.1 - A	101.62	1.24	107.46				
11/20/06	32376	32368	20	E 0.5	74.94	0.1 - A	101.27	1.37	104.87				
11/20/06	32377	32368	20	W 0.5	78.92	0.1 - A	99.92	1.31	101.82				
11/20/06	32378	32368	20	N 0.5	80.70	0.1 - A	98.36	1.95	99.67				
11/20/06	32379	32368	20	S 0.5	79.09	0.1 - A	100.67	3.22	102.52				
11/20/06	32380	32368	20	E 0.5	77.21	0.1 - A	99.53	1.04	102.06				
11/20/06	32381	32368	20	W 0.5	72.67	0.1 - A	100.09	1.45	104.85				
11/21/06	32404	32400	20	N 0.5	65.53	0.1 - A	99.43	1.07	109.24				
11/21/06	32405	32400	20	S 0.5	69.32	0.1 - A	99.26	1.25	106.10				
11/21/06	32406	32400	20	E 0.5	74.10	0.1 - A	98.30	1.07	102.21				
11/21/06	32407	32400	20	W 0.5	78.08	0.1 - A	96.50	1.64	98.63				
11/21/06	32408	32400	20	N 0.5	80.43	0.1 - A	96.93	1.16	98.30				
11/22/06	32435	32430	20	N 0.5	65.56	0.1 - A	101.25	1.65	111.22				

Continued on next page

Table A.1 – continued from previous page

Date	Run Number	Laser Run	Duration	Pointing	Mean Elevation	FIR RMS	L3 Rate	L3 Rate RMS	L3/ cos(Zn)	Dur <20 min	FIR RMS >B	Bad Hardware	Do Not Use
11/22/06	32436	32430	20	S 0.5	69.34	0.1 - A	100.06	1.27	106.94				
11/22/06	32437	32430	20	E 0.5	73.38	0.1 - A	100.45	1.17	104.83				
11/22/06	32438	32430	20	W 0.5	77.65	0.1 - A	98.78	1.35	101.12				
11/22/06	32439	32430	20	N 0.5	80.19	0.1 - A	98.49	1.35	99.95				
11/22/06	32440	32430	20	S 0.5	79.64	0.1 - A	98.41	1.54	100.04				
11/23/06	32467	32461	20	N 0.5	70.60	0.1 - A	99.55	1.18	105.54				
11/23/06	32468	32461	20	S 0.5	73.99	0.1 - A	99.02	1.27	103.02				
11/23/06	32469	32461	20	E 0.5	77.44	0.1 - A	98.38	1.16	100.79				
11/23/06	32470	32461	20	W 0.5	80.09	0.1 - A	96.37	1.05	97.83				
11/24/06	32496	32494	1	N 0.5	-	0.1 - A	-	-	-	X			X
11/24/06	32497	32494	20	N 0.5	71.23	0.1 - A	101.32	1.10	107.01				
11/24/06	32498	32494	20	S 0.5	74.63	0.2 - B	99.41	1.34	103.10				
11/24/06	32499	32494	20	E 0.5	77.91	1.1 - D	97.64	4.21	99.85		X		X

Continued on next page

Table A.1 – continued from previous page

Date	Run Number	Laser Run	Duration	Pointing	Mean Elevation	FIR RMS	L3 Rate	L3 Rate RMS	L3/ cos(Zn)	Dur <20 min	FIR RMS >B	Bad Hardware	Do Not Use
11/24/06	32500	32494	20	W 0.5	80.16	1.6 - D	87.60	7.35	88.91		X		X
11/24/06	32501	32494	20	N 0.5	80.20	5.6 - D	87.06	12.27	88.35		X		X

Table A.2: 3-Telescope data set recorded with the final configuration. The quantities on the columns are explained in the text.

Date	Run Number	Laser Run	Duration (min)	Pointing (°)	Mean Elevation (°)	FIR RMS (°C)	L3 Rate (Hz)	L3 Rate RMS (Hz)	L3/ cos(Zn) (Hz)	Dur <20 min	FIR RMS >B	Bad Hardware	Do Not Use
12/15/06	32855	32854	20	0.5 N	80.75	0.1 - A	162.77	2.8	164.91				
12/15/06	32856	32854	20	0.5 S	78.78	0.1 - A	169.22	2.73	172.52				
12/16/06	32880	32870	20	0.5 S	73.00	0.1 - A	146.73	6.58	153.43				
12/16/06	32881	32870	20	0.5 N	77.00	0.1 - A	146.24	9.46	150.09				
12/18/06	32947	32945	10	0.5 E	58.00	12.2- D	25.93	32.40	30.58	X	X		X
12/18/06	32948	32945	20	0.5 W	58.00	15.0- D	48.91	41.70	57.67		X		X
12/18/06	32949	32945	20	0.5 N	68.00	16.2- D	48.07	41.90	51.85		X		X
12/18/06	32950	32945	20	0.5 S	72.00	13.0- D	81.73	41.90	85.94		X		X
12/18/06	32952	32945	20	0.5 E	80.00	12.9- D	30.04	32.10	30.50		X		X

Continued on next page

Table A.2 – continued from previous page

Date	Run Number	Laser Run	Duration	Pointing	Mean Elevation	FIR RMS	L3 Rate	L3 Rate RMS	L3/ cos(Zn)	Dur <20 min	FIR RMS >B	Bad Hardware	Do Not Use
12/20/06	32983	32967	20	0.5 S	74.03	0.2 - B	171.42	2.97	178.30				
12/21/06	33006	32996	20	0.5 N	68.12	0.2 - B	165.58	1.59	178.43				
12/21/06	33007	32996	20	0.5 S	71.84	0.2 - B	168.06	1.42	176.87				
12/21/06	33008	32996	20	0.5 W	76.31	0.1 - A	157.97	-	162.59				
12/21/06	33009	32996	20	0.5 E	78.69	0.1 - A	167.42	1.35	170.74				
01/09/07	33274	33264	15	0.5 E	79.09	2.3 - D	146.49	7.33	149.19	X	X		X
01/09/07	33275	33264	15	0.5 W	80.29	1.7 - D	136.72	2.72	138.71	X	X		X
01/10/07	33304	33289	5	0.5 N	81.00	0.1 - A	177.00	-	179.21	X			X
01/10/07	33305	33289	20	0.5 N	79.02	0.1 - A	172.55	3.30	175.77				
01/10/07	33306	33289	20	0.5 S	74.97	0.1 - A	172.35	2.31	178.45				
01/15/07	33372	33369	20	0.5 W	73.51	0.1 - A	165.75	-	172.86				
01/15/07	33373	33369	20	0.5 E	76.46	0.2 - B	175.05	1.79	180.05				
01/16/07	33402	33401	20	0.5 N	79.88	0.1 - A	168.44	2.27	171.10				

Continued on next page

Table A.2 – continued from previous page

Date	Run Number	Laser Run	Duration	Pointing	Mean Elevation	FIR RMS	L3 Rate	L3 Rate RMS	L3/ cos(Zn)	Dur <20 min	FIR RMS >B	Bad Hardware	Do Not Use
01/16/07	33403	33401	18	0.5 S	79.95	0.1 - A	167.88	3.35	170.50				
01/17/07	33437	33441	2	0.5 W	72.00	0.1 - A	124.00	-	130.38			X	X
01/17/07	33438	33441	20	0.5 W	75.38	0.2 - B	163.65	1.94	169.13				
01/17/07	33439	33441	20	0.5 E	78.03	0.1 - A	165.28	1.66	168.95				
01/18/07	33474	33473	20	0.5 E	68.85	3.1 - D	133.66	8.91	143.31		X		X
01/18/07	33475	33473	20	0.5 W	73.81	3.8 - D	123.41	7.20	128.51		X		X
01/19/07	33494	33473	20	0.5 N	75.44	4.1 - D	109.72	8.11	113.36		X		X
02/06/05	33709	33993	20	0.5 N	74.40	0.1 - A	171.64	2.04	178.20				
02/07/05	33718	33993	20	0.5 W	79.84	0.2 - B	166.90	3.31	169.56				
02/09/05	33745	33993	20	0.5 S	79.59	0.1 - A	168.70	2.36	171.52				
02/09/05	33746	33993	20	0.5 E	79.89	0.1 - A	167.68	1.85	170.32				
02/10/07	33765	33993	20	0.5 N	68.00	1.3 - D	159.00	-	171.49		X		X
02/10/07	33766	33993	20	0.5 N	62.96	3.3 - D	107.34	8.42	120.51		X		X

Continued on next page

Table A.2 – continued from previous page

Date	Run Number	Laser Run	Duration	Pointing	Mean Elevation	FIR RMS	L3 Rate	L3 Rate RMS	L3/ cos(Zn)	Dur <20 min	FIR RMS >B	Bad Hardware	Do Not Use
02/11/07	33786	33993	8	0.5 N	63.00	2.8 - D	97.00	-	108.87	X	X		X
02/11/07	33787	33993	10	0.5 N	59.60	3.8 - D	102.45	17.30	118.78	X	X		X
02/18/07	33913	33993	30	0.5 N	70.57	1.6 - D	142.16	4.00	150.75		X		X
02/18/07	33915	33993	0	0.5 N		-	-	-	0.00	X	X		X
02/18/07	33916	33993	1	0.5 N		-	-	-	0.00	X	X		X

Table A.3: 4-Telescope data set recorded with the final configuration. The quantities on the columns are explained in the text.

Date	Run Number	Laser Run	Duration (min)	Pointing (°)	Mean Elevation (°)	FIR RMS (°C)	L3 Rate (Hz)	L3 Rate RMS (Hz)	L3/ cos(Zn) (Hz)	Dur <20 min	FIR RMS >B	Bad Hardware	Do Not Use
09/11/07	36286	36288	3		61.56	0.1 - A	91.14	1.62	103.65	X		X	X
09/11/07	36286	36289	20	0.5N	64.29	0.1 - A	150.88	24.94	167.46			X	X
09/13/07	36392	36406	20	0.5S	54.22	0.4 - C	191.03	5.03	235.47		X		X
09/13/07	36392	36407	20	0.5E	59.09	10.5 - D	131.82	49.24	153.64		X		X
09/13/07	36392	36408	20	0.5W	64.49	8.8 - D	122.32	38.12	135.53		X		X
09/14/07	36448	36454	20	0.5W	62.07	0.7 - D	207.39	6.79	234.73		X		X
09/14/07	36448	36455	20	0.5E	65.69	0.3 - C	218.97	4.18	240.27		X		X
09/15/07	36480	36492	20	0.5N	66.97	0.3 - C	205.73	2.09	223.55		X		X

Continued on next page

Table A.3 – continued from previous page

Date	Run Number	Laser Run	Duration	Pointing	Mean Elevation	FIR RMS	L3 Rate	L3 Rate RMS	L3/ cos(Zn)	Dur <20 min	FIR RMS >B	Bad Hardware	Do Not Use
09/19/07	36601	36604	20	0.5W	70.81	0.2 - B	242.78	3.24	257.06				
09/20/07	36633	36634	20	0.5S	68.74	0.1 - A	259.84	2.5	278.81				
10/10/07	37008	37009	20	0.5E	80.06	0.1 - A	246.62	2.47	250.38				
10/10/07	37008	37010	8	0.5W	80.01	0.1 - A	245.46	2.75	249.24	X		X	X
10/11/07	37034	37039	20	0.5W	79.1	0.1 - A	259	1.56	263.76				
10/14/07	37177	37195	20	0.5S	76.77	0.1 - A	254.8	2.01	261.75				
10/15/07	37228	37230	20	0.5S	77.95	0.1 - A	250.81	2.69	256.46				
10/15/07	37228	37231	19	0.5W	75.03	0.1 - A	251.8	3.92	260.65	X		X	X
10/16/07	37263	37266	20	0.5W	76.31	0.1 - A	238.31	2.39	245.28				
10/16/07	37263	37267	5	0.5E	74.33	0.1 - A	241.28	2.72	250.59	X		X	X
10/17/07	37296	37297	20	0.5S	76.49	0.1 - A	239.55	2.41	246.37				
10/17/07	37296	37298	13	0.5N	74.33	0.1 - A	237.88	1.81	247.06	X		X	X
10/20/07	37433	37438	20	0.5N	77.29	0.1 - A	239.95	3.61	245.98			X	X

Continued on next page

Table A.3 – continued from previous page

Date	Run Number	Laser Run	Duration	Pointing	Mean Elevation	FIR RMS	L3 Rate	L3 Rate RMS	L3/ cos(Zn)	Dur <20 min	FIR RMS >B	Bad Hardware	Do Not Use
11/10/07	37813	37810	0	-	77.7	-	48.02	0	49.15	X		X	
11/10/07	37813	37811	10	0.5N	78.54	1.9 - D	179.22	3.42	182.87	X	X		X
11/14/07	37955	37945	20	0.5N	70.73	0.1 - A	251.74	3.27	266.68				
11/14/07	37955	37946	20	0.5S	74.2	0.1 - A	256.74	1.65	266.82				
11/14/07	37955	37947	20	0.5E	77.57	0.1 - A	260	1.42	266.24				
11/14/07	37955	37948	20	0.5W	80.06	0.1 - A	261.22	2	265.2				
11/14/07	37955	37949	20	0.5N	80.47	0.1 - A	262.72	1.91	266.4				
11/14/07	37955	37950	20	0.5S	77.55	0.1 - A	262.93	2	269.26				
11/15/07	37969	37977	20	0.5W	66.14	4.6 - D	167.89	31.63	183.58		X		X
11/17/07	38046	38031	20	0.5W	62.76	0.1 - A	197.62	2.74	222.27				
11/17/07	38046	38032	20	0.5E	66.57	0.1 - A	217.57	17.53	237.12				
11/17/07	38046	38033	20	0.5N	71.62	0.1 - A	209.97	1.54	221.26				
11/17/07	38046	38034	20	0.5S	74.92	0.1 - A	214.22	1.76	221.86				

Continued on next page

Table A.3 – continued from previous page

Date	Run Number	Laser Run	Duration	Pointing	Mean Elevation	FIR RMS	L3 Rate	L3 Rate RMS	L3/ cos(Zn)	Dur <20 min	FIR RMS >B	Bad Hardware	Do Not Use
11/17/07	38046	38035	20	0.5E	78.21	0.1 - A	218.56	2.25	223.27				
11/18/07	38076	38060	0	-					0	X			X
11/18/07	38076	38061	20	0.5N	64.83	0.1 - A	241.7	1.92	267.06				
11/18/07	38076	38062	20	0.5S	68.59	0.1 - A	245.27	2.14	263.45				
11/18/07	38076	38063	20	0.5E	72.54	0.1 - A	255.89	13.37	268.25				
11/18/07	38076	38064	20	0.5W	76.85	0.1 - A	252.58	2.18	259.38				
12/04/07	38186	38200	20	0.5E	79.69	0.1 - A	270.89	2.17	275.34				
12/06/07	38267	38273	20	0.5W	79.91	0.1 - A	267.86	2.49	272.07				
12/14/07	38369	38362	20	0.5N	78.96	1.2 - D	238.89	22.19	243.39		X		X
12/15/07	38393	38405	20	0.5S	78.88	0.2 - B	261.79	2.2	266.8				
12/30/07	38508	38523	20	0.5N	80.33	0.1 - A	260.55	2.36	264.31				
01/02/08	38593	38588	20	0.5S	51.51	4.7 - D	164.81	12.27	210.56		X		X
01/02/08	38593	38589	20	0.5E	55.83	3.8 - D	182.62	11.85	220.72		X		X

Continued on next page

Table A.3 – continued from previous page

Date	Run Number	Laser Run	Duration	Pointing	Mean Elevation	FIR RMS	L3 Rate	L3 Rate RMS	L3/ cos(Zn)	Dur <20 min	FIR RMS >B	Bad Hardware	Do Not Use
01/02/08	38593	38590	20	0.5W	61.14	2.3 - D	178.64	6.56	203.97		X		X
01/02/08	38593	38591	20	0.5N	65.28	2.9 - D	157.39	9.7	173.27		X		X
01/02/08	38593	38592	20	0.5S	69.25	1.4 - D	144.81	6.48	154.85		X		X
01/11/08	38731	38722	20	0.5W	67.98	0.1 - A	246.15	2.9	265.52				
01/12/08	38786	38753	20	0.5E	58.28	0.1 - A	217.17	3.94	255.31			X	X
01/12/08	38786	38762	4	0.5W	77.73	0.1 - A	246.93	4.27	252.7	X		X	X
01/12/08	38786	38763	0	0.5W	77.17	0.1 - A	74.37	0	76.27	X		X	X
01/12/08	38786	38764	20	0.5W	75.4	0.1 - A	242.91	1.45	251.02				
01/13/08	38817	38798	20	0.5W	74.55	0.9 - D	247.09	3.45	256.35		X		X
01/30/08	38968	38957	20	0.5E	80.03	0.1 - A	253.37	1.75	257.25				
01/30/08	38968	38958	20	0.5W	79.61	0.2 - B	252.8	1.75	257.01				
02/02/08	39053	39035	20	0.5N	75.78	0.1 - A	251.46	2.17	259.41				
02/02/08	39053	39036	16	0.5S	77.89	0.1 - A	254.53	2.07	260.32	X		X	X

Continued on next page

Table A.3 – continued from previous page

Date	Run Number	Laser Run	Duration	Pointing	Mean Elevation	FIR RMS	L3 Rate	L3 Rate RMS	L3/ cos(Zn)	Dur <20 min	FIR RMS >B	Bad Hardware	Do Not Use
02/03/08	39096	39072	20	0.5S	79.76	0.1 - A	249.82	1.94	253.86				
02/03/08	39096	39073	20	0.5E	79.31	0.1 - A	249.5	2.26	253.91				
02/06/08	39132	39109	20	0.5W	80.25	0.1 - A	255.1	2.59	258.84				
02/25/08	39465	39459	20	0.5N	80.67	0.1 - A	155.18	2.83	157.26			X	X
02/25/08	39465	39460	20	0.5N	79.91	0.5 - D	140.9	23.1	143.11		X	X	X
02/25/08	39465	39461	20	0.5S	73.21	0.7 - D	137.53	2.59	143.65		X	X	X
03/11/08	39863	39833	20	0.5N	66.47	0.2 - B	224.29	5.75	244.63				

References

[1] Harding, A. K. *AIPC* **921**, 49 (2007).

[2] Harding, A. K. *arXiv-0710.3517v1* (2007).

[3] Aharonian, F. A. and Bogovalov, S. *New Astronomy* **8**, 85 (2003).

[4] Aharonian, F. A. and et al. *ApJ* **614**, 897 (2004).

[5] Gaensler, B. M. and Slane, P. O. *Annual Rev. Astron, Astrophys.* **44**, 17 (2006).

[6] Nolan et al, P. L. *ApJ* **409**, 697 (1993).

[7] Hillas, A. M. *ApJ.* **503**, 744 (1998).

[8] De Jager et al, O. C. *ApJ.* **457**, 253 (1996).

[9] Atoyan, A. M. and Aharonian, F. A. *MNRAS* **278**, 525 (1996).

[10] Kildea, J. PhD thesis, University College Dublin, (2002).

[11] Cogan, P. PhD thesis, University College Dublin, (2006).

[12] Roache et al., E. In *Proc. 30th I.C.R.C. Merida, Mexico*, (2007).

[13] Hall et al., J. In *Proc. 28nd I.C.R.C. Tsukuba, Japan*, (2003).

[14] White et al., R. J. In *Proc. 30th I.C.R.C. Merida, Mexico*, (2007).

[15] Weinstein et al., A. In *Proc. 30th I.C.R.C. Merida, Mexico*, (2007).

[16] Hays et al., E. In *Proc. 30th I.C.R.C. Merida, Mexico*, (2007).

[17] Ong, R. A. *Physics Reports* **305**, 93 (1998).

[18] Hillas, A. M. In *Proc. 19nd I.C.R.C. (La Jolla)*, volume 3, 445, (1985).

[19] Weekes et al., T. *Physics Reports* **160**, 1–121 (1988).

[20] Weekes, T. C. Institute of Physics, Bristol, (2003).

[21] Hess, V. F. *Physikalische Zeitschrift* **13**, 1084 (1912).

[22] Collaboration, T. P. A. *arXiv* **0806.4302v1** (2008).

[23] Morrison, P. *Nuovo Cimento* **7**, 858 (1958).

[24] *<http://glast.gsfc.nasa.gov/science/433-SRD-0001_CH-03.pdf>* (2000).

[25] Thompson et al., D. J. *Astrophysical Journal S.S* **101**, 259 (1995).

[26] *<http://www-glast.slac.stanford.edu/>* .

[27] Browning, R., Ramsden, D., and Wright, P. *Nature Physical Science* **232**, 99 (1971).

[28] Albats, P. and et al. *Nature* **240**, 221 (1972).

[29] Parlier, B. and et al. *Nature Physical Science* **242**, 117 (1973).

[30] Derdeyn et al., S. M. *NIM* **98**, 557 (1972).

[31] Bignami, G. F. and et al. *Space Science Instrument* **1**, 245 (1975).

[32] Paciesas et al., W. S. *Astrophysical Journal S.S* **122**, 465 (1999).

[33] Johns et al., W. S. In *Workshop: Imaging in High Energy Astronomy*, 329, (1993).

[34] Schonefelder et al., V. *Astrophysical Journal S.S* **86**, 657 (1993).

[35] Hartman et al., R. C. *Astrophysical Journal S.S.* **123**, 79 (1999).

[36] *<http://cossc.gsfc.nasa.gov/docs/cgro/images/egret/EGRET_All_Sky.jpg>* .

[37] Tavani et al., M. *Proceedings of the SPIE* **6266**, 626603 (2006).

[38] *<http://heasarc.gsfc.nasa.gov/docs/cgro/index.html>* .

[39] Cocconi, G. In *Proc. Moscow Cosmic Ray Conf., Moscow*, volume 2, 309, (1960).

[40] Weekes, T. C. and Turver, K. E. *Recent Advan. in Gamma-Ray Astronomy* , 279 (1977).

[41] Weekes et al., T. *ApJ* **342**, 379 (1989).

[42] Kildea, J. and et al. *APh* **28**, 182 (2007).

[43] Punch et al., M. *Nature* **358**, 477 (1992).

[44] Quinn, J. and et al. *IAU Circ.* **6178**, 1 (1995).

[45] Catanese, M. and et al. *ApJ* **501**, 616 (1998).

[46] Horan, D. and et al. *ApJ* **571**, 753 (2002).

[47] Kosack, K. e. a. *ApJ* **608**, L97 (2004).

[48] Puhlhofer, G. and et al. *APh* **20**, 267 (2003).

[49] Aharonian, F. A. and et al. *A&A* **370**, 112 (2001).

[50] Aharonian, F. A. and et al. *A&A* **393**, L37 (2002).

[51] Aharonian, F. A. and et al. *A&A* **403**, L1 (2003).

[52] Enomoto, R. and et al. *ApJ.* **638**, 397 (2006).

[53] Cortina et al., J. In *Proc. 29th I.C.R.C. Pune, India*, volume 5, 359, (2005).

[54] Baixeras, C. and et al. In *Proc. 29th I.C.R.C. Pune, India*, 227, (2005).

[55] Hoffman, W. and et al. In *Proc. 28nd I.C.R.C. Tsukuba, Japan*, volume 5, 2811, (2003).

[56] Vincent, P. and et al. In *Proc. 29th I.C.R.C. Merida, Mexico*, 163, (2005).

[57] Gingrich, D. M. and et al. *IEEE Trans. Nuclear Science* **52**, 2977 (2005).

[58] Smith, D. A. and et al. *Nuclear Physics B Proceedings Supplements* **54**, 362 (1997).

[59] Ribo, M. *arXiv:* **0801.2906v1** (2008).

[60] Hewish et al., A. *Nature* **217**, 709 (1968).

[61] Alui, E. and et al. (MAGIC Coll.). *arXiv:0809.2998* (2008).

[62] Pacini, F. *Nature* **216**, 567 (1967).

[63] Gold, T. *Nature* **218**, 731 (1968).

[64] Staelin, D. H. and Reifenstein III, E. C. *Science* **162**, 1481 (1968).

[65] Richards, D. W. and Comella, J. M. *Nature* **222**, 551 (1969).

[66] Lyne, A. and Graham-Smith, F. Cambridge University Press, (2006).

[67] Lyne, A. and Graham-Smith, F. Cambridge University Press, (2006).

[68] Ostriker, J. P. and Gunn, J. E. *ApJ* **157**, 1395 (1969).

[69] Lyne, A. and Graham-Smith, F. Cambridge University Press, (2006).

[70] Melrose, D. In *Proc. of Young Neutron Stars and Their Environments IAU Symposium*, (2004).

[71] Goldreich, P. and Julian, W. H. *ApJ* **157**, 869 (1969).

[72] Daugherty, J. K. and Harding, A. K. *ApJ.* **252**, 337 (1982).

[73] Daugherty, J. K. and Harding, A. K. *ApJ.* **458**, 278 (1996).

[74] Ruderman, M. A. and Sutherland, P. G. *ApJ.* **196**, 51 (1975).

[75] Muslimov, A. G. and Tsygan, A. I. *MNRAS* **255**, 61 (1992).

[76] Baring, M. G. and Harding, A. K. *ApJ.* **547**, 929 (2001).

[77] Arons, J. *ApJ.* **266**, 215 (1983).

[78] Muslimov, A. G. and Harding, A. K. *ApJ.* **606**, 1143 (2004).

[79] Cheng, K. S., Ho, C., and Ruderman, M. A. *ApJ.* **300**, 500 (1986).

[80] Romani, R. W. *ApJ.* **470**, 469 (1996).

[81] Grenier, I. A. and Harding, A. K. In *AIP Conference Proceedings*, volume 861, 630, (2006).

[82] Cheng, K. S., Ho, C., and Ruderman, M. A. *ApJ.* **402**, 264 (1986).

[83] Thompson et al., D. J. *ApJ.* **436**, 229 (1994).

[84] Manchester et al., R. N. *MNRAS* **328**, 17 (2001).

[85] Aharonian, F. A. and et al. *Astronomy and Astrophysics* **466**, 543 (2007).

[86] Lessard et al, R. W. *ApJ.* **531**, 942 (2000).

[87] de Naurois et al, M. *ApJ* **566**, 343 (2002).

[88] Celik et al., O. In *Proc. 30th I.C.R.C. Merida, Mexico*, (2007).

[89] Gold, T. *Nature* **221**, 25 (1969).

[90] Rees, M. J. and Gunn, J. E. *MNRAS* **167**, 1 (1974).

[91] Kennel, C. F. and Coroniti, F. V. *ApJ.* **283**, 694 (1984).

[92] Kennel, C. F. and Coroniti, F. V. *ApJ.* **283**, 710 (1984).

[93] Bogovalov, S. V. and Aharonian et al., F. A. *MNRAS* **313**, 504 (2000).

[94] Kirk, J. G., Lyubarsky, Y., and Petri, J. *astro.ph* **03116** (2007).

[95] Gould, R. J. *Phys.Rev.Letters* **15**, 577 (1965).

[96] De Jager, O. C. and Harding, A. K. *ApJ.* **396**, 161 (1992).

[97] Bolton, J., Stanley, G., and Slee, O. *Nature* **164**, 101 (1949).

[98] Shklovsky, I. S. *Dok. Akad. Naus USSR [Soviet Phys. Dokl.]* **90**, 983 (1953).

[99] Kinzer, D. A., Share, G. H., and Seeman, N. *ApJ.* **180**, 547 (1973).

[100] Thompson et al., D. J. *ApJ.* **213**, 252 (1977).

[101] Bennett, K. *Astronomy and Astrophysics* **61**, 279 (1977).

[102] Clear et al., J. *Astronomy and Astrophysics* **174**, 85 (1987).

[103] Fierro et al, J. M. *ApJ.* **494**, 734 (1998).

[104] Oser et al, S. *ApJ* **547**, 949 (2001).

[105] Jelley, J. V. *Cherenkov Radiation and its Applications.* Pergamon Press, (1958).

[106] Kosack, K. P. PhD thesis, Washington University, (2005).

[107] Ergin, T. PhD thesis, Humboldt-Universitat zu Berlin, (2005).

[108] Hillas, A. M. *Space Science Reviews* **75**, 17 (1996).

[109] Cherenkov, P. *Phys. Rev.* **52**, 378 (1937).

[110] Frank, I. and Tamm, I. *Dokl. Akad, SSSR* **14**, 109 (1937).

[111] Galbraith, W. and Jelley, J. V. *Nature, London* **171**, 349 (1953).

[112] Jelley, J. and Porter, N. *Quarterly J. of the R.A.S* **4**, 275 (1963).

[113] Reynolds et al., P. T. *ApJ* **404**, 206 (1993).

[114] Holder, J. In *Proc. 29nd I.C.R.C. Pune, India*, (2005).

[115] Davies, J. M. and Cotton, E. S. *Journal of Solar Energy* **1**, 16 (1957).

[116] Gibbs et al., K. In *Proc. 28nd I.C.R.C. Tsukuba, Japan*, (2003).

[117] Weekes et al., T. *ApJ* **17**, 221 (2002).

[118] Toner et al., J. In *Proc. 30th I.C.R.C. Merida, Mexico*, (2007).

[119] Nagai, T. In *Proc. 30th I.C.R.C. Merida, Mexico*, (2007).

[120] Jordan, P. and Krennich, F. In *<http://cherenkov.physics.iastate.edu>*, (2004).

[121] Bradbury, S. M. and Rose, H. J. *Nuclear Inst. and Methods in Phys. Rsch A* **481**, 521–528 (2002).

[122] Buckley et al., J. H. In *Proc. 28nd I.C.R.C. Tsukuba, Japan*, (2003).

[123] Hanna et al., D. In *Proc. 30th I.C.R.C. Merida, Mexico*, (2007).

[124] Heck et al., D. *Forschungszentrum Karlsruhe Report FZKA 6019* (1998).

[125] Duke, C. and LeBohec, S. *<http://www.physics.utah.edu/gammaray/GrISU/ >* .

[126] Maier et al., G. In *Proc. 30th I.C.R.C. Merida, Mexico*, (2007).

[127] Maier et al., G. *<http://veritas.sao.arizona.edu/wiki/index.php/McGill_Simulations>* .

[128] Cogan et al., P. In *Proc. 30th I.C.R.C. Merida, Mexico*, (2007).

[129] Daniel et al., M. K. In *Proc. 30th I.C.R.C. Merida, Mexico*, (2007).

[130] Hofmann, W., Jung, I., Konopelko, A., and et al. *APh* **12**, 135 (1999).

[131] Daum et al., A. *APh* **8**, 1 (1997).

[132] Aharonian, F. A. and et al. *Astronomy and Astrophysics* **457**, 899 (2006).

[133] Li, T. and Ma, Y. *ApJ.* **272**, 317 (1983).

[134] Lyne, A. and Roberts, M. E. *<http://www.jb.man.ac.uk/pulsar/crab.html>* .

[135] Lyne, A., Pritchard, R. S., and Smith, F. G. *MNRAS* **265**, 1003 (1993).

[136] Standish, E. M. *A&A* **114**, 297 (1982).

[137] *<ftp://ssd.jpl.nasa.gov/pub/ephem/>* .

[138] Wallace, P. T. *Starlink User Note* **67.45** (1999).

[139] Albert, J. and et al. *arXiv-0705.3244* (2007).

[140] Helene, O. *NIM* **212**, 319 (1983).

[141] Dombrovsky, V. A. *Dokl. Akad. Nauk. SSSR* **94**, 1021 (1954).

[142] Hirotani, K. and Shibata, S. *ApJ* **558**, 216 (2001).